SAFEGEO – Final report

Manageable seismic risks for geothermal projects in fractured reservoirs: A case study for the Californië sites in Limburg

TNO Publiek ⟩ TNO 2025 R10357
17 February 2025

Energy & Materials Transition
www.tno.nl
+31 88 866 42 56
info@tno.nl

TNO 2025 R10357 – 17 February 2025

SAFEGEO - Final report

Manageable seismic risks for geothermal projects in fractured reservoirs: A case study for the Californië sites in Limburg

Author(s)	Wassing, B., Peeters, S., Peters, E., Paap, B., Osinga, S., Kraaijpoel, D., Wollenweber, J. (all TNO) Laenen, B., Pogacnik, J., Rombouts, B. (all VITO) Baisch, S. (Q-Con) Ruigrok, E., Kruiver, P. (all KNMI)
Classification report	TNO Publiek
Title	SAFEGEO - Manageable seismic risks for geothermal projects in fractured reservoirs
Number of pages	166 (excl. front, back cover and appendices)
Number of appendices	9
Consortium partners	TNO (coordinator), NAPPA B.V., Californië Wijnen Geothermie B.V., Energie Beheer Nederlands B.V.
Associated partners	VITO, Q-con, KNMI
Programme name	TKI Urban Energy PPS-toeslag 2022
Project name	Beheersbare seismische risico's voor geothermieprojecten in verbreukte reservoirs
Project number	TKI2221403; TNO 060.55650

Het project is uitgevoerd met PPS-programmatoeslag subsidie van het Ministerie van Economische Zaken en Klimaat voor TKI Urban Energy, Topsector Energie.
http://www.tki-urbanenergy.nl

The project was carried out with a PPP program allowance subsidy from the Ministry of Economic Affairs and Climate for TKI Urban Energy, Topsector Energy.
http://www.tki-urbanenergy.nl

Management Summary

Fractured and karstified Dinantian carbonate reservoirs can hold significant potential for geothermal heat extraction and future geothermal projects. Two geothermal sites in the Netherlands, Californië Wijnen Geothermie (CWG) and NAPPA, previously Californië Lipzig Gielen (CLG) have targeted these reservoirs. The sites are located in the Venlo Graben which is part of the Neogene Roer Valley Rift System, an area with natural seismicity. The sites produced substantial sustainable heat from 2013 to 2018, but experienced small induced seismic events, leading to the suspension of operations in 2018. Magnitudes (Ml) of the induced events recorded during and shortly after the operations varied between -0.5 and 1.7.

Understanding the relationship between geothermal operations and induced seismicity in the Dinantian carbonates is crucial for safe development. Geothermal operations in fractured rocks in seismically active areas may pose increased hazards compared to conventional geothermal production from sandstones. The project aims to improve understanding of seismicity mechanisms at the Californië sites through subsurface models and data analysis. This will help assess seismic hazards and develop mitigation measures for safe geothermal production. Additionally, the project proposes a framework for seismic hazard assessment and recommendations for a potential pilot phase at the Californië site to validate models, enhance insights into seismicity and mitigation measures, and to evaluate if safe production from the fractured Dinantian carbonates is possible.

A data inventory was performed, to gather all relevant information, including operational data and seismicity records from the operational period. The study utilized data and information from five wells, well logs, well tests and production logs, original seismic lines and additional SCAN lines as input to the subsurface models. Operational data (injection/production rates, pressures and temperatures) and seismicity records during previous operations at the CWG and CLG site were used for history-matching and calibrating the subsurface models. These models were used to analyse the relationship between past operations and induced seismicity, enhancing the understanding of the mechanisms driving seismicity.

Four subsurface models were constructed: geological, dynamic reservoir, geomechanical, and velocity model. The geological, dynamic reservoir and geomechanical model were used to assess the pressure, temperature changes in the reservoirs and Coulomb stress changes on the faults during former operations. Four main fault structures were included, from West to East: the Tegelen Fault, Carboniferous Normal Fault, and a potential Western and Eastern Pop-Up Fault. Production well CAL-GT-01 (CWG) and CAL-GT-04 (CLG) produce from the damage zone of the Tegelen Fault and its antithetic Carboniferous Normal Fault. Injection well CAL-GT-03 (CWG) intersects and injects into the Carboniferous Normal Fault. Well CAl-GT-02 (CWG, blocked) and injection well CAL-GT-05 (CLG) are potentially located close to the Western and Eastern Pop-Up Fault.

Satisfactory history matches for the dynamic reservoir were achieved with the assumption that flow is fault- and fracture dominated and that there is little permeability in most areas outside the fault zones. The geomechanical simulations indicate that, during operation of the

CWG doublet, gradual cooling occurred on the Carboniferous Normal Fault due to injection in well CAL-GT-03, which intersects the Carboniferous Fault. Temperature decreases on the Carboniferous Normal Fault over time led to decreased normal stresses, which unclamped the fault, and caused positive Coulomb stress changes, bringing it (close) to failure. These Coulomb stress changes are larger than on the Tegelen Fault, mainly due to the short distance between the Carboniferous Normal Fault and injection well CAL-GT-03 and because the Tegelen Fault is ‘shielded’ from the CAL-GT-03 injection well by the Carboniferous Normal Fault. Though thermal stresses from cold water injection in CAL-GT-03 likely drove fault reactivation, they cannot fully explain the correlation between reduction in flow rates and induced seismicity, that is observed during the operation of the CWG doublet. Based on the analysis it is concluded that seismicity during the CWG production period may have been driven by the following mechanisms:

- Mechanism 1: thermal stressing promotes fault reactivation at the Carboniferous Normal Fault close to CAL-GT-03, abrupt small pressure increases due to reduction in flow rates induce seismicity on fault sections which are close-to-critically stressed due to thermal stresses

- Mechanism 2: aseismic fault slip occurs due to thermal stressing of the Carboniferous Normal Fault close to CAL-GT-03, which causes stress transfer to other deeper fault sections, either on the Carboniferous Normal Fault or (deeper) sections of the Tegelen fault. Abrupt small pressure increases due to reduction in flow rates induce seismicity on deeper fault sections affected by stress transfer.

- Mechanism 3: reduction of flow or shut-in rates causes an abrupt poroelastic decrease in normal stress. This mechanism is most likely for faults (segments) with a reduced hydraulic connectivity to well CAL-GT-03

The fault segment on the Carboniferous Normal fault has become (near-)critically stressed due to cooling as a result of injection in well CAL-GT-03, stress transfer and aseismic slip. The pressure decrease caused by production from well CAL-GT-01 and later well CAL-GT-04 provided a stabilizing effect on (deeper) sections of the fault system of the Tegelen and Carboniferous Normal Fault. During reductions of flow rates and after shut-in of the production wells (first CAL-GT-01, then CAL-GT-04) the stabilising effect disappeared. After shut-in of CAL-GT-04, pressure in the Tegelen Fault and the Carboniferous Normal Fault increased to initial reservoir pressure. Coulomb stress increased due to the pressure rise and induced seismicity, including the Ml 1.7 main event, on a segment of the Carboniferous Normal Fault affected by thermal stresses or on a (deeper) segment of the Carboniferous Normal fault and/or Tegelen Fault that experienced additional loading due to stress transfer.

During operation of the CLG doublet positive Coulomb stress changes can occur on the Western and Eastern Pop-Up Faults (i.e. if it is assumed that the pop-up structure is present), or on subseismic faults in the area close to injection well CAL-GT-05. This Coulomb stressing is caused by pressure diffusion in combination with thermal stressing and promotes fault reactivation on the potential Western and Eastern Pop-Up Fault.

A comparison between hypocenter locations, derived with an updated velocity model of the subsurface, and geomechanical results was used to identify consistency of patterns and potential causal mechanisms for the historical seismicity recorded. The hypothesized mechanisms driving induced seismicity are consistent with the locations of the majority of the seismic events near the CWG injection well and the location of a single Ml 0.2 event close to CLG injection well.

Some of the model results are subject to remaining uncertainty. The main uncertainties in the subsurface models are related to the position and orientation of the main faults, in particular the presence and extent of the large-scale pop-up structure in the east, and the depth of the intersection of the Carboniferous Normal Fault with well CAL-GT-03, the connectivity in the reservoir and in-between the wells, the magnitude of the in-situ stress field and the frictional behaviour of the faults. Additional data acquisition during a pilot test phase can help further improve the understanding of the subsurface. Several options for data acquisition during such a pilot phase are described. A practical injection & production test, with dedicated seismic monitoring is considered as the 'core' of the technical test phase, as it can generate data to support relations between operations and seismic response of the system, to provide input for- and enable assessment of the hazards associated to the operations. Other options for data acquisition include a.o., additional seismic data and seismic velocity measurements (checkshots, VSP, dipole sonic) to further constrain the geological model and hypocenter locations, well and interference tests with downhole sensors (thermal back production and tracer test) and downhole temperature surveys to further characterise reservoir flow and in-situ stress measurements and frictional behaviour of the faults to characterise fault reactivation potential. The final definition of the pilot phase and the data acquisition, practical injection & production test and monitoring network that are part of it depends on various operational and non-technical aspects and needs to be approved by the regulator.

A general framework for seismic hazard assessment for geothermal in the Dinantian carbonates in areas with natural seismicity is proposed. This framework is based on a widely accepted approach for probabilistic seismic hazard assessment. A key component of the seismic hazard assessment is the seismic source model, which relies on a physical understanding of the mechanisms driving seismicity. The multiple causal mechanisms identified in this study provide crucial input for this seismic source model. It is recommended to use a logic-tree with multiple plausible source models, weighted based on expert elicitation. Continuous calibration of model forecasts with observations is essential, requiring sufficient monitoring, and emphasizing the importance of practical injection/production test phases and a robust monitoring network. For defining magnitude-frequency relations for fracture-dominated systems in tectonically active areas, key questions include the probability of impacting the release of tectonically accumulated stress (affecting the rate/probability of large magnitude earthquakes and Mmax), the expected ratio between smaller and larger events (Gutenberg-Richter b-value), and the relation between production/injection parameters such as temperature and rate on the total seismicity rate.

The study concludes that data acquisition prior to projects in the fractured reservoirs in a natural tectonic setting is essential, to ensure that well trajectories relative to larger fault structures can be properly assessed, to enable accurate modelling and to allow for better analysis of the causes of seismicity and potential mitigation strategies. Establishing a local seismic monitoring network, including baseline measurements, prior to the project is also important. This network ensures continuous monitoring, timely intervention if necessary, and generates data as input to seismic hazard assessment and mitigation measures. Operational data and seismicity records from the initial operations at the CWG and CLG sites have proven essential for history-matching, calibrating subsurface models and understanding the mechanisms driving seismicity.

page left blank intentionally

Contents

1 Introduction

Ambitions to accelerate development of geothermal energy production require development of new geothermal targets in areas where conventional/sandstone reservoir targets are absent. One such a target in northwestern Europe for production of geothermal energy is the Dinantian fractured carbonates play (Buijze et al., 2019). The Dinantian carbonate reservoirs, with their porosity and permeability enhanced by karstification, fractures, and faults, form a significant potential for geothermal heat extraction, and may be important for future development of (ultradeep) geothermal projects. To date, two geothermal sites have targeted the Dinantian carbonates in the Netherlands, i.e. Californië Wijnen Geothermie (CWG) and NAPPA, previously Californië Lipzig Gielen (CLG). Both are located in the Venlo Graben which is part of the Roer Valley Rift System in the southeastern part of the Netherlands, an area that is known for the occurrence of natural seismicity, with regularly occurring natural seismicity exceeding magnitude 1.5. The sites target the fractured and partially karstified carbonates of the Zeeland Formation which is of Early Carboniferous (Dinantian) age and the underlying fractured quartzites of Devonian age. The doublets produced substantial amounts of sustainable heat from 2013 to 2018, while several small seismic events were detected. Operations at geothermal site CWG were suspended in May 2018, whereas operations at the CLG-site were suspended end of August 2018. A few days after the final shut-in of the doublet at the CLG-site a Ml 1.7 magnitude earthquake occurred. All production activities at the site are currently on hold as a result of that event.

Alternative geothermal reservoirs and other alternative sources for sustainable heat are limited within the region of Californië, while there is significant heat demand in the area from greenhouses as well as the built environment. The fractured carbonate system is therefore an important possible source for sustainable heat within this region, if the reservoir can be safely developed and operated. It is therefore essential to increase our understanding of the relation between geothermal operations and induced seismicity in the Dinantian carbonates. In fractured reservoirs warm water is extracted from highly permeable fractures in- or near naturally stressed fault zones and relatively cold water is re-injected into the reservoir. It is generally expected that the geothermal operations in fractured rocks in naturally seismically active areas pose an increased seismic hazard compared to the conventional production from porous sandstone. However, currently there is scattered knowledge, experience, data, and calibrated modelling technology available to reliably assess and mitigate the seismic hazard and risk associated with geothermal extraction in fractured rocks in naturally seismically active areas. This gap in understanding contributes to the stagnation of geothermal project development in this geological setting, leaving proven significant potential for sustainable geothermal heat provision untapped in a region where other options for geothermal heat are limited.

The overall objectives of the TKI-SafeGeo project are summarized as follows:

<u>The first objective</u> of the project is to improve our understanding of seismicity mechanisms at the Californië geothermal sites by developing subsurface models based on all currently available data. The Californië area is an ideal candidate for a case study because it has been producing for a considerable time and has production and seismicity data available. The

SafeGeo project aims to gain insights from this data on the relationship between operations and induced seismicity. A comprehensive mechanistic understanding of the relationship between operational activities, fault reactivation, and induced seismicity is crucial for an assessment of the seismic hazard associated with geothermal operations in fractured reservoirs. Additionally, this mechanistic understanding is essential to identify and evaluate effective mitigation measures to minimize these seismic hazards and ensure safe and sustainable potential future geothermal energy production from these types of geological settings. In this context, the project aims to sketch and propose a general framework for a seismic hazard assessment for geothermal operations in the fractured Dinantian reservoirs in a seismically active setting.

The second objective is to sketch recommendations and options for a potential practical pilot / test phase at the Californië site. In such a pilot additional data could be generated under dedicated monitoring and a carefully designed operational setup. These data could be used to further validate the models and enhance our insights into the mechanisms driving seismicity and mitigation measures, as well as determining the operational scope within the established norms. It is noted that such a practical test will require a site-specific seismic hazard and risk assessment and specification of a risk management system, which is outside the scope of the current project.

Ultimately, the information and insights from the modelling studies and pilot phase may help determining if and under what conditions geothermal energy can safely be produced from the Californië geothermal site and/or fractured reservoirs in the broader area of the Roer Valley Rift System in southeastern Netherlands.

1.1 Report structure

Chapter 2 provides a brief overview of the history and main characteristics of the Californië sites. Chapters 3 to 6 describe the subsurface models and simulation results, which include a geological model, a velocity model, a history-matched dynamic reservoir model and a geomechanical model. The geological model, reservoir model and geomechanical model are used to analyze the spatio-temporal changes in pressure, temperature, stress, and fault reactivation potential. The velocity model is used to determine hypocenter locations and associated uncertainties. The initial phase of the modelling focusses on examining the relationship between past operations and historically induced seismicity. A comparison is made between geomechanical results and hypocenter locations to identify consistent patterns and potential causal mechanisms for the historical seismicity recorded. Additionally an operational test scenario for a potential future pilot phase is defined and simulated. Chapter 7 presents a general framework for seismic hazard assessment and compares it to the current methodology for the Seismic Hazard Analysis (SHA) for geothermal operations. Chapter 8 describes performance of different options and configurations for a seismic monitoring network, and Chapter 9 summarizes options and recommendations for a potential pilot phase, general recommendations for geothermal in fractured carbonate reservoirs and summarizes the final conclusions of this study.

1.2 TKI-SafeGeo consortium

The SafeGeo consortium, consisting of TNO, Nappa, Californië-Wijnen Geothermie (CWG), and Energie Beheer Nederland (EBN), along with associated consultants VITO and Q-con.

The research has been executed by technical experts and scientists from TNO, Q-con and VITO. Nappa, Californië-Wijnen Geothermie (CWG) and EBN have provided valuable information and technical input in technical workshops and discussions, and performed a review of the final report.

KNMI was not part of the consortium but participated in technical discussions and conducted the assessment of the seismic monitoring network performance (Chapter 8).

Disclaimer: This report is public; however, the underlying data and generated results are confidential and cannot be used or disclosed without prior permission.

2 Historical overview of geothermal activities in Californië

2.1 Background information

This chapter gives a brief overview of the history and key characteristics of the Californië sites. Detailed data and information used as input for the subsurface modelling are described in the subsequent chapters on geological, velocity, dynamic reservoir, and geomechanical modelling.

The Californië Wijnen Geothermie (CWG) and Californië Lipzig Gielen (CLG) geothermal sites (together hereafter referred to as Californië sites) are located in the southeastern part of the Netherlands, near the small community of Californië, which is located approximately 5 km northwest of the city of Venlo, within the province of Limburg (Figure 2-1). All five well heads are located within the Horst aan de Maas municipality. The two southernmost deviated wells CAL-GT-01 and CAL-GT-03 cross the municipality border with Venlo in the subsurface. The wells CAl-GT-01, CAL-GT-02 and CAL-GT-03 were exploited by Californië Wijnen Geothermie B.V. The wells CAL-GT-04 and CAL-GT-05 were exploited by Lipzig Gielen Geothermie B.V.

The Californië geothermal sites are located in the Venlo Graben, just northeast of the Tegelen Fault, which forms part of the Roer Valley Rift System. The sites are located in a tectonically active area, where historical natural seismicity has been recorded (see Figure 2-2). Most natural seismicity (with magnitudes up to Ml 5.8) has occurred in the Roer Valley Graben to the southwest of the geothermal sites, but some natural seismic events have occurred in the Venlo Block as well (see also Figure 3.1.5).

The wells target the fractured and partially karstified carbonates of the Zeeland Formation (Early Carboniferous – Dinantian - age) and the underlying fractured quartzites (Devonian age). Production wells of the CWG (CAL-GT-01 and CAL-GT-03) and CLG (CAL-GT-04) project aimed for the increased permeability of the Tegelen fault zone. The injection wells of CWG (CAL-GT-02) and CLG (CAL-GT-05) were drilled away from this faulted area.

For a detailed description of the geological setting of the Californië sites, see section 3.

The CWG and CLG geothermal systems are based on a balanced circulation of fluids, which means that an approximate fluid balance is maintained by re-injecting all water produced from the production well into an injection well.

Originally, two production wells (CAL-GT-01 and CAL-GT-03) were planned for the CWG-doublet, targetting the permeable sections at the top of the Dinantian carbonate reservoir and the damage zone near the Tegelen Fault. CAL-GT-02 was planned as a single injection well in a karstified reservoir section away from, and to the northeast of the Tegelen Fault

Zone. However, after CAL-GT-02 technically failed it could not be used for its intended injection purposes, and CAL-GT-03 was used as an injector, despite the fact that it was located relatively close to the Tegelen Fault zone. As part of the well section of CAL-GT-03 at reservoir level had collapsed into a fault zone, injection took place at shallower levels, i.e. into the younger strata of the Zeeland Formation (Burghout et al., 2019, Ter Heege et al., 2020).

The CLG doublet, located ~1.5 km to the northeast of the CWG doublet has one production well (CAL-GT-04) and one injection well (CAL-GT-05) (Burghout et al., 2019). The CLG doublet targets the same Dinantian carbonates of the Zeeland Formation as the CWG-doublet, but produces from a slightly deeper level. Both the CAL-GT-01 and CAL-GT-04 production wells are interpreted to produce from permeable zones close to the Tegelen Fault Zone (Burghout et al., 2019, Ter Heege et al., 2020). In contrast to CAL-GT-03, injection well CAL-GT-05 targets a reservoir section at a significant distance from the Tegelen Fault zone (Figure 2-1).

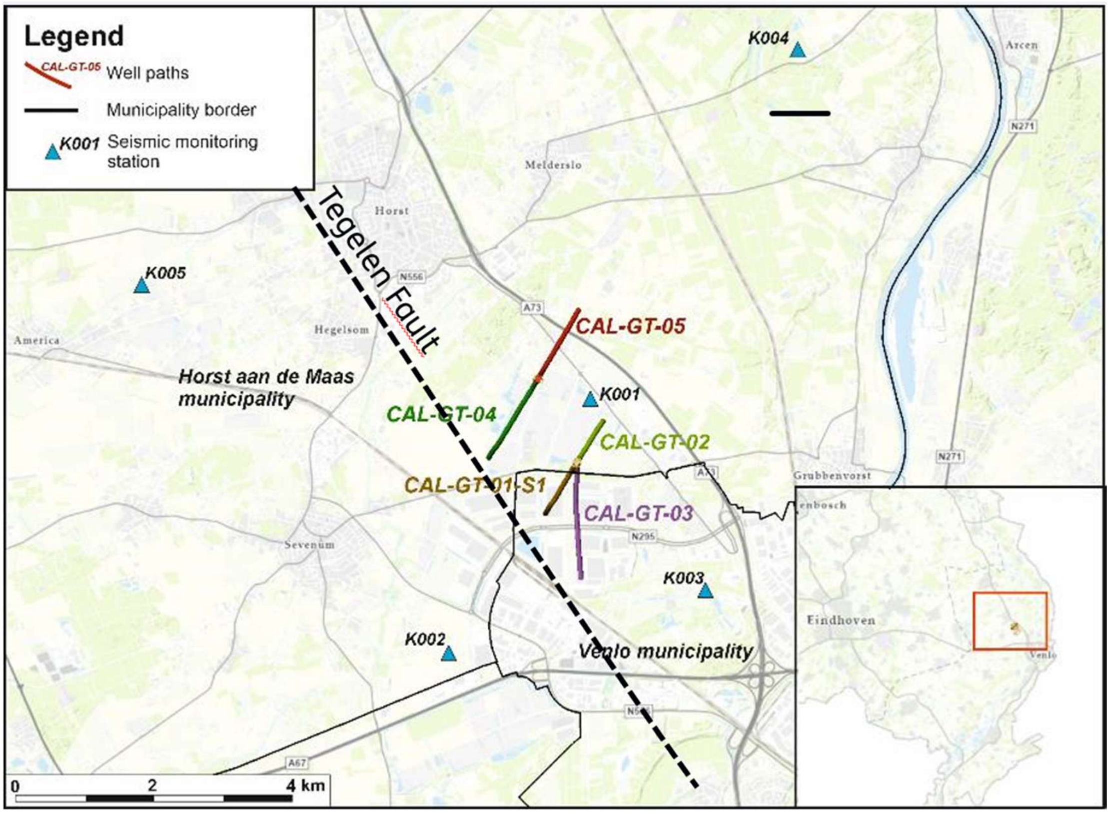

Figure 2-1. Topographic map indicating the position of the well heads and the well trajectories/paths. The colours of the trajectories correspond with the colours of the labels for each individual well. The red square within the inset map in the lower right corner of the map indicates the location of the area of interest within the southeastern part of the Netherlands. Dashed lines present approximate locations of faults. For a updated interpretation of the location of the faults, see Chapter 3 on geological modelling.

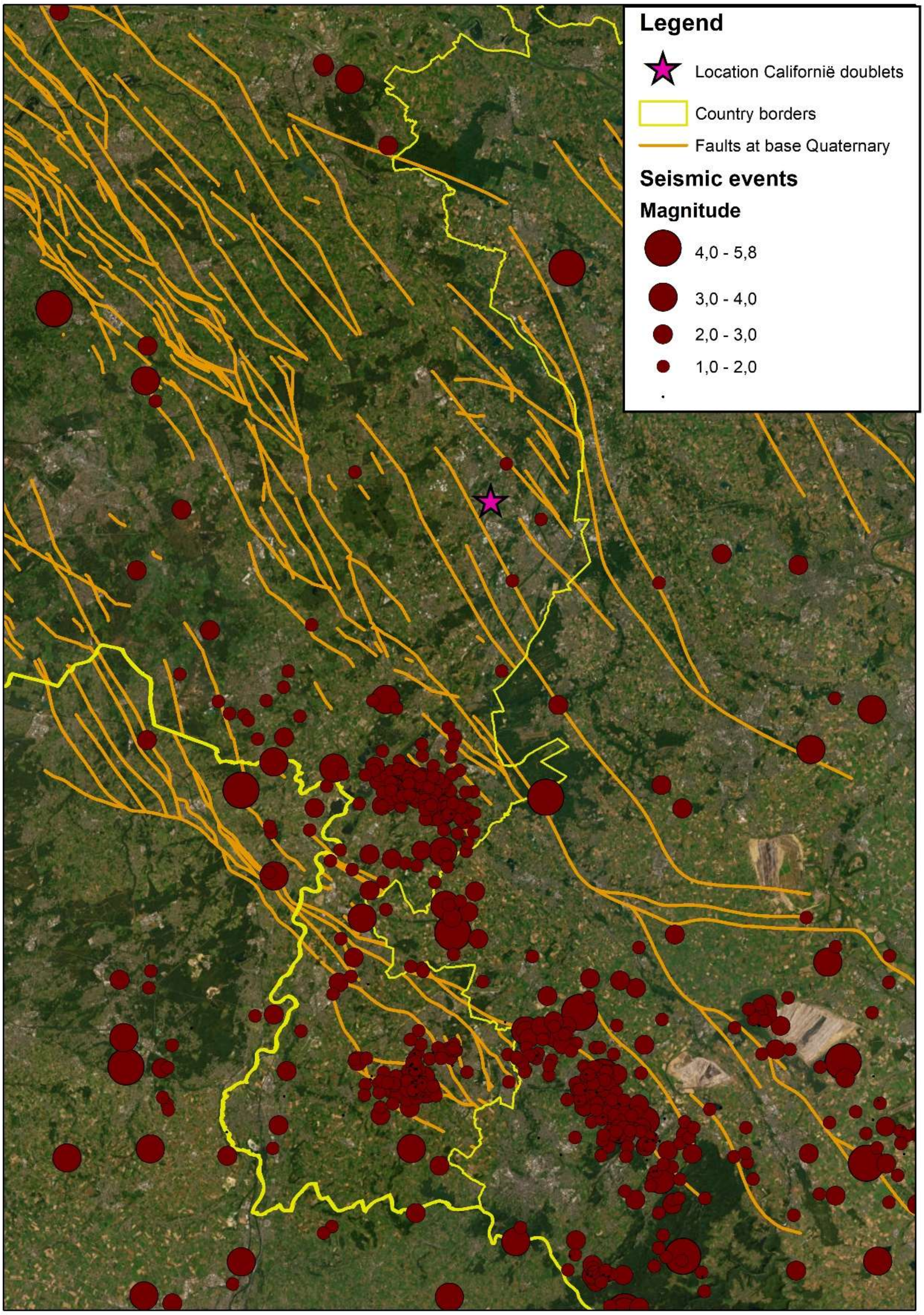

Figure 2-2. Natural seismicity in the southern part of the Netherlands. Pink star indicates location of the Californië geothermal doublets, orange lines are faults derived from the GeoEra database. Red bullets indicate seismsic events. Data obtained from: www.knmi.nl/kennis-en-datacentrum/dataset/aardbevingscatalogus

2.2 Description of the wells

Production well CAL-GT-01, at site CWG

The first production well, CAL-GT-01, was drilled in 2012. The well was deviated towards the southwest to target the permeable sections at the top of the carbonate sequence and near the Tegelen Fault. It intersects the top of the carbonate sequence at 1635 meters Measured Depth (MD), which corresponds to 1486 m True Vertical Depth (TVD). From 1735 m MD, there were complete losses of drilling fluid, and well logging (caliper) revealed cavities down to 1800 m depth. The well was side-tracked, and a liner was installed down to 1802 m MD before the final section was drilled (CAL-GT-01-S01). Additional mud losses occurred around 2330 m MD, which corresponded to the depth at which the Tegelen Fault was anticipated. The well reached its final depth at 2730 m MD (2510 m TVD, within the fractured sandstones of the Devonian Evieux Formation. The well has been used as a production well as part of the CWG doublet, in the period from August 2013 to May 2018.

Note: From now on, for simplicity, CAL-GT-01 is often used to indicate CAL-GT-01-S1 in this report unless specifically mentioned otherwise. Please note that in initial documentation CWG uses CAL-GT-01-S2 to indicate this side track.

Injection well CAL-GT-02, at site CWG

Injection well CAL-GT-02 was drilled in 2012 and was deviated to the northeast, targeting the high permeability karstified top of the Dinantian carbonates away from the Tegelen Fault zone. The top of the Zeeland Formation was encountered at 1386 m MD (equivalent to 1224 m TVD). The well reaches a total depth of 1694 m MD (1482 m TVD) in the Evieux Formation. Some minor mud losses were observed at a depth of 1415 mMD at the top of the carbonates and more substantial losses during circulation after drilling of the well. Well CAL-GT-02 was originally intended to be an injection well as part of the CWG doublet, but was never used as injection well, as tests performed in 2013 indicated that the well was blocked at the top of the open hole section. Attempts made between 2013 and 2017 to open the blocked section of the well failed.

Injection well CAL-GT-03, at site CWG

Well CAL-GT-03 was drilled in 2012-2013, initially intended as a second production well for the CWG geothermal doublet. CAL-GT-03 is deviated to the south, with its reservoir section is located south of CAL-GT-01. The well reaches the top of the Zeeland Formation at a depth of 1615 m MD (equivalent to 1375 m TVD) and ends at a depth of 2977 m MD (2254 m TVD) in the fractured sandstones of the Evieux Formation. The well was used as an injection well for the CWG doublet, thus replacing the previously blocked CAL-GT-02 injection well. In response to requirements of State Supervision of Mines (SodM) additional measurements were performed to determine the specific reservoir zones in which water was injected, confirm that water was not injected directly into the Tegelen fault zone, and assess the pressure impact on the fault. An obstruction was encountered at 2409 m MD during liner installation in 2013, and a PLT survey conducted in 2014 could not be completed beyond 2389 m MD. The PLT data confirmed that no water was injected below this depth.

Production well CAL-GT-04, at site CLG

Well CAL-GT-04 was drilled in December 2015 to February 2016 as the first well of the CLG doublet. The well has a similar orientation as CAL-GT-01 and is located a bit over a kilometer to the north along the Tegelen fault (Figure 2-1). The well encountered the top of the Zeeland formation at 1811 mMD (1577 m TVD). TD was called at 3030 mMD (2584 mTVD). The well was completed with an uncemented liner and perforated at a loss zone around

2550 mMD and around the Tegelen fault (around 2750 mMD). The well was used as a production well as part of the CLG doublet and was operated between June 2017 and 28 August 2018.

Injection well CAL-GT-05, at site CLG

Well CAL-GT-05 was drilled in February to April 2016 as the injector of the CLG doublet. The well has the same orientation as CAL-GT-02. The top of the Zeeland Formation was found at 1560 mMD RT (1378 m TVD) and TD was called at 2433 mMD RT (2011 m TVD) in the sandstones of the Evieux Formation. No mud losses were observed during drilling of the well. The well is completed barefoot and the open hole section starts at 1547 mMD RT. It was attempted to stimulate the well using Radial Jet Drilling, but this proved unsuccessful. An acoustic log showed very little evidence of fault or fractures in the Zeeland Formation. PLT logs show that inflow is mostly in the sandstones of the lower part of the Bosscheveld Formation and in the Evieux Formation.

Well tests were carried out on all wells to derive properties of the reservoir layers, mostly shortly after drilling. Well tests have been re-interpreted for this project and results have been reported in a separate report by VITO (Pogacnik, 2024. Report SafeGeo: Well Test Analysis, see Appendix E). Properties derived from this re-interpretation served as input to the dynamic reservoir model described in section 5.

2.3 Seismic monitoring and relations operations and seismicity

Injection and production operations at the CWG site started in August 2013. The CWG doublet was produced from August 2013 to May 2018, when it was shut down as no permit for continuous injection into CAL-GT-03 was granted by the regulator. Injection and production operations at the CLG site started in June 2017, and the CLG doublet produced until end of August 2018. Following a seismic event of Ml 0.0 on 25 August, 2018 and decisions by SodM operations at the CLG project are currently still on hold. Note that the original local magnitudes, which were based on the KNMI-scale, have been re-processed by Q-con using the main-shock as the calibration event (S. Baisch, pers. comm, 2023). This provides an internally consistent scale, but the new magnitude values of the smaller events as reported in Table 2-2 differ from those values that were previously reported. The local magnitude Ml 0.0 of 25 August, 2018 has later been updated to Ml 0.2).

The CWG doublet produced (and re-injected) a total volume of ~9.1×10^6 m^3 fluid over it's operational lifetime. Initially, between January and October 2014 monthly production from the CWG doublet is roughly constant at a rate of ~1.1×10^5 m^3 /month. Then four additional stages of increasing production can be distinguished; peak productions are ~1.8×10^5 m^3 /month in March 2015, ~2.4×10^5 m^3 /month in February 2016, ~2.8×10^5 m^3 /month in January 2017, and ~2.9×10^5 m^3 /month in January 2018. Figure 2-3**Error! Reference source not found.** shows that the production roughly follows demands, with higher demands and rates during winter and lower demands and rates during summer.

CLG did operate only one year and did not realise its maximum production due to limited heat demand. The system was limited because of the restrictions in injection pressure imposed by State Supervision of the Mines (R. Vorage, pers. comm., 2024). The CLG doublet produced and re-injected a total of ~1.3×10^6 m^3 fluids over its operational lifetime. The monthly production rates of the CLG-doublet are much smaller than for the CWG doublet.

The peak of production and re-injection for this doublet (1.6x10^5 m^3/month) lies in winter 2017/2018, with a maximum production rate of ~6000 m^3/day in March 2018.

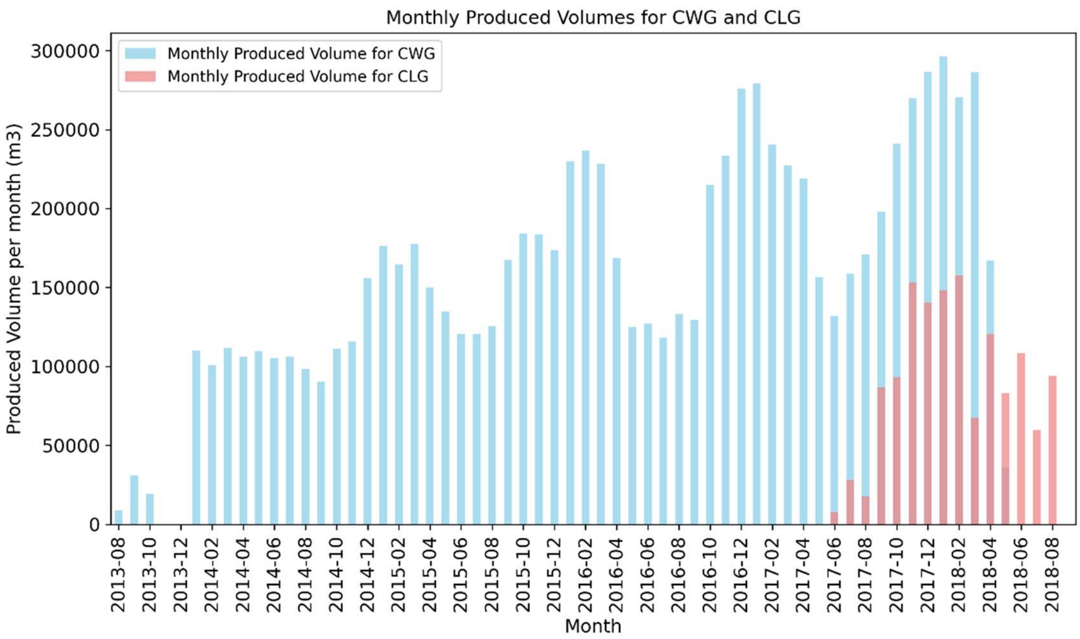

Figure 2-3. Monthly produced and re-injected volumes of fluids by the CWG and CLG doublets.

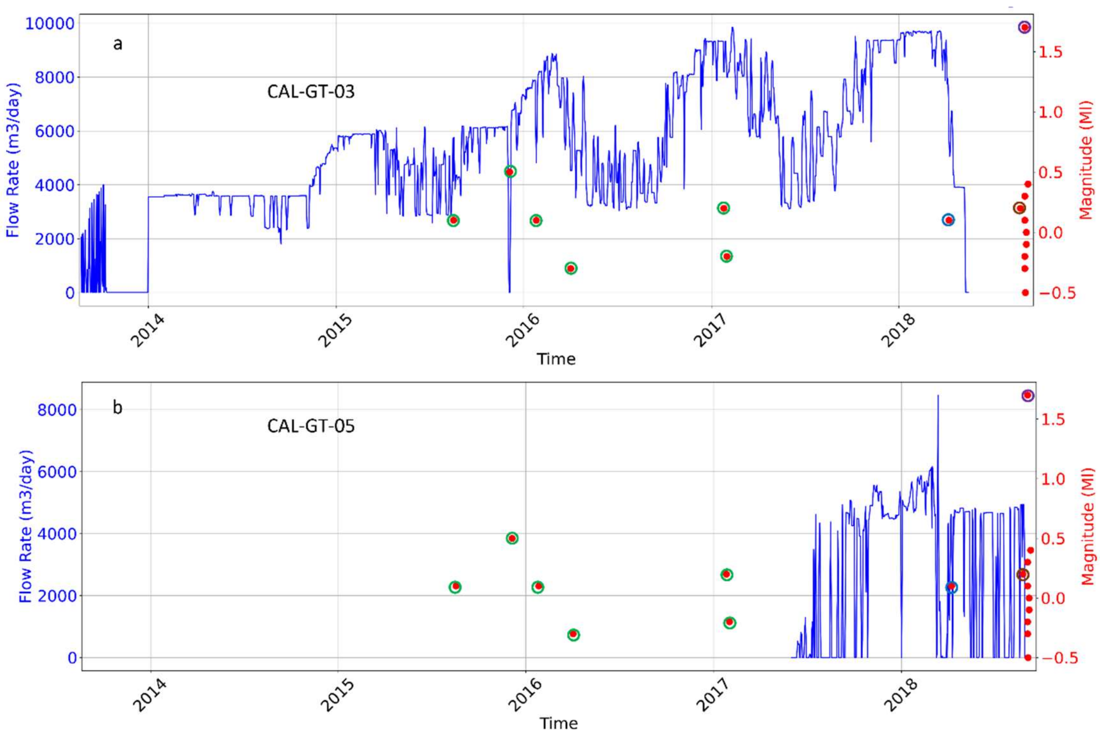

Figure 2-4. Seismicity and flow rates at the CWG and CLG geothermal sites. Red dots present recorded seismic events, green circles depict seismic events during production of CWG doublet only, which show a strong correlation with reduction of flow rates, blue circle depicts seismic event which occurred on April 8,

2018, during simultaneous production of CWG and CLG doublet, brown circle depicts seismic event at August 25, 2018, just before shut-in of CLG doublet and purple circle depicts main event Ml1.7 after shut-in of CLG-doublet, blue solid lines present flow rates for injection wells a) CAL-GT-03 (CWG) and b) CAL-GT-05 (CLG).

Figure 2-4 shows the daily flow rates in the CWG- and CLG doublet and the occurrence of the seismic events during the production phases. Detailed information on flow rates, pressures and temperatures are reported in session 5. Detailed information on hypocenter locations is given in chapter 4.

In March 2012, KNMI installed the first seismometer at the well site before drilling the initial production well CAL-GT-01 at the CWG site. Due to high noise levels, the seismometer was relocated in May 2012 to the northern side of the CWG site, positioned one meter below the surface. That same month KNMI installed two additional seismometers nearby. In August 2014, Q-con GmbH set up a three-station network (i.e. stations K01-K03 (Figure 2-1) to monitor seismic events near the geothermal system of CWG, replacing some of the original stations. This network was further expanded in November 2015 with two more stations (K04 and K05, see Figure 2-1), enabling the monitoring of events near the CLG wells drilled between 2015 and 2016. Time-continuous waveform data are available for the period August 2014 – November 2015 (3 stations), November 2015 – 2019 (5 stations) and from 2019 – now (2-3 stations) (Vörös and Baisch, 2022, Ter Heege et al., 2020).

A traffic light system was implemented to mitigate seismic risks. The traffic light system was based on peak ground velocity (PGV) with a green light for PGV < 0.1 mm/s, orange for PGV >=0.1 mm/s and red for PGV >= 0.3 mm/s. Associated actions are summarized in Table 2-1 (Vörös and Baisch, 2022).

Table 2-1. Specifications of traffic light system at Californië geothermal sites

Level	PGV	actions
Green	<0.1 mm/s	No actions
Orange	>=0.1 mm/s<0.3mm/s	(1) Investigate likely cause and potential mitigation measures (2) report to regulator
Red	>=0.3 mm/s	(1) Stop operations (2) Report immediately to regulator (next business day)

SodM states that "CLG was allowed to produce geothermal heat under the condition that production would be stopped if an earthquake occurred in the area". Production and injection in the CLG doublet was stopped after a seismic event of Ml 0.0 event on 25 August 2018 (later re-processed to Ml 0.2, see Table 2-2), which caused a with PGV of ~0.03 mm/s. The Ml 1.7 event that occurred after shut down of the CLG-doublet caused a PGV of ~1.1 mm/s, exceeding the traffic light threshold for stop of operations ((Ter Heege et al., 2020, Vörös and Baisch (2022).

In total 17 seismic events were detected by the seismic monitoring network doublet between August 2015 and September 2018, during the operational period of the two doublets and the few days after shut-in of the CLG wells (see Table 2-1 and Figure 2-4). Magnitudes of the seismic events lie between -0.5 and 0.5, except for the main event on September 3rd 2018, which had a Ml of 1.7.

The timing of the six earthquakes that were detected during the period that only the CWG doublet was active (August 2013 – June 2017), and the earthquake that occurred in April 2018 when both doublets were producing, show a clear correlation with the moments flow in the CWG doublet was either reduced or stopped.

Table 2-2. Overview of seismic events: Timing, local magnitudes and hypocenter locations recorded by the seismic monitoring network at the Californië sites, as reported in Vörös and Baisch(2022) and Q-Con report SGEO001, December 6, 2023. Local magnitudes have been re-processed by Q-con using the main-shock Ml 1.7 as the calibration event (S. Baisch, pers. comm, 2023). This provides an internally consistent scale, but the new magnitude values of the smaller events differ from those values that were previously reported. Note: Updated hypocenter locations based on a new geological and velocity model, determined in TKI-SafeGeo are reported in section 4.

date	time	lat	lon	depth [m]	M_L^R
18-Aug-2015	02:47:05	51.40991	6.0893466	-2192	0.1
05-Dec-2015	08:07:28	51.41001	6.0933441	-2445	0.5
26-Jan-2016	02:47:00	51.412404	6.0902309	-2434	0.1
02-Apr-2016	14:17:16	51.418007	6.0833162	-2536	-0.3
25-Jan-2017	16:27:12	51.408784	6.0917092	-2376	0.2
31-Jan-2017	04:01:56	51.415842	6.083939	-2366	-0.2
08-Apr-2018	10:29:27	51.409846	6.0893043	-2448	0.1
25-Aug-2018	16:43:27	51.425307	6.0802734	-2506	0.2
03-Sep-2018	18:11:23	51.410266	6.0893983	-2396	-0.2
03-Sep-2018	18:12:35	51.411083	6.0899763	-2368	0.1
03-Sep-2018	18:20:31	51.410368	6.0897539	-2441	1.7
03-Sep-2018	18:26:37	51.412097	6.0901977	-2205	0.3
03-Sep-2018	20:44:12	51.410382	6.0855934	-2435	-0.3
04-Sep-2018	00:13:15	51.409097	6.0906	-2418	-0.5
06-Sep-2018	15:27:20	51.410323	6.0884887	-2355	0
06-Sep-2018	15:58:22	51.410548	6.0884689	-2398	-0.1
09-Sep-2018	20:50:22	51.411986	6.086946	-2384	0.4
07-Feb-2022	19:57:52	51.410429	6.0896632	-2445	0

In Vörös and Baisch (2022) this correlation was found to be statistically significant. The CWG doublet shut down in May 2018, as there was no prospect for an extension of the approval by the supervising authorities to inject in CAL-GT-03. The CLG doublet remained operational after the shut down of CWG. A magnitude Ml 0.0 (later re-interpreted as Ml 0.2) occurred on August 25th 2018, after which operations of the CLG doublet were suspended as well. The shut down of the CLG doublet on August 28, 2018 was followed a few days later by two small events, a magnitude Ml 1.7 event (main event) and several small seismic events up to magnitude Ml 0.4. In March 2020 the monitoring contract for stations K04 and K05 was ended. Seismic monitoring was continued with the original stations K01, K02 and K03. In September 2021 station K02 was shut-down. From September 9, 2018 no more seismic events were detected by the seismic monitoring network. An additional event on February 7, 2022 was derived from template matching, performed by Q-con for the TKI-SafeGeo project (Q-con report SGEO001, December 6, 2023, see Appendix F).

Initial studies by Q-con and KNMI showed a large uncertainty related to the hypocenter depths, due to a poorly constrained shear-wave velocity model (Baisch and Vörös (2019), Spetzler et al (2019)). Vörös and Baisch, 2022 reported new hypocenter locations and depths, which are based on a seismic wave velocity model calibrated with recordings of several perforation shots fired in well CAL-GT-04, and constrain the hypocenter depths in the interval between ~2200 and 2500 m depth (see also event locations and depth in Table 2-1).

The majority of the hypocenters reported in their study are located to the southeast of well CAL-GT-03. The authors identify cooling and thermal contraction around CAL-GT-03 as the cause of induced seismicity, leading to seismic activity at times shortly after reduction of flow rate or shut down of operations, when reservoir pressure returned to or near pre-operational levels.

Data and information from the available five wells, well logs, well tests and production logs, original seismic lines and additional SCAN lines were used in this study as input to the subsurface models. Operational data (injection and production rates, pressures and temperatures) and seismicity recorded during the former operations at the CWG and CLG site provided valuable and essential information for history-matching and calibration of the subsurface models, to analyse the relationship between past operations and historically induced seismicity to improve the understanding of the mechanisms that drive seismicity.

3 Geological modelling

This chapter describes the results of the static geological modelling (hereafter: geological model) and describes the construction of the P-wave velocity model. The geological model functions as input for the dynamic reservoir modelling (chapter 5) and the geomechanical modelling (chapter 6). The geological modelling is based on interpretations derived from seismic- and well data. To tie the well data (in meters depth) to the seismic data (in ms TWT), a time depth conversion was performed by using a P-wave velocity model. This velocity model adheres to the geometries derived from the seismic data and was also build by using local and regional sonic data (other velocity data, such as VSP, or checkshot data are not available for the Californië wells). The constructed velocity model is also used to locate the position of the hypocenters of the seismic events in the subsurface (chapter 4).

In this chapter, first an introduction is given in paragraph 3.1 regarding the geological setting of the area of interest and the stratigraphy that is present. The methods regarding the construction of the geological and velocity models are described in paragraph 3.2. Paragraph 3.3 describes the results of the well log interpretation (3.3.1), and the seismic interpretation (paragraph 3.3.2), which together form the input for the geometry of the velocity model (paragraph 3.3.3) and the geological model (paragraph 3.3.4). In paragraph 3.4 the results and the uncertainties regarding the interpretations are discussed.

3.1 Geological introduction

This paragraph introduces the regional geologic and tectonic evolution of the wider area of interest (paragraph 3.1.1), the local geological setting (paragraph 3.1.2) and the local stratigraphy and lithology that are present (paragraph 3.1.3).

3.1.1 Regional and tectonic evolution

Like the rest of the Netherlands and adjacent areas, the area of interest was originally part of the Avalonia microcontinent (Smit et al., 2018) (Figure 3.1.1). During Ordovician to Early Devonian times, Avalonia collided both with Laurentia to the northwest and with Baltica to the northeast, subsequently forming the continent of Laurussia (Ziegler, 1990). During this Caledonian orogeny, major mountain ranges known as the Caledonides formed several hundreds of kilometers north of the current area of interest (e.g. Ziegler, 1990; Smit et al., 2018). During the Late Devonian and Early Carboniferous, the southern North Sea Area (including the area of interest) underwent major extension, which was likely caused by oceanic slab roll-back and associated back-arc extension due to the northward subduction of oceanic lithosphere at the southern margin of Laurussia (Smit et al., 2018). This extension created the large North West European Carboniferous Basin (NWECB) that stretched from the British Islands in the west, via the Netherlands and Belgium in the centre, towards Germany and Poland in the east (Ziegler, 1990; Kombrink et al., 2008; van Hulten, 2012; Smit et al., 2018; Ter Borgh et al., 2018).
Alternating structural highs and lows developed within the NWECB, which are generally NW-SE oriented in the region of interest (Figure 3.1.1). The target intervals for the Californië doublets were deposited in the NWECB and include; fractured sandstones and shales of the Upper Devonian Condroz Group and Bosschveld Fm. (Famennian-Tournaisian age), the

Lower Carboniferous Pont d'Arcole (Tournaisian age) and the fractured and partially karstified carbonates of the Zeeland Fm (Dinantian age; hereafter referred to as Dinantian carbonates) (Figures 3.1.2 and 3.1.3; See paragraph 3.1.4 for a more detailed overview of the stratigraphy of the target reservoirs).

The Upper Devonian sandstones were likely sourced from the Mid German crystalline high from the south (Kombrink, 2008). After a transgression during the early Carboniferous (Kombrink, 2008), the NW-SE oriented intra-basinal highs were preferential sites for the development of carbonate platforms during the Dinantian (Total, 2007; Reijmer et al., 2017; Figures 3.1.1 and 3.1.4). The growth of these platforms was influenced by local bathymetry, faulting, and sea level fluctuations, leading to a variety in carbonate facies types (Total, 2007; Van Hulten, 2012; Reijmer et al., 2017; Figure 3.1.4). Mostly wacke, pack- and grainstones were deposited on or near the platforms and mudstones or shales were deposited in the deep basinal part of the system (Van Hulten, 2012; Reijmer et al., 2017).

During the Namurian, carbonate production ceased, likely as a result of a large-scale transgression, ongoing (thermal) subsidence and the subsequent drowning of the carbonate system (Bless, 1979; Fraser & Gawthorpe, 1990; Van Buggenum & Den Hartog Jager, 2007). As a consequence, vast amounts of shale were deposited in the deeper parts of the NWECB, including the area of interest, which are lithostratigraphically part of the Epen Fm. (which in turn is part of the Limburg Group) (Figures 3.1.2 and 3.1.3; Van Hulten, 2012; Ter Borgh et al., 2018). On seismic data, the Namurian shales have been observed to partly onlap onto the Dinantian carbonate platforms (Total, 2007; Kombink et al., 2010; Van Hulten, 2012; Figure 3.1.4). In the northern part of the Dutch offshore sediment influx from the Caledonides in the north, lead to the influx of coarser grained siliciclastic sediments via fluvio-deltaic systems forming the Klaverbank and Millstone Grit Fms. (Ter Borgh et al., 2018; Houben et al., 2020; Figure 3.1.1).

During the Westphalian, the paleo depositional environment changed also in the current area of interest from marine to increasingly more continental as fluvial systems within a lower floodplain setting deposited intercalations of sands, clays and coals (Bless et al., 1980; Van Buggenum & Den Hartog Jager). These siliciclastic sediments were sourced from the south, where uplift started to occur from the Namurian onward due to the collision of Variscan terranes with the southern margin of Avalonia (Ziegler, 1990; Oncken et al., 1999; Smit et al., 2018; Figure 3.1.1).

Towards the end of the Carboniferous, the Rheic ocean was fully closed and continental collision occurred forming the Variscan orogenic Belt along the Rheic Suture (Figure 4.1.2), towards the south of the area of interest (Van Hulten, 2012). This Variscan orogeny caused widespread inversion and uplift also within the Variscan foreland north of the Variscan front, leading to erosion evidenced by the Base Permian Unconformity (BPU). This phase is reflected by a hiatus in the geological record between Carboniferous sediments of the late Carboniferous (Late Westphalian, or in some places Stephanian) and the Upper Rotliegend sediments of the Slochteren Fm. (Geluk, 2007; Reijmer et al., 2017). Isochore maps suggest that in the Netherlands up to 1800 m of Namurian and Westphalian rocks have been eroded (Buggenum & den Hartog Jager, 2007). Structural restorations and maturity studies performed during the SCAN program show that locally, even significantly larger amounts of Namurian and Westphalian rocks were eroded during the Latest Carboniferous- Middle Permian phase of uplift (Bouroullec et al., 2019). Via seismic interpretation studies performed in the offshore Netherlands, UK and onshore Belgium, it is shown that apart from regional uplift also local transpressional movements (i.e. a combination of strike-slip and thrust movements) played an important role during the Variscan inversion in the former

Variscan foreland basin (Bouckaert and Dusar, 1987; George and Berry, 1997; Thomas and Woodcock, 2015; Deckers et al., 2023).

The larger fault (systems) that formed during the Paleozoic deformation phases, became mechanically weak zones in the subsurface, which were reactivated during later deformation phases (e.g. Geluk, 2007; Bouroullec et al., 2019; Deckers et al., 2021). The main Mesozoic and Cenozoic deformation phases that affected the area of interest are: Triassic and Jurassic extension, Late Cretaceous and early Paleogene inversion and Neogene extension (Duin et al., 2006; Geluk, 2007; Bouroullec et al.., 2019; Deckers et al., 2023; Figure 3.1.2).

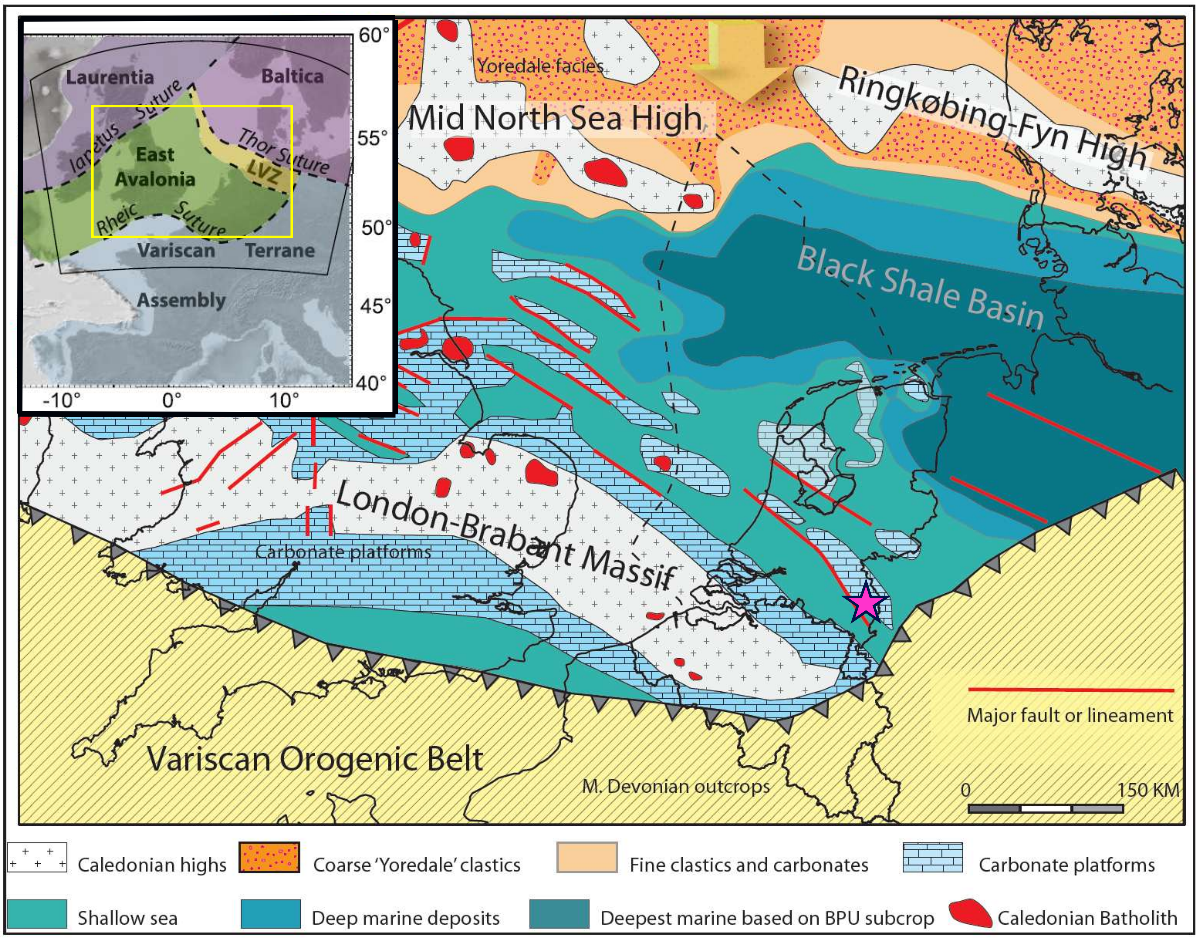

Figure 3.1.1. Paleogeographic map of the Dinantian showing the North West European Carboniferous Basin (NWECB). The pink star indicates the location of the Californië doublets. Paleogeographic map from: Van Hulten (2012). The yellow line in the inset map shown in the upper left indicates the location of the paleogeographic map within the paleo continental domains of northwestern Europe. Inset map in upper left from: Smit et al., (2018). Note that subduction along the Rheic margin was directed northwards (not southwards as suggested by this paleogeographic map), according to the current understanding (Smit et al., 2018), causing extension in the overriding (i.e. paleo Avalonia domain) due to slab-rollback during the Late Devonian and Early Carboniferous (Smit et al., 2018).

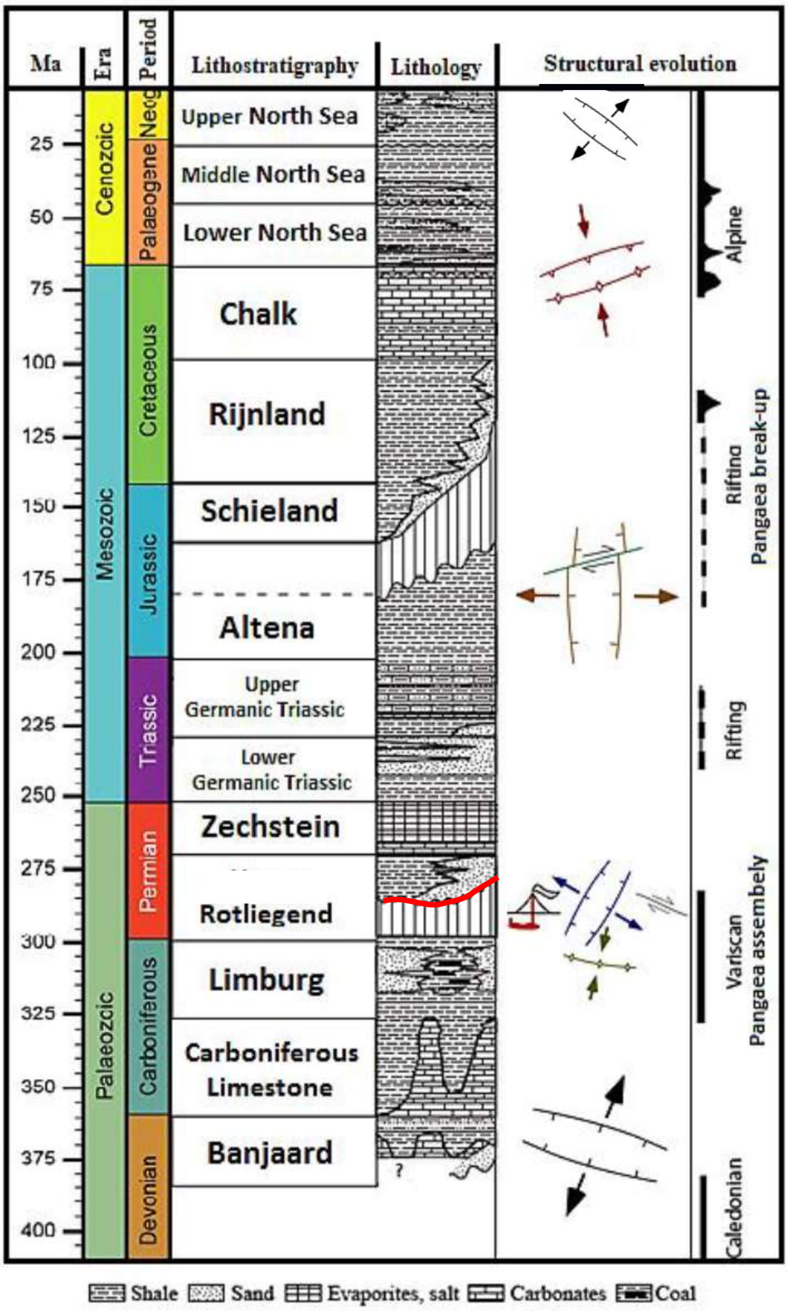

Figure 3.1.2. Chart showing the timing of the main tectonic events for Netherlands as part of the wider southern north sea area. Note that for the area of interest, the late Carboniferous-Early Permian inversion was likely accompanied with a strong transpressional component (e.g. Deckers et al., 2023). The Base Permian Unconformity, which resulted from this inversion phase is indicated by the red line in the lithology column. Also shown are the main lithostratigraphic groups. Note that the Namurian shales of the Epen formation are part of the Limburg Group. The Dinantian carbonates are part of the Kolenkalk Goup (here referred to as: Carboniferous limestone) and the Devonian Evieux and Bosschveld Fms. are part of the Banjaard Group. Figure modified from Mozafari et al., 2019, compiled after Van Hulten, 2012, Ter Borgh et al., 2018b and references there in.

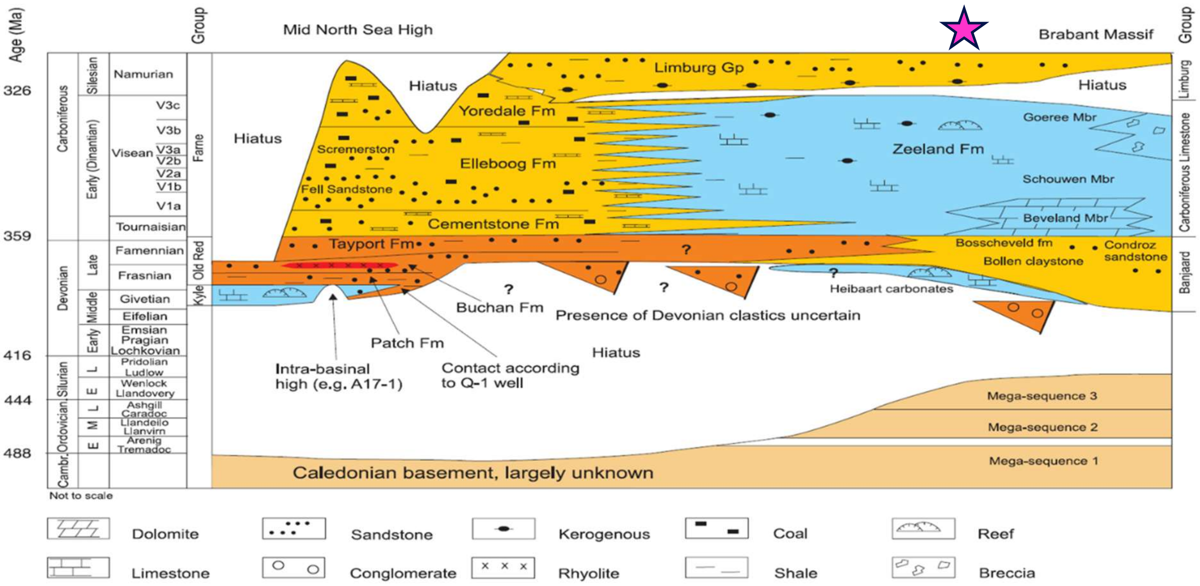

Figure 3.1.3. Regional chronostratigraphic chart of the Namurian – Cambrian interval. The approximate location of the Californië doublets is indicated by the pink star. The Namurian shales present in the area of interest are part of the Limburg Group. The Dinantian carbonates are part of the Zeeland Fm. The Dinantian carbonates overly shales, carbonates and sandstones of the Earliest Carboniferous - Upper Devonian Bosschveld Fm. and Condroz Group. Figure from Geluk et al., 2007.

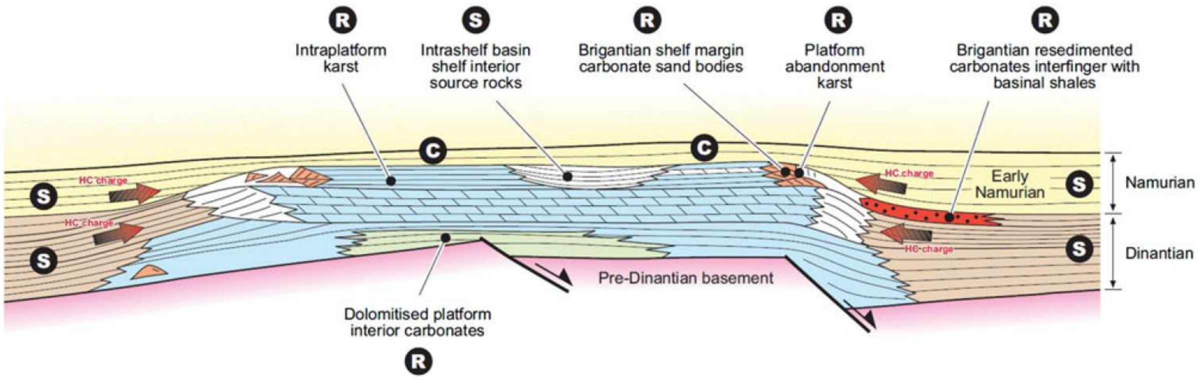

Figure 3.1.4. Schematic Cross-section across a Dinantian carbonate platform. Note the onlap of Namurian shales. Figure from Total (2007).

3.1.2 Local geological setting

The Californië doublets are located in the Venlo Graben, just northeast of the Tegelen fault and a couple of kilometers southwest of the Viersen Fault (Figure 4.1.6). The Venlo Graben or Venlo block is part of the larger Peel Maasbommel Complex and is a transitional area between the Roer Valley Graben in the southwest and the Krefeld High in the northeast (Kombrink et al., 2012). The Venlo Graben is part of the Neogene Roer Valley Rift System (Deckers et al., 2021), but Mesozoic and Neogene extension have been less profound than in the Roer Valley Graben (Kombrink et al., 2012). The Roer Valley Graben is also the main focus of recent natural seismicity but some natural seismic events have occurred north of it as well (Deckers et al., 2021; Figure 3.1.5).

As a result of the Variscan orogeny and subsequent (partial) erosion of the Namurian and Westphalian, the top of the Dinantian at the Californië doublets is located relatively shallow between approximately 1200 and 1600 m (depending on the exact location; see also paragraph 3.3.1) (Figure 3.1.6). Towards the southwest, the depth of the Dinantian increases rapidly (Veldkamp et al., 2023; Figure 3.1.6). The area of interest is located approximately 100 km north of the main Variscan front (Figure 3.1.1), but Late Carboniferous-Permian inversion is likely to have had a significant effect on the Paleozoic interval within the area of interest (see Paragraph 3.3.2). This inversion phase was likely accompanied by a major component of transpression leading to strike-slip faults and associated pop-up structures, as is inferred from the Donderslag and Gruitrode transpressional fault systems that were recognised on seismic data at the nearby Belgium Campine Block (Deckers et al., 2023).
In terms of carbonate facies, the Dinantian carbonates
were deposited in a platform carbonate setting (Mozafari et al., 2019; Figure 3.1.7; see also paragraph 3.4).

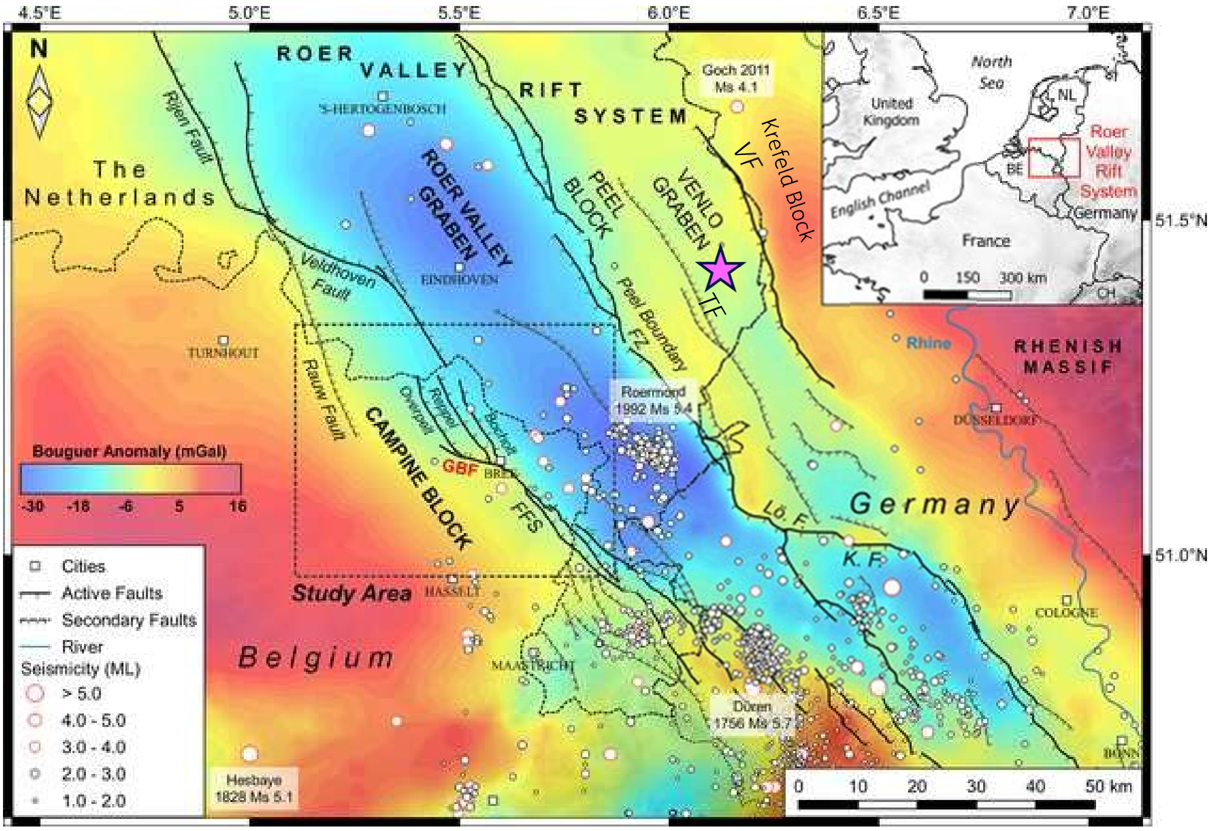

Figure 3.1.5. Map showing the Roer Valley rift system with the different tectonic blocks, main border fault configuration of Neogene active faults and seismicity in relation to the Bouger anomaly. The pink star indicates the location of the Californië doublets. Figure from Deckers et al., 2021.

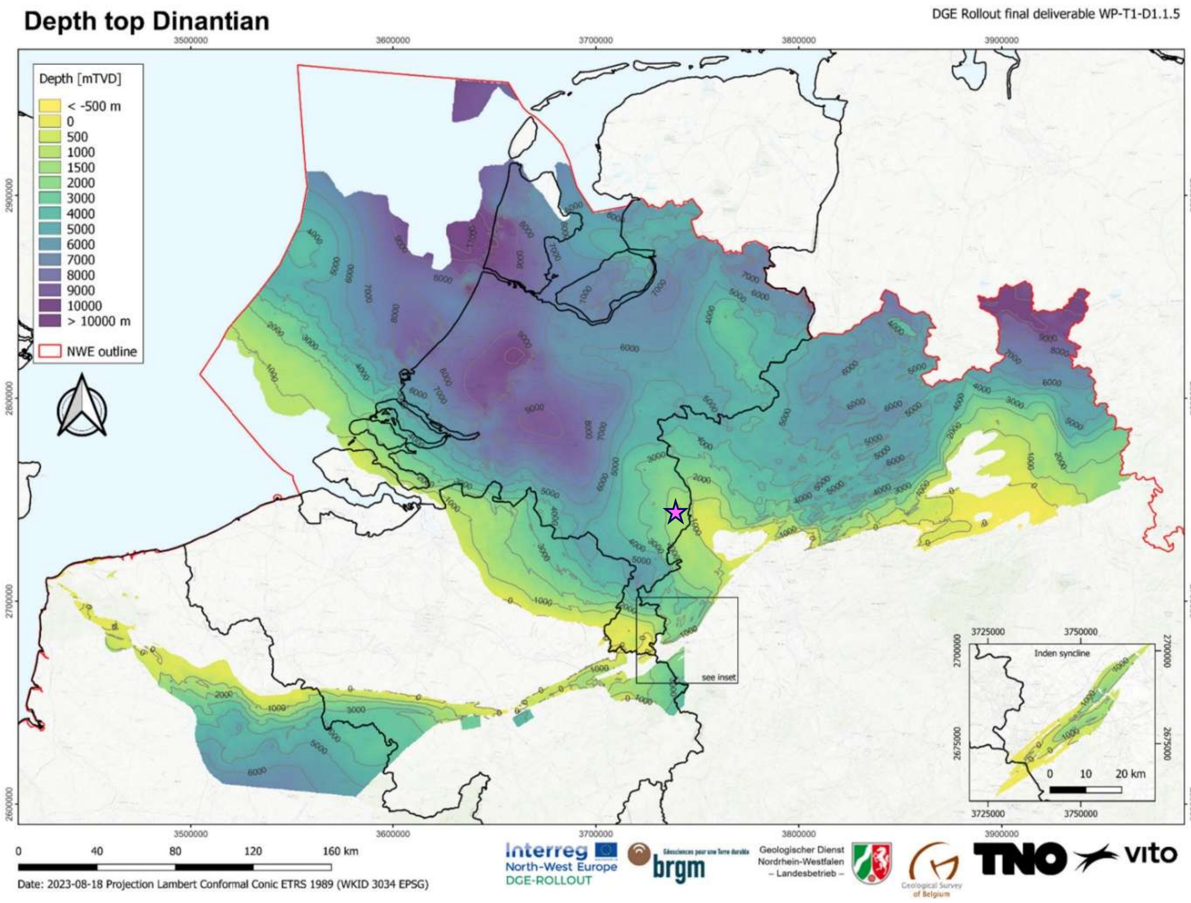

Figure 3.1.6. Depth map showing the top of the Dinantian in northern France, Belgium, the southern part of the Netherlands and within North-Rhine-Westphalia (Germany). The position of the Californië wells are indicated by the pink star. Figure from Veldkamp et al., 2023

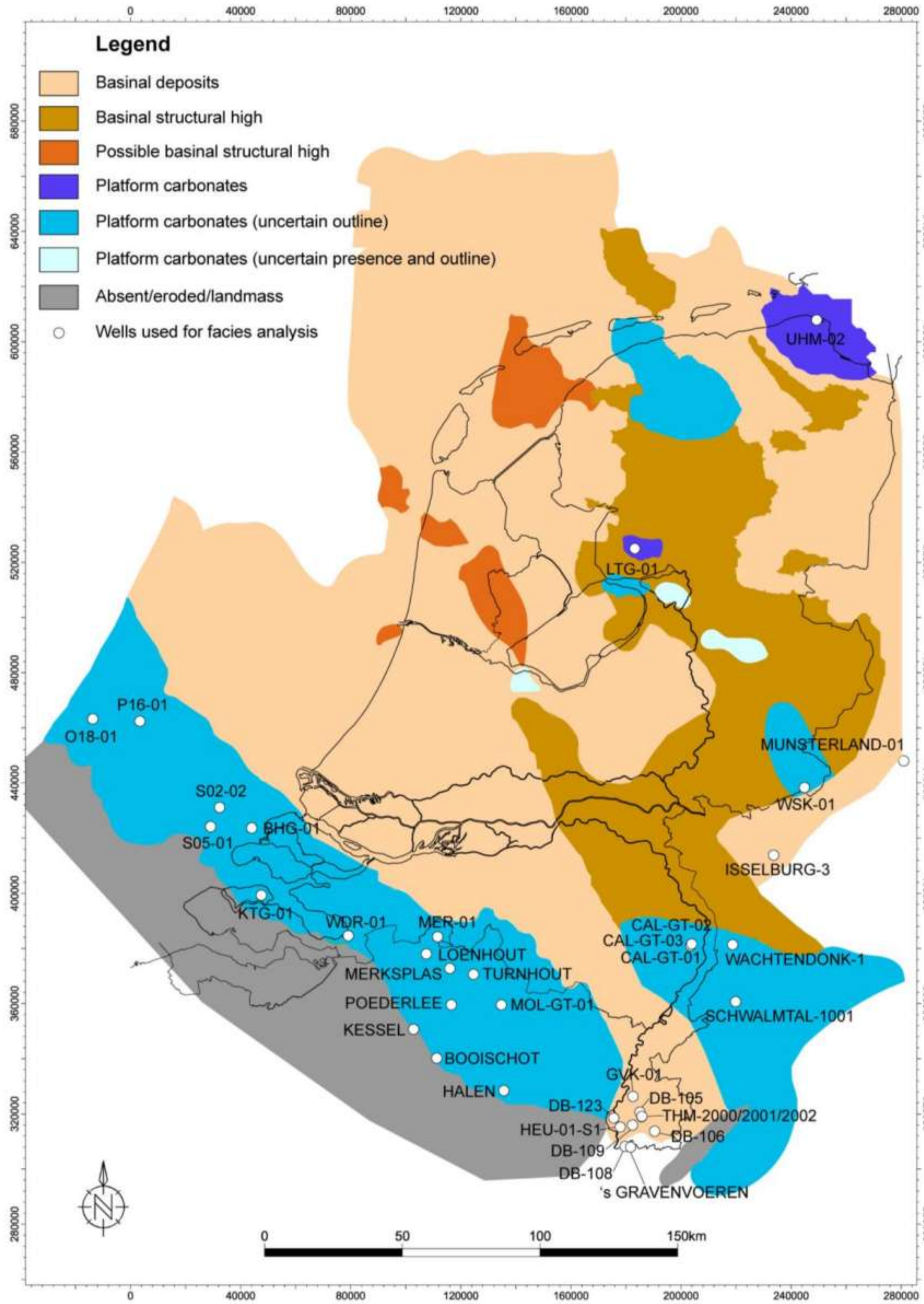

Figure 3.1.7. Reconstructed facies map showing the conservative distribution of the carbonate platforms during the Visean (Molinacian to Livian interval, and Warnantian). The white dots indicate wells that drilled into the Dinantian. Figure from Mozafari et al., 2019.

3.1.3 Stratigraphy and lithology

In this section, the stratigraphy of the target reservoirs for the Californië doublets is explained in more detail. The target reservoirs for the Californië doublets were deposited during the Late Devonian and Early Carboniferous and include fractured sandstones (quartzites) and shales of the Upper Devonian Condroz Group and Bosschveld Fm. (Famennian-Tournaisian age), the Lower Carboniferous Pont d'Arcole (Tournaisian age) and the fractured and partially karstified carbonates of the Zeeland Fm (Figure 3.2.3). The lithological descriptions as well as the interpretations regarding facies and diagenesis that are described in this paragraph are mainly obtained from work that has been conducted on cuttings from the Californië wells by Poty (2014) and by Mozafari et al., (2019) during the 2019 SCAN Dinantian project. For more detailed lithological descriptions and interpretations as well as for figures of the petrographic analyses on the cutting samples, we refer to these reports.

The lowest part of the interval of interest is the Upper Devonian (Fammenian) Evieux Fm., which is part of the Condroz Group. This interval consists mainly of alternations between shale, siltstone and argillaceous quartzite, locally also carbonates occur (mainly calcitized dolomites) (Poty, 2014; TNO-GDN, 2024, Figure 3.3.1).

The overlying Upper Devonian (Famennian) - Lowest Carboniferous (Tournaisian) Bosscheveld formation is characterised by a coarsening upwards sequence with quarzitic siltstones at the base and calcareous cemented sandstones (quartizites), calcitized dolomites and some cherts at the top (Poty, 2014; TNO-GDN, 2024). The carbonates are composed of bioclastic grainstones which were deposited in conditions ranging from low to high energy above normal wave base (Mozafari et al., 2019). Overall the Bosscheveld Formation could represent a cyclic carbonate platform, which is not too far from a source of siliciclastic sediments (Mozafari et al., 2019). Due to cementation of the pores, the primary matrix porosity of the sandstones is very low (Panterra, 2012). The Pont d'Arcole Fm. is poorly represented in cutting samples, but consists mainly of dark grey shales alternated with chertified argillaceous layers of carbonate (Laloux et al., 2000; Mozafari et al., 2019).

The Dinantian carbonates of the Zeeland Fm. (Tournaisian – Visean age) largely consists of dolomitised limestones, which have been partly dedolomitised (Poty, 2014; Mozafari et al., 2019) and silicified (Poty, 2014). Some cherts also occur within the carbonates (Poty, 2014). The dolomitization and other diagenic processes in general obliterate the original depositional structures of the carbonates. Some original bioclastic coated grains and partly dolomites limestones are also present in the cuttings, these samples are mainly identified as grainstones and wackestones (Mozafari et al., 2019). In the cuttings of well CAL-GT-01, neither deepwater microfacies nor biohermal ones (microbialite) were recognised (Poty, 2014). Overall the microfacies of the carbonates suggest a deposition of the Dinantian interval on a shallow water carbonate platform (Poty, 2014; Mozafari et al., 2019), but not a reef (Mozafari et al., 2019). From the cutting facies of well CAL-GT-01 is also derived that most of the dolomitization and dedolomitization is present in the lower Tournaisian part of the Dinantian carbonates (Poty, 2014). The upper Viséan part of the carbonates is also diagenetically altered, but is much more silicified, containing silicified dolomite and limestone, cherts and quartzites from quartz veins. The diagenetic alterations could have been caused by hydrothermal water circulations within the damage zone of faults (Poty, 2014; Mozafari et al., 2019). The top part of the Dinantian is likely affected by karstification (Mozafari et al., 2019). Evidence for major karstification was found in well CAL-GT-01, which encountered a large karst feature (i.e. void) between 1737 and 1758 m depth (measured along hole), which resulted in a total loss of drilling fluids (Mozafari et al., 2019).

In terms of matrix porosity, both the Devonian sandstones as well as the Dinantian carbonates can be considered generally as tight (Reijmer et al., 2017; PanTerra, 2012; Leverink & Geel, 2019; Mozafari et al., 2019). Within the Dinantian carbonates, microporosity may occur in some places (generally related to dolomitization), but generally these micropores are not connected and therefore not leading to significant permeability (Panterra, 2012; Carlson, 2019; Leverink & Geel., 2019). Hence, flow from these reservoirs has to come from fractures and/or karst (Leverink & Geel., 2019). The distribution and characteristics of fractures is challenging to predict and influenced by various factors which depend on the (hydro)geological history, paleo and current stress distributions, bed thickness, facies and lithology (e.g. Wennberg et al., 2007; Michie et al., 2014; Choi et al., 2016; van der Voet et al., 2020; van der Voet et al., 2022).

Generally e.g. there is a positive correlation between fault displacement, damage zone width and hence the amount and extent of fractures herein (Michie et al., 2014; Choi et al., 2016). Additionally, a correlation is present between limestone bed thickness and fracture density, as thicker limestone beds tend to display a lower fracture density (Wennberg et al., 2007). More specifically on Dinantian carbonates, Van der Voet et al., (2022) found via statistical outcrop analyses in southern Belgium that fracture density and intensity are significantly larger within the dolomites than in the limestones. Additionally it was found that also fracture connectivity was higher in the dolomites than in the limestones (Van der Voet et al., 2022).

3.2 Methods

This paragraph describes the methods regarding the construction of the geometry of the geological model, which was constructed by using Petrel software. The geometry of the geological model is based on the interpretations of the available seismic and well log data. The cells of the geological model were subsequently populated with properties derived from well log data and production data (Chapter 5). The construction of the 3D geological voxel (i.e. geocellular) model comprises five main steps (some of the steps are explained in more detail in the paragraphs 3.2.1 - 3.2.4):

1. Creating 3D surfaces of horizons and faults
    - Three surfaces were constructed based on 2D seismic- and well log interpretations:
        - Base Permian Unconformity (BPU)
        - Top Dinantian (i.e. Base Namurian)
        - Top Bosscheveld Fm. (i.e. Base Pont d'Arcole)

    The areas devoid of seismic and well data are filled by a convergent interpolation gridding algorithm supplemented with manual adjustments to fit the interpreted local and regional geological trends (see paragraphs 3.2.2 and 3.2.3 for more details about the methods regarding seismic interpretation and understanding the seismic signal).
2. Applying a time depth conversion (see paragraph 3.2.4 for more detail regarding the methods of the velocity model)
3. Pillar Gridding
    - During this step, faults were connected to each other and the grid was created for the geological model which follows the geometrical boundary conditions as constructed in step 1

4. Zone Creation
    - Based on the surfaces created within step 1. The following zones were created:
        - Namurian: from BPU to Top Dinantian.
        - Dinantian Carbonates: from top Dinantian to base Dinantian/Top Pont d'Arcole. The Top Pont d'Arcole was defined by taking an average thickness of 50 m, and converging via interpolation to well data points within a distance of 300 m from the wells.
        - Pont d'Arcole: from Top Pont D'Arcole to Top Bosscheveld Fm.
        - Bosscheveld Fm.: from Top Bosscheveld to Base Bosscheveld Fm. The Base of the Bosscheveld Fm. was defined by taking an average thickness of 100 m, and converging via interpolation to well data points within a distance of 300 m from the wells.
        - Evieux Fm.: From Base Bosscheveld Fm. to bottom of the model, for which a constant value of 3000 m was taken. Note that besides the lower part of the wells (until approximately 500 m below the Base Bosscheveld Fm. at well CAL-GT-03), no information is present about the lithology below the Evieux Fm.
5. Layering creation
    - The Zones created in step 4 were divided into layers to increase the vertical resolution of the model. The reservoir layers were modelled with a higher vertical resolution than the overlying Namurian and underlying Evieux Fm.

After applying these steps, a 3D geological voxel model was created for the Paleozoic interval which captures the geometries of the structural layering as well as the main faults cross-cutting the area and interval of interest.

3.2.1 Available seismic data

Eight 2D seismic lines are available in the direct vicinity of the Californië sites (Figure 3.2.1). Five 2D seismic lines were acquired relatively recently as part of the SCAN campaign, initiated by EBN in the period 2019 to 2022. These lines are:

- L2EBN2020ASCAN016 (referred to in Figure 4.2.1 as SCAN16)
- L2EBN2021ASCAN020 (Referred to in Figure 4.2.1 as SCAN20)
- L2EBN2020ASCAN029 (referred to in Figure 4.2.1 as SCAN29)
- L2EBN2021ASCAN031 (referred to in Figure 4.2.1 as SCAN31)
- L2EBN2022ASCAN046 (referred to in Figure 4.2.1 as SCAN46)

Two Lines were acquired as part of the Californië campaign in 2009. These lines are:

- L2CAL2009A-1_09-01 (Referred to in Figure 4.2.1 as 09-01)
- L2CAL2009A-1_09-02 (Referred to in Figure 4.2.1 as 09-02)

One seismic line that was used, was acquired by the Geological Survey (i.e. Rijks Geologische Dienst or RGD) in 1982. This is the line:

- L2RGD1982A-1_RGD82-04B(10001) (Referred to in Figure 3.2.1 as 04B)

The seismic data on all the lines adhere to the European polarity convention, meaning that an increase in acoustic impedance (i.e. a “hard kick”) is reflected as a through, which on the seismic lines shown in this report is depicted by a blue colour. A decrease in acoustic impedance (i.e. a “soft kick”) is reflected as a peak, which is in this report depicted by a red colour.

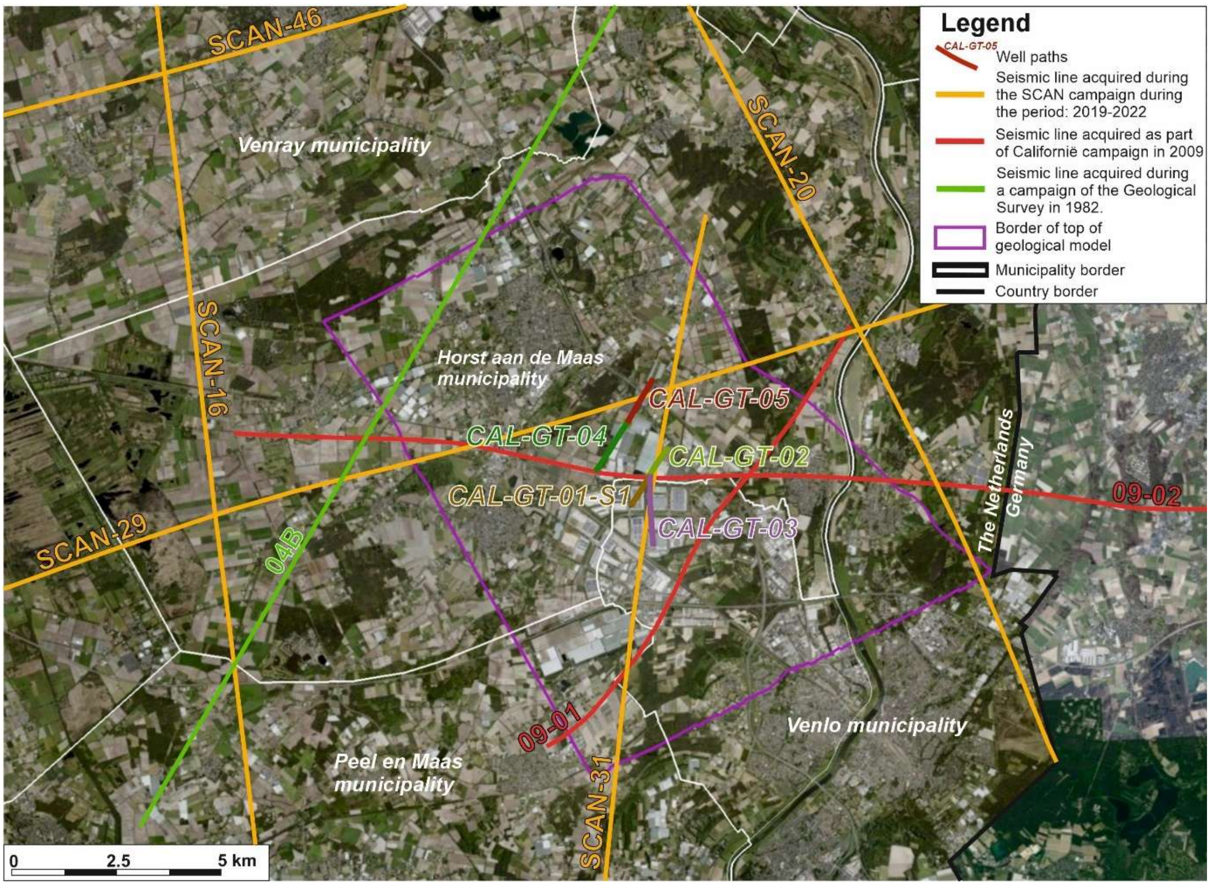

Figure 3.2.1. Satellite image indicating the position of the well heads and the well trajectories/paths. The colours of the trajectories correspond with the colours of the labels for each individual well. Also shown is the outline of the top of the geological model, as well as the seismic lines that were used as input data for the geological modelling.

3.2.2 Seismic interpretation

An initial seismic interpretation was performed by VITO in the 1st quarter of 2024 by using GoCad software. The seismic interpretation was conducted on the eight 2D seismic lines described in paragraph 3.2.1 (Locations shown in Figure 3.2.1) and consisted of 6 horizons (These results of these interpretation are shown by the squares in the seismic lines displayed in the paragraphs 3.3 and 3.4):

- Base Upper Cretaceous
- Base Lower Cretaceous
- Base Permian Unconofrmity (BPU)
- Top Dinantian
- Base Bosscheveld Fm.
- Base Devonian (conceptual)

The quality of the seismic data (including the relatively recently acquired SCAN seismic lines) is poor in several places, especially in the deeper Paleozoic interval. Additionally, no checkshot data or VSP (i.e. Vertical Seismic Profile) data is available to allow for a high certainty time-to depth conversion. Another element adding to the interpretation uncertainty is the fact that only 2D seismic data is available. None of the well trajectories align exactly with the seismic data. For plotting the well tops onto the seismic lines, an along azimuth projection of 165 degrees was applied to line up with the dominant orientation of the main NNW-SSE oriented high and general orientation of the layering following that high (see also paragraph 3.4.2).

Because of these uncertainties and the complex geological setting, different scenarios are possible, as can also be concluded from the variety of different geological models that were created for the Californië sites in the past (Broothaers & Laenen, 2010; Geel, 2017; Reith/EBN, 2018, see also paragraph 3.4.1). Based on different choices regarding the interpretation of the data, two-end member scenarios are proposed to explain the observed thickness differences of the Dinantian interval within the different Californië wells:

1. A model where the Dinantian thickness differences are mainly explained via faults, thereby assuming a more constant Dinantian thickness
2. A model where the Dinantian thickness differences are mainly explained via stratigraphic thinning and syn-depositional fault activity, complemented with a component of karst.

Because of limited resources, it was not possible to construct multiple static geological models and subsequently multiple reservoir and geomechanical models. Therefore a hybrid geological model was constructed, which incorporates elements from both end-member scenario's. During the dynamic reservoir modelling (chapter 5) and geomechanical modelling (chapter 6), different scenarios regarding e.g. the presence or absence of a certain fault could still be tested by using the hybrid geological model as a starting point. The hybrid geological model was constructed based on an updated interpretation performed in the 2nd quarter of 2024 by using Petrel software. The following horizons were interpreted for this model:

1. Base Permian (BPU)
2. Top Dinantian (i.e. Base Namurian)
3. Top Bosscheveld Fm. (i.e. Base Pont d'Arcole)

It is noted that the hybrid geological model is supported by geologists from both VITO and TNO as a practical solution, deemed fit for purpose for this study. It is emphasized though that uncertainties are present about the true geological setting at the Californië sites, and that in theory one of both end-member models could still be possible (see also paragraph 3.4.1 where uncertainties are discussed in more detail). The results of the final hybrid interpretation are described in paragraphs 3.3.1 and 3.3.2. The individual end-member scenarios are discussed in paragraph 3.4.1.

3.2.3 Synthetic seismogram

To aid the final seismic interpretation, used for the hybrid geological model, a synthetic seismogram was created for well CAL-GT-01 to gain better understanding of the expected seismic signal. This well has a sonic log and a complete succession of the Upper Devonian and Dinantian intervals. A density log is missing, but the expected density was calculated by using the empirically derived Gardner's equation, where ρ = bulk density in g/cm³ and V_p = P-wave velocity in m/s:

$$\rho = 0.31V_p^{0.25}$$

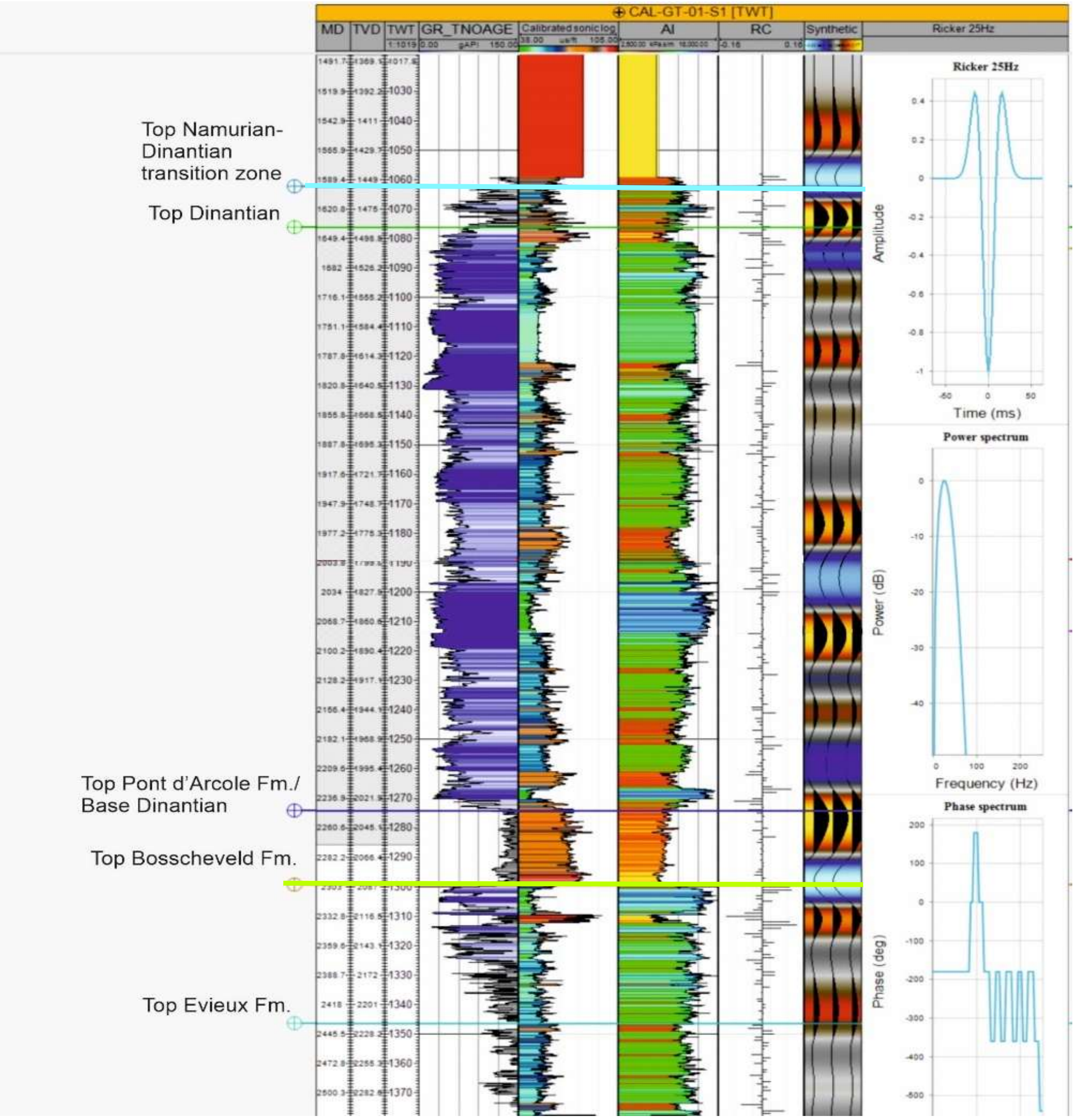

Figure 3.2.2. Synthetic seismogram for well CAL-GT-01- (S1) for the Upper Devonian and Dinantian interval. Abbreviations used: MD: Measured depth (in m); TVD (True vertical depth (in m); TWT: Two-Way-Travel Time (in ms); GR: Gamma-Ray (in gAPI); AI: Acoustic Impedance (in kPa.s/m), RC: Reflection Coefficient.

Note that the top of the transition zone between the Namurian and the Zeeland Fm. (i.e. Dinantian carbonates) is characterised by an expected increase in acoustic impedance, caused by a relatively low velocity (and density) of the Namurian shales of the Epen Fm with the Carbonates that are (partly) present in the Namurian-Dinantian transition zone. The top of the Dinantian was mapped on seismic data for the hybrid on this first hard kick (i.e. on the first major increase in acoustic impedance, which is the relatively thick and horizontal light blue line in Figure 3.2.2). Another strong increase in acoustic impedance is expected at the base of the Pont d'Arcole, marking the transition between the clay-rich Pont d'Arcole to the cemented sandstones and carbonates of the Bosscheveld Fm (i.e. the relatively thick and horizontal bright green line in Figure 3.2.2). It is important to note that based on the interval velocities and the frequency of the data, there is a certain limit to the interfaces that can be pick up by seismic data. This vertical seismic resolution is in the order of 10 to 30 meters for the datasets used. Lithological transitions and fault displacements lower than the vertical seismic resolution will not be visible in the seismic data.

3.2.4 P-wave velocity model

A velocity model was created to convert the seismic data in ms Two-Way-Travel-Time (TWT) and to determine the hypocenter locations of the seismic events (see chapter 6). The velocity model created in this project is a 'layer cake' type velocity model, where the seismic velocity (i.e. compressional P-wave velocity) is modelled for distinct stratigraphic intervals. Seven stratigraphic intervals are distinguished:

- Upper North Sea Group
- Lower and Middle North Sea Groups
- Mesozoic
- Namurian
- Dinantian
- Pont d'Arcole
- Bosscheveld Fm. + Condroz Group

The seismic velocity is largely determined by the hardness of the rock (which largely correlates with the density of the rock), that is controlled by the lithology and the burial (or more specifically: diagenetic) history of the rock (Paap et al., 2024). Sedimentary rocks compact due to sedimentary loading when they get buried over geological time. This compaction results in an increase in density (and hence; hardness) of the rock, leading to an increase in acoustic velocity with (maximum burial) depth (Paap et al., 2024; Figure 3.2.3). This process is described by the following linear relation, which is also used in the regional velocity model of the Netherlands, VELMOD 3.2 (Paap et al., 2024):

$$V = V_0 + kZ$$

Where V [m/s] is the instantaneous velocity, V_0 [m/s] is the normalized velocity at depth Z=0, k [m/s/m] is the velocity-depth gradient and Z [m] is the depth. For the regional VELMOD velocity model, the V_0 and k parameters are determined by determining a regional velocity-depth gradient (Paap et al., 2024). One k value is derived for each stratigraphic interval, which reflects the regional velocity-depth gradient (Paap et al., 2024). For the V_0 value, regional V_0 map are constructed in VELMOD 3.2 using a local base fit calibration method of Japsen (1993) (Paap et al., 2024). These V_0 distribution maps should capture regional trends regarding lithology (e.g. facies changes) (Paap et al., 2024, Figure 3.2.4). This method gives good results for regional purposes. The structural complexity in the subsurface is captured by gridded surfaces that are derived from seismic interpretations based on the DGM-deepV5 model (TNO-GDN, 2019; Paap et al., 2024). For the Cenozoic and Mesozoic interval, many reliable data points are available in the form of sonic, VSP and checkshot data. Additionally, the gridded surfaces of the corresponding intervals are of sufficient detail to capture the structural trends within the area of interest. Hence, the regional VELMOD model version 3.2 is considered reliable and fit for purpose to use within this project for the Cenozoic (i.e. North Sea Groups) and Mesozoic interval.

The Cenozoic interval was modelled as two stratigraphic intervals (i.e. the Upper North Sea Group (1st interval) and the Lower and Middle North Sea Groups combined (2nd interval). The V_0 and k values, as well as the gridded surfaces were directly obtained from VELMOD 3.2 (Paap et al., 2014). The Mesozoic interval within the area of interest consists of a thin Zechstein interval (approximately 50 m, largely composed of siliciclastic material intercalated with some carbonates), which is overlain by a relatively thick package of Lower Triassic Nederweert sandstone (approximately 300 m). The Jurassic interval is absent and the Cretaceous interval is with approximately 50-60 m again relatively thin within the area of interest. Hence, the V_0 and k values, as well as the gridded surfaces were directly obtained from the Lower Triassic interval from VELMOD 3.2 (Paap et al., 2014).

The Namurian interval is the lowest and oldest interval that is incorporated in the VELMOD 3.2 model, but the interval is lacking a detailed gridded surface in this regional model and also the velocity data points are scarce. Consequently, VELMOD 3.2 is considered unreliable and not fit for purpose for the area of interest and the aims of the current project.

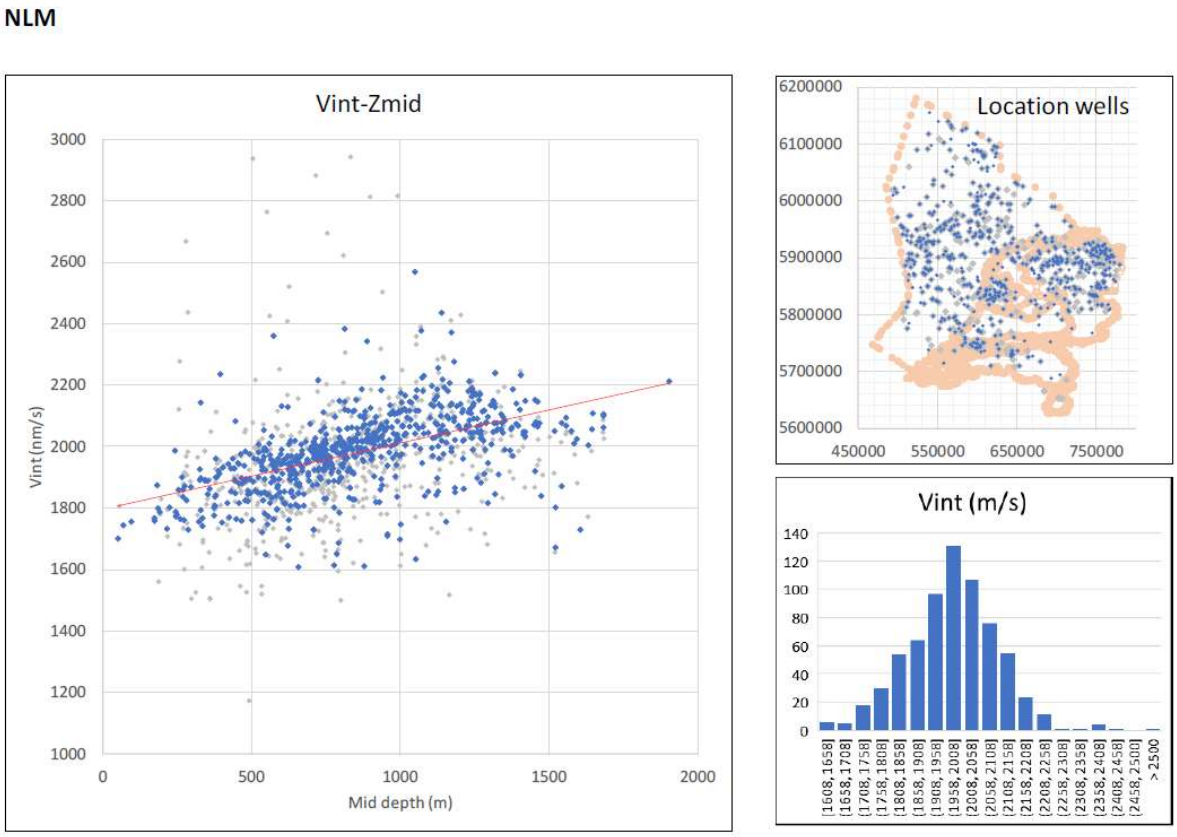

Figure 3.2.3. Average interval velocities (V_{int}) plotted against mid depth for a set of wells with reliable velocity data as an example for the Middle and Lower North Sea Groups combined in the Netherlands. Note the increase in average interval velocities with increasing depths. Figure from VELMOD 3.2 (Paap et al., 2024)

The Dinantian as well as the underlying intervals are not incorporated in VELMOD 3.2 at all. Hence the entire Paleozoic interval is modelled based on the local sonic data available for well CAL-GT-01, the gridded surfaces which follow from the seismic interpretation performed during this project and insights from the sparse Paleozoic data points available from the region. The results for the velocity model are described in paragraph 3.3.3.

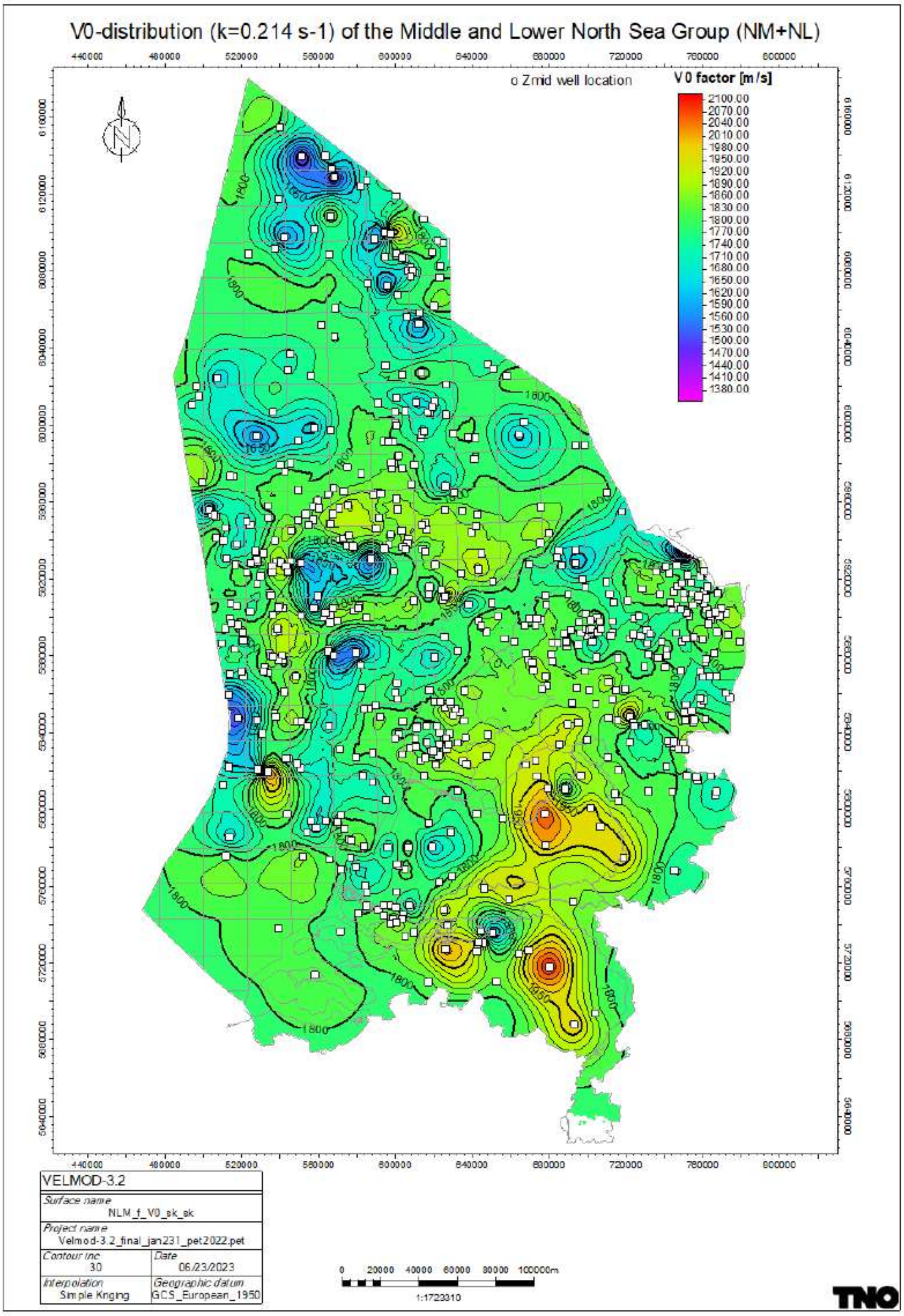

Figure 3.2.4. Example of a V_0 distribution map for the Middle and Lower North Sea Groups from VELMOD model 3.2. The varying V_0 values should reflect lithology (e.g. facies changes) within the interval of interest. Figure from VELMOD 3.2 (Paap et al., 2024).

3.3 Results

In this paragraph, the results are presented of well log interpretations and correlations (paragraph 3.3.1), the seismic interpretation, which forms the base for the hybrid geological model (paragraph 3.3.2), the seismic P-wave velocity modelling (paragraph 3.3.3) and the geological modelling (paragraph 3.3.4).

3.3.1 Well log interpretations and correlations

Figure 3.3.1 shows a well panel of the five Californië wells with the available log data. The Dinantian carbonates clearly stand out as they're characterised by low gamma ray values (dark blue colours) and additionally by the high sonic values (i.e. high acoustic velocities, depicted in blueish, greenish and turqois colours in the right-hand side of the sonic log in well CAL-GT-01-S1). The Pont d'Arcole, as well as the Namurian, underlying and overlying the Dinantian carbonates respectively, can also clearly be recognised as relatively high gamma ray values, depicted in the greyish colours and as relatively low acoustic velocities (especially visible for the Pont d'Arcole, depicted by the brown and orange colours). The transition between the Namurian and Dinantian carbonates is characterised by a gradual transition (usually over an interval of a few 10's of meters) from carbonate rich to clay-rich strata via a karstified zone. The Bosscheveld Fm. is underlying the Pont d'Arcole Fm. and is again characterised by relatively low gamma-ray values and relatively high sonic values. The bottom of the Bosscheveld Fm. (i.e. top of the Evieux Fm.) is taken at the start of the coarsening upward sequence that characterises the Bosscheveld Fm., but the exact bottom of the Bosscheveld Fm. is not always evident.

The Dinantian carbonates between the 5 different wells are characterised by major thickness differences (Figure 3.3.1). The Dinantian carbonates are approximately 550 m thick in the wells CAL-GT-04 and CAL-GT-01-S1. 250 m thick in well CAL-GT-03 and less than 150 m thick in the wells CAL-GT-05 and CAL-GT-02. These thickness differences have been explained in different ways during previous studies (Geel, 2017; Reith, 2018). In the final hybrid interpretation created during this study, these thickness differences have been primarily explained via faulting (supplemented with some degree of stratigraphic thinning towards the northeast and karstification on top of the structural high, see Paragraph 3.3.2).

A normal fault, which was active during the Carboniferous, has been interpreted on seismic data (Paragraph 3.3.2, Figures 3.3.4-3.3.6). Well CAL-GT-03 has been interpreted to cross-cut this Carboniferous normal fault at the top of the Dinantian, causing the upper part of the Dinantian to have been faulted out (the position of the fault is indicated by the red horizontal line, highlighted with the red star in figure 3.3.2). Northeast of the Carboniferous normal fault, a transpressional fault (i.e. Western Pop-Up fault) has been interpreted. Based on well log-, and seismic data, it has been interpreted that the wells CAL-GT-02 and CAL-GT-05 cross-cut this fault (Paragraph 3.3.2, Figures 3.3.4-3.3.6). Consequently, only a minor part of the Dinantian has been preserved within these wells (Figure 3.3.2).

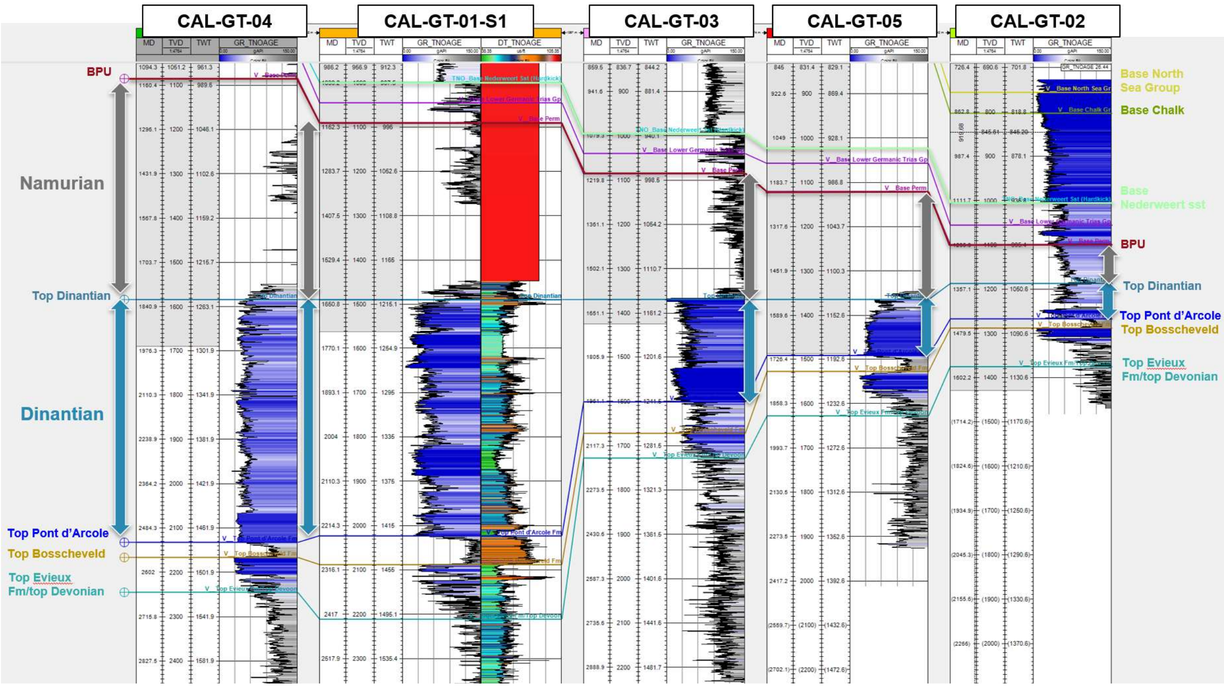

Figure 3.3.1. Interpreted well logs: stratigraphy only, displaying Gamma Ray (GR), and for CAL-GT-01-S1 also sonic (DT) logs. For the GR-logs: Blue colours indicate relatively low GR values. Grey colours indicate relatively high GR values. White colours display intermediate GR values. For the sonic log in well CAL-GT-01-S1: orange colours indicate relatively high sonic values, which correspond to relatively low interval velocities. The bright green colours indicate relatively low sonic values, which correspond to relatively high interval velocities. Blue colours indicate intermediate sonic values. See Figures 3.2.1 or 3.3.3 for the location of the wells. Abbreviations used: MD: Measured depth (in m); TVD: True vertical depth (in m); TWT: Two-Way-Travel Time (in ms); GR: Gamma-Ray log (in gAPI); DT: sonic (i.e. compressional P-Wave) log (in µs/ft). See Appendix A for a high resolution version of this figure.

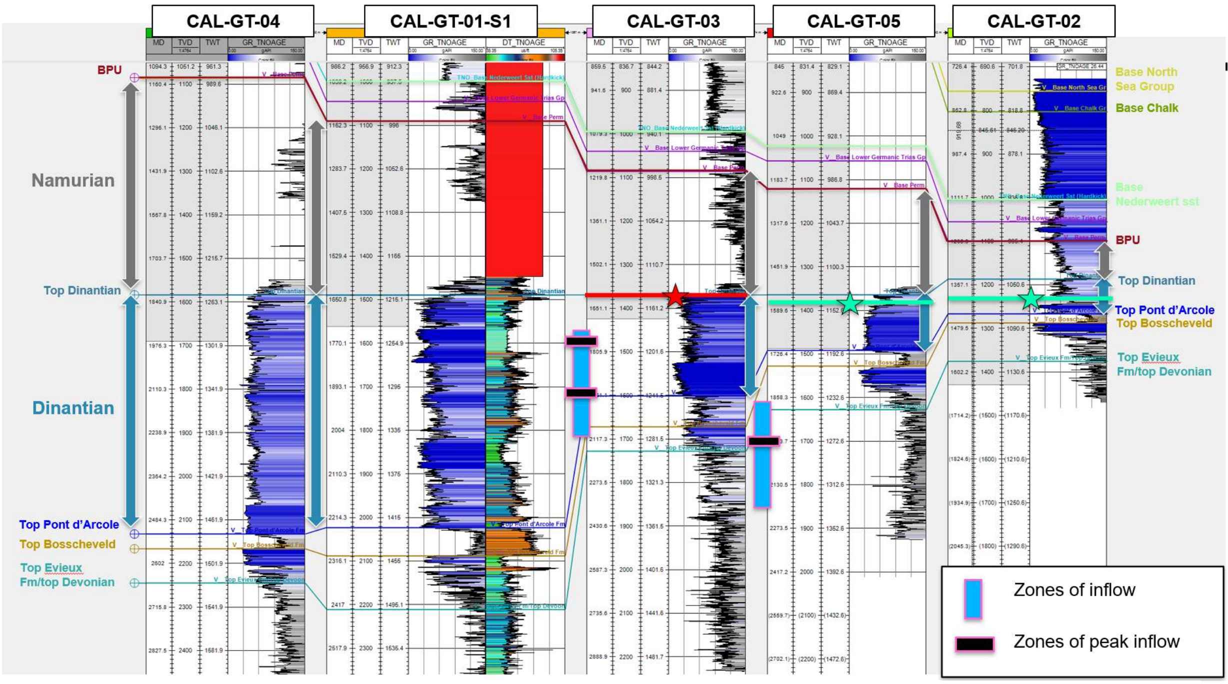

Figure 3.3.2. Interpreted well logs: faults and stratigraphy for the hybrid interpretation. Displaying Gamma Ray (GR), and for CAL-GT-01-S1 also sonic (DT) logs. The horizontal red and light green lines indicate the position of faults, which have faulted out parts the Dinantian. The horizontal red line in well CAL-GT-03 (highlighted with the red star) indicates the position of the Carboniferous normal fault. The horizontal light green lines (highlighted with the light green stars) indicates the position of the western pop-up fault in the wells CAL-GT-02 and CAL-GT-05. See Figures 3.2.1 or 3.3.3 for the location of the wells. Abbreviations used: MD: Measured depth (in m); TVD: True vertical depth (in m); TWT: Two-Way-Travel Time (in ms); GR: Gamma-Ray log (in gAPI); DT: sonic (i.e. compressional P-Wave) log (in µs/ft). See Appendix A for a high resolution version of this figure.

3.3.2 Seismic interpretation

Figures 3.3.4 to 3.3.6 show the final seismic interpretation for the three seismic lines that are closest to the Californië doublets (i.e. SCAN29, 09-02 and SCAN-31). The seismic interpretation displayed in these figures formed the base for the final geological hybrid model and is described in this paragraph. The seismic interpretation follows from the observations and stratigraphic correlations conducted on the well logs (paragraph .3.1), and the learnings derived from both the velocity modelling (paragraphs 3.2.4 and 3.3.3), the synthetic seismogram (paragraph 3.2.3), as well as from the regional understanding of the deposits and their tectonic evolution (paragraphs 3.1.2 and 3.1.3).

Interpreted faults

From east to west, 6 faults were interpreted that were incorporated in the model (Figures 3.3.3 - 3.3.6 and Appendix B for a high resolution version of these figures):

- Western boundary Fault (NE dipping fault, forming the southwestern boundary of the geological model)
- Tegelen Fault (NE dipping fault, with approximately 200-250 m of normal displacement)

- Carboniferous Normal Fault (SW dipping fault, with approximately 150-200 m of normal displacement at the top of the Dinantian and 250-300 m of normal displacement at the base of the Dinantian)
- Western pop-up fault (NE dipping transpressional fault, with approximately 150-200 m of thrust displacement, the amount of strike-slip displacement is unknown)
- Eastern pop-up fault (SW dipping transpressional fault, with approximately 100-150 m of thrust displacement, amount of strike-slip displacement is unknown)
- Velden Fault (NE dipping fault, forming the northeastern boundary of the geological model)

Two faults were interpreted with a higher uncertainty of being present (Indicated by the dashed lines in Figures 3.3.4 – 3.3.6, named: possible fault and possible thrust fault). Because of the distance to the Californië doublets, these faults were also inferred to be of less relevance for the reservoir and geomechanical modelling.

Interpreted geological structures
The northeastern part of the area of interest is characterised by a relatively shallow position of the paleozoic strata (referred to as Paleozoic High (PH) in Figures 3.3.4 - 3.3.6). At this Paleozoic High (PH), the Westphalian and Namurian strata are completely absent and the overlying Mesozoic strata, comprised of upper Permian (i.e. Zechstein), Triassic and Cretaceous, onlap onto the PH (indicated by the semi-horizontal white arrows in the Figures 3.3.4 - 3.3.6). The onlapping Mesozoic strata indicate that a large part of the PH was subaerially exposed from the Upper Permian to the Cretaceous, comprising a period of around 150 million years. The PH is characterised by a sharp delineation at its northeastern margin, which is formed by the Velden Fault. Towards the southwest of the PH, an increasingly thick interval of Namurian is preserved which is concordantly overlying the Dinantian carbonates and is truncated at the top by the BPU (indicated by the upward directed white arrows in the Figures 3.3.4 - 3.3.6).

Just southwest of the PH, the Paleozoic strata are offset by two relatively steeply dipping faults, which have been interpreted together as a pop-up structure (PU). Both the PH and the PU, likely formed during the latest Carboniferous-Early Permian phase of transpressional tectonics (see introduction paragraph 3.1.2) and display similarities in geometry with fault systems that were recognised in the Belgium Campine Block, just south of the Roer Valley Graben (see also, introduction paragraph 3.1.2 and Deckers et al., 2023). Wells CAL-GT-02 and CAL-GT-05 penetrate the western pop-up fault and therefore do not encounter a significant part of the top of the Dinantian (Figure 3.3.2). It is interpreted that CAL-GT-05 also penetrates the eastern pop-up fault within its lower section (Figure 3.3.4). Within the PU, Paleozoic strata dip relatively steep (locally up to 55°). Above the PU, a convex bending of reflectors is observed within the Mesozoic interval, which is interpreted to have been the result of some reactivation of the PU during Late Cretaceous inversion. Additionally, differences in compaction within the Mesozoic sediments on either side of the pop-up structure might also (to some extent) explain the curved Mesozoic strata above and along the sides of the pop-up.

The hard kick (i.e. blue reflector), slightly above the BPU, is the base of the Nederweert Sandstone Mb (See Figures 3.3.4-3.3.7). Below this sandstone, a hard limestone unit, which is part of the marginal Zechstein facies is encountered where the drilling speed drops (Figure 3.3.7). These marginal Zechstein carbonates are composed of carbonate platforms or build-ups, which were deposited around paleo highs during the Late Permian. The mound like structures that can be observed on the seismic data reflect these carbonate platforms, which typically display rapid lateral thickness changes depending on the carbonate facies (see e.g. white star in Figure 3.3.5). Structures displaying similar geometries on seismic data can be found elsewhere in the southern North Sea around paleo highs (e.g. Van de Sande et al., 1996; Patruno et al., 2017; Peeters et al., 2023).

Towards the southwest of the PU, the Paleozoic interval is generally dipping towards the southwest with an inclination between 15 and 30°. The Dinantian interval is becoming thicker towards the southwest, which is best observed in the area between the Carboniferous normal fault and the Western Pop-Up fault (Figure 3.3.3 and Figures 3.3.4 – 3.3.6). The thickness of the Dinantian increases further across the Carboniferous normal fault, where the Dinantian is thicker in the hanging wall than in the footwall, which indicates that this fault was active as a normal fault during deposition of the Dinantian (likely at the end of the Dinantian, based on analogies with similar structures observed in the Campine Basin). Well CAL-GT-03 is interpreted to cross-cut the Carboniferous normal fault at the top and therefore does not encounter the top part of the Dinantian (Figures 3.3.2 and Figures 3.3.4 - 3.3.6). The area between the Carboniferous normal fault and the Tegelen fault is a narrow graben, referred to as the Californië Graben (CG in Figures 3.3.4 - 3.3.6). The wells CAL-GT-01 and CAL-GT-04 drill into this CG, encountering the thickest and complete interval of Dinantian. Based on seismic interpretations, well CAL-GT-04 likely drills into the Tegelen fault in its lower section. For well CAL-GT-01 it is less clear if the Tegelen fault is reached. Further towards the southwest (i.e. on the footwall side of the Tegelen Fault) the Dinantian remains of approximately constant thickness, which is likely similar to the thickness within the CG. Additionally, the Dinantian and surrounding intervals are found at increasing depths towards the southwest (Figure 3.1.7 and Figures 3.3.4 - 3.3.6).

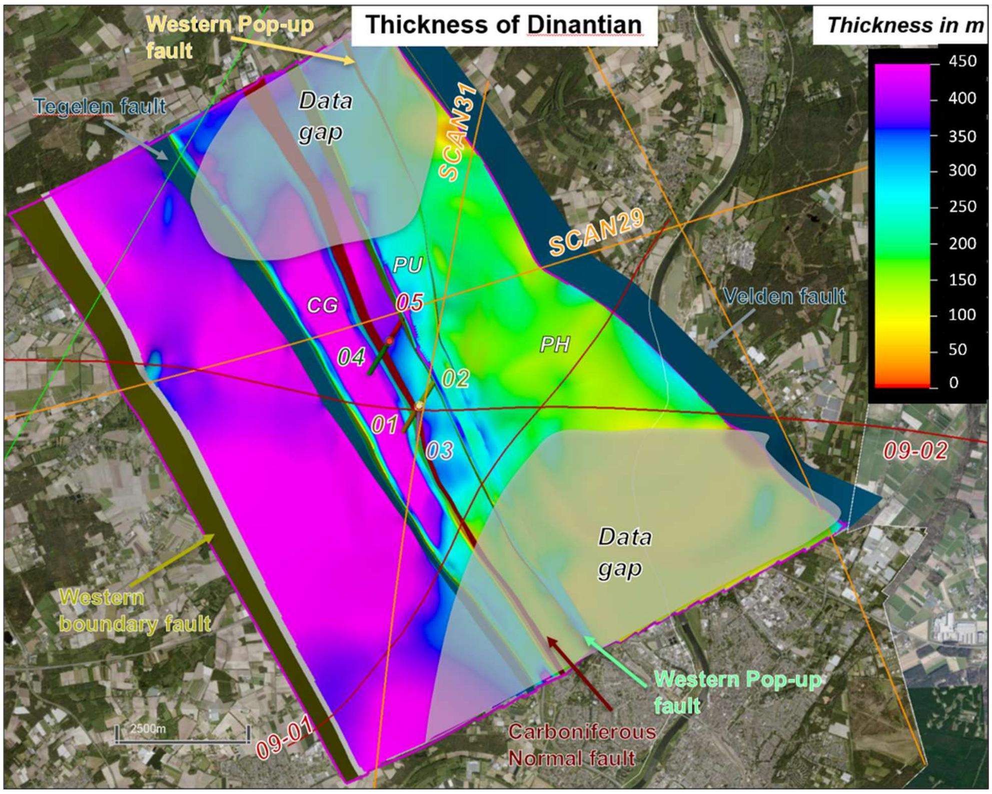

Figure 3.3.3. Thickness map of the Dinantian Note the southwestward thickening from the Paleozoic High (PH) towards the area southwest of the Tegelen Fault. Abbreviations used: CG; Californië Graben, PH; Paleozoic High; PU; Pop-up.

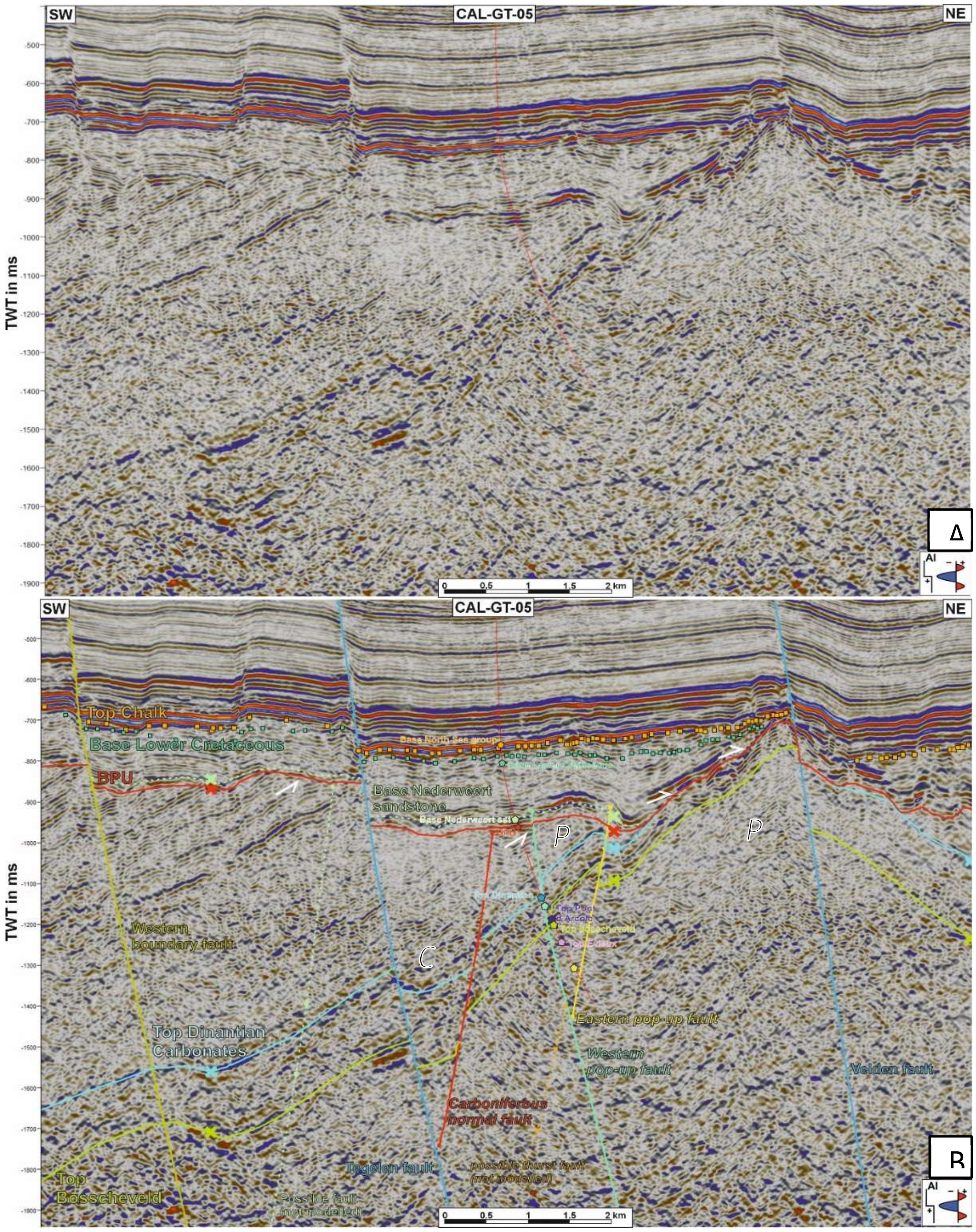

Figure 3.3.4. SW-NE oriented Scan line 029. A) Uninterpreted seismic line. B) Interpreted seismic line. Abbreviations used: BPU, Base Permian Unconformity; PH, Paleozoic High (PH). The three thick lines (i.e. BPU, Top Dinantian Carbonates and Top Bosscheveld) indicate the final seismic interpretations, which together with the well data, formed the base for the final geological Hybrid model. The squares indicated the position of the Top Chalk and the Base of the Lower Cretaceous; both are not used in the geological hybrid model. The dashed light green line positioned slightly above the BPU indicates the interpreted Base of the Nederweert Sandstone (also not used in the final geological hybrid mode)l. The white arrows indicate both truncations against BPU (upward directed) and onlaps against the PH (horizontally directed). See Figures 3.2.1 or 3.3.3 for the location of the seismic line. ***See Appendix B for a high resolution version of this figure.***

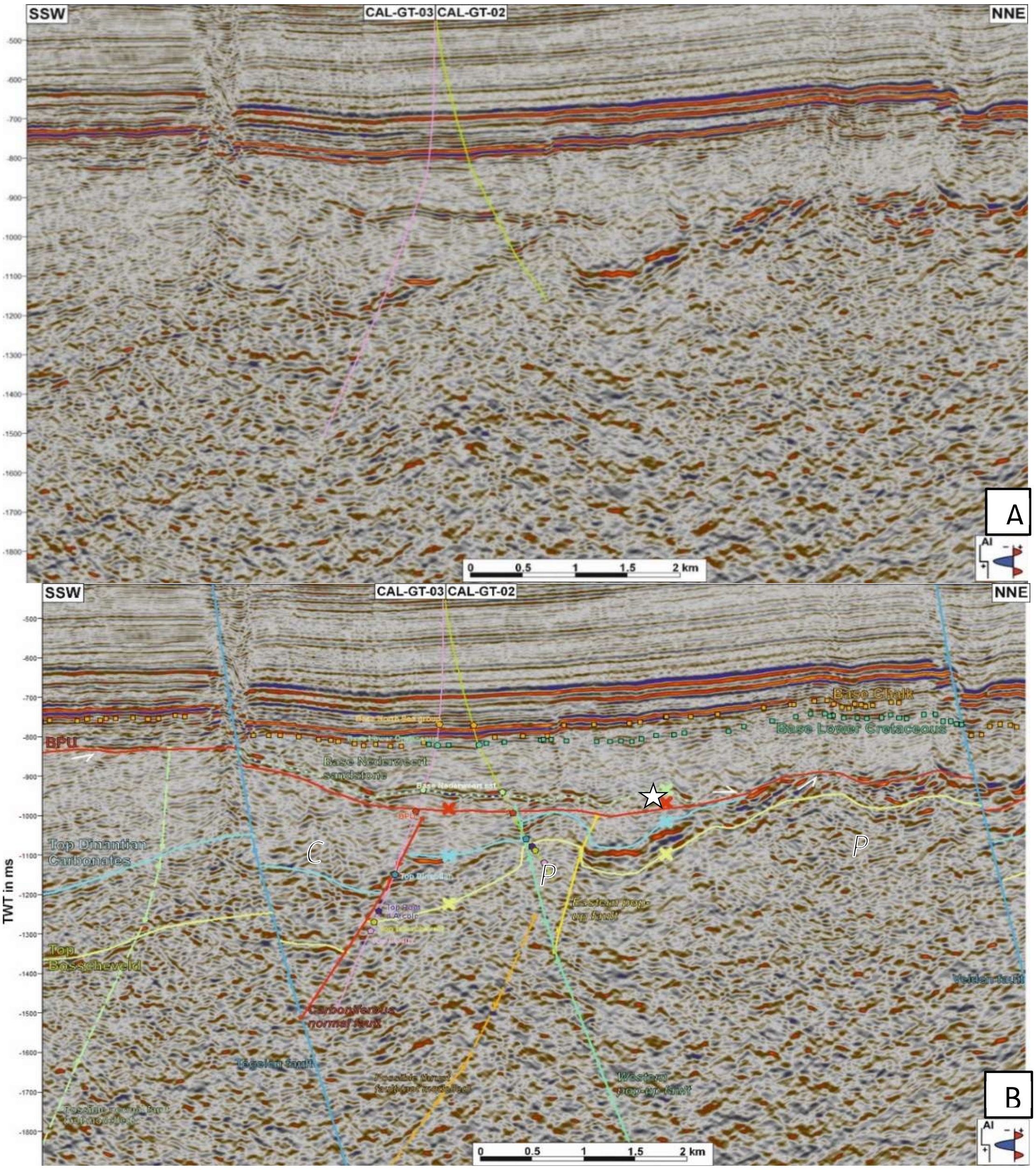

Figure 3.3.5. SSW-NNE oriented Scan line 031. A) Uninterpreted seismic line. B) Interpreted seismic line. Abbreviations used: BPU, Base Permian Unconformity; PH, Paleozoic High (PH). The three thick lines (i.e. BPU, Top Dinantian Carbonates and Top Bosscheveld) indicate the final seismic interpretations, which together with the well data, formed the base for the final geological Hybrid model. The squares indicated the position of the Top Chalk and the Base of the Lower Cretaceous; both are not used in the geological hybrid model. The dashed light green line positioned slightly above the BPU indicates the interpreted Base of the Nederweert Sandstone (also not used in the final geological hybrid mode)l. The white arrows indicate both truncations against BPU (upward directed) and onlaps against the PH (horizontally directed). See Figures 3.2.1 or 3.3.3 for the location of the seismic line. ***See Appendix B for a high resolution version of this figure.***

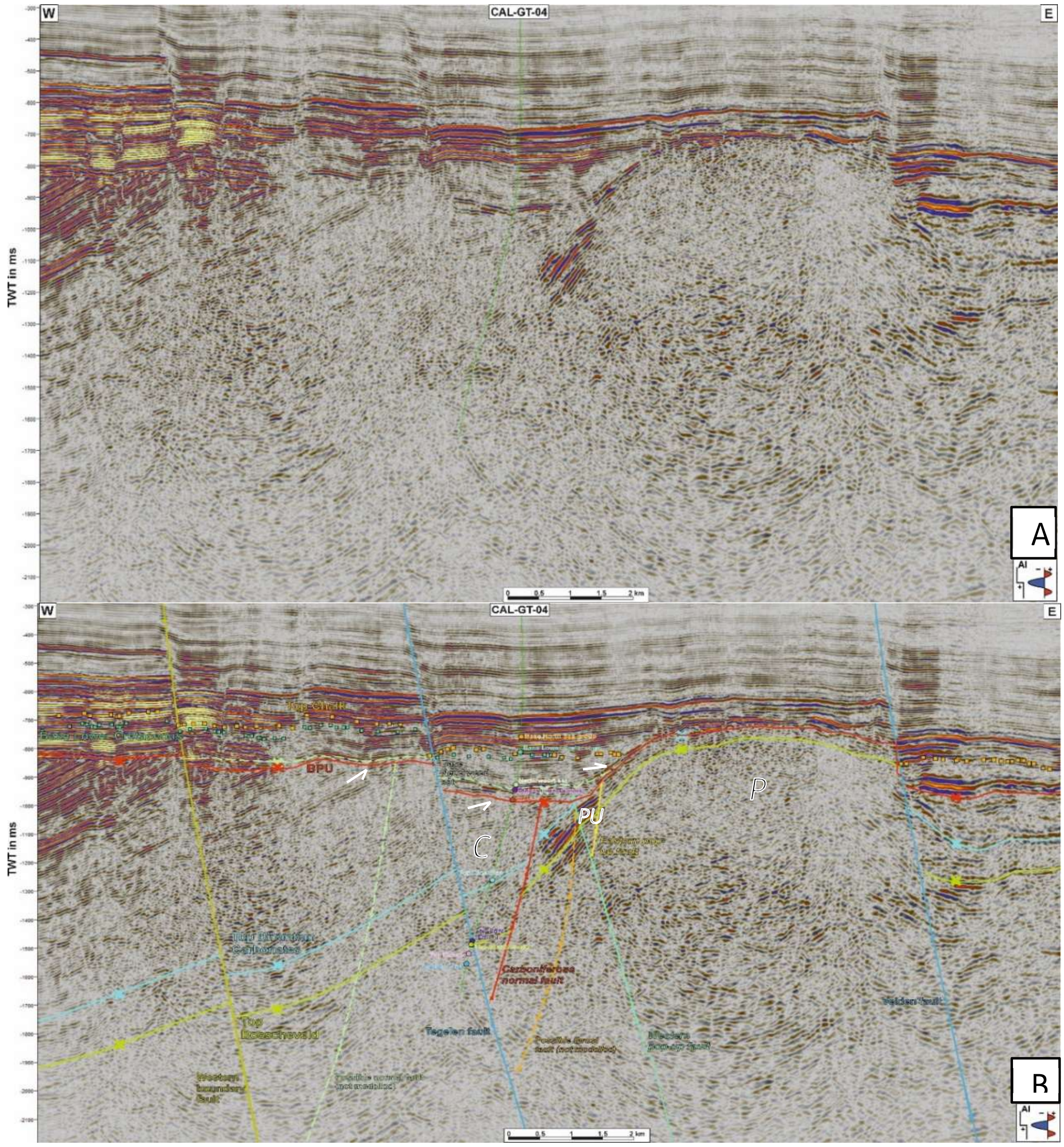

Figure 3.3.6. W-E oriented line 09-02. A) Uninterpreted seismic line. B) Interpreted seismic line. Abbreviations used: BPU, Base Permian Unconformity; PH, Paleozoic High (PH). The three thick lines (i.e. BPU, Top Dinantian Carbonates and Top Bosscheveld) indicate the final seismic interpretations, which together with the well data, formed the base for the final geological Hybrid model. The squares indicated the position of the Top Chalk and the Base of the Lower Cretaceous; both are not used in the geological hybrid model. The dashed light green line positioned slightly above the BPU indicates the interpreted Base of the Nederweert Sandstone (also not used in the final geological hybrid mode)l. The white arrows indicate both truncations against BPU (upward directed) and onlaps against the PH (horizontally directed). See Figures 3.2.1 or 3.3.3 for the location of the seismic line. ***See Appendix B for a high resolution version of this figure.***

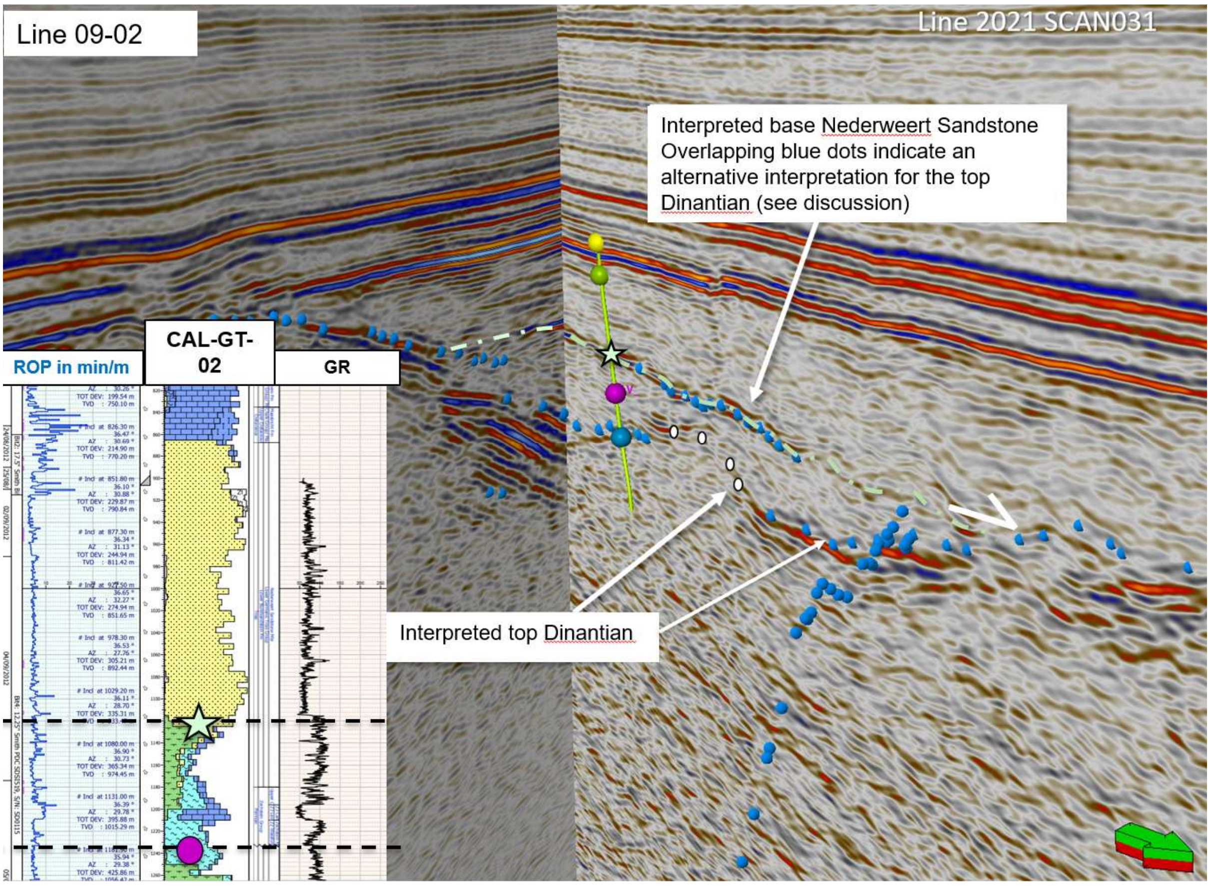

Figure 3.3.7. Oblique view towards the southwest displaying the intersection between the E-W oriented seismic line 09-02 and the SSW-NNE oriented SCAN line 031. The trajectory of well CAL-GT-02 is displayed in bright green. The hard kick (in the blue seismic reflector) which is highlighted with the light green dashed line, is the base of the Nederweert Sandstone mb. Note that the Rate of penetration (ROP) decreases from the Nederweert Sandstone into the underlying Zechstein interval, which is largely composed of Carbonates. In the absence of a sonic or density log, this is indicate for an increase in acoustic impedance at the transition between the Nederweert Sandstone and the Zechstein carbonates.

3.3.3 P-wave Velocity model

This paragraph describes the main results for the P-wave velocity analysis, focussing on the Paleozoic interval. For the Cenozoic and Mesozoic interval, the velocity relations were adopted from the regional velocity model VELMOD 3.2 because of the regional availability of relatively reliable velocity data and relatively reliable gridded surfaces (see also paragraph 3.2.4 and chapter 6) (Paap et al., 2014).

The Paleozoic part of the velocity model was based on the sparse data that is available being: the local sonic data from CAL-GT-01, the gridded surfaces which follow from the seismic interpretation performed during this project and insights from the sparse Paleozoic data points available from the region (Figures 3.3.8 and 3.3.9). To capture the main lithological units, the Paleozoic interval was subdivided into four main lithostratigraphic units:

- Namurian

- Dinantian
- Pont d'Arcole
- Bosschveld Fm. and Condroz Group

Namurian

Sonic data for the Namurian is only available for the lowest part of well CAL-GT-01-S1 (1564MD- 1637MD (i.e.1428 mTVD-1488 mTVD). The lowermost part of the Namurian displays acoustic velocities that are generally well above 4500 m/s (see yellow part of graph in Figure 3.3.8A), which would be on the high side of what can be expected for shales at this depth (see stars in Fig. 3.3.8A, representing average Namurian velocities from nearby wells) . Additionally, lithological cutting descriptions reported in the litholog mention a mixture of shales and carbonates for this interval. Therefore the interval between 1583 MD and 1637 MD has been interpreted as a transition zone between the Namurian shales and the Dinantian Carbonates (i.e. 1444 mTVD- 1488 mTVD) (See also Figure 3.3.1). It is therefore inferred that this particular interval is not representative for the rest of the Namurian interval. The very top part of the sonic log (1564 MD- 1583 MD (i.e. 1428 mTVD -1444 mTVD) is characterised by significantly lower acoustic velocities in the Namurian which are on average around 3600 m/s (see grey part of graph in Figure 3.3.8A). These values are somewhat lower than Namurian velocities observed at nearby wells. Considering the scarce amount of available velocity data, it is considered likely that these relatively low velocities better reflect the genuine acoustic character of the Namurian interval at the Californië sites. To stick to the regional velocity trends observed the k-value for the Namurian (i.e. 0.26) was obtained from the regional VELMOD 3.2 velocity model (Paap et al., 2024). The V_0 value was chosen to fit the regional k value of VELMOD 3.2 and the average velocity of the (assumed) genuine Namurian interval (i.e. 3624 m/s at 1436 m TVD) (1564MD-1583MD (i.e.: 1428TVD-1444TVD)) (Figure 3.3.8 and Table 3.3.1).

Dinantian

The Dinantian carbonate interval at well CAL-GT-01-S1 contains a sonic log over the entire interval. This sonic data within this interval do not show a clear correlation between velocity and depth (Figure 3.3.8B). For carbonate rocks in general, such a correlation is expected, but this correlation is generally more complex than for siliciclastic rocks as diagenetic processes of dissolution, cementation and recrystallization have a significant influence on the hardness of the carbonate and may alter the rock's fabric before compaction begins to have a significant influence (Anselmetti & Eberli, 1999; Wilson, 1997; Jeppson and Kitajima, 2021). The high variations in acoustic velocity within the Dinantian interval at well CAL-GT-01-S1 suggest that diagenetic processes and possibly facies trends are also the dominant controlling factors in determining the hardness and hence acoustic velocity of the Dinantian carbonates at this well. When the limited amount of regional available velocity data is taken into consideration, it is also difficult to get a good fit between velocity and depth. The dashed yellow line in Figure 3.3.8B shows a hypothetical linear fit between the average velocities of the Dinantian carbonates for the wells KSL-02, GVK-01, SWLT-01. From Figure 3.3.8B can be derived that this fit is poor for these three wells (again indicating that diagenetic (and possibly facies trends) are dominant over the (maximum burial) depth and would also overestimate the velocity observations for well CAL-GT-01-S1. Hence, because a regional fit could not be obtained for the Dinantian velocities and because diagenetic processes (and possibly facies trends) are the dominant controlling factors, it was chosen to assign the average velocity of the Dinantian interval at well CAL-GT-01-S1 to the velocity model (indicated by the red dashed line in Figure 3.3.8B and Table 3.3.1).

Pont d'Arcole and Bosscheveld + Condroz interval

Sonic data is available for the entire Pont d'Arcole interval, the entire Bosscheveld interval and part of the underlying Condroz Group up to 2708 MD (i.e. 2488 m TVD). Despite its limited thickness, the Pont d'Arcole was incorporated as a distinct layer in the velocity model because it is characterised by significantly lower acoustic velocity than the overlying Dinantian and underlying Bosscheveld and Condroz intervals. The V0 and k values for the Pont d'Arcole interval were obtained by fitting the average acoustic velocities of the Pont d'Arcole at well CAL-GT-01 and the average acoustic velocities of the Pont d'Arcole at well GVK-01 (Figure 3.3.9A). This gives a k value of approximately 0.24 and a V_0 value of 3409 m/s (Figure 3.3.9A and Table 3.3.1). The Bosscheveld and Condroz intervals were modelled as one velocity interval. The V_0 and k values for the combined Bosscheveld and Condroz intervals were obtained by fitting the acoustic velocity trend from the combined intervals at well CAL-GT-01 with the average acoustic velocity from well KSL-02 (Figure 3.3.9B). This gives a k value of 0.2 and a V_0 value of 4750 m/s (Figure 3.3.9B and Table 3.3.1).

All the velocity relations used for the velocity model are described in table 3.3.1. It is noted that for the Cenozoic and Mesozoic intervals, relations are obtained from VELMOD 3.2 (Paap et al., 2024, see also paragraph 3.2.4). It is also noted that the velocities from the Upper and Lower Carboniferous are on average approximately 800-900 m/s less than in the Campine Basin (e.g. average Vint of 5900 m/s for the Dinantian in the Campine Basin) (Rombaut et al., (*in prep*)). Fast uplift and subsequent erosion of upper Carboniferous sediments during Stephanian-early Permian times might explain the relative undercompaction of sediments and the relatively low velocities in this area compared to the main part of the Campine Basin.

Table 3.3.1. Summarizing table of the surfaces, relations, as well as parameters used for the Safe Geo Velocity Model. The Source of the surfaces and values is indicated in between brackets. Note that for the Upper North Sea Group, the Middle and Lower North Sea Groups and for the Mesozoic interval, V0 maps are used, which are directly derived from the regional velocity model VELMOD 3.2 (Paap et al., 2024; see also paragraph 3.2.4)

Interval	**Base Surface used (*source*)**	**Relation used**	**k value (*source*)**	**V0 value in m/s (*source*)**
Upper North Sea Group	Base NU (*DGM-deep V5*)	V=V0+k*z	-0.44 (*VELMOD 3.2*)	NU_f_V0_sk_sk (*VELMOD 3.2*)
Middle and Lower North Sea Groups	Top chalk (*Safe Geo*)	V=V0+k*z	-0.21 (*VELMOD 3.2*)	NLNM_f_V0_sk_sk (*VELMOD 3.2*)
Mesozoic	BPU including Dinantian high (*Safe Geo*)	V=V0+k*z	-0.4 (*VELMOD 3.2*)	RB_f_V0_sk_sk (*VELMOD 3.2*)
Namurian	Top Dinantian (*Safe Geo*)	V=V0+k*z	-0.26 (*VELMOD 3.2*)	3226 (SafeGeo)
Dinantian	Base Dinantian (*70 m above Top Bosscheveld from Safe Geo*)	V=V0=Vint	NA	5050 (SafeGeo)
Pont d'Arcole	Top Bosscheveld (*Safe Geo*)	V=V0+k*z	-0.24 (SafeGeo)	3409 (SafeGeo)
Bosscheveld Fm. and Condroz Group	Base Devonian (*constant at Z=5000 m*)	V=V0+k*z	-0.2 (SafeGeo)	4750 (SafeGeo)

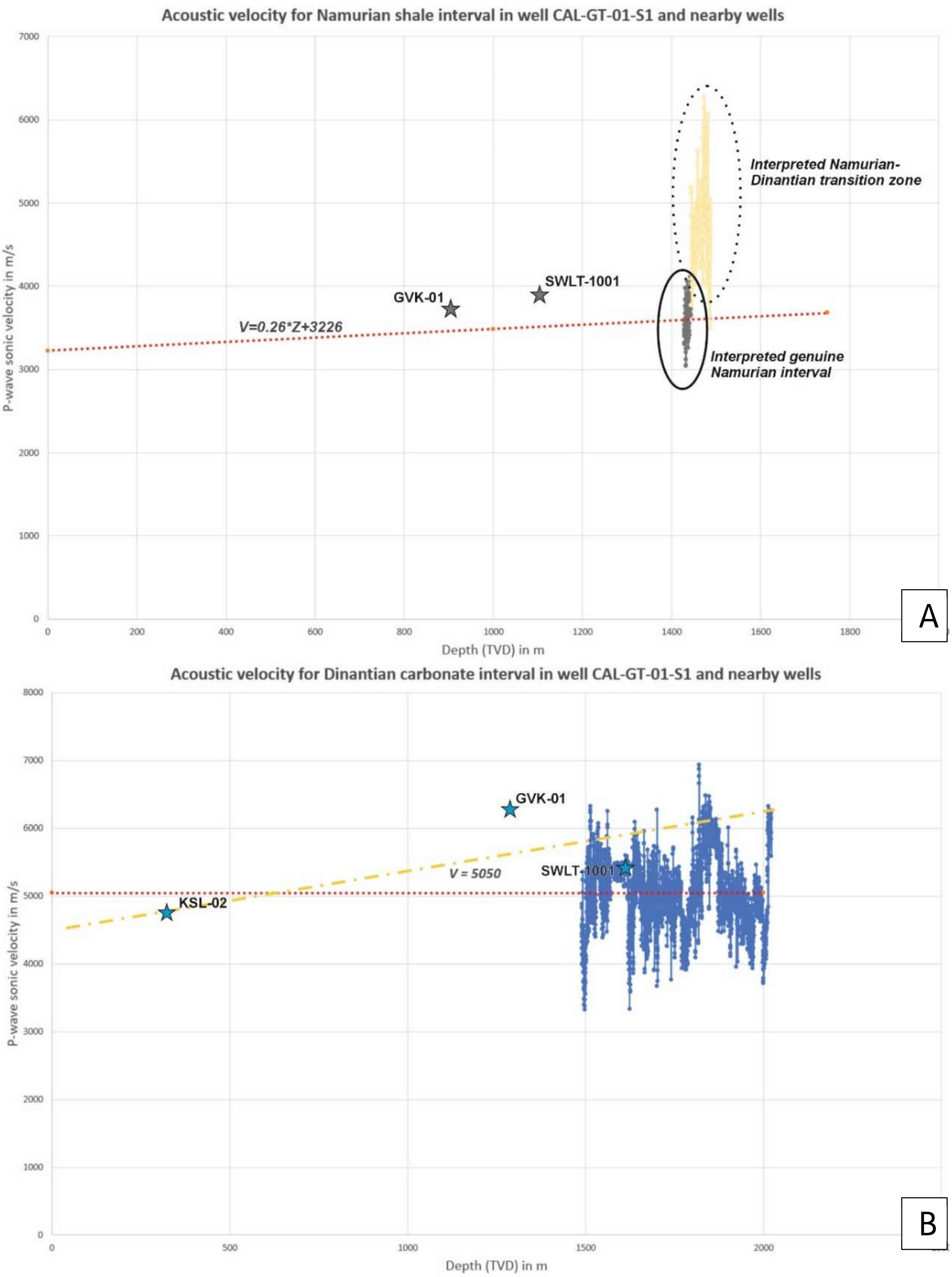

Figure 3.3.8. Acoustic velocity (i.e. P-wave sonic velocities) - depth plots for the Namurian shale interval (A) and the Dinantian carbonate interval (B) for well CAL-GT-01-S1. The stars indicate average P-wave sonic velocities from nearby wells plotted against the mid-depth for the specific interval. The red dashed lines indicate the trend lines that were used for the velocity model. Abbreviations used: GVK (Geverik), GVK KSL (Kastanjelaan), SWLT (Schwalmtal).

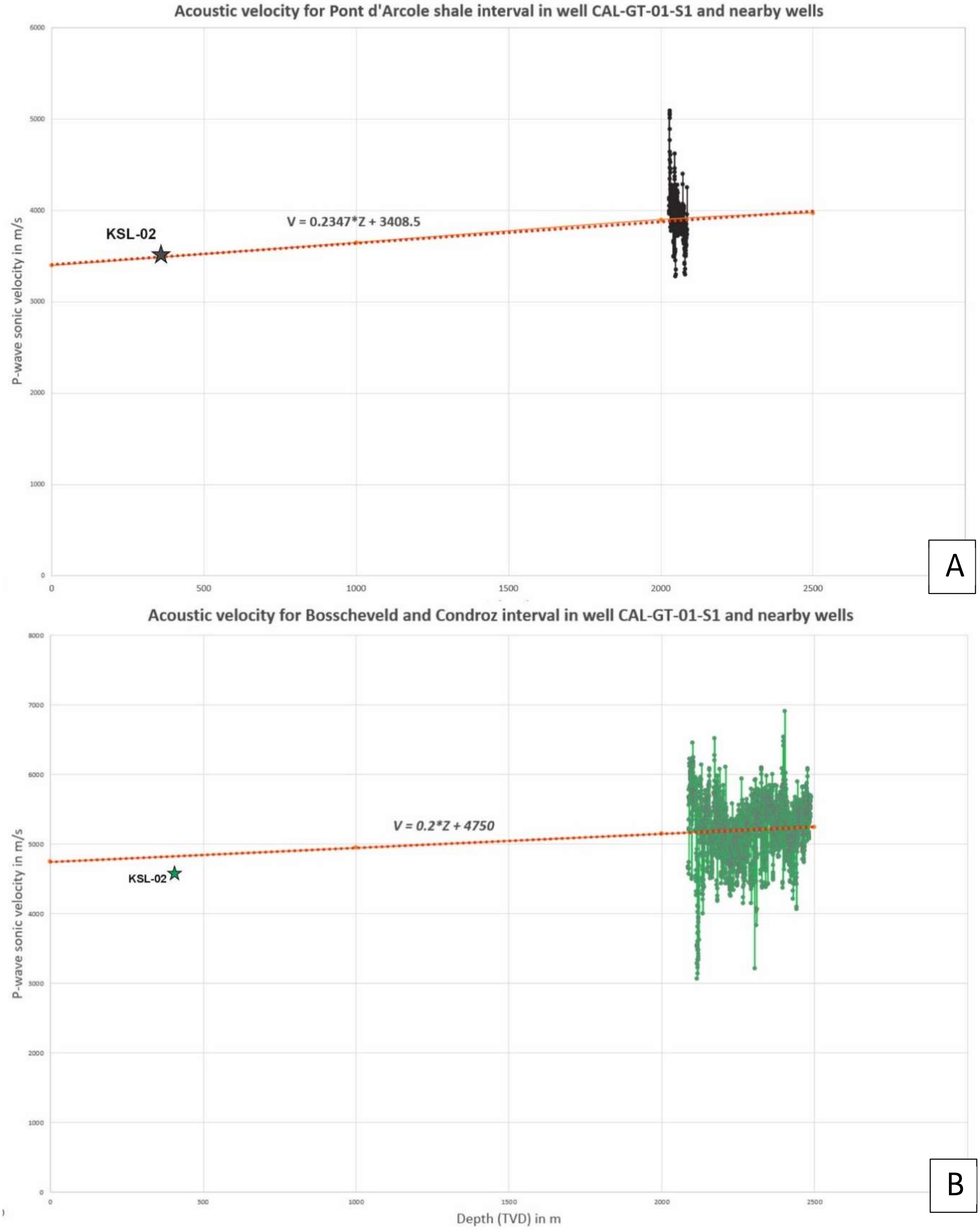

Figure 3.3.9. Acoustic velocity (i.e. P--wave sonic velocities) - depth plots for the Pont d'Arcole interval (A) and the Bosscheveld and Condroz interval (B) for well CAL-GT-01-S1. The star indicates average P-wave sonic velocities from the nearby well Kastenjelaan-02 (KSL-02). The red dashed lines indicate the trend lines that were used for the velocity model.

3.3.4 Geological model

The geological model fits the observations and interpretations described in the paragraphs 3.3.1 and 3.3.2. Figure 3.3.10 describes a schematic representation of the modelled geometry. The thickness differences in the Dinantian between the different wells are explained via a combination of:

- Wells that are cross-cutting faults: wells CAL-GT-03, CAL-GT-05 and CAL-GT-02 only encounter the lower part of the Dinantian in their trajectories. This faulting is interpreted as the main reason for the thickness differences (Figures 3.3.2, 3.3.4, 3.3.5 and 3.3.10).
- Some degree of stratigraphic thinning towards the northeast, including some syn-depositional fault activity along the Carboniferous normal fault (Figures 3.3.4 - 3.3.6 and 3.3.10).
- Some erosion and karstification of the Dinantian interval on the PH, caused by Early Permian uplift and exposure during a large part of the Mesozoic (Figures 3.3.4 - 3.3.6 and 3.3.10).
- The well deviation with respect to the general orientation and dip of the geological layering (Figures 3.3.4 - 3.3.6 and 3.3.10).

Figures 3.3.11 and 3.3.12 display two oblique views of the final geological hybrid model, illustrating the outcome of the geological voxel model. The model consists of 1.082.620 cells. On average, these cells have the following dimension (XYZ): 60 m x 51 m x 105 m. The dimensions in the horizontal X and Y direction follow approximately the average dimensions. For the Vertical (Z) direction, the vertical resolution depends on the geometry of the model and the amount of layers assigned to a specific interval (see point 5 in paragraph 3.2). It is noted that the Dinantian, Bosscheveld and to some extent the Evieux formations were modelled with a higher vertical resolution than the Namurian, because most of the flow occurs within these intervals. The amount of layers per zone and the subsequent vertical resolution is as follows:

- Namurian: 3 layers, average vertical resolution of 175 m
- Dinantian: 4 layers, average vertical resolution of 56 m
- Pont d’Arcole: 1 layer, average vertical resolution 41 m
- Bosscheveld Fm.: 2 layers, average vertical resolution of 51 m
- Evieux Fm.: 10 layers, average vertical resolution of 122 m

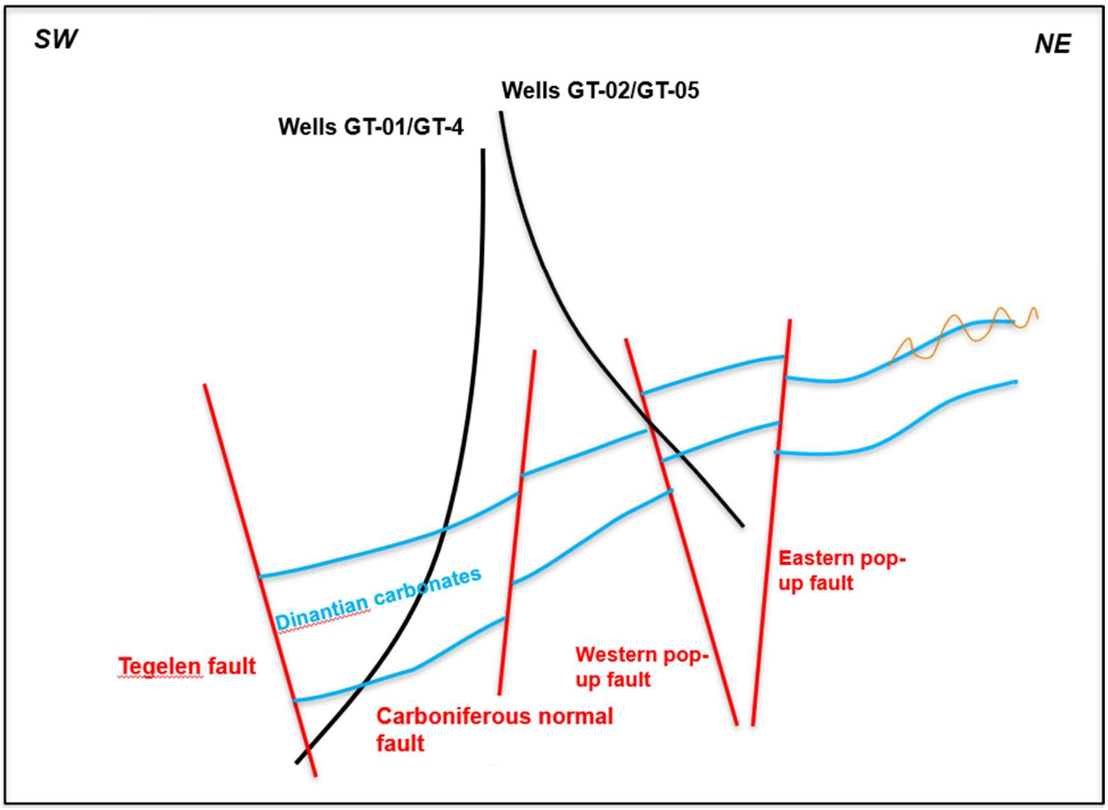

Figure 3.3.10: SW-NE cross section schematically illustrating the interpreted geology around the Californië doublets. The Blue lines indicate the approximate outline of the Dinantian carbonates. The sinusoidal orange lines indicates partial erosion and karstification on the Palaeozoic High. Cross-section not to scale.

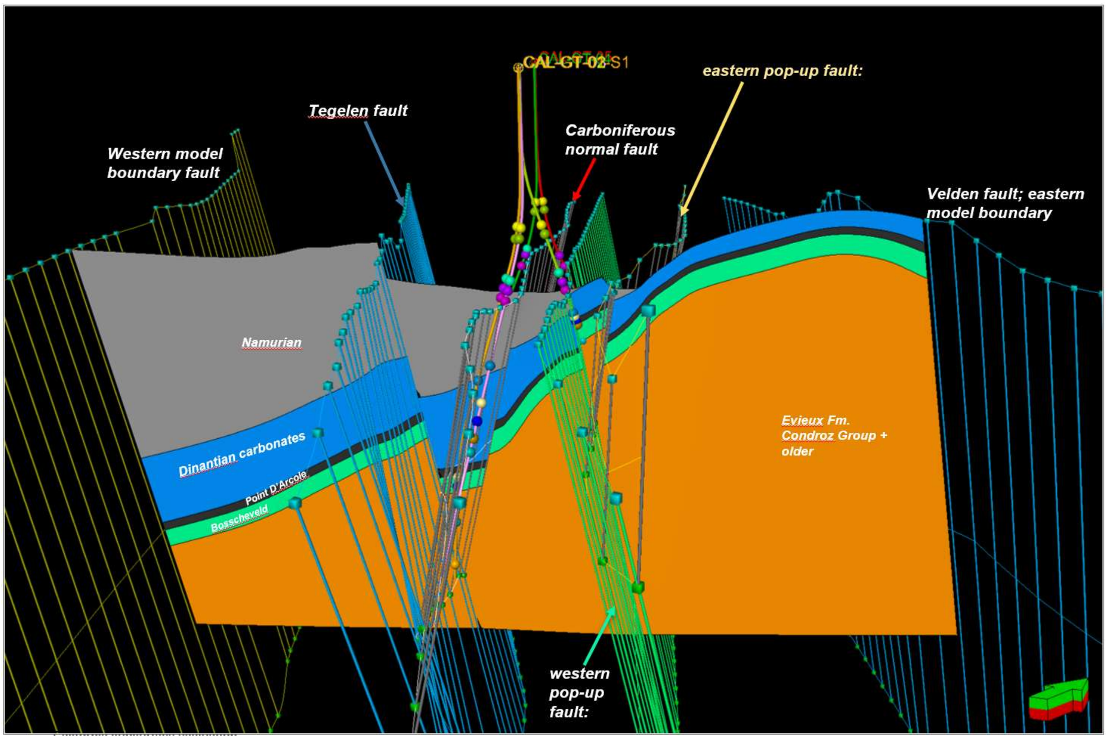

Figure 3.3.11: Oblique 3D view towards the northwest illustrating the geometry of the created geological voxel model.

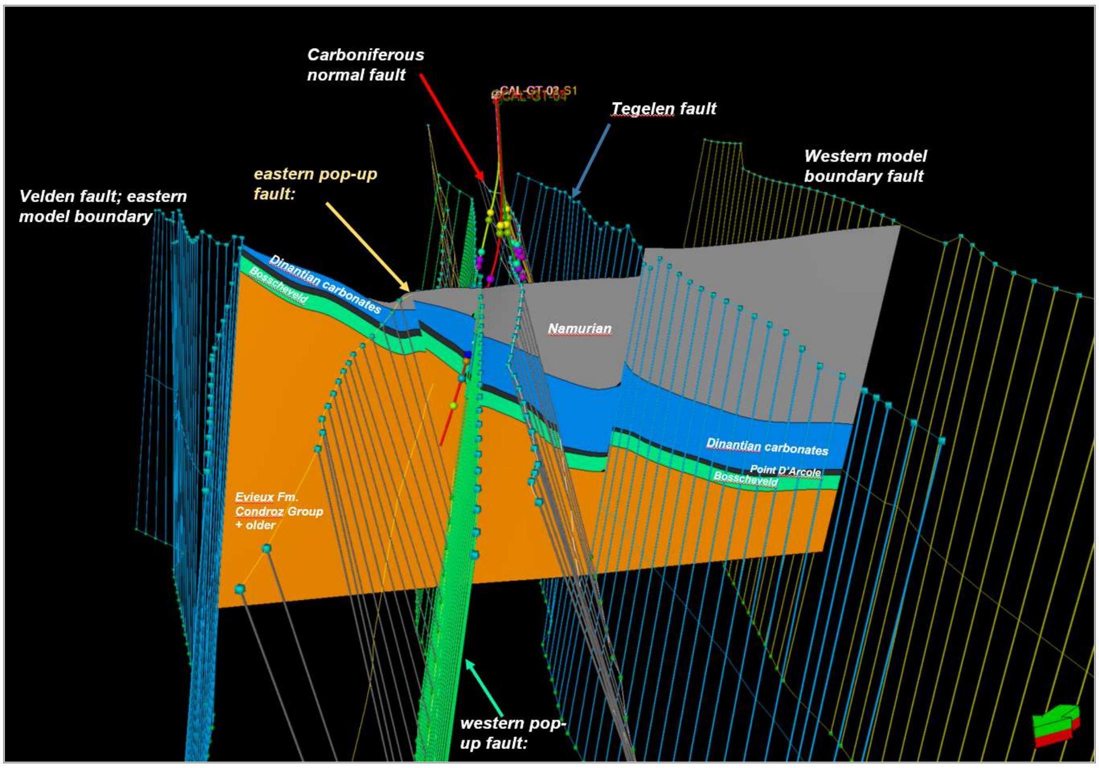

Figure 3.3.12: Oblique 3D view towards the southeast illustrating the geometry of the created geological voxel model.

3.4 Discussion

The seismic interpretations and stratigraphic correlations described in chapter 3.3 represent the interpretations forming the base for final hybrid geological model that was created (paragraph 3.3.4). However, because of the complex geology and the lack off (good quality) data (see also paragraph 3.2.2), it is emphasized that there are major uncertainties present in this interpretation. Paragraph 3.4.1 describes two alternative interpretations proposed during this project, which although deemed less likely than the hybrid model presented in chapter 3.3, can’t be ruled out unless new (good quality) data is acquired (see also paragraph 3.4.2). Additionally, this paragraph discusses some of the outcomes of previous models created for the Californië geothermal sites. Paragraph 3.4.2 describes the main reasons why there is a significant degree of uncertainty regarding the interpretation of the seismic data.

3.4.1 Alternative interpretations

The final hybrid interpretation that was modelled can be seen as an intermediate solution between two end-member interpretations. One endmember would be a scenario where the Dinantian carbonates are characterised by approximately the same thickness throughout the region. The observed differences in Dinantian thickness are then (almost solely) attributed to faulting (Figure 3.4.1). A relatively uniform upper Dinantian or Visean thickness (excluding the youngest Dinantian or Brigantian, but this part is likely already missing in CAL-GT-01 based on the absence of the overlying Geverik Member (Harings, 2014)) has been observed in areas further south, where studies performed on a combination of well (sedimentology and biostratigraphy) and seismic data from the Belgium Campine block or from outcrops further south show relatively uniform thicknesses for these carbonates across the Campine Basin (Hance, 2022; PanTerra, 2023; Rombaut et al., (*in prep*)). In the CAL-GT-02, CAL-GT-03 and CAL-GT-05 wells it is within this normally uniform part that several hundreds of meter is missing.

Figures 3.4.2, 3.4.3 and 3.4.4 show this interpretation where the pink squares indicate an interpretation of the Top Evieux Fm, which in the wells is stratigraphically located around 100-150 m below the top Bosscheveld (which is interpreted for the final hybrid model; see also Figure 3.3.1). A main observation opposing this interpretation is the lack of clear reflections at the Paleozoic High (PH) at deeper intervals, which would be expected to occur at the base of the Dinantian and at the top and the base of the Pont d’Arcole (Figure 3.2.2). Another point of discussion for this interpretation is that the amount of displacement on the pop-up faults would have to be higher than currently interpreted for the final hybrid model (in the order of 400-500 m). This higher displacement on the pop-up faults would push the top of the Dinantian upwards, thereby roughly coinciding with a reflector that has been interpreted as the base of the Nederweert Sandstone Mb. in the final hybrid model (Figure 4.3.7, see also Figures 4.3.4 - 4.3.6). Consequently, the Zechstein subgroup would not be present above and northeast of the pop-up. Additionally, the Mesozoic onlaps that are observed onto the PH indicate that the Dinantian interval was exposed during a large part of the Mesozoic, making it likely, despite the hardness of the Dinantian interval, that at least part of it would have been eroded over such a long period. The exact amount of erosion though is open for debate.

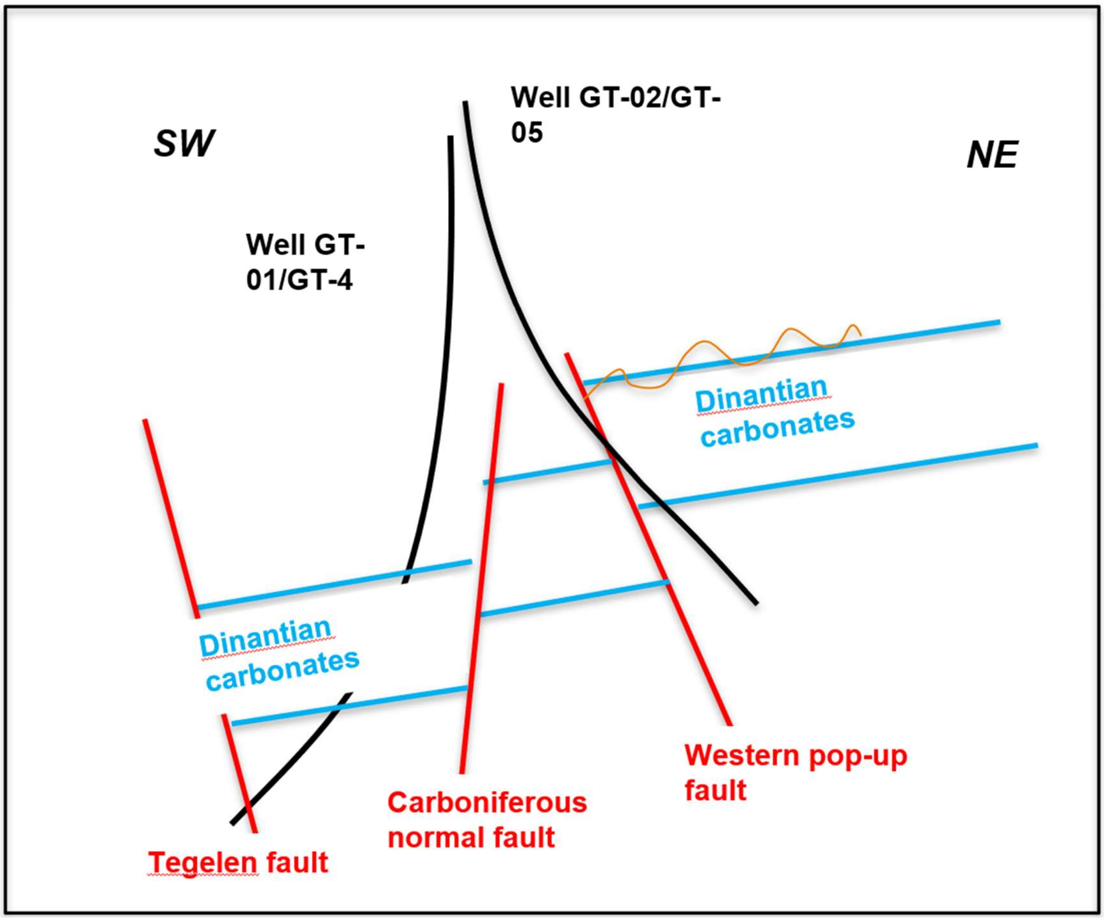

Figure 3.4.1: SW-NE oriented cross section, schematically illustrating an alternative scenario for the interpreted geology based on a (by approximation) equal thickness of the Dinantian carbonates and only (minor) erosion at the PH.

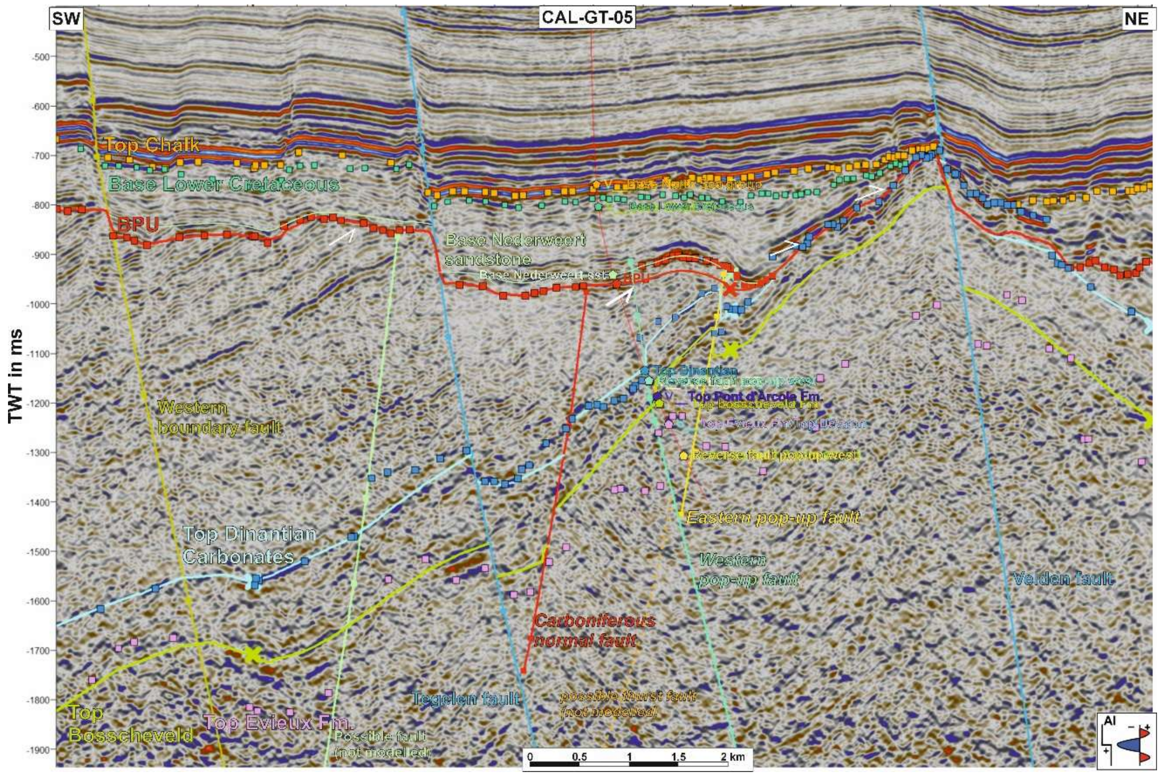

Figure 3.4.2: SW-NE oriented seismic line: Scan line 029. The thick horizon lines indicate the position of the final hybrid interpretation as described in paragraph 3.3.2. The squares in the corresponding colours indicate the position of the alternative interpretation which assumes a more ore less constant thickness of the Dinantian interval. Note that the top of the BPU (in red squares) is being moved upwards with respect to the final hybrid interpretation. This is at the cost of the Zechstein interval, which in this scenario would not be present above the Pop-up structure and part of the PH. See Figures 3.2.1 or 3.3.3 for the location of the seismic line and see Figure 3.3.4 for the uninterpreted seismic line. ***See Appendix C for a high resolution version of this figure.***

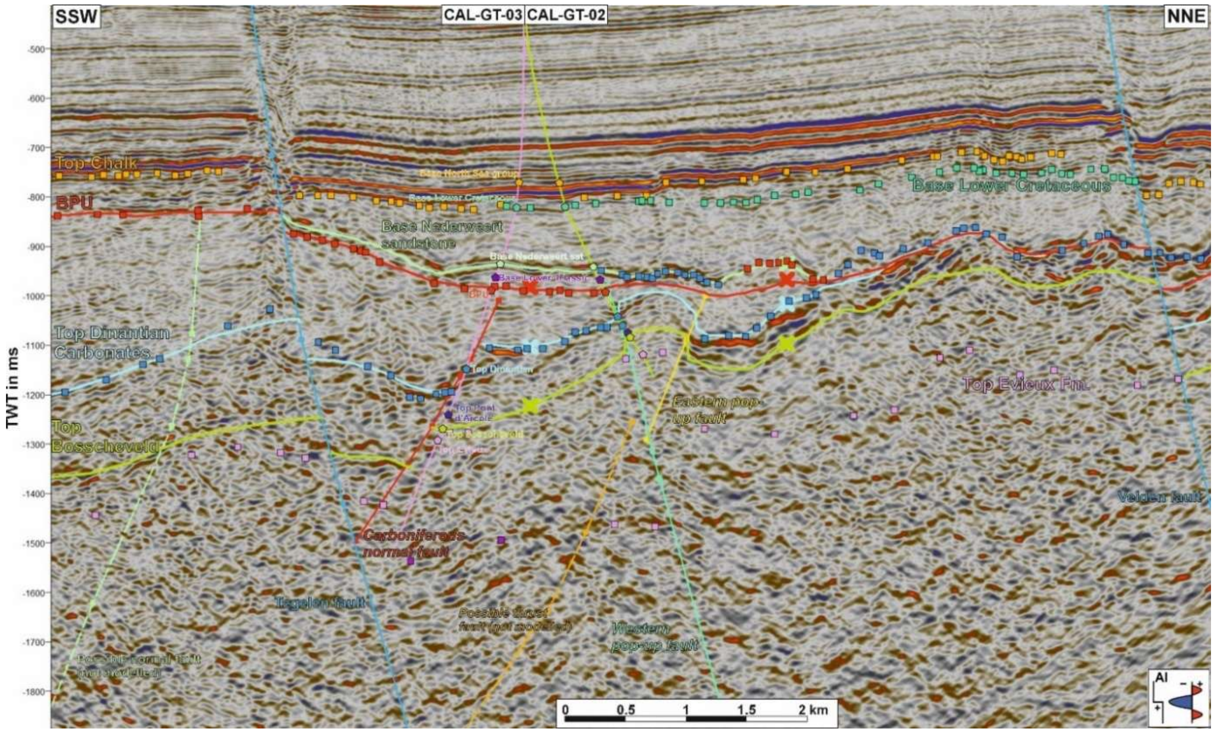

Figure 3.4.3: SWW-NNE oriented seismic line: Scan line 31. The thick horizon lines indicate the position of the final hybrid interpretation as described in paragraph 3.3.2. The squares in the corresponding colours indicate the position of the alternative interpretation which assumes a more or less constant thickness of the Dinantian interval. Note that the top of the Dinantian carbonates (in blue squares) and consequently the BPU (in red squares) are being moved upwards with respect to the hybrid interpretation. This is at the cost of the Zechstein interval, which in this scenario would not be present above the Pop-up structure and part of the PH. See Figures 3.2.1 or 3.3.3 for the location of the seismic line and see Figure 3.3.5 for the uninterpreted seismic line. ***See Appendix C for a high resolution version of this figure.***

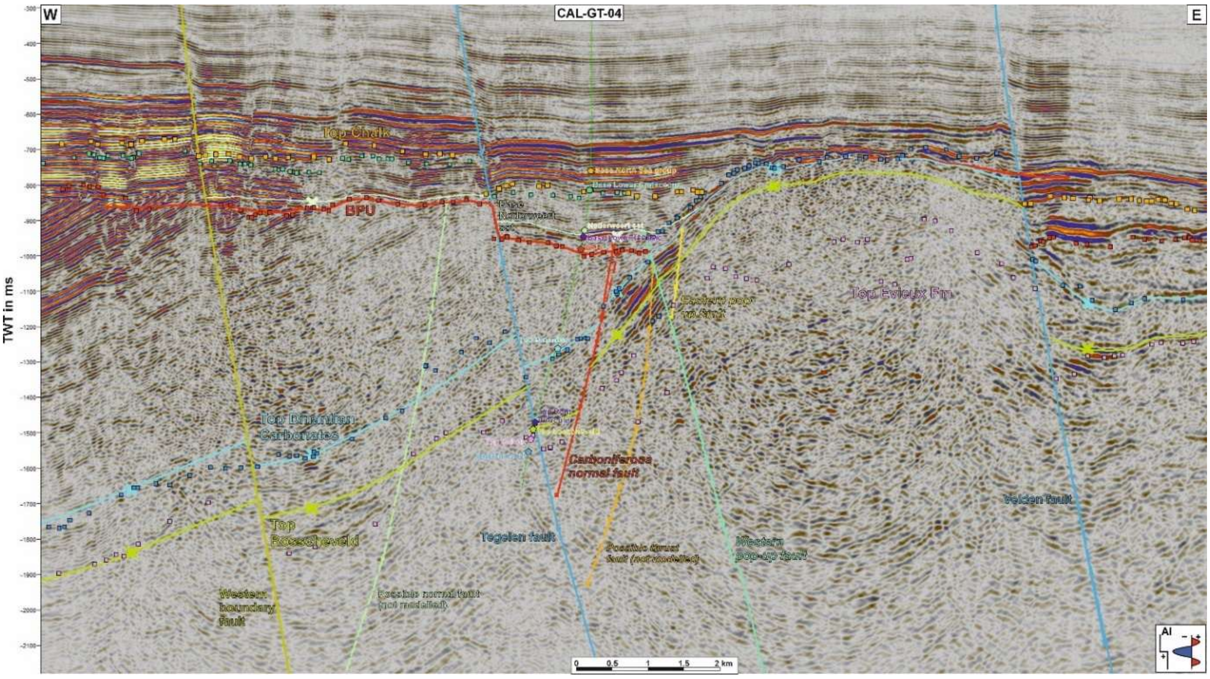

Figure 3.4.4. E-W oriented 09-02 vintage seismic line. The thick horizon lines indicate the position of the final hybrid interpretation as described in paragraph 3.3.2. The squares in the corresponding colours indicate the position of the alternative interpretation which assumes a more or less constant thickness of the Dinantian interval. See Figures 3.2.1 or 3.3.3 for the location of the seismic line and see Figure 3.3.6 for the uninterpreted seismic line. ***See Appendix C for a high resolution version of this figure.***

The other endmember would be a scenario which is characterised by a rapid stratigraphic thickening towards the southwest, combined with a significant component of syn-depositional fault activity at the Carboniferous normal fault, and a significant amount of erosion and karstification on the Paleozoic High (PH). In this endmember, the presence of the western pop-up fault would not be necessary to explain the thickness differences of the Dinantian between the different wells. It is also noted here that no losses have been observed in the wells CAL-GT-02 and CAL-GT-05 at the location where the western pop-up fault has been interpreted on seismic data (See also Figure 3.3.2 and chapter 5). The eastern pop-up fault could be part of a series of southwestward dipping thrust faults that likely also underly the Paleo High towards the northeast, similar to thrusts observed more towards the northwest of the Peel-Maasbommel Complex (Bouroullec et al., 2019).

Important precondition for this interpretation is that it assumes relatively higher Namurian velocities than derived from the sonic data (see paragraph 3.3.3 and Fig 3.3.8A). The wells plotted in the Figures 3.4.6 and 3.4.7 are based on an average Namurian velocity of 4200 m/s, which is similar to what was used by Reith (2018), when modelling the area. As described in paragraph 3.3.3 the sonic data from well CAL-GT-01 indicates that the genuine Namurian interval is characterised by a velocity of approximately 3600 m/s at a depth of approximately 1500 m. When compared to regional velocities from the area, this is relatively low (Fig. 3.3.8A). Regarding this, it is also important to emphasize that based on the sonic data from well CAL-GT-01, a relatively low velocity for the Namurian interval seems justified (also being in line with the relatively low Dinantian velocities observed when compared to the Campine Basin (see also paragraph 3.3.3)), but that there is just one sonic log for all the wells available, which only covers a limited part of the entire Namurian interval (See Paragraph 3.3.3). Because limited velocity data is available for the Namurian interval, uncertainties regarding the exact Namurian velocities will remain until new data would be acquired (see also paragraph 3.4.2).

There is a possibility that the current final hybrid interpretation underestimates the Namurian velocities. In case the interval velocities for the Namurian are indeed higher, this would also have implications for the interception of well CAL-GT-03 with the Carboniferous normal fault (Figure 3.4.3). In the case of higher Namurian velocities (of approximately 4200 m/s on average), the well would encounter the fault in the lower part of the Dinantian, thereby faulting out part of the lower part of the Dinantian, as well as the Pont d'Arcole. When looked at the GR, the Pont d'Arcole seems to have an anomalous gamma ray character at well CAL-GT-03, which could be the result of encountering a damage zone, potentially being characterised by a mixture of clay and carbonate clasts (Figure 3.4.8).

A component of stratigraphic thickening towards the southwest is deemed likely and therefore incorporated in the final hybrid model. Previous authors also recognised a thickening of the Dinantian in a southwestward direction (Reith, 2018; Mozafari et al., 2019). However, to solely explain the thickness differences between the wells CAL-GT-02 and CAL-GT-05 on one side and the wells CAL-GT-04 and CAL-GT-01 on the other side, is deemed unlikely because it implies a vertical stratigraphic thickness change of approximately 400 m over a lateral distance of approximately 2 km (Figures 3.3.1 and 3.3.3). Even for a rapid facies change (e.g. from platform to distal), this would be extreme and this is observed nowhere else in the region, where the Dinantian carbonates are usually characterised by a relatively uniform thickness (Hance, 2022; PanTerra, 2023; Rombaut et al., (*in prep*)).

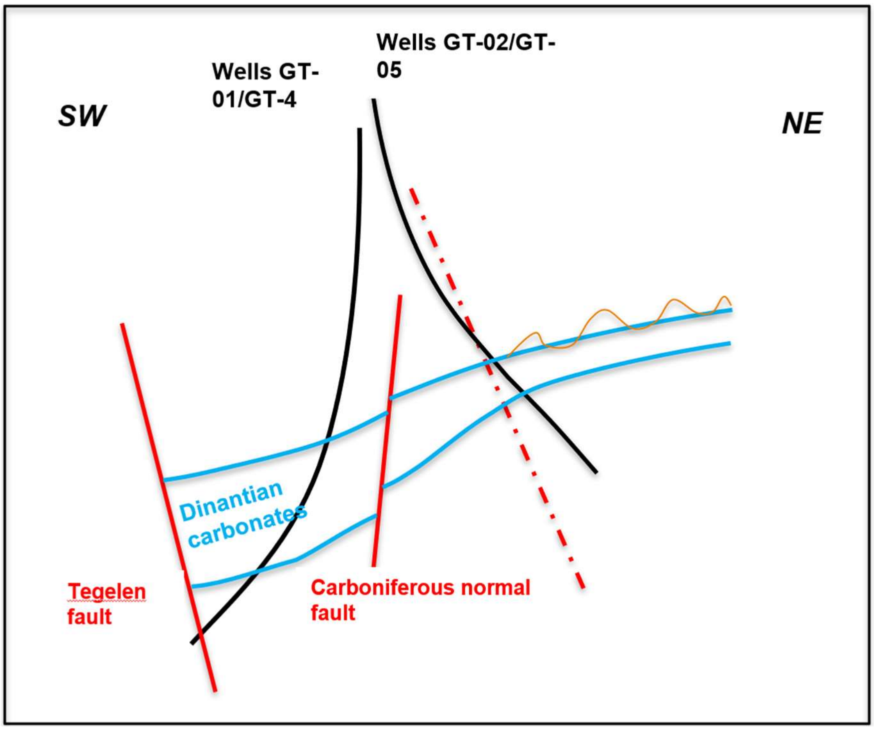

Figure 3.4.5: SW-NE oriented cross section, schematically illustrating an alternative scenario for the interpreted geology based on rapid stratigraphic thinning towards the southwest, syn-depositional activity related to the Carboniferous normal fault and significant erosion and karstification at the PH during the Mesozoic. The western pop-up fault (indicated by the dashed red line) would not be present in this end-member scenario.

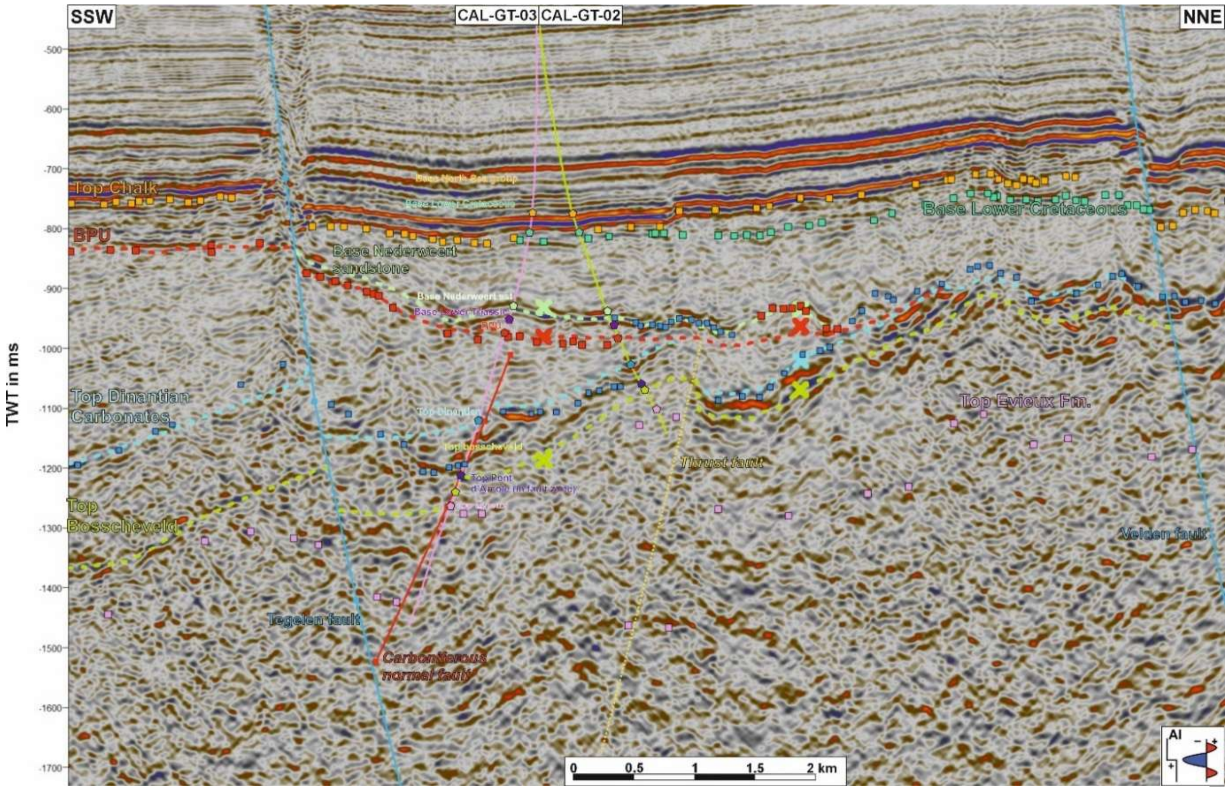

Figure 3.4.6: SSW-NNE oriented seismic line: Scan line 31. The dashed horizon lines indicate the position of alternative interpretation 2 where the thickness differences within the Dinantian are primarily explained by stratigraphic thinning, karstification on the PH and syn-depositional activity along the Carboniferous normal fault. The squares in the corresponding colours indicate the position of the alternative interpretation 1, which is based on an approximately equal thickness distribution of the Dinantian carbonates. See Figures 3.2.1 or 3.3.3 for the location of the seismic line and see Figure 3.3.5 for the uninterpreted seismic line. ***See Appendix D for a high resolution version of this figure.***

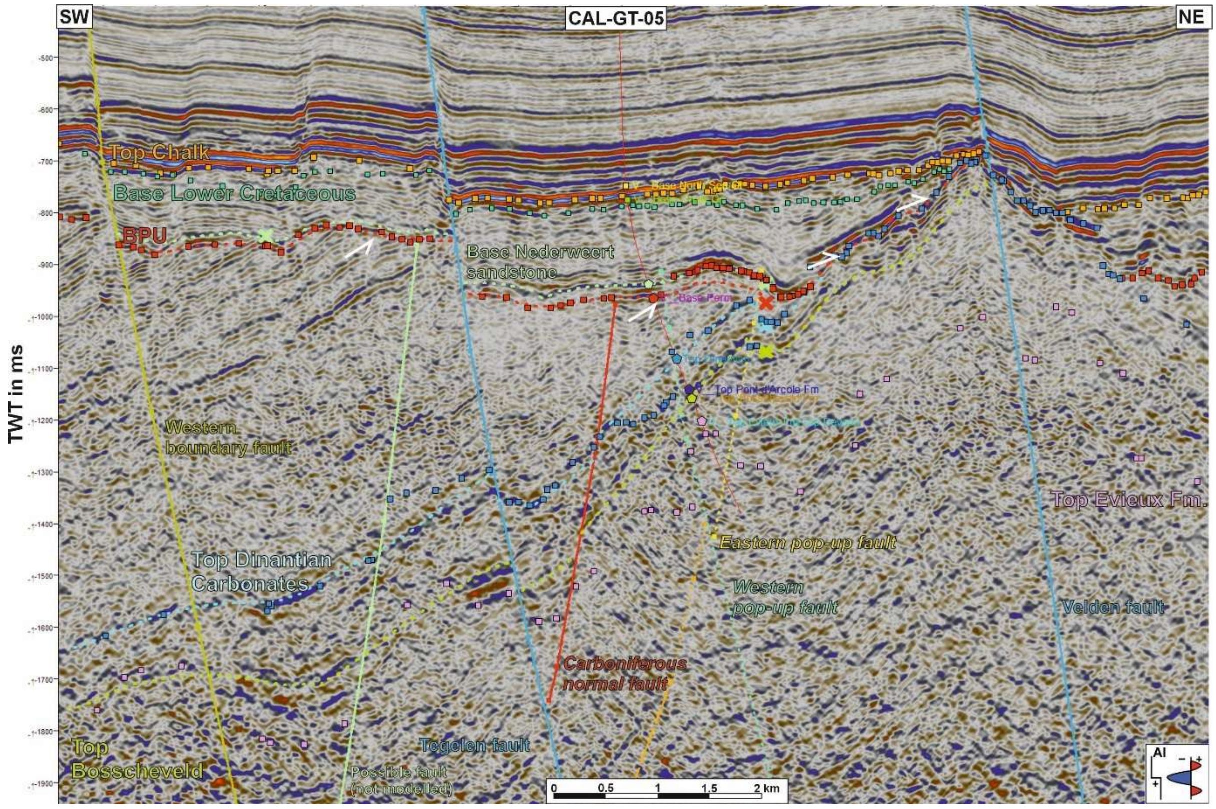

Figure 3.4.7: SSW-NNE oriented seismic line: Scan line 29. The dashed horizon lines indicate the position of alternative interpretation 2 where the thickness differences within the Dinantian are primarily explained by stratigraphic thinning, karstification on the PH and syn-depositional activity along the Carboniferous normal fault. The squares in the corresponding colours indicate the position of the alternative interpretation 1, which is based on an approximately equal thickness distribution of the Dinantian carbonates. See Figures 3.2.1 or 3.3.3 for the location of the seismic line and see Figure 3.3.4 for the uninterpreted seismic line. ***See Appendix D for a high resolution version of this figure.***

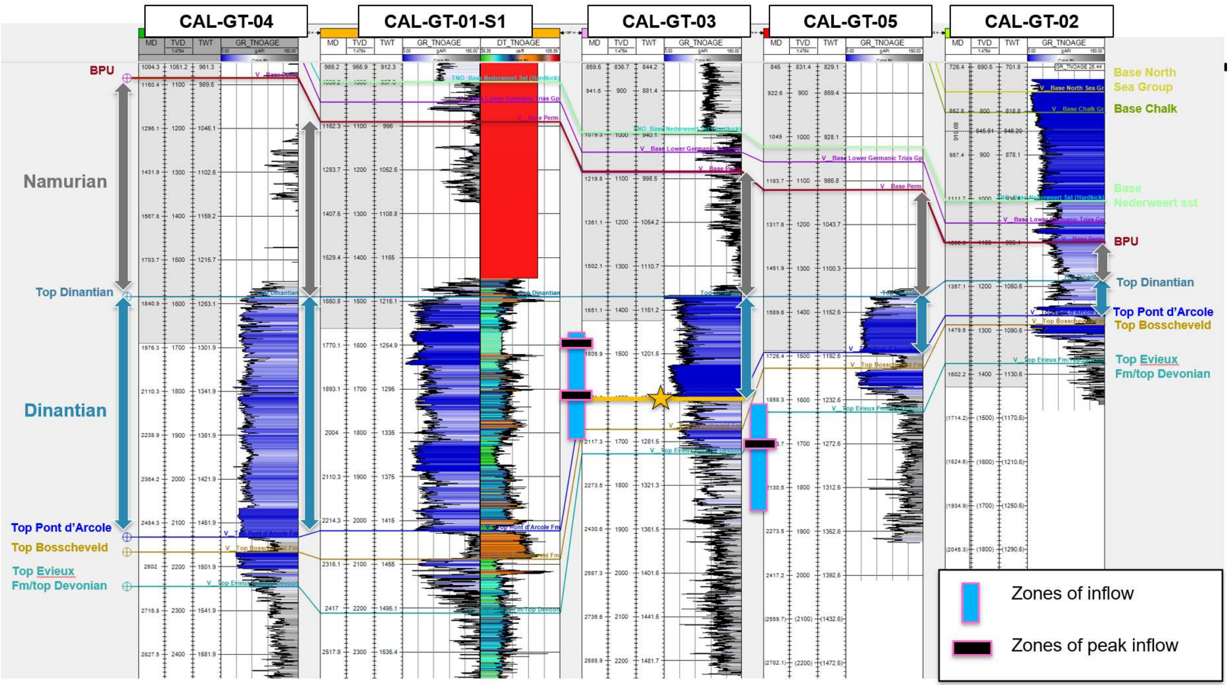

Figure 3.4.8: Well log correlation panel displaying an alternative interpretation for the interception between well CAL-GT-03 and the Carboniferous normal fault (here indicated by the horizontal orange line and highlighted with the orange star). Note also the anomalous character of the Pont d'Arcole in well CAL-GT-03 with respect to the other wells. Abbreviations used: MD: Measured depth (in m); TVD: True vertical depth (in m); TWT: Two-Way-Travel Time (in ms); GR: Gamma-Ray log (in gAPI); DT: sonic (i.e. compressional P-Wave) log (in µs/ft).

3.4.2 Data uncertainty

There are four main reasons why there is a significant degree of uncertainty regarding the interpretation of the seismic data:

1. The quality of the seismic data in general is relatively poor. The imaging is especially poor in the deeper Paleozoic domains, making it challenging to distinguish the genuine geological signal from seismic artefacts, such as noise and multiples.
2. There are no checkshot data, or VSP (i.e. Vertical Seismic Profile) data available that allows for a high certainty time-to depth conversion on the location of the Californië sites. This means that there are uncertainties regarding the seismic velocities of the geological intervals and hence uncertainties regarding the seismic interpretation, which is performed in ms TWT. During this project, velocity estimates were based on sonic data from well CAL-GT-01 for the Paleozoic interval, but this sonic only covers part of the Namurian interval (see also paragraph 3.3.3). As illustrated in paragraph 3.4.1, a velocity change of 15-20% for the Namurian interval leads to different interpretations in the way the well trajectory encounters the fault.
3. The seismic data is in 2D only and the orientation of the seismic lines usually does not align with the well trajectories. Especially in combination with the high angle geological layering and the presence of faults, this adds uncertainty in the projection of well data onto the seismic lines.
4. The local Paleozoic geology is complex, as the intervals are characterised by relatively steeply inclined strata and rapid thickness changes. Moreover, the Paleozoic

interval is heavily faulted due to a complex geological history of several deformation phases, which have repeatedly reactivated pre-existing faults (Paragraph 3.1). It is also noted that only relatively major faults with a displacement that exceeds the seismic resolution (generally > 20 m, depending on the interval velocities), can be recognised. From outcrop studies it is known that in the vicinity of major faults, several smaller scale faults are often present, which may not be visible on seismic (if the displacement does not exceed the seismic resolution) (Paragraph 3.1.4).

Further discussion on options for data acquisition to further constain the geological model can be found in Chapter 9.

4 Velocity modelling and seismic event localization

An update of the geological model has its implications on the seismic velocity structure and hence both on time-depth conversion of interpreted horizons and faults on seismic reflection data, as well as on the inference of the hypocenter locations of observed seismic events. The use of the revised P-wave velocity model for time-depth conversion of interpreted seismic reflection data was presented in Chapter 3. The current section presents results of the updated P- and S-wave velocity model and its effect on the relocation of the seismic events.

4.1 Input data

4.1.1 Velocity data

A new velocity model was achieved by populating the interpreted stratigraphy from the revised geological model (see chapter 3) with P- and S-wave velocities based on separate velocity data. The selected velocity data consisted of:

- Sonic logs from CAL-GT-01 well, and from other wells in southern Netherlands and Belgium where the same stratigraphic layers were sampled.
- VELMOD-3.2, which is the regional velocity model of the Netherlands and provides P-wave velocities at a spatial resolution of 1 km (Paap et al., 2024).
- Information on Vp/Vs ratio which relates the p-wave velocity to s-wave velocity. Here extensive knowledge from the Groningen site on Vp/Vs ratios was used (Spetzler et al., 2018) as well as Vp/Vs log data from the GT-01 well.

4.1.2 Seismicity data

Seismic monitoring of the CWG doublet was conducted by Q-con. The monitoring network was installed in September 2014 and initially consisted of three monitoring stations (stations K01, K02, and K03 as depicted in Figure 4-1). Two additional stations (K04 and K05) were deployed in November 2015. In total 17 local earthquakes were detected by the network in the magnitude range Ml = −1.2 to Ml = 1.7 from August 2015 until September 2018 during the operational period of the Californië projects (Vörös and Baisch, 2022). The seismic stations consist of a 3-C short-period surface seismometer (Lennartz LE3D) sampled at 100 Hz. The waveform data of the detected seismic events and the corresponding picked arrival times of P- and S- phases were provided by Q-con to TNO to be further analysed within the SafeGeo project.

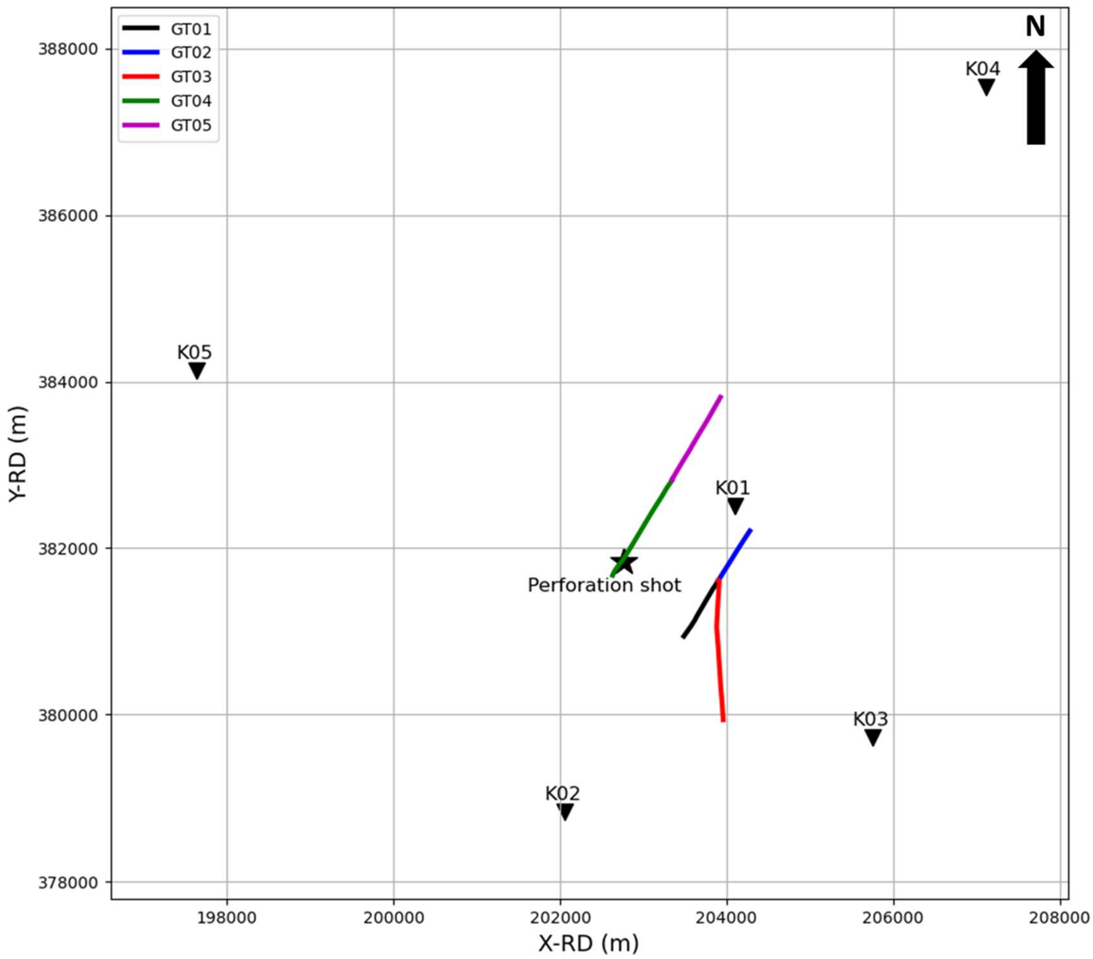

Figure 4-1. Lay-out of the monitoring network at the Californië site. The five seismic stations are labelled K01-K05. The heads and bases of the different wells are indicated with the x symbols.

4.2 Workflow for using revised velocity model to locate seismic events

Figure 4-2 shows the conceptual workflow where the input data (seismicity data, velocity and geological data) is used to compose the velocity model. In turn the velocity model is used in combination with a probabilistic inversion code to calculate earthquake hypocenters. Simultaneous to the construction of the geological model (see chapter 3) the velocity model was composed. From VELMOD (Doornenbal et al., 2020; Paap et al., 2024) we adopt the convention to use a velocity that increases linearly with depth within each stratigraphic unit:

$$V_{inst}(x, y, z; u) = V_0(x, z; u) + k(u)z \qquad \text{(eq. 4.1)}$$

Where V_{inst} is the instantaneous velocity, z the depth, V_0 is the normalized velocity at z=0 m and k is the velocity-depth gradient. The index u represents the stratigraphic unit. Table 4-1.shows the final V_0 and k values corresponding to the geological model as described in Chapter 3. No data was available from the Californië site on S-wave velocity distributions except for a small depth interval (~1450-1570 m) covered by a Vp/Vs log in the GT-01 well in 2012. Therefore, due to the lack of S-wave velocity data in this area, as a starting point we adopted Vp/Vs ratios from an earlier study of Spetzler et al. (2018) which was based on extensive knowledge from the Groningen site on (2018), as listed in Table 4-1. It should be noted, however, that there are some clear differences in the types and properties of the stratigraphic layers (especially for the deeper parts) at the Californie site compared to the Groningen site, which also affect the representativity of the assumed Vp/Vs ratios for the Californie site.

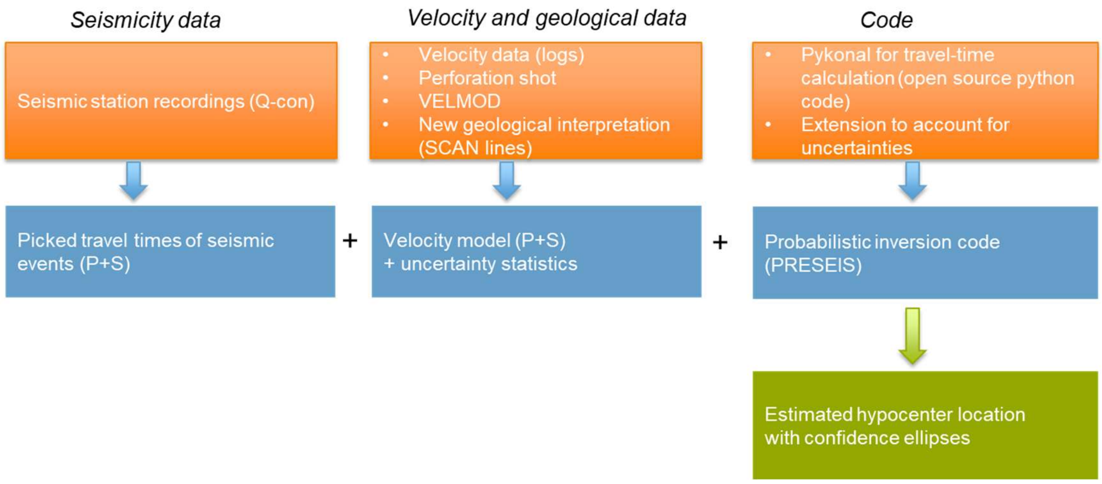

Figure 4-2. Conceptual workflow used to determine earthquake hypocenters

Earlier studies have been conducted where hypocenters specifically for the main seismic event (Spetzler et al., 2018; Spetzler et al., 2024) as well as for all seismic events (Vörös and Baisch, 2022) of the Californië site have been calculated. Spetzler (2018) compared the effect of different 1-D flat layered velocity model types, where they used a 3D ray tracer to calculate synthetic travel times for P- and S- arrivals. Spetzler et al. (2024) used a 1D velocity model in combination with full-waveform modelling to calculate synthetic travel times. In turn they conducted probabilistic inversion of travel-time residuals to calculate the hypocenter of the main event, where they used (1) only P-S travel time differences per station, (2) P-wave travel time difference per two stations and (3) a combination of both. Note that the work by Spetzler et al., (2018, 2024) only focused on the location estimation of one seismic event at the Californie site (i.e. the main event). Vörös and Baisch (2022) used well perforation shots to determine a mixed velocity term per seismic station which was used to calculate the hypocenters of all 17 seismic events. The source location approach followed by Vörös and Baisch (2022) was not based on the representation of an actual layered geological model and corresponding velocity model, which is however a more common approach.

Therefore, this chapter addressed how the refined geological model from chapter 3 and corresponding velocity model (which currently are the most detailed model representations of this site) affect the location of seismic events as determined by a probabilistic source inversion algorithm. Also, an attempt was made to better constrain the S-wave velocity model based on a perforation shot that was recorded earlier at station K01, where arrivals of both P- and S- phase could be identified. Although the location of the perforation shot is known quite accurately, there is no independent accurate information on the timing. As a result, only the time delay between the P- and S-phase can be used. While freezing the P-wave velocity model, we have perturbed the S-wave velocity model using simple multiplication factor to match the synthetic and observed delay time. The newly calculated hypocenter locations are also compared against the earlier locations reported by Vörös and Baisch (2022).

The probabilistic source inversion algorithm used here, requires a probabilistic description of the relation between the hypocenter time and location and the arrival times of both the P- and S-phase at the monitoring stations. As we assume a deterministic (single realization) wave velocity model, all model uncertainties need to be absorbed in the arrival time distribution model. As customary we assume a normal distribution of the arrival times. For the marginal standard deviations we adopt the values from Ruigrok et al. (2023) who studied travel-time residuals of induced events on a national level spanning a three year period. For induced events with 0-20 km epicentral distance they report standard deviations σ_p=0.115 s and σ_s=0.186 s (see table 2.4 of Ruigrok et al. (2023). As these values have been compiled for data from a much wider region, (e.g. many observations from Groningen), with less detailed reference model, and somewhat larger epicentral distances, they may be a bit conservative, or on the lhigh side. A dedicated local forward modelling study could be performed to reduce these. Reduced marginal standard deviations will result in tighter constraints on the hypocenter locations. However, as is also customary and for lack of data, we ignore the spatial correlations between the arrival time observations at different monitoring stations as well as the correlations between the two phases. Taking these correlations into account generally leads to lower resolution and looser constraints. Future studies may be able to improve on this.

Within SafeGeo, the 17 seismic events were located with the PRESEIS package developed by TNO, which computes probability distributions of seismic source locations based on (first) arrival time data using Bayesian inference (also see PRESEIS on github). First synthetic travel times were calculated using the pykonal package (also see pykonal on github) which solves the eikonal equation in 3D providing P- and S- arrival times for all source-receiver pairs on a 3D grid. Next the observed P and S- travel times for the different seismic events were used to infer the spatial probability distributions of the hypocenter locations using Bayesian inversion, following the approach proposed by Tarantola and Valette (1982). Here we summarize the spatial probability distributions in terms of the mean (expectation value, or first order moment) and the covariance (or second order moment) of the probability distributions. The combination of mean and covariance is used to construct 68% confidence ellipses. These ellipses are mainly meant for illustration purposes, as they are actually derived from a multinormal distribution with the same mean and covariance as the inferred probability distribution, which captures its gross features, but not its details. See Paap and Kraaijpoel (2022) for further details on the used earthquake localization approach.

Table 4-1. Overview of velocity parameterization values used to compose the velocity model.

System	Abbreviation base	V0 source	k-value	Initial Vp/Vs (from Spetzler, 2018)	Revised Vp/Vs with Vs increased by 2.5%
Basis Upper North Sea Group	NU	VELMOD-3.2 (NU_f_V0_sk)	0.44	3	2.93
Basis Lower North Sea Group	NLNM	VELMOD-3.2 (NLNM_f_V0_sk)	-0.21	3	2.93
Basis Trias (Trias is ~400mthick) also includes a bit of chalk	RB	VELMOD-3.2 (RB_f_V0_sk)	-0.4	2.5	2.44

(50 m) and zechstein (50 m))					
Basis Namurian	DC	Sonic log data, V0=3226 m/s (constant)	-0.26	1.7	1.66
Basis Dinantian Limestones	CL	Sonic log data, V0=5050 m/s (constant)	0	1.7	1.66
Basis Onder Carboon	BOC	Sonic log data, V0=3409 m/s (constant)	-0.24	1.7	1.66
Basis Devoon	OB	Sonic log data, V0=4750 m/s (constant)	-0.2	1.7	1.66

4.3 Results

Figure 4-3 shows a comparison of a) the regional VELMOD-3.2 model (Paap et al., 2024) in combination with DGM-5 and b) the revised velocity model in combination with new geological model for Californië site. From left to right Figure 4-3 shows the P-wave velocity, S-wave velocity, and the Vp/Vs ratios that are based on Table 4-1. The comparison of the two models shows a clear difference in stratigraphic layering and velocity distribution, emphasizing the relevance of the revised geological and velocity model.

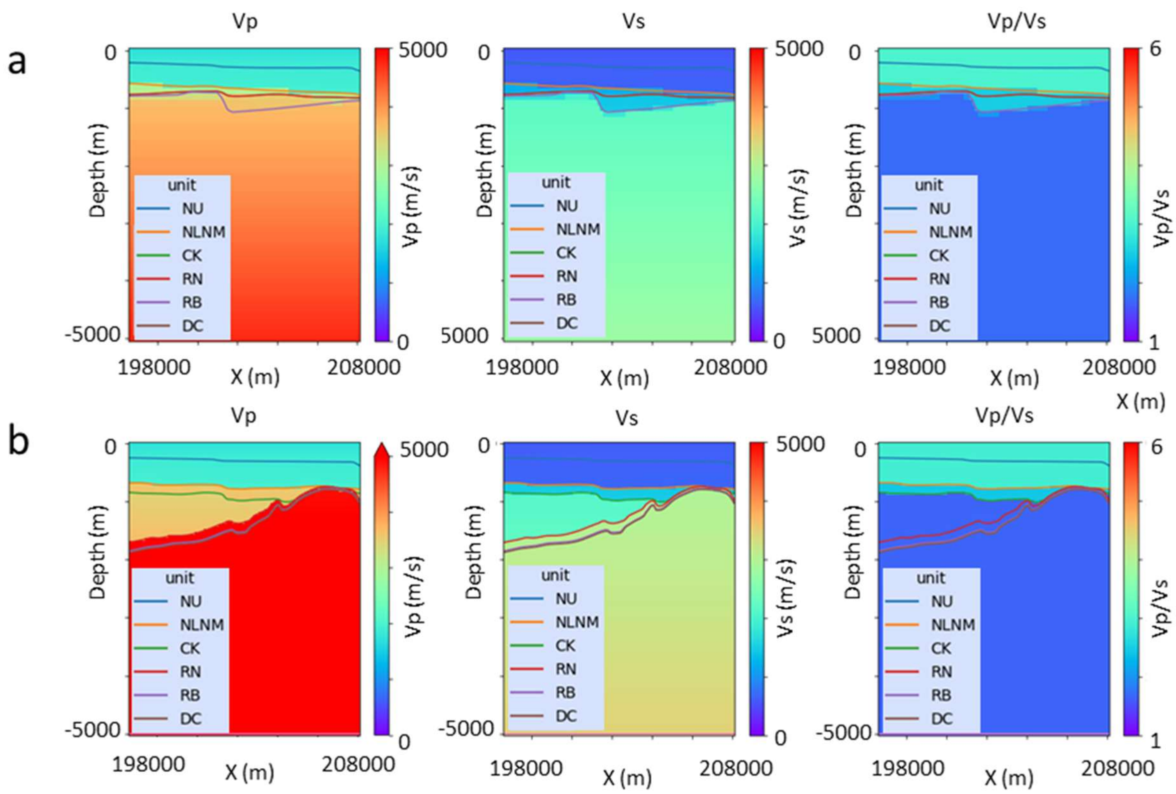

Figure 4-3. Cross-sections through two different types of velocity models showing from left to right the P-wave velocity, S-wave velocity and Vp/Vs ratio. A) Velocity model where stratigraphic layers from DGM5 model are populated with VELMOD-3.2 velocities. B) Velocity model where stratigraphic layers

from the new geological model from SafeGeo (see chapter 3) are populated with velocity data listed in Table 4-1.

We attempted to improve the S-wave velocity model using the perforation shot data. Three perforation shots were conducted in 2016. Upon closer inspection of perforation shot data in our opinion only 1 perforation shot ('ID20160130T203858.328') contained sufficient signal-to-noise ratio to confidently discriminate the P- and S-wave arrivals on its three components. Figure 4-4 shows an example of channel 2 from this perforation shot, where the arrival of P and S-wave energy is visible as broadband signal in the time-frequency plot (a) and on the waveform data (b).

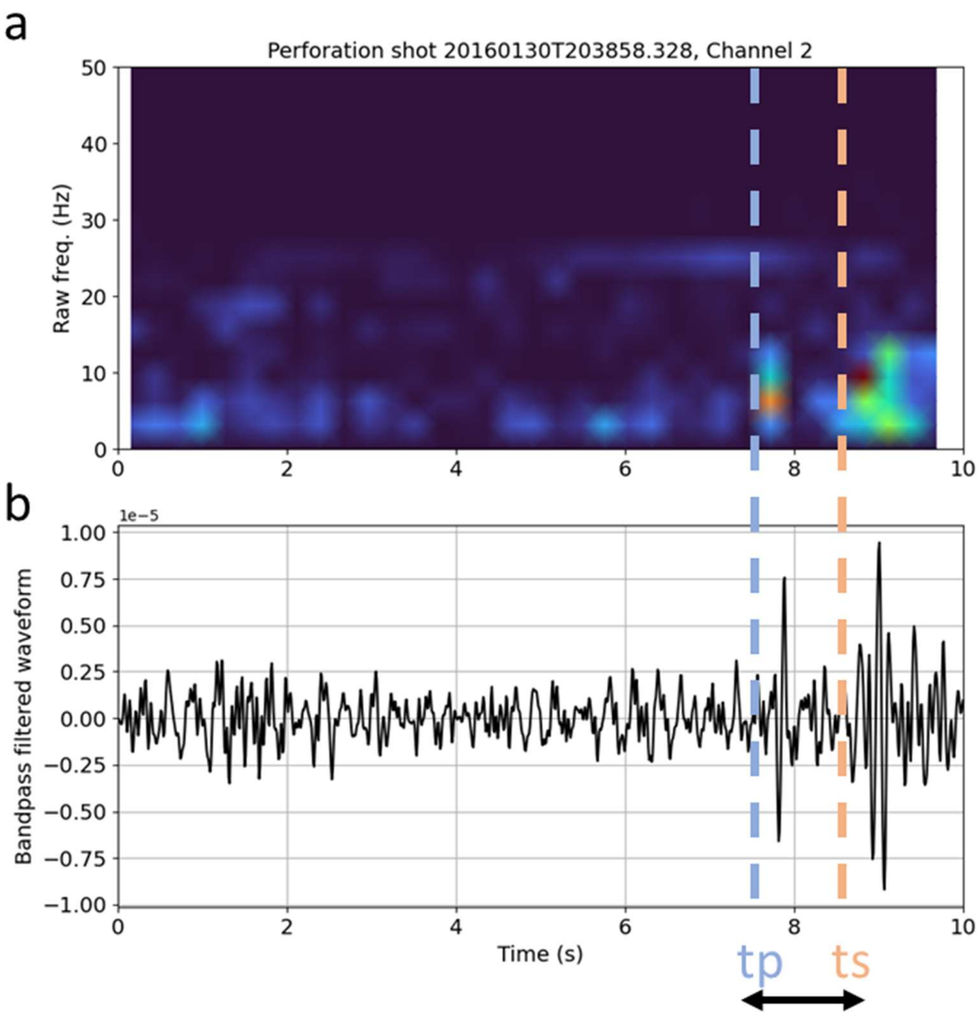

Figure 4-4. Data of channel 2 of station K01 for the perforation shot ID20160130T203858.328'. a) time frequency plot of raw data. B) Waveform data after bandpass filtering (3-20 Hz). The P and S-wave arrival are indicated by blue and orange dashed lines respectively, from which the delay time was derived (ts-tp).

After determining the PS delay times (i.e. ts-tp) on the three channels of this perforation shot, we froze the P-wave velocity model (see Figure 4-3b) and perturbed the S-wave velocity model by applying a varying constant factor (i.e. Vs_factor) to all layers of the initial Vs model. In this way the best fit between synthetic- and observed delay times could be determined. Figure 4-5 shows the results indicating the misfit as a function of Vs factor for the maximum delay time (green), minimum delay time (blue) and mean delay time (black) based on the three channels of the perforation shot data. This figure indicates that when applying a Vs factor of 1.025 (i.e. 2.5% S-wave velocity increase) the misfit between synthetic and mean observed delay time (black) is smallest and thus the fit is optimal. Consequently, we adopted the +2.5 % Vs model perturbation in the final S-wave velocity model that was in turn used to locate the observed seismic events. Note that instead of perturbing the full S-wave velocity for all layers by a constant factor as we did, it would be preferable to refine this exercise by conducting layer specific Vs variations based on additional prior knowledge of layer specific Vs uncertainties in an iterative approach. However, this would require a considerable extra effort which was beyond the scope of this project.

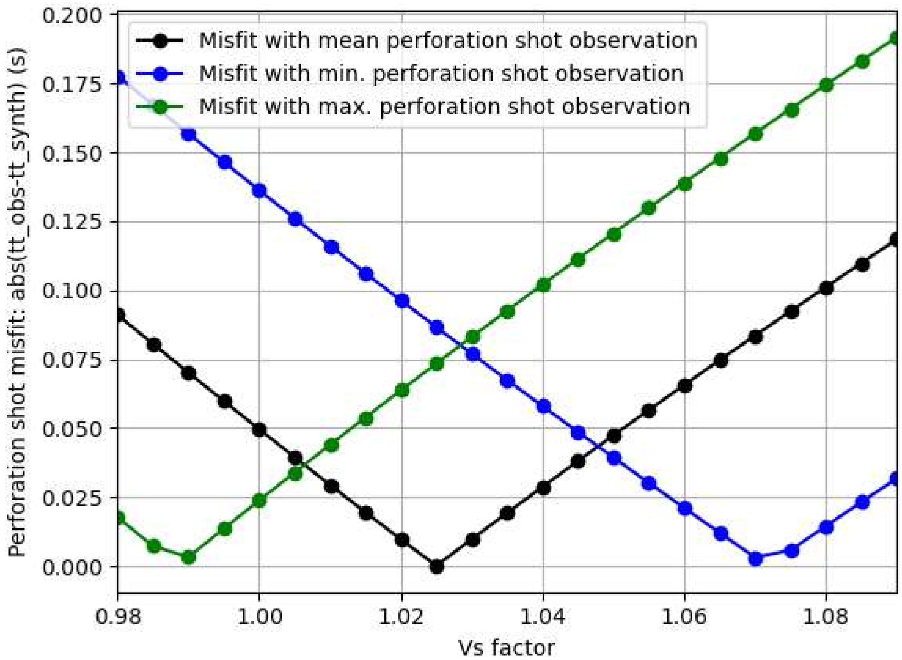

Figure 4-5. Misfit between average observed ts-tp delay time at station K01 for perforation shot ('20160130T203858.328') as a function of the Vs factor multiplied with the initial Vs model. The black, blue and green lines respectively correspond to the mean observed delay time, minimum observed delay time, and maximum observed delay time determined on the three channels of the considered perforation shot.

Next, the events were located using the probabilistic inversion workflow in PRESEIS. This was done on a grid with 50 m grid spacing in the x, y and z dimensions. The result of the new localization outcome for the main seismic event of Ml=1.7 that occurred on September 9th, 2019 is shown in Figure 4-6. This shows the marginalized probability density distributions (i.e., summed over the third, out-of-plane direction) in green together with the mean hypocenter (blue + symbols) and the 68% marginal confidence ellipse, looking from three directions. The hypocenter calculated earlier by Q-con is shown by the black + symbols in Figure 4-6.

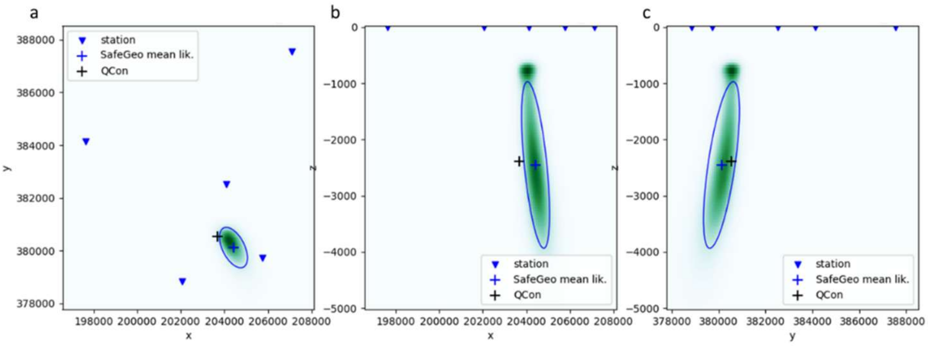

Figure 4-6. Comparison of mean the location for the main seismic event for the revised velocity model from SafeGeo (seeTable 4-1). The confidence ellipses (68%) are indicated in blue. Hypocenters determined earlier by Q-con are indicated by the black + symbols. The three panels display 68% confidence ellipses fitted to the marginalized probability densities in three distinct out-of-plane dimensions. A) Map-view (X-Y) . B) W-E- view (X-Z) and C) S-N-view (Y-Z).

Results of the localization of all 17 seismic events are shown in Figure 4-7 together with well trajectories. It shows the mean location (blue) found here, compared against the locations from Vörös and Baisch (2022)/Q-con (orange) together with the shift in hypocenter pairs for the two different studies. Furthermore the 68% confidence ellipses are plotted in blue for the different events. Figure 4-8 and Figure 4-9 shows map views (xy-plane) of the seismic event hypocenters with 68% confidence ellipses based on the probability density distribution marginalized in the vertical dimension (Z), together with faults and well trajectories. See section 6.3 for a further interpretation of these results in a geomechanical context. The distances between the hypocenter locations found within SafeGeo with the ones found by Vörös and Baisch (2022)/Q-con are shown in Figure 4-10 in the W-E (a), N-S (b) and vertical (c) direction. Figure 4-10d shows the distance in all 3 dimensions between the two hypocenter outcomes together. The distance between the two sets of hypocenters has a mean value of 723 m (dashed black line in Figure 4-10d). Table 4-2 lists the results of the localization for all seismic events together with their standard deviation (see Table 4-2 for further explanation).

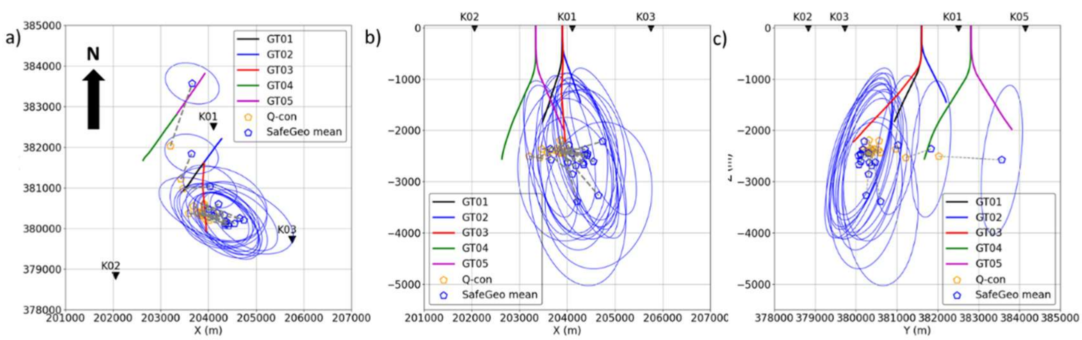

Figure 4-7. Map view and cross-section views of results of mean event locations for all 17 seismic events determined within SafeGeo (blue dots, mean location) and Vörös and Baisch (2022)/Q-con (orange). The shift between event pairs are indicated by the grey dashed lines. Additionally, the 68% confidence ellipses are shown in blue together with the well trajectories. The three panels display 68% confidence ellipses fitted to the marginalized probability densities in three distinct out-of-plane dimensions. A) Map-view (X-Y) . B) W-E- view (X-Z) and C) S-N-view (Y-Z).

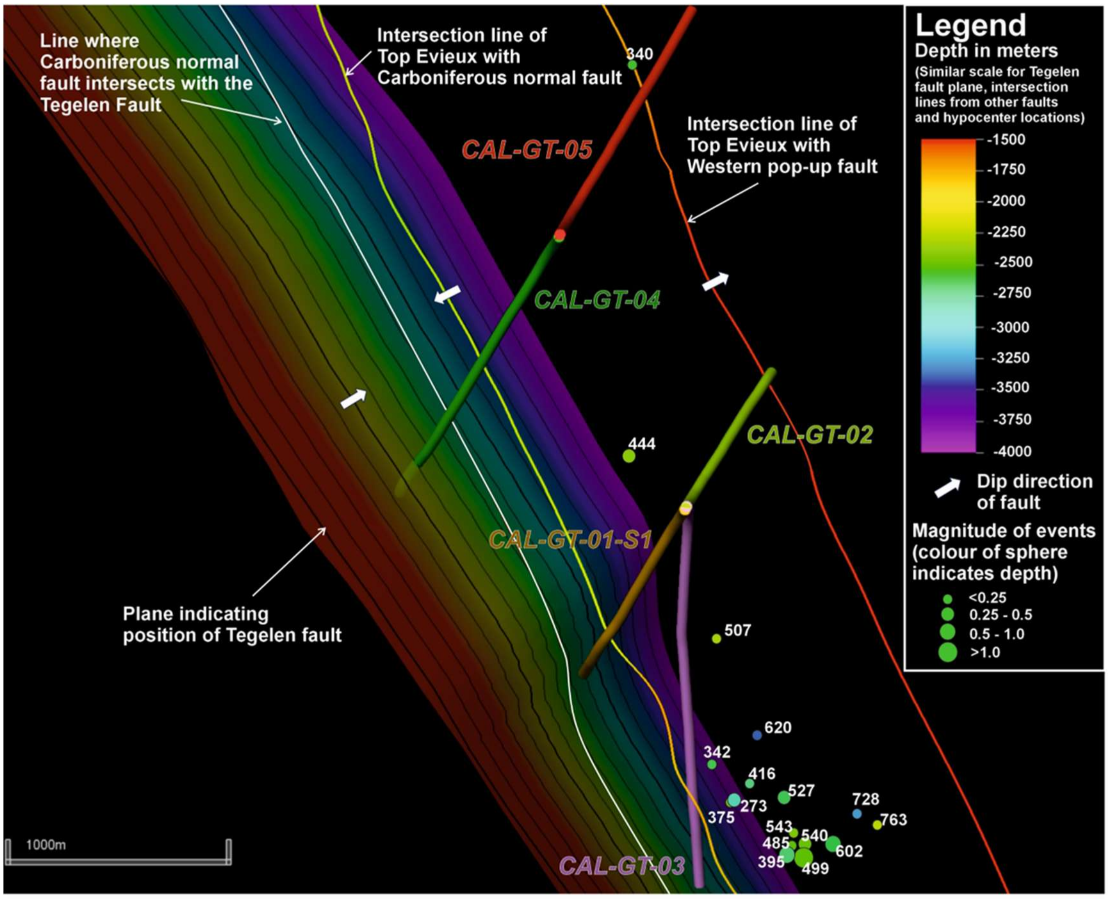

Figure 4-8. Map view indicating mean locations of seismic events as determined in SafeGeo. Numbers at the hypocenters indicate closest distance (m) to nearest fault. The size of the hypocenters indicates the event's magnitude (see legend). Colours of both the Tegelen fault plane, the fault intersection lines and the hypocenter spheres indicate the depth of that particular feature. Note that the depth of the intersection of the Carboniferous normal fault with the Tegelen fault can be read from the location of the white line on the Tegelen fault plane. The depth position of the fault and the hypocenter depth of the seismic events are indicated by the color bar (i.e. red to purple corresponding to shallow to deep).

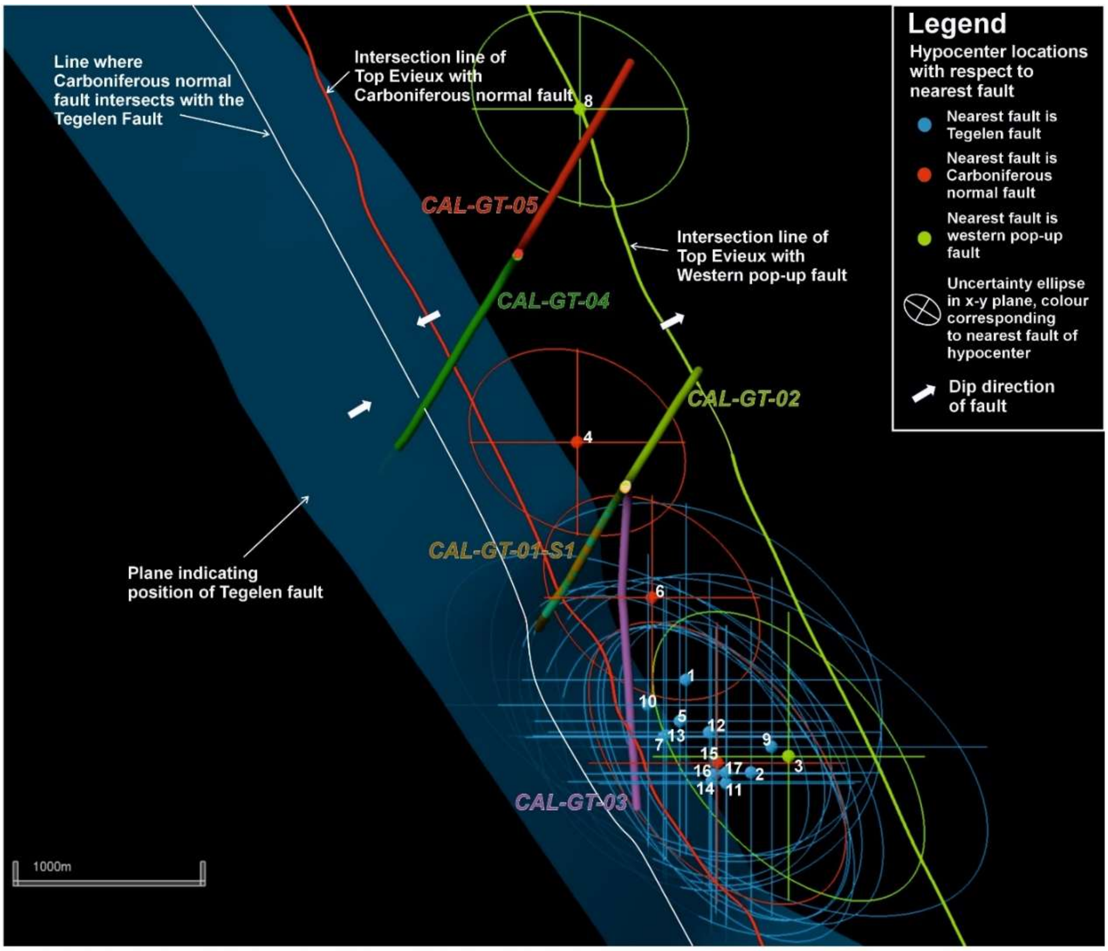

Figure 4-9. Map view indicating mean locations of seismic events and their 68% confidence ellipses in the horizontal X-Y plane. Colours of the hypocenters correspond to the nearest fault. For the distance to the nearest fault see Figure 4-8. The numbers at the hypocenter locations correspond to the event locations in

Table 4-2

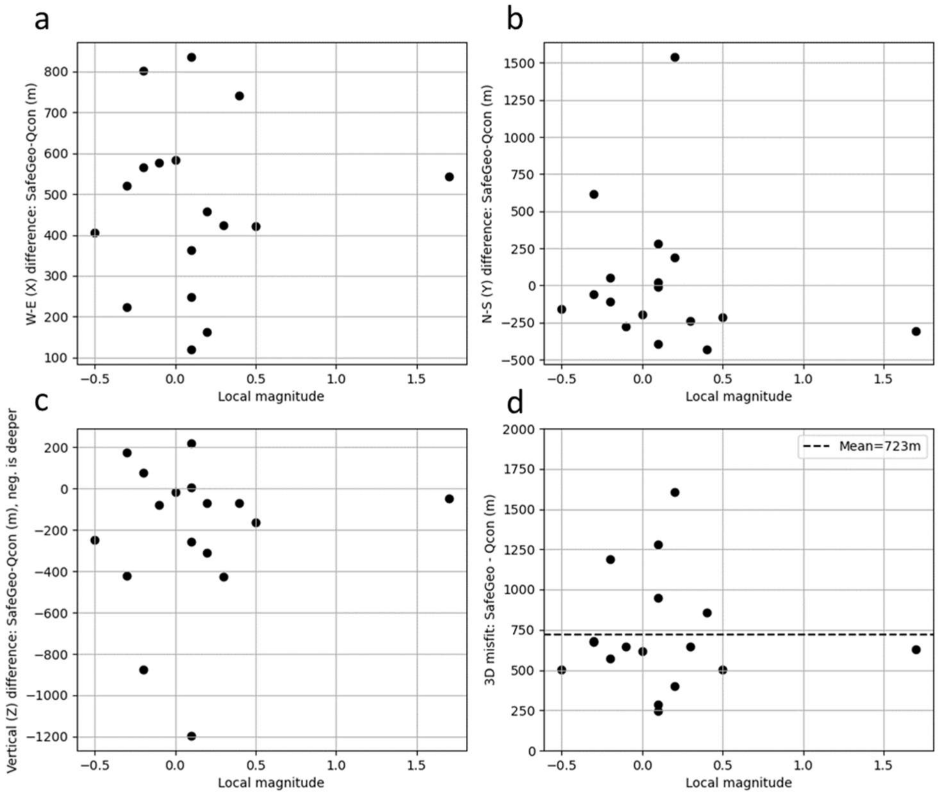

Figure 4-10. Scatter plots showing the misfit between hypocenter locations determined within SafeGeo (based on mean of the marginalized probability distribution) with hypocenters from Q-con/Vörös and Baisch (2022). A) W-E difference (X), where a positive number indicates SafeGeo events are located more to the east compared to Q-con locations. B) N-S difference (Y), where a positive number indicates SafeGeo events are located more to the north compared to Q-Con locations. C) Vertical difference, where a negative number indicates SafeGeo events are located deeper compared to Q-con locations. D) Absolute difference in 3D-space and the mean absolute difference indicated by the black dashed line.

Table 4-2. Overview of hypocenter location for the different events determined in SafeGeo, based on the mean probability density distribution. Furthermore standard deviations (Std) are given marginalized in the different dimensions(m). Locations (x,y,z) are defined according to Rijksdriehoekstelsel (RD_new). The seismic event number corresponds to the numbers shown in Figure 4-8 and Figure 4-9. Note that here only the 17 events are considered that were observed during the operational period. Table 2-2 includes 1 extra event dating from 2022 (outside the production period) that was in hindsight identified during the course of the SafeGeo project by Q-con.

Seismic Event	Seismic event number	Ml	SafeGeo mean x (m)	SafeGeo mean y (m)	SafeGeo mean z (m)	Std x (m)	Std y (m)	Std z (m)
20150818T024705	1	0.1	204213	380601	-3388	673	609	1088
20151205T080728	2	0.5	204550	380119	-2608	455	522	993
20160126T024700	3	0.1	204745	380204	-2215	468	498	947
20160402T141716	4	-0.3	203646	381836	-2362	372	322	882
20170125T162712	5	0.2	204180	380386	-2688	523	484	956
20170131T040156	6	-0.2	204034	381028	-2288	372	351	898
20180408T102927	7	0.1	204096	380304	-2444	499	486	1033
20180825T164327	8	0.2	203661	383568	-2575	373	336	963
20180903T181123	9	-0.2	204656	380253	-3270	744	583	949
20180903T181235	10	0.1	204013	380471	-2625	696	519	1017
20180903T182031	11	1.7	204421	380063	-2491	441	546	1066
20180903T182637	12	0.3	204332	380328	-2629	593	546	946
20180903T204412	13	-0.3	204109	380311	-2856	545	515	980
20180904T001315	14	-0.5	204345	380073	-2668	517	530	963
20180906T152720	15	0	204375	380168	-2373	442	486	911
20180906T155822	16	-0.1	204366	380113	-2478	453	506	931
20180909T205022	17	0.4	204422	380119	-2453	425	508	982

4.4 Discussion and recommendations

At first glance the results show that the new hypocenter locations determined in SafeGeo in general lie in the vicinity of the Q-con locations. On a more detailed level, the SafeGeo hypocenter locations are located more eastward compared to the Q-con locations and we found a larger depth spread amongst the 17 events (~2200-3400 m, see Table 4-2), while the Q-con locations are more closely confined around reservoir depth (~2200-2500 m). Further improvements could be made by acquiring and accommodating new S-wave velocity data in the velocity model to further enhance the corresponding S-wave velocity model. Additionally more insights into the effect of uncertainties in the velocity model on confidence ellipses and hypocenter estimates can be gained by forward modelling analysis accounting for spatial variations in the velocity distribution.

5 Dynamic reservoir modelling

5.1 Introduction

Based on the geological model described in Chapter 3 a dynamic model has been created. This will be described in this chapter. The grid resolution as described in section 3.3.4 has been used for the dynamic model. Simulations have been performed using Eclipse™ by SLB in thermal mode. To capture some of the uncertainty, a number of permeability scenarios was defined. Three history matched scenarios were finally delivered. First the model input will be described including the production data and well completions. Conceptual scenarios will be described and the results of the history match presented in the next section. Using the three history matched scenarios, simulations are done to support choices for a potential pilot phase in the last section.

An analysis of the performance of the wells from well tests and production logging was done prior to this work by VITO. This is reported in Appendix E. The results have been used for the construction of the reservoir models. It should be noted however, that the quality of the well tests is relatively poor and the uncertainty in the interpretation is large.

5.2 Model input

5.2.1 Production data

Most of the production data are available at 5-minute intervals and were shared by the operators. For the simulation this was upscaled to daily values. In addition, the data used in the paper of (Vörös and Baisch, 2022) was made available (also 5-min intervals). Furthermore monthly data was made available by the Advisory Group to Economic Affairs (part of TNO) and miscellaneous excel and data files were shared by the operators. First the data is described in more detail and next the workflow used for upscaling is discussed.
The simulations start on 23/8/2013. The testing phase in March and April 2013 of the CWG wells was not included in the simulations, nor is the testing period in March 2016 in CAL-GT-04/05, because the model is not suitable to represent well tests. The following data was available:

- CWG:
  - CAL-GT-01 pressure and temperature:
    - 5-min data from 23/2/2014 until the shut-in of the wells at 11/5/2018.
    - for the period 1-1-2014 to 23-2-2014 only monthly data was available, of which only the production temperature was usable.

        - Prior to 1-1-2014, some data from tests were available. Missing values were supplied from the monthly data where needed.
    - CAL-GT-03:
        - Injection pressure is available at 5-min intervals from (Vörös and Baisch, 2022) after 23/2/2014. For the period 1-1-2014 to 23-2-2014 only monthly data was available. Prior to this date, some data from tests were available. Missing values were supplied from the monthly data where needed.
        - Injection temperature is available at 5-min intervals only in the period from February 2014 to May 2015. For the rest only monthly averages were available.
    - Flow rate: from 23/2/2014 onwards 5-min data of the flow rates are available from (Vörös and Baisch, 2022). Before that time, monthly averages from NLOG are available and some information from test periods in separate xlsx files.
- CLG: a single output file was received from CLG which contained all required data at 5-min intervals.

As input into the simulator, flow rate and injection temperature are used. The pressure and production temperature are used to history match (calibrate) the model.
The flow rate is upscaled by calculating the sum of the flow rate per day. Pressure and temperature were averaged over the period in which the flow rate was non-zero. For days in which the wells are flowing only part of the day, the uptime or well efficiency factor is required. Uptime is the fraction of time during which the flow rate was non-zero during the 24-hr period. In the reservoir simulator, the bottom hole pressure is calculated with the instantaneous flow rate, but for the calculation of the total inflow into the reservoir (the mass balance) the day-sum is used. Therefore uptime was also calculated for all days and exported to the simulator.

<u>Cleaning up the data</u>
The data contained some short gaps/missing values. They were only filled in for the flow rate. For the pressure, missing data is not a problem because they are used for calibration and for the injection temperature an average temperature was used (see discussion below). The following approach was followed for filling in the gaps/cleaning up:
- When gaps/non-zero rates were identified during shut-in periods (based on e.g. the injection pressure), rates were set to zero instead.
- Values < 10 m^3/hr were set to zero because the system was not operated at such low rates and these values are most likely to be noise.
- The short gaps (< 1/2 hour values) were filled in by duplicating the last flow rate.

The daily averaged flow rate is shown in Figure 5-1 for both the CWG and CLG doublets. The daily observed pressure and temperature will be shown in the section with the history match results.

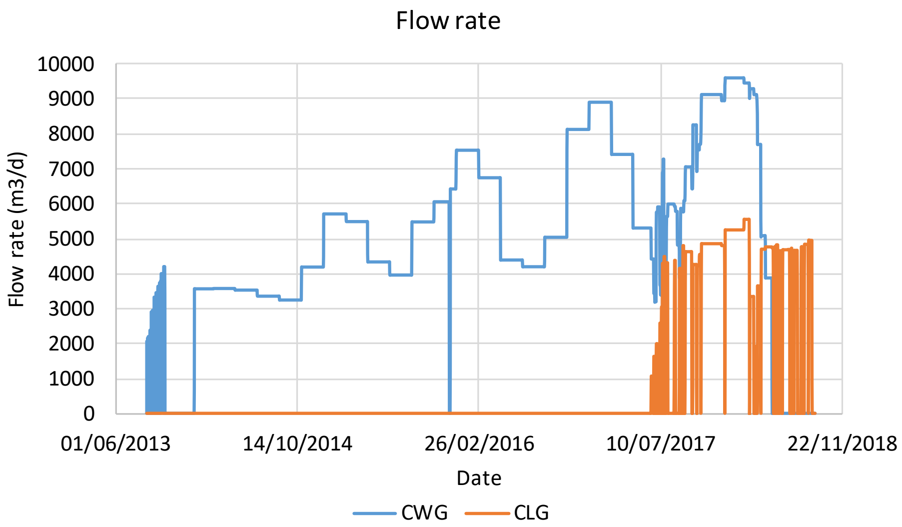

Figure 5-1. Daily average flow rate for the CWG doublet (CAL-GT-01 and CAL-GT-03) and for the CLG doublet (CAL-GT-04 and CAL-GT-05).

<u>Injection temperature</u>
The injection temperature does not vary very much over time. Overall, it is most important that on average the temperature is correct. Table 5-1 shows the mean, standard deviation, minimum and maximum of the daily averaged injection temperature for CAL-GT-03 and CAL-GT-05. The mean is calculated as the injection-volume weighted mean. The standard deviation of CAL-GT-03 is very low, because detailed information was only available from February 2014 to May 2015. Monthly data was available for the other periods. For CAL-GT-05 5-min information was available for the entire injection period. For simplicity a constant injection temperature of 35°C and 40°C has been used for CAL-GT-03 and CAL-GT-05 respectively.

Table 5-1 Injection temperature statistical characteristics (based on daily averages, mean is calculated weighted by the injection volume).

Well name	Mean (°C)	St Dev (°C)	Min (°C)	Max (°C)
CAL-GT-03	35.3	1.4	27.7	40.0
CAL-GT-05	39.4	6.2	14.1	59.7

In the period 4 to 6 April 2018, flow rates are listed in the raw data file. However, the injection pump was broken in this period (personal communication R. Vorage). Therefore, these flow rates have been manually set to zero. During the course of 6 April, the wells were started-up again.

5.2.2 Well completions and VFP

<u>Completions</u>
Well CAL-GT-01 is an open hole completion and is modelled as such.

Well CAL-GT-03 has a slotted liner from 1800 mMD to a depth of 2410 mMD, below which the well is blocked. From 1618 mMD to 1800 mMDm a blind liner is installed, which is not cemented in place. Flow can occur behind the this blind liner, which could partially explain the large inflow at the start of the slotted liner in the PLT. The blind liner is implemented in the model as a cemented casing as is the blocked part of the below 2400 mMD. The slotted liner is implemented as perforated casing.

The completions for CAL-GT-01 and CAL-GT-03 are illustrated in Figure 5-2.

Well Cal-GT-04 has an uncemented casing with perforations. This means that the flow can go behind the casing to the perforations, but with higher pressure drop the further away the inflow is from the perforation. This cannot be represented directly in a reservoir simulator. In the current model, only the perforations can be included and not the flow behind the casing. If only the perforations are included, the inflow zone is too short. As an intermediate solution, the perforations have been implemented longer than they really are:

- Perforation 1: perforations are 2547 – 2553 mMD and 2557 – 2563 mMD which are implemented as 2540 to 2565 mMD.
- Perforation 2: perforations are 2747 – 2753 mMD, 2759 – 2765 mMD and 2771 – 2777 mMD which are implemented as 2740 to 2779 m MD.

For well CAL-GT-05, the entire open hole section is included. The completions for CAL-GT-04 and CAL-GT-05 are illustrated in Figure 5-3.

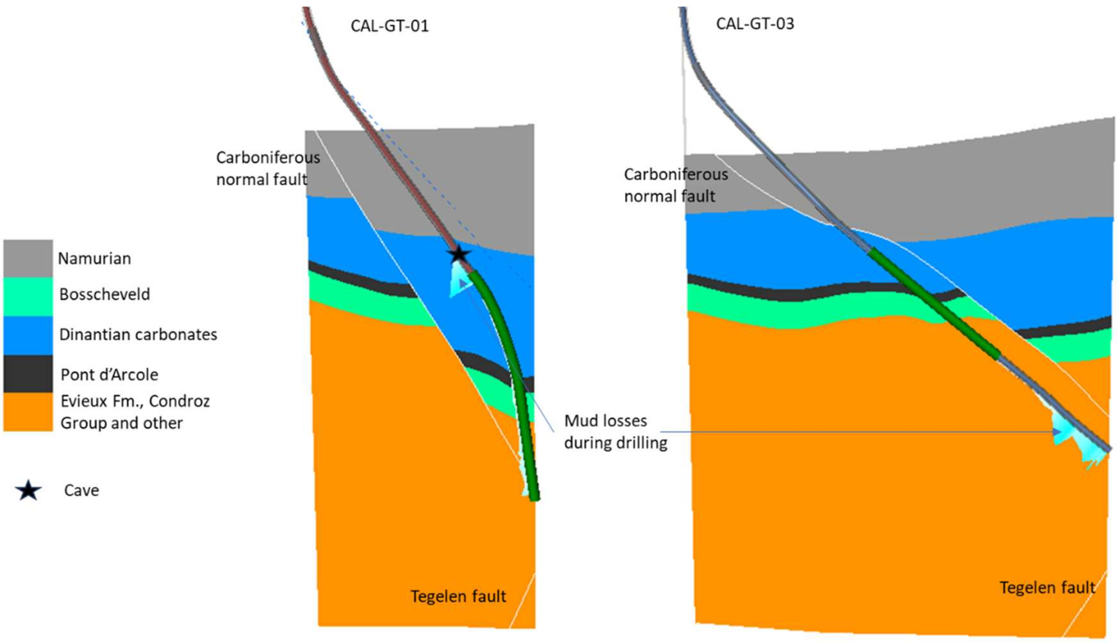

Figure 5-2 Illustration of the well completions for CAL-GT-01 and CAL-GT-03 in cross-sections showing the formations. Inflow sections indicated in green. White lines show the position of the faults.

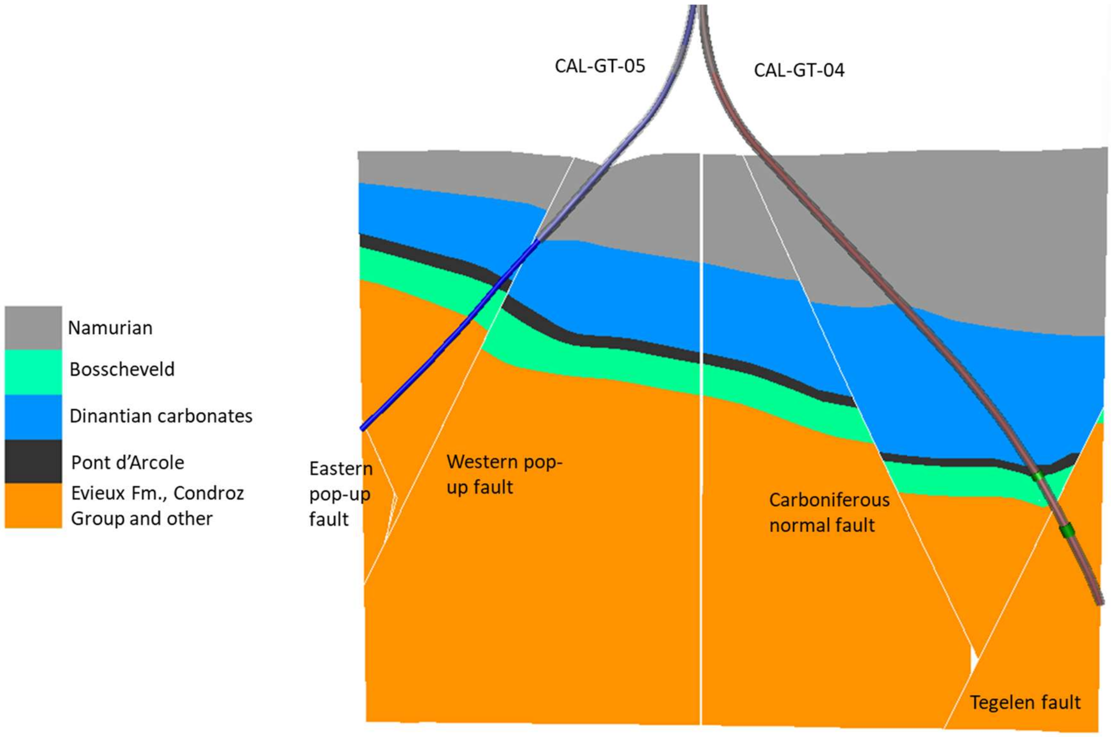

Figure 5-3 Illustration of the well completions for CAL-GT-04 and CAL-GT-05 in cross-sections showing the formations. Cross section seen from the west. Thin white lines indicate faults. Wide, vertical white line is the boundary between the cross-sections of the wells. Inflow zones for CAL-GT-04 are shown in green and for CAL-GT-05 the open hole section is shown in blue.

<u>Implementation of skin</u>

Skin interpreted in well tests cannot be used directly in reservoir simulation models, because of differences in assumptions. For example, if the well test was not interpreted using a dual porosity assumption, the skin is not applicable. Also differences in the assumptions on the completions and shape of the reservoir influence the results. The following choices have been made based on the re-analysis of the well tests and PLT data in Appendix E:

- CAL-GT-01: no estimate of skin is available. The analysis of the multi-rate test was done with skin=0. No skin has been applied in the reservoir model.
- CAL-GT-03: no estimate of skin available is at the start of production. Only relative skin was used to account for the increase in injectivity for the analysis of the PLT data of different years, which is not included in this model. Therefore no skin was applied in the reservoir model.
- CAL-GT-04: A high negative skin was interpreted from the well tests, but the assumptions in the model fitted in the well test differed considerably from the model assumptions in the reservoir model used in this report: dual versus single porosity, different completion, flow along the fault versus radial inflow model. Therefore it was decided not to use the skin.
- CAL-GT-05: For CAL-GT-05 a multi-rate well test interpretation with a dual porosity model was done resulting in an estimate of a mechanical skin decreasing from 1.6 to -4 for increasing rates (Juez-Larré and van Kempen, 2017). The skin of -4 is relevant for the production rates. In line with the analysis of the PLT data in Appendix E, a skin of -3.5 was used for well Cal-GT-05.

Vertical Flow Performance

Because the pressure observations are not at reservoir depth, vertical flow performance (VFP) tables have been calculated for all the wells using PipeSIM, a multi-phase well-bore flow simulator by SLB, which is integrated in Petrel. A VFP table tabulates the pressure difference between reservoir depth and gauge depth as a function of flow rate and other variables if required such as the gas fraction. For CAL-GT-01 and 04, the VFP tables list the pressure drop between the gauge depth at the ESP and the top of the open hole section/perforations. For the injectors, the VFP table cover the section from the top of the open hole section to surface.

For the VFP tables for CAL-GT-01 and 03, a brine specific gravity of 1.05 (at standard conditions) has been used, consistent with a salinity of 75 g/l. Temperature for CAL-GT-01 is 80°C and for CAL-GT-03 35°C. For the VFP tables for CAL-GT-04 and -05, a brine specific gravity of 1.06 (at standard conditions) has been used, consistent with a salinity of 90 g/l. Temperature for CAL-GT-04 is 89°C and for CAL-GT-05 38°C. See also Table 5-2 for a summary of salinity and temperature of the wells. The gas content is relatively low (34,0-43,9 l gas per m^3 for CAL-GT-01 and 210 l gas per m^3 for CAL-GT-04 (information provided by VITO based on fluid analysis of the wells) and has not been included in the VFP calculation.

The following settings are the same for all tables: specific heat capacity of the fluid is 4.2 kJ/kg/C and thermal conductivity is 52.3 kJ/m/d/C. The ambient temperature which is used to calculate the heat exchange with the environment is set to 40°C as an average over the entire depth range of the wells above the top of the inflow zone. Pipe roughness used is 0.0015 cm. The heat transfer coefficient is 981.2 kJ/d/C/m^2.

For both production wells, the gauge depth is at the ESP intake. Also for both wells the depth of the ESP has changed. This has not been implemented in the simulation runs. Only the initial depth has been used, which is 295 m below ground level for CAL-GT-01 and 529 m MD RT for CAL-GT-04 . The depth change is approximately 50 m in both cases and results in a (nearly) constant difference in pressure of approximately 5 bar. The change in depth occurred in December 2015 for CAL-GT-01 and in June 2018 for CAL-GT-04. Please note that in CAL-GT-01, the initial testing on 15/4/2013 was done with an ESP at a depth of ~500 m. The depth was changed before the production started.

5.2.3 Reservoir and fluid properties

Dual porosity simulation

The flow occurs mostly in the Dinantian Carbonates, Bosscheveld and Evieux Formation. Both typically are characterised by fracture flow and have a tight matrix. For the purpose of the flow modelling only, a single porosity model probably would produce acceptable results, because the matrix contributes little to flow. However, for the thermal modelling including the matrix is essential. In a dual-porosity system, the cold injection water progresses much faster than in a single porosity system, because the cooling of the matrix is delayed. Therefore, it was decided to use dual porosity simulation. The assumption that single porosity models gave a poor match to the thermal breakthrough was tested and found to be accurate.

Permeability and porosity
Initial values for fracture bulk permeability are available from the analysis of the well tests and PLT data (Appendix E). These will be adjusted during history matching and are discussed in detail in the next section.

Matrix permeability was measured to be in the range 0.005 up to 0.150 mD (Goense, 2018) for the Dinantian carbonates. Higher values were measured parallel to the bedding than across the bedding (Goense, 2018). For the horizontal permeability the permeability parallel to the bedding is most relevant. For the Bosscheveld and Evieux Formations not much data are available, but both are expected to be tight formations (see Section 3.1.3 for information on lithology). The Namurian deposits above the Dinantian carbonates are mostly shales and are expected to have low porosity and permeability overall (see Section 3.1.1). Therefore a uniform value for matrix permeability was used, namely 0.01 mD. A sensitivity run with 0.1 mD showed little sensitivity to this values in the history match.

The matrix porosity of cores from the Dinantian carbonates was measured to be very low: 0.2-1 % (Goense, 2018). Also estimates of porosity based on matching the well tests was estimated in the range of 1 to 2% (Juez-Larré and van Kempen, 2017). This doesn't however include the impact of karst, which can locally increase porosity significantly. For the deeper formations no measurements are available, but the porosity is also likely to be in the order of a few %. Although the uncertainty is large the impact on the history match of the production phase is small. Matrix porosity affects the results very little: only the heat capacity and total compressibility are influenced. Matrix porosity was set to 5% in the entire model area for simplicity. The fracture porosity has much more impact, because it determines how fast the water and the thermal front advance. However, it is much more uncertain. A uniform value of 1% has been used for the entire model area. This is not the porosity inside the fracture, but the fraction of the total volume occupied by fractures.

Matrix-fracture interaction
The interaction between matrix and fracture depends strongly on the fracture density, but also on the geometry of the fault network and permeability of the fracture walls. It is often used as a history matching parameter, because it cannot be observed directly. The matrix-fracture coupling factor σ can be approximated by (Kazemi et al., 1976):

$$\sigma = 4\left(\frac{1}{l_x^2} + \frac{1}{l_y^2} + \frac{1}{l_z^2}\right)$$

Where l_x, l_y and l_z are the fracture distances in x, y and z-direction respectively. The factor σ acts like a multiplier on the transmissivity between the matrix and fractures. Little information is available on the density of permeable fractures. Based on the massive losses in CAL-GT-01, 03 and 04, the flow in the area of the Tegelen and Carboniferous normal faults is in large, open fractures rather than in a network of small fractures. The PLT in CAL-GT-03 shows that 50 to 70% of the flow is injected in 3 discrete, high permeability, narrow inflow zones, which are possibly fractures, karstified fractures or other karst features. This suggests that a relatively large distance between fractures is appropriate, resulting in low fracture-matrix interaction. In well CAL-GT-01 an FMI was run from 1580 to 1760 mMD, which is the top part of the Dinantian Carbonates (Leverink and Geel, 2019). This part is not produced. The last 22 m of the log was not useable, because of a large karst feature. A total of 13 conductive faults and fractures has been identified over the measured interval (~150 m). The number of partially conductive faults/fractures is much larger and can reach a density of up to 10 per m, however based on the PLT their contribution is probably not very large. In the history match, the fracture-matrix interaction in this area is calibrated based on the thermal breakthrough in CAL-GT-01.

For the Devonian sandstones in CAL-GT-05, the flow appears to be in a more distributed fracture network with more, but smaller fractures. The PLT results show that more than 80% of the flow is injected in large distributed flow zones with a permeability of some tens of mD. Based on an acoustic log in CAL-GT-05, which was run in the open hole section up to a depth of 2100 mMD, the fracture density is in the order of up to 1 fracture per 1 or 2 meters in the best producing zone. From the acoustic log, it could not be identified whether the fractures are drilling-induced or not and whether they are conductive. Also the resolution of the acoustic log is less than an FMI, which means that small or thin fractures may have been missed. Based on this fracture information, the matrix-fracture coupling factor has been set to 5 in the permeable areas in the Bosscheveld and Evieux Formations around CAL-GT-05. In de rest of the model, the value determined in the history match based on the thermal breakthrough in CAL-GT-01 is used. The values are given in Section 5.3.

Thermal properties of the rock
The thermal properties of the rock have been taken constant in the entire reservoir and the same as in the earlier model created by the Advisory Group and used by D. Reith (Reith, 2018). The thermal conductivity of the rock and fluids is 224 kJ/m/d/C. The heat capacity of the rock ranges from 2650 kJ/m3/C @ 60°C to 2750 kJ/m3/C @ 100°C.

Fluid properties
The fluid properties in the reservoir show a gradient with depth (Table 5-2). However, this has not been included in the model. Instead a constant salinity (NaCl) of 80 g/l has been used to calculate the fluid properties. Water composition analysis from CAL-GT-01 shows that the water has mainly dissolved NaCl with some Ca^{2+} and K^{+}.

The variation of brine density as a function of temperature is not included in the model, because the density changes due to the temperature are not very large. The density at standard conditions is 1057 kg/m^3 with a compressibility of 3.7E-5 1/bar. The viscosity is a function of temperature and calculated based on the correlations by (Batzle and Wang, 1992). The heat capacity of the brine is based on (Grunberg, 1970) and (Sun et al., 2008) and also depends on the temperature. Both are shown in Figure 5-4.

It might be worthwhile to investigate whether density-driven flow due to the injection of the cold brine with high salinity could play a role. The injection fluids have increased salinity compared to the in-situ fluids, because the injection is at shallower depth than the production for both doublets. In particular during shut-ins the high-density brine would tend to sink in areas with high vertical permeability. It was beyond the scope of the current project to investigate this.

Table 5-2 Overview of observed Total Dissolved Solids (TDS) and temperature. Data from CAL-GT-01 to 03 from VITO, analysis production test report CAL-GT-03 from 2013, For CAL-GT-04 and for CAL-GT-05 from VITO report form 2016 (**ENES/1310289/2016-0003**). Depth is the open hole section for CAL-GT-01 to 04 and the perforation depth for CAL-GT-05.

Well name	Depth (mTVD GL)	Total TDS (g/l)	Temperature* (°C)
CAL-GT-01	1592 - 2470 mTVD GL	75 g/l	89°C and production T ~80°C
CAL-GT-02	1236 – 1482 mTVD GL	40 g/l	60°C
CAL-GT-03	~1490 – 1885 mTVD GL**	48 g/l	65°C
CAL-GT-04	2150-2166 and 2327 -2355 mTVD GL***	85 à 100 g/l	Production T ~92°C
CAL-GT-05	1361-1994 mTVD GL	61 g/l	76°C

* max. recoded temperature at the end of drilling.

** inflow could also be shallower, because the blind liners are not cemented.

*** perforations in a uncemented casing

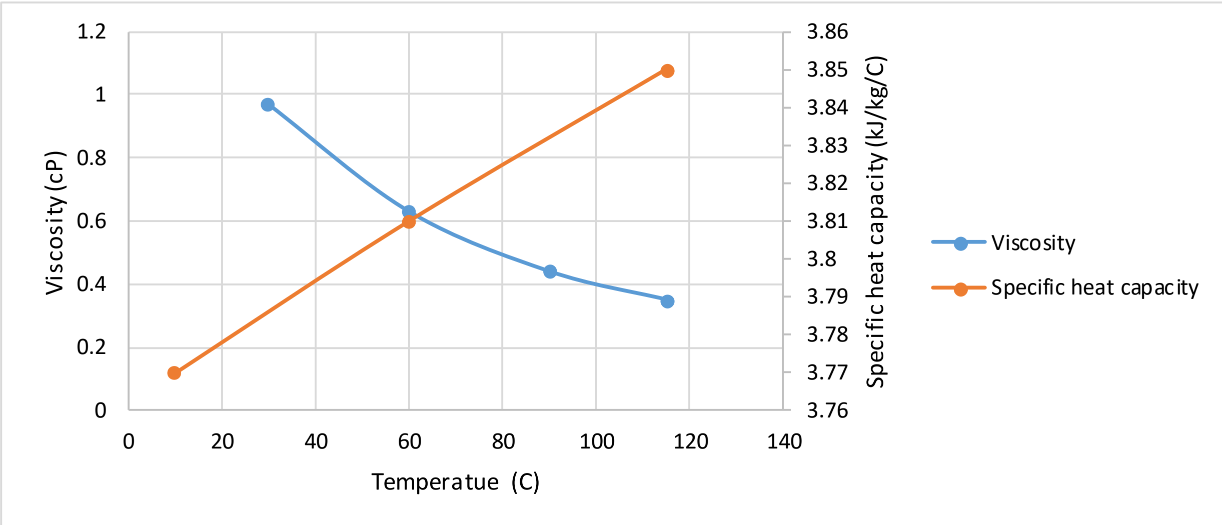

Figure 5-4 Fluid viscosity and specific heat capacity as a function of temperature.

5.2.4 Initial and boundary conditions

Initial pressure

Initial pressure was based on PLT information because this is more reliable than information at the ESP. Recalculation from ESP depth to reservoir requires detailed information on the fluid composition and temperature in the well, which is generally lacking. In CAL-GT-03, a PLT run was conducted in 2013 which provided a reliable initial pressure measurement of 183,6 bar at a depth of 2370 m MD (1828 m TVD MSL). Using the density in the reservoir simulation model (1040 kg/m^3 or a gradient of 1.04 bar/10 m) results in the initial pressure of 150 bar at 1500 m depth below mean sea level (1527 m below surface).

Initial temperature

Temperature measurements made during or directly after drilling and completing the wells often tend to underestimate the temperature due to cooling of the near-well area during drilling and cleaning of the well if they are not corrected. A temperature log of CAL-GT-02 after a long period of shut-in showed a temperature as high as 58.5°C at 1170 m TVD. Therefore, three temperature scenario's were tested (Figure 5-5) during the history match and the MID scenario was found to predict the initial production temperature of CAL-GT-01 and 04 best. This scenario has a thermal gradient of 34 °C/km up to depth of 600 m and a higher gradient of ~36 °C/km below.

Boundary conditions

The boundary conditions are a mix of no flow boundaries and connected aquifers:

- For the lateral boundaries on the south-west and north-east a no-flow boundary condition is used.
- For the top and bottom boundary and the lateral boundaries on the north-west and south-east, Fetkovich-type (Fetkovich, 1971) aquifers have been implemented. The total volume and productivity of the aquifers have been fine-tuned in the history match. Initial estimates were based on the size and permeability of the model. The final values area listed in Table 5-6. All aquifers are initially in pressure equilibrium

with the grid blocks to which they are connected, they have total compressibility of 0.000145 1/bar and salt concentration of 80 kg/m^3.

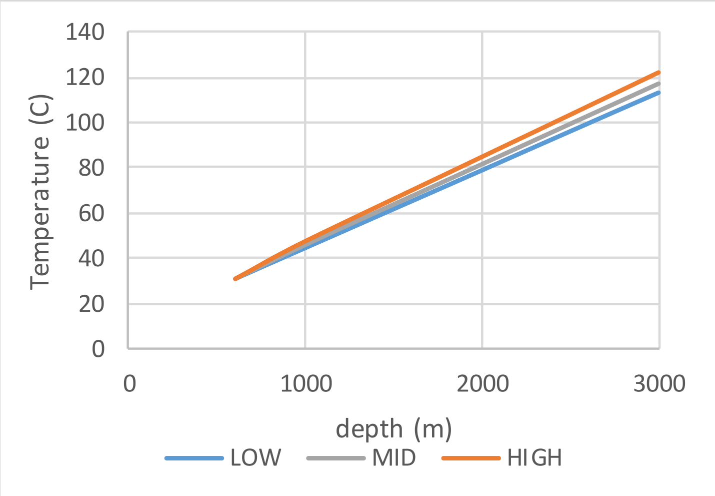

Figure 5-5 Initial temperature scenario's. Mid scenario is used for the history matched models.

5.3 History match

5.3.1 Scenarios

The approach used for history matching is to create conceptual scenarios based on the structural geological model described in Chapter 3 and history match those. The goal was to get history matched models with a different pressure and temperature distribution in the reservoir in order to capture some of the uncertainty. The focus was not to get the most accurate numerical match to the pressure and temperature in the well, but capture trends and overall behaviour of the system.

During the manual history match different sensitivities were tested and different models created. Finally three history matched scenarios were selected to be used for the geomechanical analysis in Chapter 6 and these are presented in detail below. The main learnings from the history matching procedure are also included in the description of the scenarios and results.

For all scenarios it was assumed that the main permeability is related to the damage zones of the faults (i.e. the zones around faults with increased fracture density and an increased permeability). The permeability of the damage zones could be enhanced by karst. The main directions in permeability are assumed to be along the faults in horizontal and vertical direction. The permeability perpendicular to the faults is assumed to be considerably lower. How much lower differs per scenario. It is also assumed that the permeability continues along the entire extent of the Tegelen Fault and doesn't change in terms of permeability per formation. For the other faults, the assumptions vary per scenario, which will be discussed below.
The following scenarios are defined:

- HM1: Each fault has a damage zone, with high anisotropy (factor 10), leading to little connectivity in the reservoir. In line with the general observation that faults with large displacement have more intense damage zones (see section 3.1.3), the permeability of the Tegelen damage zone is higher than of he other faults. An overview is given in Table 5-3 and Figure 5-6.

- HM5: This scenario reflects the option that the faults of the pop-up structure are not influencing the flow and that the fractured zone found in CAL-GT-05 is present throughout the model area. This results in more lateral continuity in the Bosscheveld Formation and Devonian sandstones. Although in CAL-GT-03 no flow is observed in the PLT in these layers, this might be due to the much higher permeability in the zones above, which is at least a factor 10 higher. Also anisotropy in the damage zones is assumed to be lower and the damage zone to be a bit wider. An overview is given in Table 5-4 and Figure 5-7.
- HM8: Also in this scenario the anisotropy in the damage zones is assumed to be lower and the damage zone to be a bit wider compared to HM1. This scenario is different due to the stronger aquifer support which reduces the drawdown resulting from production in CAL-GT-04. An overview is given in Table 5-5 and Figure 5-8.

The Pont d'Arcole is handled differently from the other formations. From the PLT logs (appendix E) it is know that this formation is contributes very little to the flow. In line with this the acoustic log in CAL-GT-05 shows no visible fractures in this formation. Therefore background permeability was assumed for this formation, except in the Tegelen fault. It is assumed that the damage zone of the Tegelen fault is so extensive that it also affects this layer. This is supported by the observations in CAL-GT-04 where also losses occurred in the Pont d'Arcole. For the Carboniferous Normal Fault, different scenarios were used, because in CAL-GT-03, the Pont D'Arcole is less clear than in the other wells (see Figure 3.3.2 and the discussion in that section). In HM1, the Pont d'Arcole is assumed to be permeable in the damage zone of the Carboniferous Normal Fault. In HM5 and 8, the Pont d'Arcole is given background permeability and thus forms a barrier to the vertical connectivity.

The Western pop-up fault does not have a damage zone in any of the scenarios, because this conflicts with the PLT data showing no inflow in the Dinantian carbonates in CAL-GT-05. However, the wide damage zone from the Eastern pop-up fault covers the lower part of the Western pop-up fault as well.

The permeability of the fault core is often assumed to be lower than in the damage zone (e.g. Billi et al. 2003). This is difficult to implement in the coarse models used in this study, because the gridblocks are in the order of 50 m wide. A different way to implement this is via a multiplier on the transmissivity on the faults. It was investigated if a history match could be achieved when the transmissivity across the fault was low, however this did not appear to be a feasible option for the Carboniferous Normal fault because of its proximity to CAL-GT-03. Therefore this was not further investigated for the Tegelen and Carboniferous Normal fault. It was implemented for the pop-up fault in HM1, where a row of grid blocks along the faults was set to background permeability.

In the current model approach, it has been assumed that the effect of karst is mainly to increase the permeability in the fault damage zones. No further implementation of permeability due to karst was included. In one history match scenario, a layer of high permeability close to the top of the Dinantian carbonates was implemented in line with a previous model (layer L2 in Vörös and Baisch, 2022). However this hardly affected the history match and has not been pursued any further. However, large caves like the one seen in CAL-GT-01 will affect the storage (porosity) and distribution of the flow. The impact of this is however very difficult to asses and beyond the scope of this project.

In the currently available observations, there is no clear evidence for communication perpendicular to the faults such as might occur in a permeable layer with karst. On the interference between CAL-GT-04 and CAL-GT-05 different conclusions have been drawn. (Laenen and Broothaers, 2016) concluded that no conclusions on interference between the wells could be given from the well tests from Feb/March 2016, except that it cannot be very large. Due to simultaneous changes in production in CAL-GT-01, a possible response could not be interpreted. The impact could at most be ~0.3 m head (or ~0.03 bar) difference during an injection test of 28 hrs. Based on a different analysis (Juez-Larré and Kempen, 2017) concluded that interference was present. Based on further testing in June 2017 in which only injection occurred in CAL-GT-05, Broothaers and Vorage (2018) concluded that the interference is very small because no response was seen at the ESP depth in CAL-GT-04. This shows how difficult it is to interpret such tests and that uncertainty remains.

For both injectors an increase in injectivity is observed over time (Appendix E and Figure 5-9). In CAL-GT-05 this was mainly seen in the first months (Tables 5 and 6 in Appendix E but for CAL-GT-03 the increase in injectivity continues (Table 2 in Appendix E). Initially this might be due to cleaning up of the well. In later time, this is more likely caused by the cooling around the well. This has not been included in the model. It could be included in the model by changing the permeability of the near-well area over time or via a negative skin. However, this does not add to the understanding of the flow system as a whole and has not been implemented. The history match has focused on matching the pressure after the initial fast change in injectivity.

Background bulk fracture permeability has been set to 2 mD. The matrix-fracture interaction coefficient is 0.25 for HM1 and 0.2 for HM5 and HM8, except in the fractured area of the Devonian sandstones identified in CAL-GT-05. As discussed in Section 5.2.3, the matrix-fracture interaction coefficient is set to 5 in this area because of the higher fracture density.

Table 5-3 Settings for the damage zone width and the bulk fracture permeability for HM1

Fault Name	Hanging wall		Footwall	
	Width of the damage zone	Bulk fracture permeability (I/J/K direction)	Width of the damage zone	Bulk fracture permeability (I/J/K direction)
Tegelen fault	150 m	130/1300/1300 mD	150 m	130/1300/1300 mD
Carb. normal fault	150 m	55/550/550 mD	150 m	35/350/350 mD
Western pop-up fault	-	-	-	
Eastern pop-up fault	350 m	30 mD	350 m	30 mD

Table 5-4 Settings for the damage zone width and the bulk fracture permeability for HM5. Permeability in bottom Bosscheveld/top Condroz is 19 mD.

Fault Name	Hanging wall		Footwall	
	Width of the damage zone	Bulk fracture permeability (I/J/K direction)	Width of the damage zone	Bulk fracture permeability (I/J/K direction)
Tegelen fault	150 m	400/1200/1200 mD	150 m	400/1200/1200 mD
Carb. normal fault	250 m	150/500/500 mD	150 m	100/350/350 mD
Western pop-up fault	-	-	-	-
Eastern pop-up fault	-	-	-	-

Table 5-5 Settings for the damage zone width and the bulk fracture permeability for HM8

Fault Name	Hanging wall		Footwall	
	Width of the damage zone	Bulk fracture permeability (I/J/K direction)	Width of the damage zone	Bulk fracture permeability (I/J/K direction)
Tegelen fault	150 m	400/1200/1200 mD	150 m	800/1500/1500 mD
Carb. normal fault	250 m	150/500/500 mD	150 m	100/350/350 mD
Western pop-up fault	-	-	-	
Eastern pop-up fault	250 m	18 mD	250 m	18 mD

Table 5-6 Final settings of the aquifers used in the reservoir model

Aquifer	Volume (m3)	Productivity Index (sm3/d/bar)
Top aquifer	4E8 m3	2500 (HM1 and 5) ; 5000 (HM8)
Bottom aquifer	4E8 m3	2500 (HM1 and 5) ; 10,000 (HM8)
NW aquifer	1E9 m3	5000 (HM1 and 5) ; 50,000 (HM8)
SE aquifer	1E9 m3	5000 (HM1 and 5) ; 50,000 (HM8)

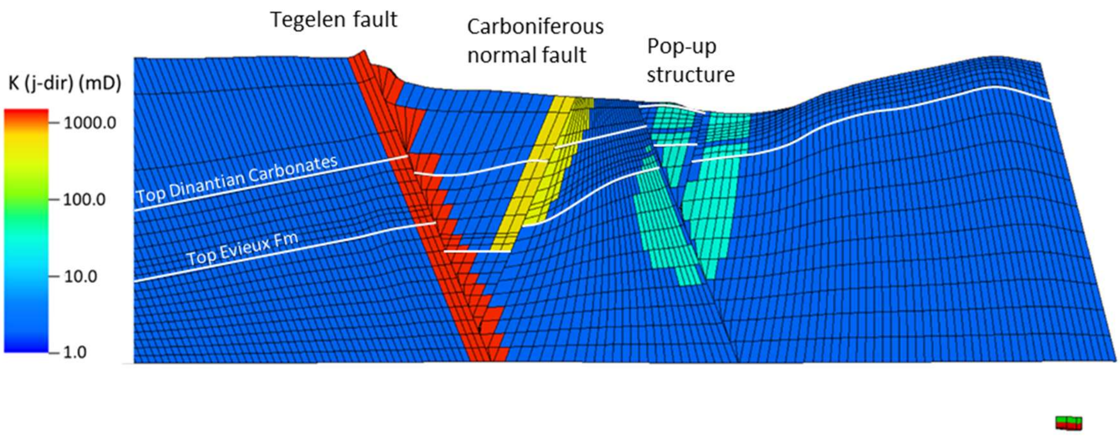

Figure 5-6. Cross-section of the model (viewed from the south-east, in between the doublets CWG and CLG) showing the bulk fracture permeability for HM1. White lines indicate the top of the Dinantian Carbonates and the Evieux Formation.

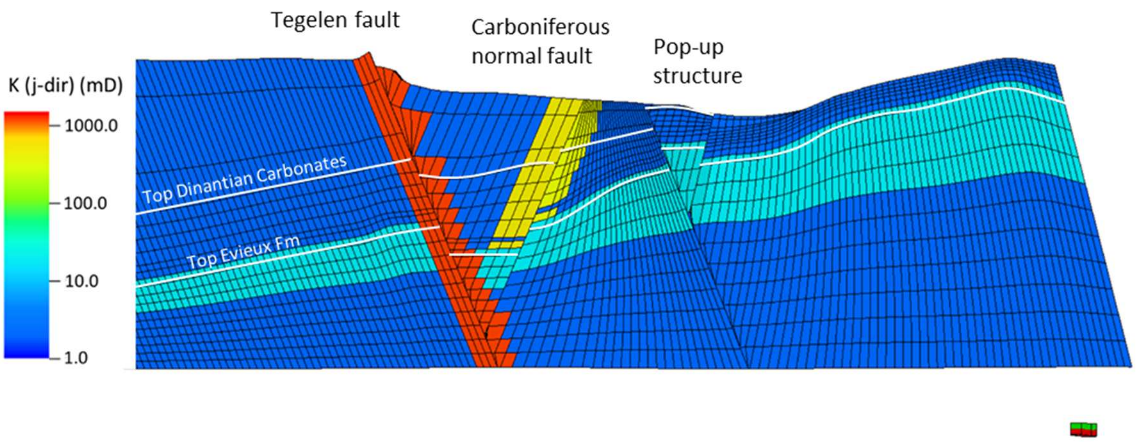

Figure 5-7. Cross-section of the model (viewed from the south-east, in between the doublets CWG and CLG) showing the bulk fracture permeability for HM5. White lines indicate the top of the Dinantian Carbonates and the Evieux Formation.

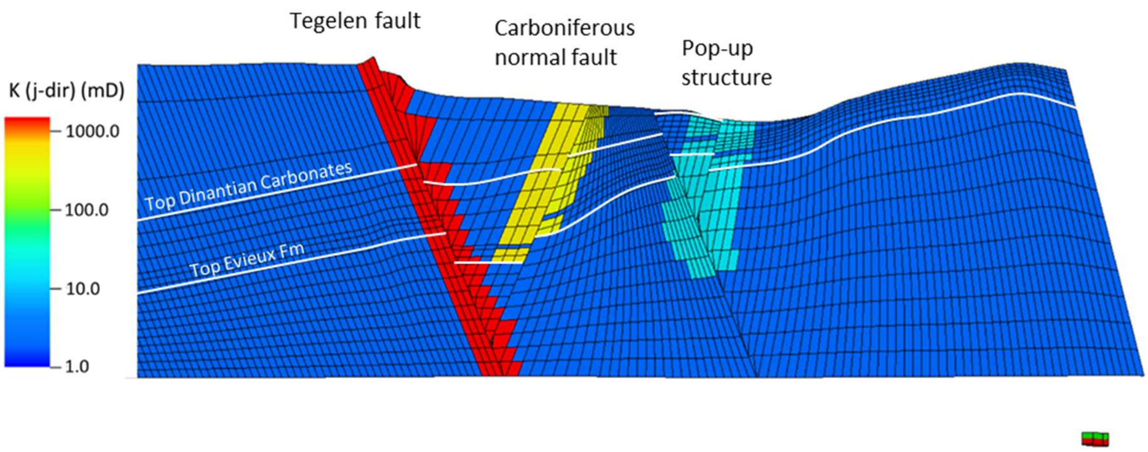

Figure 5-8. Cross-section of the model (viewed from the south-east, in between the doublets CWG and CLG) showing the bulk fracture permeability for HM8. White lines indicate the top of the Dinantian Carbonates and the Evieux Formation.

5.3.2 Results

Figure 5-9 shows the simulated and observed pressure at the four operational wells for the three history match scenarios. For all wells, the variability in the pressure is reproduced well, with the exception of the jumps caused by the ESP depth changes (see section 5.2.2 for explanation), the initial pressure in CAL-GT-01 (see discussion in the next paragraph) and the initial increase in injectivity in the injection wells. Please note that a possible increase in near-well permeability due to cooling was not implemented. Although the models differ in the permeability distribution, the resulting pressure behaviour in the wells is not very different because of the history match. The main differences occur in the reservoir.

Figure 5-10 shows the simulated and observed production temperature at CAL-GT-01 and CAL-GT-04. The simulated temperature is at bottom hole, whereas the observed temperature is at ESP depth. The simulated temperature in CAL-GT-01 is higher than observed, but the trend of the decrease in temperature is similar. A few degrees lower temperature at ESP depth can be expected due to cooling in the well. A jump in the observed temperature of CAL-GT-01 of about 2°C is visible in December 2014. This coincides with a change in the ESP pressure (see Figure 5-11 for a detailed representation of the pressure, temperature and flow rate at the ESP of CAL-GT-01 during this period). The increase in flow rate in Nov/Dec-2014 does not coincide with a decrease in pressure as happens in other periods. Instead there are a few jumps which might be caused by a shallower inflow zone opening up, possibly enhanced by the injection at CAL-GT-03. This change in inflow zones is not included in the numerical model. The history match is focused on the period after Dec-2014. It should be noted that due to the long open hole section of CAL-GT-01, the production temperature is strongly influenced by the distribution of the permeability along the well. The deepest part of the well produces from the damage zone of the Tegelen Fault, while at shallower depth the production comes from the damage zone of the Carboniferous Normal fault.

The thermal breakthrough in CAL-GT-01 is largely controlled by the fracture density, which is implemented in the simulations by means of the matrix-fracture interaction coefficient. For large fracture spacing (i.e. low matrix-fracture interaction coefficient), the cold water moves through the fractures fast, bypassing the matrix. For smaller fracture density, such as in the Devonian sandstones around CAL-GT-05, the heat exchange with the matrix is much larger and the thermal front in the fractures doesn’t reach as far. In the matrix, the cooled area becomes smaller but with lower temperature.

The variability in the temperature is less well reproduced in CAL-GT-04 than in CAL-GT-01. The variability is probably not well reproduced, because the flow behind the casing is not included in the model. Also when the well reopens at the start of April 2018 after a shut-in, the temperature has dropped by about 1 degree. Flow was reduced in CLG from 3 April to 10 May 2018, so the drop in temperature is not likely to be caused by that. Possibly a change in inflow zones occurred after the shut-in.

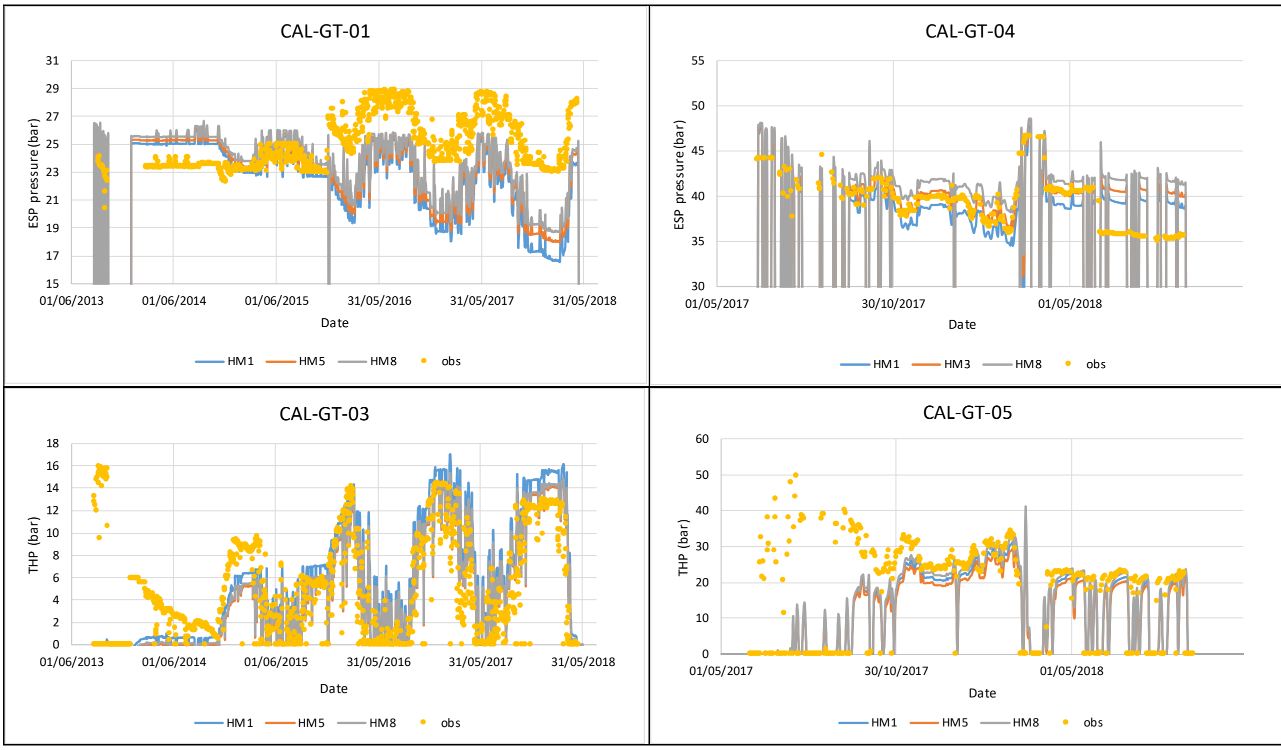

Figure 5-9. Results of the three history match scenarios HM1 (blue), HM5 (orange) and HM8 (grey) showing for the producers CAL-GT-01 and CAL-GT-04 the pressure at the ESP and for the injectors the pressure at the tubing head (THP). Yellow dots are the daily averaged observed pressures.

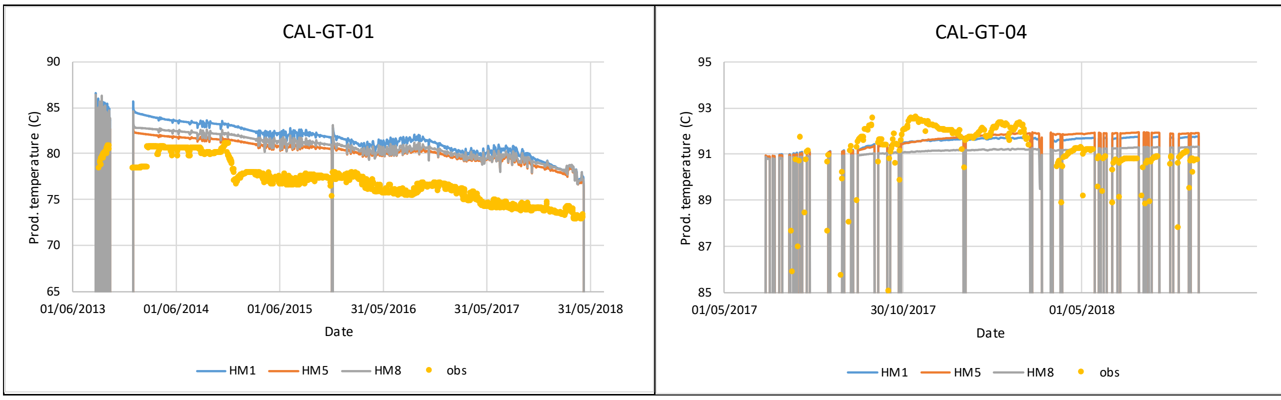

Figure 5-10. Results of the three history match scenarios HM1 (blue), HM5 (orange) and HM8 (grey) showing for the producers CAL-GT-01 and CAL-GT-04 the production temperature (°C). Yellow dots are the daily averaged observed temperature.

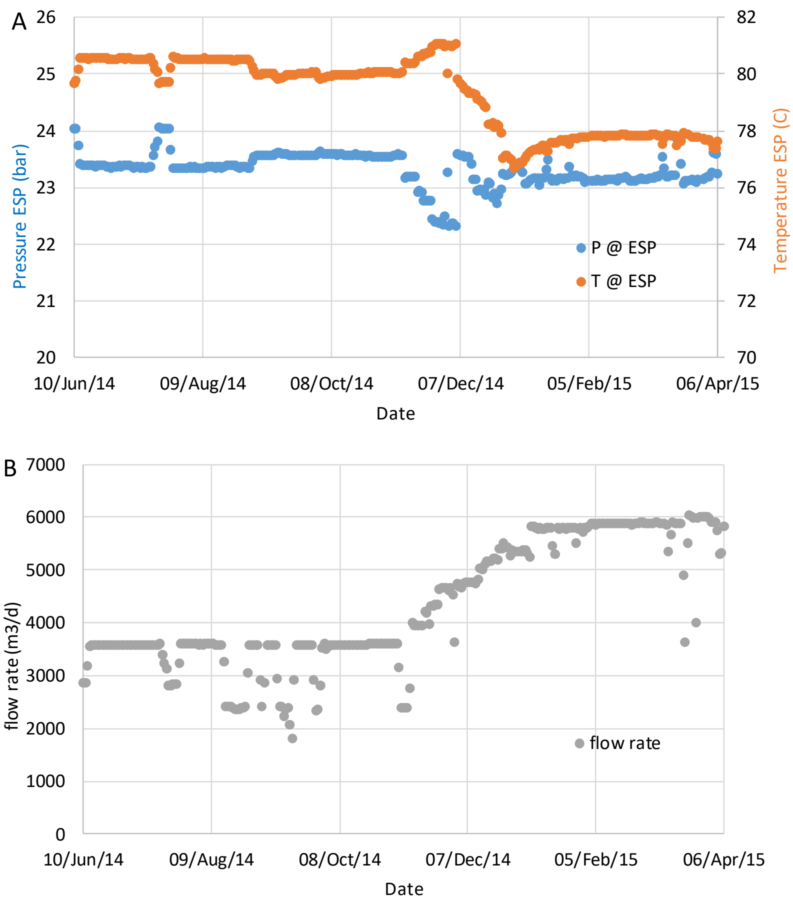

Figure 5-11 Details of the pressure and temperature at the ESP (A) and flow rate (B) for the period in December 2014 in CAL-GT-01 showing jumps in the temperature and pressure with an increasing flow rate.

<u>Permeability around the faults</u>

The permeability of the damage zone around the Carboniferous Normal Fault is consistently estimated to be lower than that of the damage zone around the Tegelen Fault in all three scenarios (Table 5-3, Table 5-4 and Table 5-5), which is consistent with the smaller offset of the Carboniferous Normal Fault. The permeability around the Carboniferous Normal Fault is controlled by the pressure in CAL-GT-03 and CAL-GT-01 and in the Tegelen Fault by the pressure in CAL-GT-04 and CAL-GT-01. The temperature in CAL-GT-01 is determined by inflow from both damage zones, which provides additional constraint on the relative contribution of flow from the two fault damage zones, reducing the uncertainty in the results. The lower temperature in CAL-GT-01 compared to CAL-GT-04 indicates clearly that a part of the flow should come from shallower depth. The position of well compared to the faults (e.g. Figure 5-2) shows that this is most likely the damage zone of the Carboniferous Normal Fault (hanging wall side). Alternatively, a high permeability layer at the top of the Dinantian carbonates could cause this inflow. However the good injectivity in CAL-GT-03 in combination with the PLT information that shows most inflow in the lower part of the Dinantian carbonates and the top of the Bosscheveld (Appendix E) supports the conceptual model with a damage zone rather than a layer with permeability. A layer with high permeability results in poor connectivity across the Carboniferous normal fault due to the fault off set. As mentioned earlier, if there is no connectivity across the Carboniferous normal fault, the injectivity of CAL-GT-03 is too low.

<u>Interference between the two doublets</u>
Due to their close proximity the doublets interfere with each other. This is particularly well visible in the temperature in CAL-GT-01 at the end of March 2018: when CAL-GT-04 reduces the production, the temperature goes up in CAL-GT-01 (Figure 5-12). This is probably caused by an increase in pressure in the damage zone of the Tegelen Fault from which CAL-GT-04 produces, increasing the inflow from the Tegelen fault to CAL-GT-01. This behaviour is well reproduced by the numerical models (Figure 5-12).

The drawdown due to CAL-GT-04 appears to be overestimated a bit in the models. Figure 5-13 shows the flow at CAL-GT-01 as a function of the pressure at the ESP. In the observed data, three different flow periods can be identified. The uppermost curve is the one after the ESP depth change. The blue dots give the behaviour of scenario HM8. For HM8, after the start of CAL-GT-04 the required drawdown increases for the same rate resulting in a lowering of the curve. This is less visible for the observed data: only 0.2 bar versus ~1 bar for the simulations. This could be due to an overestimation of the drawdown at CAL-GT-04, too much connectivity between CAL-GT-01 and CAL-GT-04 or too little pressure support for wither CAL-GT-04 or CAL-GT-01 or both.

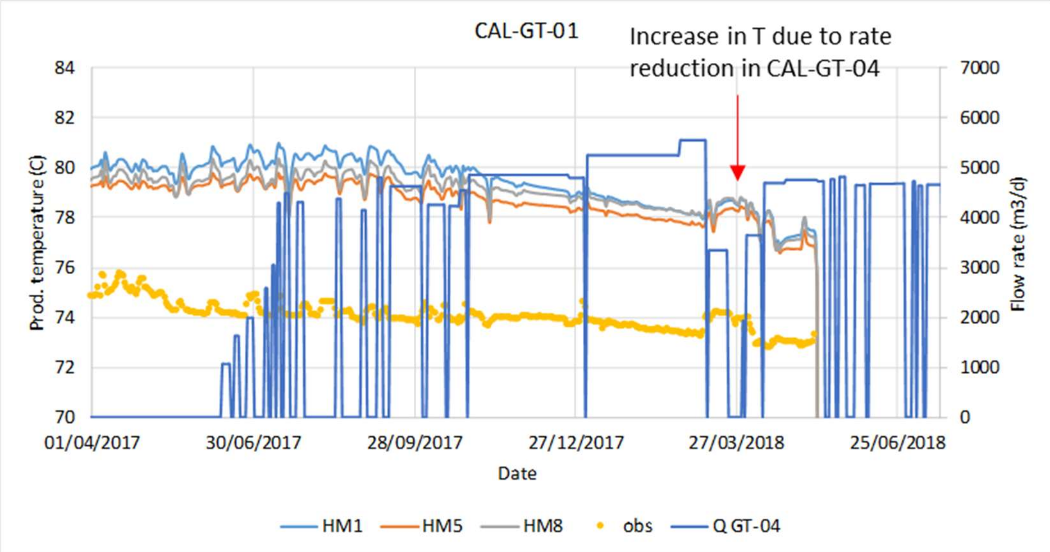

Figure 5-12. Production temperature of CAL-GT-01 (observed and for the three model scenarios) as in Figure 5-10 and the flow rate Q of CAL-GT-04 added (dark blue). Red arrow indicates the period with increased temperature due to a decrease in rate in CAL-GT-04.

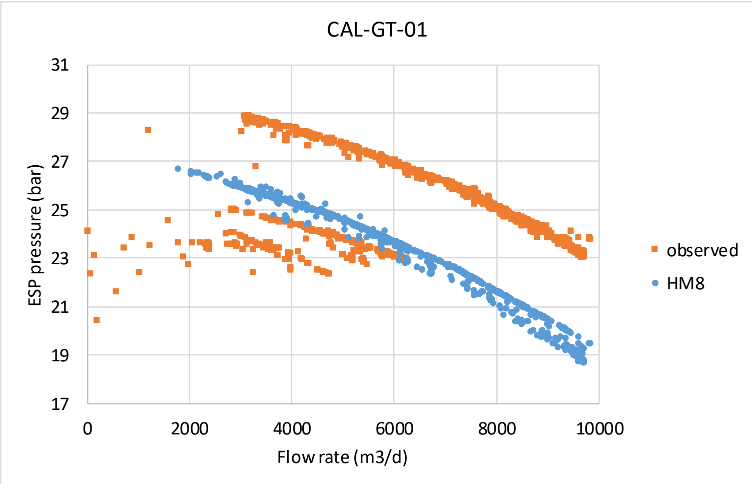

Figure 5-13. Performance curve of the ESP at CAL-GT-01 showing the pressure versus the flow rate: observed (red) and simulated for scenario HM8 (blue).

5.4 Simulations for the pilot phase

In support for developing operational scenarios for the pilot phase, simulations are done using the three history matched scenarios. The simulations give insight into the response time and interference between the wells in the models. Measurement of these characteristics will then allow to check the assumptions of the model. It should be noted that the model is not history matched for the short transient responses as they occur in well tests. The history match focused on the production data, because the model is too coarse to properly represent those transients. Transients are very sensitive to porosity and compressibility, but longer term behaviour not, so these values have not been matched in this project. Therefore a sensitivity has been run with smaller porosity to show the impact of this.

The reason to also simulate the interference between the wells, is that differences in interference can give information on the permeability orientation and possibly the presence of fault damage zones.

5.4.1 Description of the simulations

In the simulations we assume that the pilot phase will include three stages:

Stage 1 well testing: Focus is on testing the production behaviour of the individual wells and their interference. Results of the tests in practice can be used to understand the flow behaviour better and provide information to check and validate the geological and reservoir models. An important aspect of the reservoir model that might be validated during this stage is the dual-porosity behaviour and how it affects the long-term response. Another aspect is the interference between the wells. In the models in this study, wells that are located in the same fault(s) (CAL-GT-01 and CAL-GT-04 in Tegelen Fault and CAL-GT-05 and CAL-GT-02 in the pop-up structure) are hydraulically connected, but perpendicular to the faults is little connectivity. For CAL-GT-01 and 04 the connectivity has been shown historically. If a connectivity between CAL-GT-05 and 02 could be identified, this would provide support for the assumption that a fault is present which connects these wells.

Stage 2 ramp-up warm operations: For the second phase, we propose a longer test-period in which a doublet is slowly started up. We propose to start up with low rates with a temperature that is close to the reservoir temperature and slowly increasing rates with long (> 2 weeks) flow periods per rate. This will allow to fully stabilize the pressure in the flow periods and allow for monitoring of potential (micro-)seismicity.

Stage 3 ramp-up cold operations: In the third phase also a similar ramp-up of rates is proposed but now with cooling of the injected fluid to 40C. In this phase, the impact of the cooling on the injectivity and potential (micro-)seismicity in the vicinity of the well can be evaluated. Because the cooling of the matrix is more important for seismicity than the cooling of the fractures, this phase can potentially extend quite long.

Choice of the wells
Because the purpose is to learn more about possible faults near injectors, the focus lies on the area with CAL-GT-02 and 05. Simulations are run for the wells at both the CWG and CLG site, but most simulations for the pilot phase have been run with CAL-GT-04 and CAL-GT-05, because:

- CAL-GT-05 is located in the area of interest for which information is to be gathered.
- CAL-GT-05 the only operational injector since CAL-GT-02 is known to be inaccessible and CAL-GT-03 is known to be unsuitable as an injector due to the location near major faults.
- If CAL-GT-05 is used as injector, CAL-GT-04 is the most convenient production well.

Drilling of a new well or a side track for CAL-GT-02 as injector could be a possibility. Ideally such a new injector would be located away from any faults. However due to the uncertainty about fault locations, it will be very difficult to make sure that the new injector is not located near any faults. So even for a new well, it would need to be taken into account that it is near

a fault that was not seen on seismic data. Because the details of a possible new well are difficult to predict, most work was done with CAL-GT-05 as injector. The result are focused on more generic learnings rather than the details of CAL-GT-05.
The schemes for flow rates, production periods and shut-in periods for the simulations are summarized below. It is noted here that the actual values in practice may differ because of practical limitations. For example, initial injectivity in CAL-GT-05 was much lower, which was not included in the simulations. It is unknown what the injectivity will be when the well is opened again, so the flow rates might not be feasible. For the second and third stage, the values will also need to be based on the results of the first phase. We emphasize that the simulations are not meant as an overview of the tests to be done during a pilot phase, but to illustrate different options as a starting point for the pilot phase. The simulations also don't present an investigation of the value of the information provided by the different tests.

Simulations are run for the wells at both the CWG and CLG site. Although well CAL-GT-02 is currently not operational, we will use this well in our simulations to show its possible value for monitoring and for understanding the flow in the reservoir.

It should be noted that the models used in these simulations are too coarse for designing well tests and to fully represent the fast responses in the stage 1 runs.

The schemes for flow rates, production periods and shut-in periods for the simulations are summarized below. It is noted here that the actual values in practice may differ because of practical limitations. For example, initial injectivity in CAL-GT-05 was much lower, which was not included in the simulations. It is unknown what the injectivity will be when the well is opened again, so the flow rates might not be feasible. For the second and third stage, the values will also need to be based on the results of the first phase. We emphasize that the simulations are not meant as an overview of the tests to be done during a pilot phase, but to illustrate different options as a starting point for the pilot phase. The simulations also don't present an investigation of the value of the information provided by the different tests.

<u>Overview of the settings:</u>
<u>Stage 1: Test set 1:</u> test shut-in for well CAL-GT-05 (for history match scenario HM5)
- Using pre-production P and T
- 12 hr flow period with 4 wk shut-in (the long shut-in can be used to see when the pressure stabilizes and is not intended as a proposed shut-in time for field tests)
- 24 hr flow period with 4 wk shut-in
- 4 d flow period with 8 wk shut-in injection in CAL-GT-05 only
- 4 d flow period with 8 wk shut-in production/injection in CAL-GT-04/CAL-GT-05

<u>Stage 1: Test set 2:</u> interference/well test for each of the wells (for history match scenario's HM5 and HM8)
- Using pre-production P and T
- Produce/inject in each of the wells in turn during 1 full day followed by shut-in of 2 weeks (shut-in period will depend on the results of test set 1)
- Production from GT-01 and 04
- Injection in GT-02 and 05

Considering the goal of the tests and the short duration, no geomechanical simulations will be run for stage 1.

Settings for all runs in stage 1:
- Observe BHP and BHT in all 5 wells.

- Constant flow during the flow periods
- Downhole shut-ins
- Injection/production rate 180 m^3/hr
- Injection temperature 25°C (approximately surface temperature which is often seen in injection tests without simultaneous production)

Stage 2: Ramp-up warm operations
history matched scenario: HM5
Test: Long duration test in wells CAL-GT-04/05 (the same setup can be applied to CAL-GT-01/02)
- ramp-up flow with injection at approximate reservoir temperature (65°C); flow rates 180 – 210 – 240 m^3/hr, each flow period lasts 1 month
- Shut-in of 1 month

Stage 3: Ramp-up cold operations
history matched scenario: HM5
Test: Long duration test in wells CAL-GT-04/05 (the same setup can be applied to CAL-GT-01/02)
- ramp-up flow with injection at 40 C; flow rates 180 – 210 – 240 m^3/hr, each flow period lasts 1 month
- Shut-in of 1 month

The simulations from stage 2 and 3 will also be analysed geomechanically, which will be discussed in the following chapter.

5.4.2 Results

The first set of runs shows the response to different injection durations in CAL-GT-05 (Figure 5-14 and Figure 5-15 showing a zoomed in y-axis). The 4-day injection clearly shows that steady state has not been reached yet. The simulated shut-in after the 4-day injection is 8 weeks. It takes several weeks for the pressure to go back to pre-injection pressure which is visible in Figure 5-15. Figure 5-16 shows the pressure response in CAL-GT-02 as a result of the injection in CAL-GT-05. The response to the 12 hr and 24 hr injection is very small (< 0.1 bar). The 4 d injection results in a response of about 0.3 bar, which is small but might be large enough for monitoring. The response in the other wells is smaller than in CAL-GT-02, because CAL-GT-02 has the best hydraulic connection to CAL-GT-05 via the faults of the pop-up structure.

Two sensitivity runs were added. The 4-day injection run was also done with simultaneous production form CAL-GT-04, because in practice injecting the large volume associated with 4 days injection is difficult to achieve. The other is a run of 1 day injection at CAL-GT-04 with lower porosity to show the impact of this in the pressure transients, because the history match provided little information to constrain these properties. This model used for this sensitivity run has 1% matrix porosity below the Dinantian Carbonates instead of 5% and 0.5% fracture porosity instead of 1%. In Figure 5-16, which shows the response of CAL-GT-02 to injection in CAL-GT-05, these sensitivities have been added. Including production from CAL-GT-04 reduces the response in CAL-GT-02. For the decreased porosity, the response in CAL-GT-02 is much faster and larger. The late time behaviour is much more similar to simulations with larger porosity. This sensitivity illustrates that the results of the simulations for stage 1 should be interpretated in terms of trends rather than absolute values.

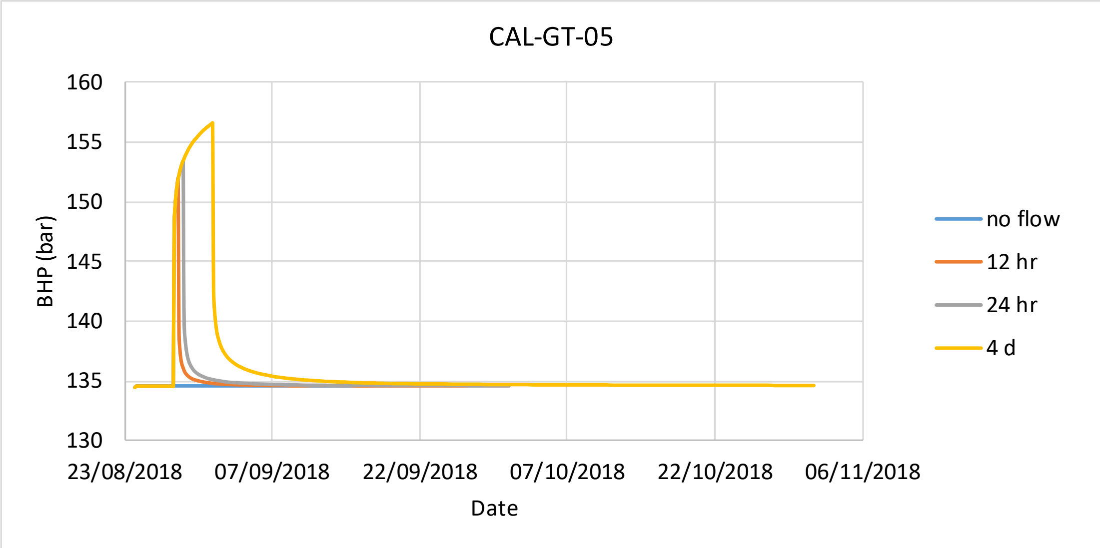

Figure 5-14 Bottom Hole Pressure (BHP) in bar in CAL-GT-05 as a result of injection of different durations (flow rate is 180 m^3/hr)

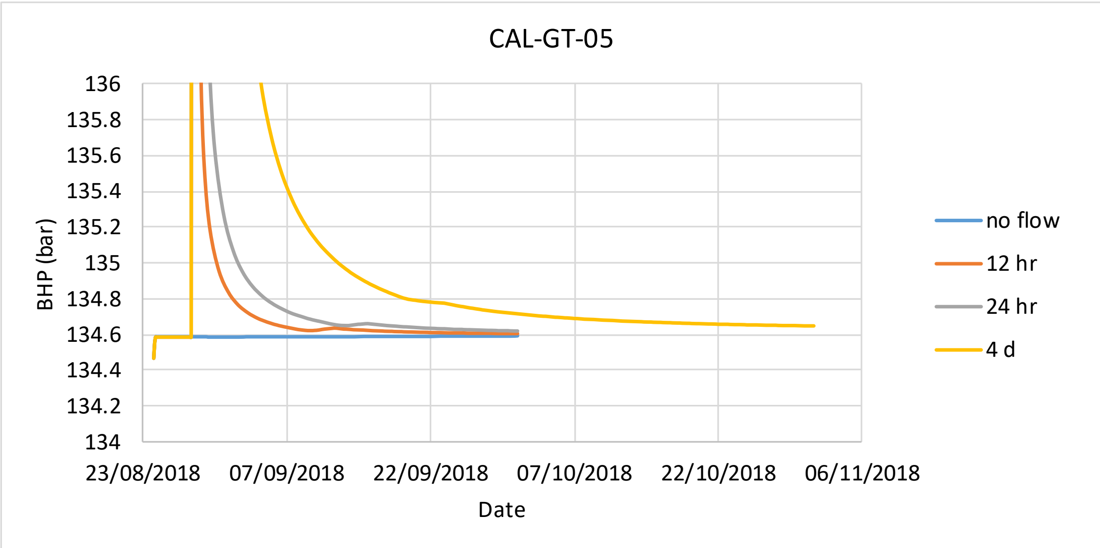

Figure 5-15 Bottom Hole Pressure (BHP) in bar in CAL-GT-05 as a result of injection of different durations (flow rate is 180 m3/hr) zoomed in to show more detail in the pressure.

The injection in CAL-GT-05 is not only visible in the pressure in CAL-GT-02 but also in the temperature. This can only be observed/simulated when the well produces. In simulations with model scenario HM5, the response is in the order of 1 degree for the 4-day injection period. However, for this to happen, the well not only needs to produce, but it needs to produce from a sufficiently long inflow zone to be influenced by the change in pressure in part of the inflow zone.

The impact of injection in CAL-GT-05 on CAL-GT-04 is small: ~0.04 bar from the 4-day injection at CAL-GT-05 for HM5, which is less impact than the maximum estimated interference (see section 5.3.1, max ~0.03 bar after a 28 hr test). From the 24 hr injection tests, the simulated impact was less than 0.01 bar. This is however sensitive to the porosity and pore volume compressibility that were used in the model. The sensitivity analysis with a reduced porosity showed a response of ~0.02 bar in CAL-GT-04 due to 24 hours of injection at CAL-GT-05.

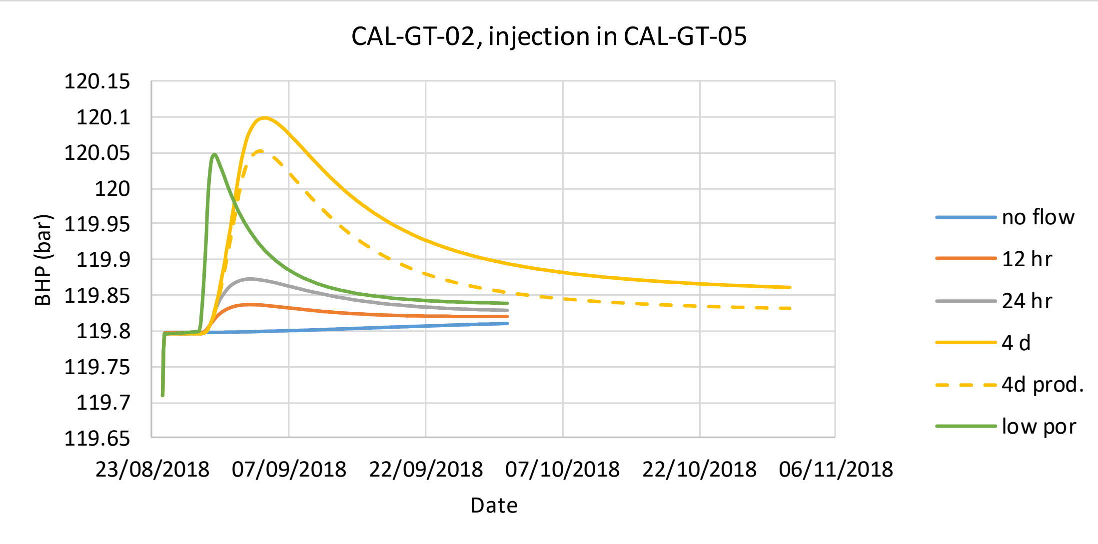

Figure 5-16 Response in the bottom hole pressure in CAL-GT-02 as a result of the injection in CAL-GT-05 for a duration of 12 hrs, 24 hrs and 4 days. Dashed line indicates a simulation with simultaneous production from CAL-GT-04. The green line represents the sensitivity run with reduced porosity.

The differences between the history match scenarios are not very large: HM5 shows more connectivity perpendicular to the faults and less along the fault than the other scenarios. In Figure 5-17 an example the influence of the history match scenario is shown. This shows the BHP in CAL-GT-02 for a 1-day injection in CAL-GT-05 for two scenarios: HM5 and HM8. Because this is along the fault, HM8 shows more response than HM5.

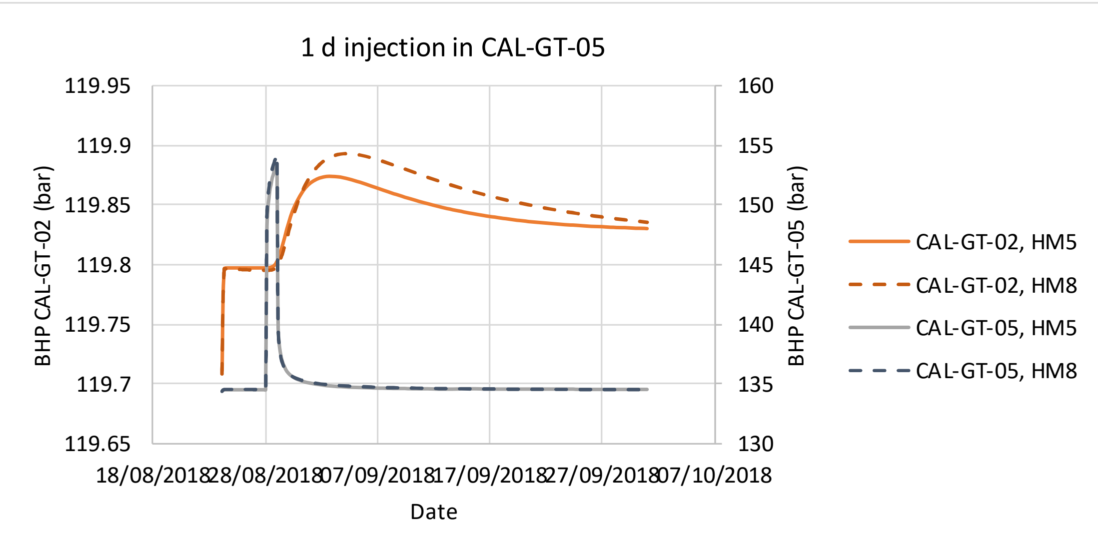

Figure 5-17 Response in the BHP in CAL-GT-02 (left axis) to 1 day of injection in CAL-GT-05 (BHP on right axis) for HM5 and HM8.

Results stage 2 and 3
For the stage 2 and 3, the simulations were done with scenario HM5. The simulations are restarted from the history match after a shut-in of around 7 years untill 1/1/2025. The cooling in the matrix hasn't dissipated much in this period, which is expected because the heat dissipation from the tight matrix has to happen via heat conduction. Because the cold was distributed quite far via the fractures, the temperature gradients are low: the cold 'bubble' is relatively diffuse compared to a single porosity system. It should be noted that bottom heat flow is not included in this model, so the heat recovery might be underestimated a little.

Figure 5-18 shows the bottom hole pressure during the cold injection. The results of the warm injection are not very different, except for the BHP in CAL-GT-05. Figure 5-19 shows the pressure in CAL-GT-01 and CAL-GT-02 in more detail. In both wells, the response is slow and not stabilized yet and is in the order of 1 bar for both. The impact on the faults will be discussed in the next chapter.

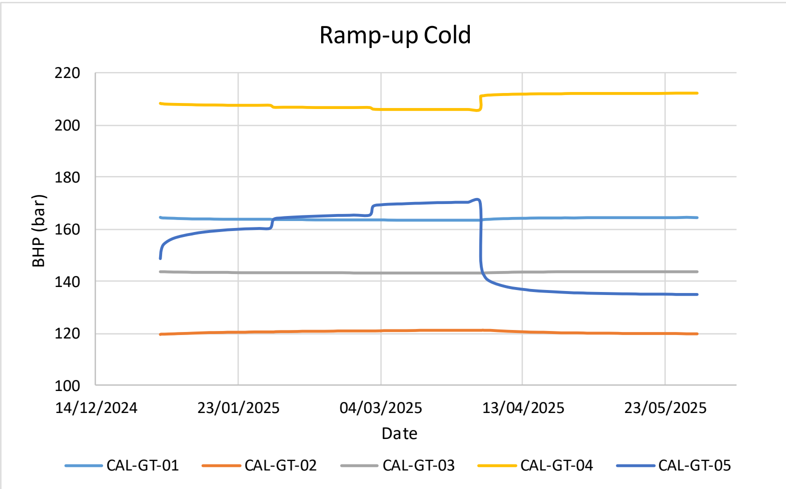

Figure 5-18 BHP in all five wells during a production-injection in CAL-GT-04 and 05. Injection temperature is 40°C. the flow rates increase from 180 to 210 and 240 m^3/hr.

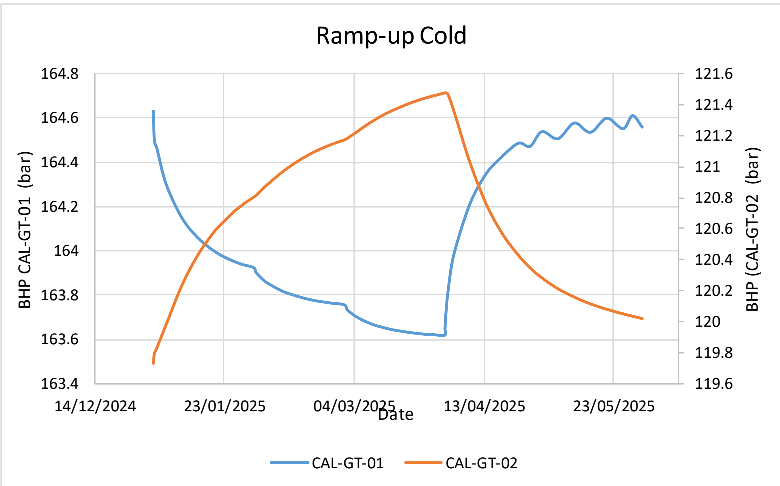

Figure 5-19 Response in the BHP in CAL-GT-01 and CAL-GT-02 during the ramp-up production/injection with cold injection.

5.5 Conclusions, discussion and recommendations

In this chapter, three scenarios were created for permeability and matched to the available observations of pressure and temperature in the wells. It was possible to match most of the observed behaviour with the assumption that permeability is mainly related to the faults. However, that does not mean that other scenarios are impossible. The permeability distribution cannot be fully constrained based on the pressure and temperature in the wells only. This means that there is still considerable uncertainty about the subsurface conditions. In addition, the evaluated scenarios are controlled by the geological interpretation. For a full characterisation of the uncertainty, also geological scenarios should be explored and a wider range in reservoir properties including heterogeneity and variability in the boundary and initial conditions.

However this does not mean that the uncertainty was not reduced. On some topics the history matching did improve our understanding:

- From the PLT information it is clear that the background permeability in many areas is low. PLT information shows zones of little to no inflow in both CAL-GT-03 and CAL-GT-05, which indicates low permeability. Satisfactory history matches were indeed achieved with the assumption that there is little permeability in most areas outside the fault damage zones.
- Some form of fracture flow or dual-porosity is necessary to match the temperature decrease in CAL-GT-01. For a single porosity medium, the cooling front stays close to the injection well CAL-GT-03, because the entire rock volume is cooled down.
- Some inflow, either from the top or bottom or from the sides, appears to be necessary to match the limited drawdown that CAL-GT-04 causes in CAL-GT-01, unless the permeability distribution is very different from what has been assumed here. This could be possible due to permeability related to karst outside of the fault damage zones. In particular this would require much more connectivity between CAL-GT-04 and -05 and much less between CAL-GT-04 and -01, neither of which is supported by the currently available information.

Some results of the simulations are very consistent for all scenarios:

- The cooling is mostly in the Carboniferous Normal Fault, because the well CAL-GT-03 intersects this fault and is parallel to it for a large part.
- The pressure changes in the Tegelen fault are not very large, because of the high permeability.
- The proximity of CAL-GT-05 to the Western pop-up fault causes cooling on these faults. Due to the assumption that the fracture distance is relatively small (smaller than near the Tegelen Fault and Carboniferous Normal Fault), the cooling of the matrix is larger but in a smaller area.
- The high injection pressure in CAL-GT-05 causes relatively large pressure changes on the pop-up faults.

Many of the sensitivity runs for the pilot phase showed small changes in the pressure and slow response times. This is a considerable challenge in practice. It will be very hard to observe these subtle changes, due to the long inflow zones, changes in temperature in the well and near-well area and geomechanical response of the fracture network. In addition, the long term behaviour is also very sensitive to boundary conditions, which may increase the difficulty of interpretation. It might therefore be beneficial to look at alternative ways to test the system. Examples could be:

- Thermal back production test
- Push-and-pull tracer tests

Further discussion on options for monitoring can be found in Chapter 9. It should be noted that the response does depend on the assumptions made in the models, in particular porosity and compressibility, which were not history matched.

Another aspect that might be useful to investigate is the variability in salinity. Salinity, like temperature, shows a strong relation with depth which is evident from Table 5-2. Measurement and simulation of the salinity could provide additional insight into the system. In addition the density difference due to differences in salinity could impact the water flow, in particular in areas with high vertical permeability such as the Tegelen fault.

6 Geomechanical and seismicity modelling

6.1 Introduction

In chapter 5 the spatial and temporal evolution of the pressures and temperatures around the two doublets of CWG and CLG are described. These variations in pressure and temperature induce stress changes in the reservoir rocks and along the faults intersecting the Californië sites. This chapter focuses on analysing the effects of pressure and temperature changes on the faults, specifically in terms of Coulomb stresses and potential fault reactivation. The geomechanical model uses input from both the history-matched and forward dynamic reservoir models. As a form of model validation, the results of the geomechanical simulations are compared to the main characteristics of the observed seismicity.

Main objective of the geomechanical model is to obtain insight into the mechanisms that drove induced seismicity during the past geothermal operations. A better understanding of the relations between operations, fault reactivation and seismicity during the past injection and production activities at both the CWG and CLG site can help managing seismic risks associated with future geothermal operations in Californië and other Dinantian geothermal sites in the Netherlands.

6.2 Model description

6.2.1 Model geometry, lithologies and faults and boundary conditions

In this project a numerical geomechanical model was developed using the commercial software FLAC3D (version 9.0, Itasca, 2024). Figure 6-1 shows the geometry of the geomechanical model in FLAC3D. The model dimensions are 5.6 km x 9.2 km x 4.5 km, exceeding the dimensions of the dynamic reservoir model, i.e. the FLAC3D geometry encompasses the entire Eclipse reservoir model, and also includes over-, under- and sideburden of the reservoir. The geometrical framework (layering and faults) of the geomechanical model are derived from the 3D geological Petrel model described in Chapter3. The geomechanical model includes the lithostratigraphical units of the Upper Carboniferous Coal Measures Group, the Carboniferous Limestone Group (Dinantian carbonates), the Pont d'Arcole and the (undifferentiated) underlying Bosscheveld and Evieux Formations (for further details on lithostratigraphy, refer to Chapter 3). In addition to these lithostratigraphical layers, the model includes four mapped faults, i.e. from west to east: the Tegelen Fault, the Carboniferous Normal Fault, the Western Pop-Up Fault and the Eastern

Pop-Up Fault (see Figure 6-1 and Figure 6-4). The faults have been included as contact elements (called 'zone joints') in FLAC3D with no thickness. Vertical no-displacement boundary conditions have been imposed on the bottom of the FLAC3D model. Horizontal no-displacement boundaries have been imposed on the vertical boundaries of the model.

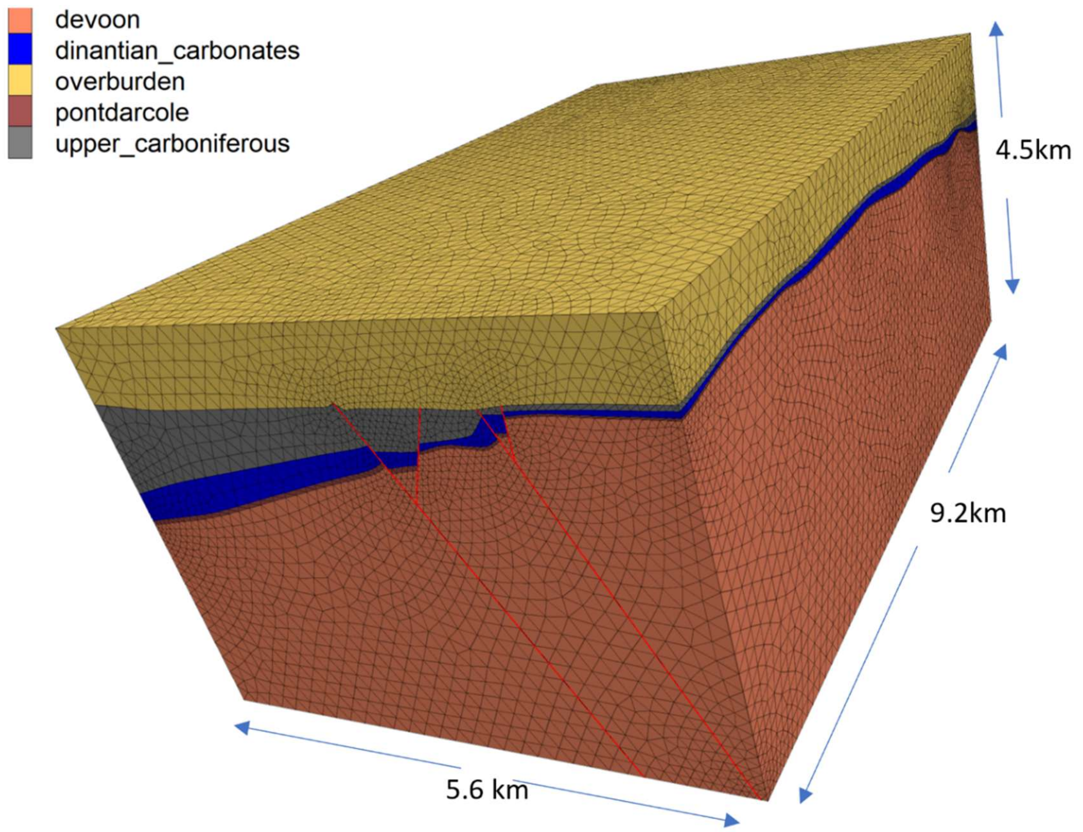

Figure 6-1. Geometry of the FLAC3D geomechanical model. The four faults (from left to right: Tegelen Fault, Carboniferous Normal Fault, Western Pop-Up Fault and Eastern Pop-Up fault) are shown as red solid lines.

6.2.2 Pressure and temperature input

The historical rates for the CWG and CLG doublets and the times and magnitudes of the seismic events recorded were shown in Figure 2-4. The historical data was used as input to the dynamic reservoir model. Pressure and temperature (P-T) fields as input for the geomechanical model were derived from both the global and detailed history-matching dynamic reservoir models. The resulting pressure and temperatures were interpolated and mapped onto the geomechanical mesh in FLAC3D. Three global history-matching scenarios were used as input, with their P-T fields sampled at three-months intervals between August 2013 and September 2018, and sampled yearly between January 2019 and January 2025. The period August 2013 to September 2018 covers the operational history of the CWG and CLG geothermal sites.

Simulation of the flow and temperature was done using a dual porosity approach. The dynamic reservoir model simulates fracture and matrix pressures and fracture and matrix temperatures. Section 6.2.5 describes how these parameters are used in the geomechanical model.

6.2.3 Geomechanical parameters and uncertainties

Limited site-specific geomechanical data is available for the Californië geothermal sites. Besides information on rock and fault parameters derived from general literature, the following sources / data were used for characterisation of the geomechanical properties of rocks and faults:

- Dynamic elastic parameters derived from sonic velocities in sonic well log in well CAL-GT-01
- Results from experimental work on Dinantian carbonate rock samples of other geothermal sites and quarries, E. Kane, pers. comm. (2024), Goense, T.(2018).
- TKI-SeiMod project: Data derived from well logs for the Balmatt geothermal site in Belgium and triaxial and acoustic data on samples derived from analogue material from quarries in Belgium (Wassing et al., 2022).
- Data on in-situ stress direction reported in Osinga et al. (2019) and magnitudes of stresses in Buijze et al., 2024 (submitted) and described in Hinzen (2003).

Table 6-1 summarizes the main parameters used as input for the geomechanical model. The model runs in FLAC3D are based on the assumption of fully elastic material behaviour for both the rocks and faults; i.e. no permanent plastic deformation in rocks or fault slip has been explicitly modelled.

No data is available in the public domain on the magnitude of the in-situ stress field at the Californië geothermal sites (Osinga and Buik, 2019). Based on the interpretations of 4-arm caliper logs and borehole image logs, Osinga and Buik (2019) derive a SHmax direction between 301° and 310° in the Dinantian rocks for well CAL-GT-01. Hinzen (2003) derived information on the in-situ stress field from fault plane solutions from earthquakes in the northern Rhine area, including the Lower Rhine Embayment which is located to the east of the Feldbiss Fault. They find that earthquake data from the Lower Rhine Embayment indicate a normal faulting regime. Injection tests in well CAL-GT-05 reveal a sudden increase injectivity from 3m3/hr/bar to 10m3/hr/bar at a surface pressure of 45 bara at surface level at an injection rate of 150m3/hr, which may be indicative of fracture opening when the minimum horizontal stress is exceeded (W. Botermans (Nappa), pers. comm., 2024, Figure 6-2). PLT data show an inflow zone between 1600 and 1850m TVD. Based on initial pressures modelled at those depths would translate into a minimum horizontal stress gradient of ~0.124 – 0.128 bar/m, which is on the low end of the stress gradients for the minimum horizontal stress reported in Bakx et al., 2019. It is noted that these stress gradients have not been derived by a standardized controlled minifrac or extended leak-off tests and may represent a lower bound of the minimum horizontal stress.

Table 6-1. Parameters used for modelling.

Parameter	Value
Bulk density (kg/m3)	2450 (2200 – 2650)[1]
Youngs modulus (GPa)	40 (20-70)
Poisson's ratio (-)	0.28 (0.2-0.3)
Biot coefficient (-)	1 (0.3-1) [2]
Thermal expansion coefficient (°C^{-1})	1.0e-5 (0.8-1.2)
Friction coefficient faults (-)	0.6 (0.6-0.7)[3]
Cohesion faults (MPa)	0[4]
Extensional stress regime	Sv > SHmax > Shmin[5]
Orientation Shmax	305°
Vertical stress - Sv	From density
Maximum horizontal stress – Shmax	1.1*Shmin [5]
Minimum horizontal stress - Shmin	0.59Sv [5]
Pressure, temperature	From dynamic reservoir model

[1] Range of densities with 2200 kg/m3 for overburden and 1700 kg/m3 for Dinantian carbonates and Devonian sandstones. As the focus is on stress changes only, the density does not affect the results – see also [5].

[2] A Biot coefficient of 1 is used, which gives a maximum poroelastic response. Carbonate rocks generally have a low Biot coefficient, Goense (2018) gives values between 0.4-1.0 for the Dinantian carbonates. Biot coefficients of the Devonian sandstones have not been tested. A recent publication by De Simone et al. (2023) suggests Biot coefficients largely vary with the fracture orientation and density.

[3] Friction coefficients of the Dinantian carbonates lie between 0.6 – 0.7 (E. Kane pers. comm, 2024).

[4] Worst case scenario of cohesionless fault

[5] Absolute magnitude of the in-situ horizontal principal stress is unknown – focus of the current analysis is on Coulomb stress *changes,* not on absolute stress magnitudes, and assumptions on absolute magnitudes of the principal in-situ stresses will not affect the Coulomb stress changes calculated – values are used to initiate extensional stress conditions. Tectonic stress regime assumed is extensional, with a direction of SHmax of 305°).

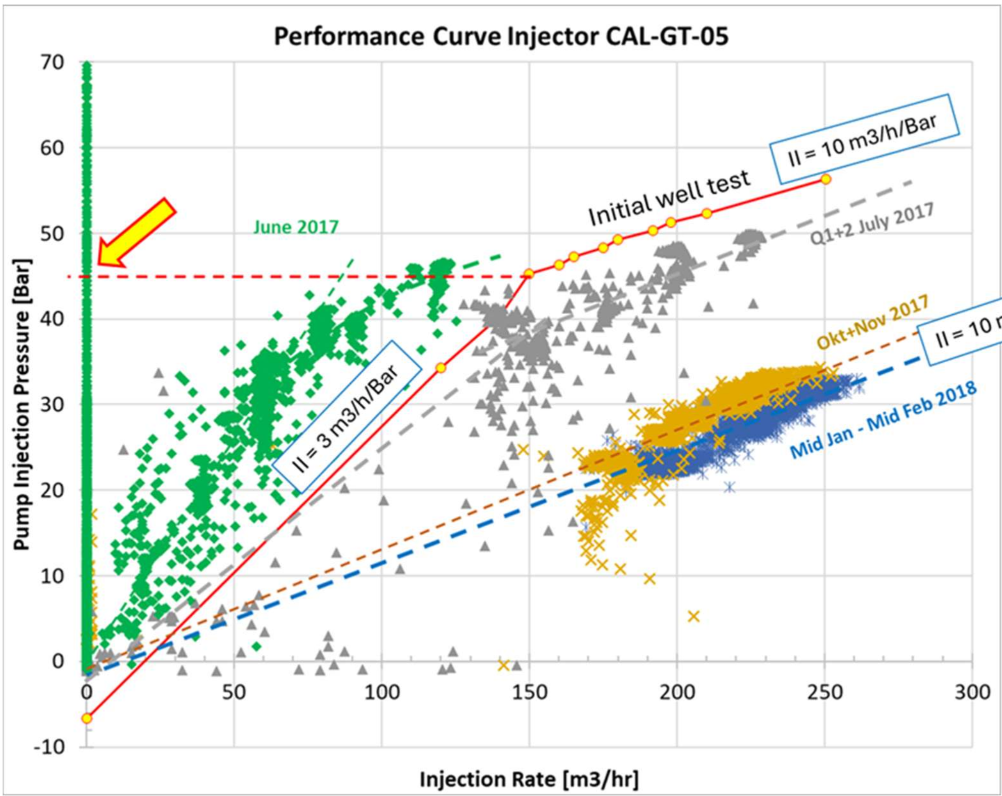

Figure 6-2. Relation between Injection pressure and injection rate, injectivity for well CAL-GT-05. Pers. comm and courtesy of W. Botermans (Nappa), 2024.

In this study, focus is on Coulomb stress changes, assuming an extensional tectonic regime and an SHmax orientation of 305°. As no analysis of failure or fault slip is performed, the absolute magnitudes of the initial principal stresses Sv, SHmax and Shmin will not affect the Coulomb stress changes calculated.

6.2.4 Historical seismicity

Results of geomechanical simulations are compared to observations and general characteristics of historical induced seismicity. The main characteristics are summarized below:

- A correlation is observed between reductions in flow rate during operation of the CWG doublet and seismicity
- The main event occurred 6 days after shut-in of the CLG doublet at the end of August 2018
- All but one earthquake cluster to the east of Carboniferous Normal Fault, near well CAL-GT-03 (see Figure 4-8 and Figure 4-9)
- The Ml 0.2 seismic event of August 25, 2018 falls outside this cluster. For this event different hypocenter locations are interpreted by Q-con and TNO. Based on the earlier Q-con analysis the M0.2 plots close to Carboniferous Normal fault, whereas based on the recent TNO analysis the event plots relatively close to well CAL-GT-05 (and potentially the Western Pop-Up Fault) – see Figure 4-8 and Figure 4-9).
- Mean hypocenters of the seismic events lie between -2215 m and -3388 m depth, which is in the Devonian sandstones, but error bounds for vertical depths are significant (Figure 4-7).

Table 4-2 gives an overview of the seismic events at the Californië site, relocated based on the new velocity model developed in this study (see also section 4).

6.2.5 Geomechanical analysis

To further the understanding of the driving mechanisms for induced seismicity, four mechanisms that contribute to fault loading were distinguished (see also Figure 6-3):

1. Pore pressure diffusion (so-called direct pressure effect) – the initial normal and shear stress that act on a fault plane depend on the magnitude of the tectonic stress and the fault's orientation. In case of a fractured rock mass like the Dinantian carbonates, fractures are expected to dominate fluid flow and diffusion. When pressure at the fault plane increases, such as from fluid injection, the effective normal stress on the fault decreases, bringing the fault closer to failure.

2. Poroelastic stressing – Pressure changes in the fractures and matrix induce volumetric strains, resulting from fracture deformation and contraction or expansion of the rock matrix. This volume change alters the stress within the rock mass affected by pore pressure variations, as well as in the surrounding rocks.

3. Thermoelastic stressing – in case of injection of cold water, the temperature decrease in the rocks leads to shrinking of the rock mass. The volume change due to cooling affects stresses inside the cooled volume as well as in the surrounding rocks.

4. Stress transfer by seismic and aseismic (creep) slip – Fault slip, whether seismic or aseismic (creep), reduces the average shear stress on the slipping fault and redistributes stress to nearby fault segments or surrounding areas. As a result, some segments become more critically stressed, while others become less critically stressed.

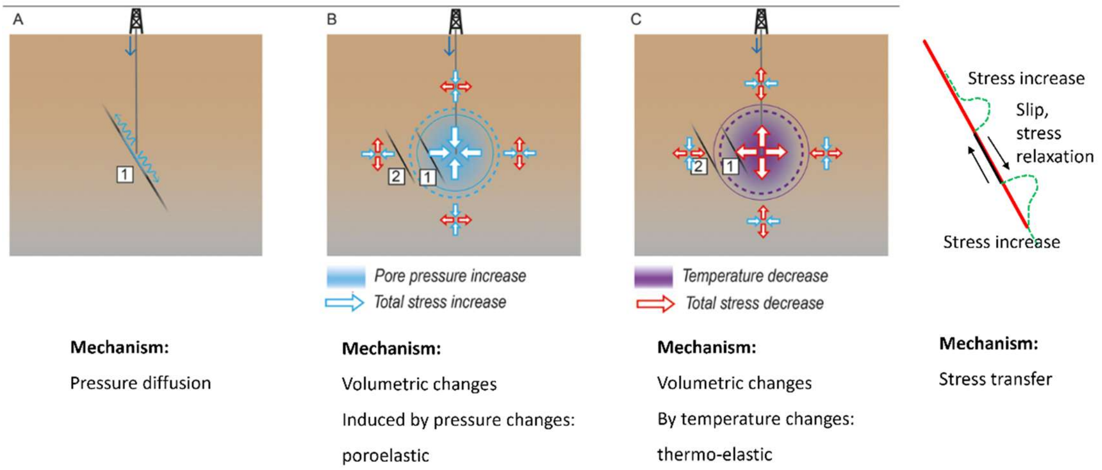

Figure 6-3. Schematic presentation of 4 mechanisms of pressure diffusion, poroelasticity, thermo-elasticity and stress transfer. Adapted from Buijze et al., 2019.

For the analysis of fault stability both Coulomb stress and Coulomb stress change on the four faults are computed as a proxy for the potential destabilization, reactivation and seismicity potential of the faults. Coulomb stress (τ_{cs}) and Coulomb stress change ($\Delta\tau_{cs}$) are defined respectively as:

$$\tau_{cs} = \tau - \mu\sigma'_n = \tau - \mu(\sigma_n - Pf)$$
$$\Delta\tau_{cs} = \Delta\tau - \mu\Delta\sigma'_n = \Delta\tau - \mu\Delta\sigma_n + \mu\Delta Pf$$

with symbol Δ denoting a change, τ is shear stress, σ_n is total normal stress on the fault (compressive stress is positive), σ'_n is effective normal stress on the fault, μ is friction coefficient of the fault and Pf is the pore pressure in the fault (i.e. fracture pressure from the dual porosity model in Eclipse). It is noted here that a maximum shear stress is used in the analysis, i.e. no distinction is made between the along-strike or dip-slip components of the shear stress. A negative Coulomb stress means that a fault is stable, a Coulomb stress >= 0 means that fault strength is exceeded; whereas a positive or negative Coulomb stress *change* indicates that the stress on that fault segment follows a destabilizing path, respectively stabilizing stress path moving the stresses on the fault towards, respectively away from the failure envelope.

The components on the right-hand side of both equations provide insight into the contribution of the four mechanisms to fault loading. The first two components represent the cumulative effects of changes in shear and normal stress due to poroelastic and thermoelastic stressing as well as stress transfer mechanisms; the component μP accounts for the direct pressure effect resulting from pressure diffusion into the faults.
The modelling approach described is one-way coupled, meaning that pressure and temperature fields are utilized to derive geomechanical stress changes, but these stress changes do not affect pore pressures and do not cause permeability changes due to the opening and closure of fractures.

Additionally, the dynamic reservoir model in Eclipse is run in dual-porosity mode, yielding pressure and temperature outputs for both fractures and matrix rocks. Conversely, the geomechanical model in FLAC3D operates with a single pressure and temperature field.

In our model fracture pressures are employed to compute effective stresses on the faults, while matrix pressures are utilized to assess poroelastic stress changes resulting from the deformation of the bulk rock mass due to pressure variations. Cold fluids in the faults (represented by the fracture temperature from Eclipse) cause a slow but progressive cooling of the walls of the faults and consequently a change in stress in the matrix rock, which influences the normal and shear stress on the fault. Matrix temperatures are used to assess the thermoelastic deformation of the bulk rock mass and thermal stress changes.

Although this simplified one-way coupling does not capture the fully-coupled response of fractured rocks, we believe that this simplification is justified given the uncertainties in geology and reservoir dynamics, and it still provides valuable insight into the mechanisms that may have contributed to the seismicity observed at the Californië geothermal sites. The limitations of this approach are further discussed in section 6.3.

6.2.6 Model results

We analyse the evolution of pressure, temperature and stress at the four individual faults (see Figure 6-4) within the model.

Note: In the results section pressures are mentioned in bar, to keep consistency with the reservoir section. For stresses also MPa is used, particularly when reference is made to the figures or stress changes are very small. 1 bar = 0.1 MPa.

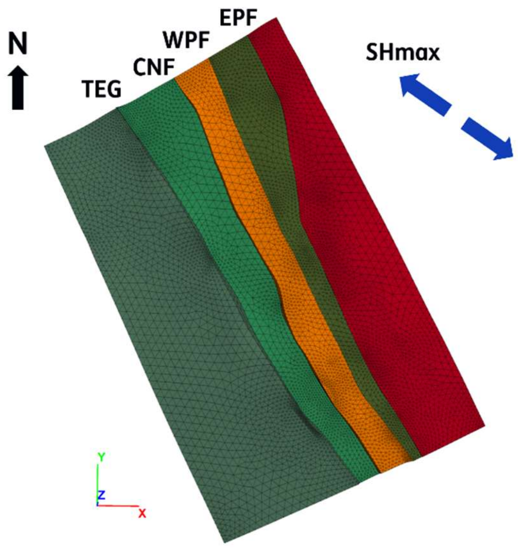

Figure 6-4. Top view of the Tegelen (TEG), Carboniferous Normal Fault (CNF), Western Pop-up Fault (WPF) and Eastern Pop-up Fault intersecting the top of the Dinantian reservoir. Blue arrows indicate direction of maximum horizontal stress SHmax.

6.2.7 Coulomb stressing on the Tegelen Fault

Figure 6-5 presents the change in pore pressure, temperature and Coulomb stress on the Tegelen fault, based on history-match scenario 8 (HM8) of the dynamic reservoir model. The results for the other history-match scenarios are presented in the Appendix G.
Figure 6-5a shows a maximum pressure drop (as compared to the initial undisturbed situation) of 1 to 2 bar at the Tegelen fault in January 2018, due to the simultaneous production from wells CAL-GT-01 and CAL-GT-04, with well CAL-GT-04 having a significant impact. The simulated maximum temperature decrease in the matrix rocks at the fault is about -1.2°C (compared to the initial undisturbed situation), driven by the extraction of cold water by CAL-GT-01 from shallower levels and breakthrough of the cold water injected in CAL-GT-03. The small increase in temperatures near CAL-GT-01 is attributed to the production of warmer water from deeper levels (Figure 6-5b).
Figure 6-5c shows the Coulomb stress changes on September 3, 2018, at the timing of the main event shortly after the CLG-doublet was shut-in, with maximum changes (as compared to initial conditions before the start of production) remaining below 2 bar.
Figure 6-5d shows the difference between Coulomb stress at shut-in (28-08-2018) and on September 3, 2018, during the Ml 1.7 event. The shut-in of production well GT-04 caused a slight increase in Coulomb stresses over the fault, with a maximum increase of

approximately 0.4 bar observed near production well GT-04. Coulomb stress changes after shut-in in the area of the CWG doublet are very small (<= +0.3 bar).

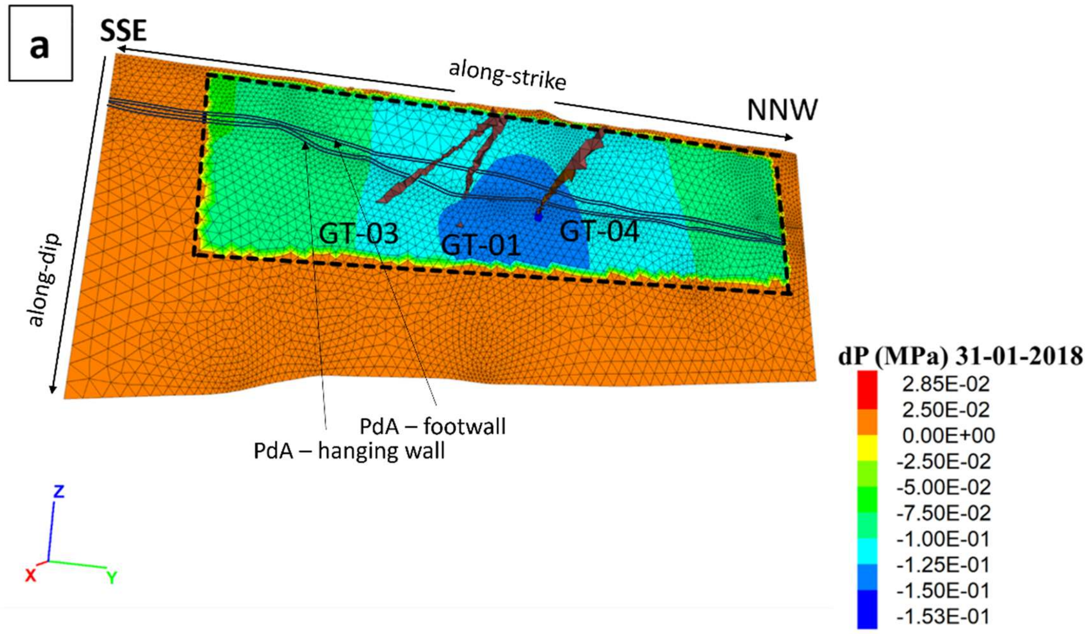

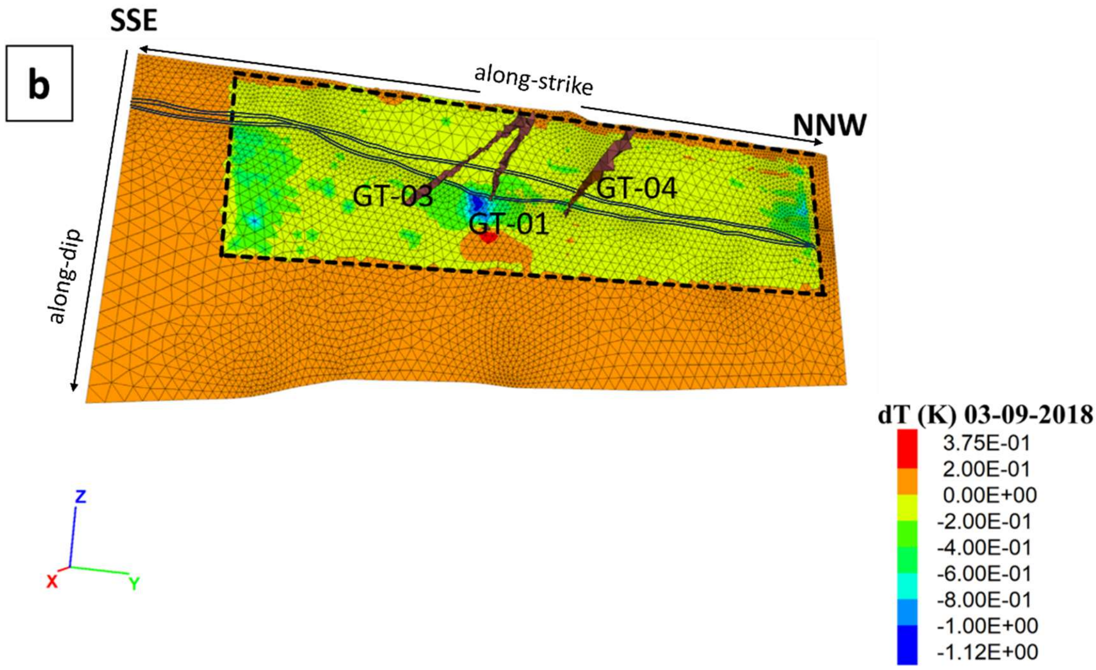

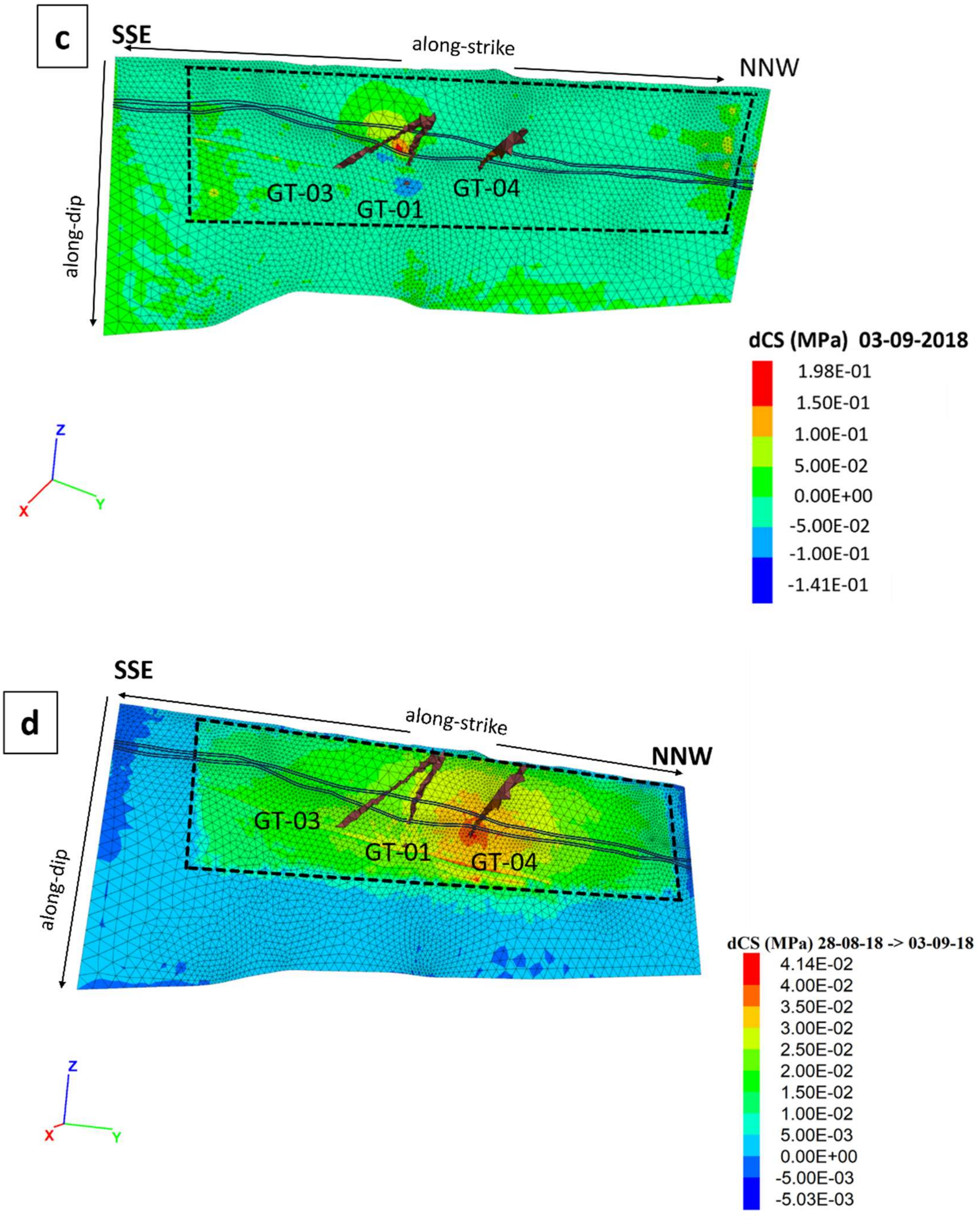

Figure 6-5. Pressure and stress on the Tegelen Fault. a) Pressure change in the fault 31-01-2018 as compared to initial conditions, black dashed line indicates dimensions of dynamic reservoir model b) temperature change at the fault 03-09-2018 as compared to initial conditions, c) Coulomb stress change on the fault at 03-09-2018 as compared to initial conditions, d) Coulomb stress change between 28-08-2018, just before the final shut-in of the CLG doublet and the time of the Ml 1.7 seismic event at 03-09-2018. Dark blue lines indicate depth of intersection with the Pont d'Arcole Formation.

Figure 6-6 illustrates the temporal evolution of temperatures, pressures, and stresses at the fault, sampled at three-monthly intervals. Sampling intervals are selected such that peaks in pressure changes within a month are captured.

Figure 6-6a plots the temperature changes on the Tegelen Fault at the location of maximum temperature decrease near production well CAL-GT-01, where a gradual cooling occurs until late summer 2018. After shut-in of the CLG doublet at August 28, 2018 (point 5) some additional cooling of the matrix rocks occurs, which is mainly due to the equilibration of temperatures between fractures and the matrix rocks. The cooling results in thermal contraction, leading to a decrease in normal stress that destabilizes (a small segment of) the fault, as indicated by the black line in Figure 6-6b. The unclamping due to cooling contributes positively to the Coulomb stress (red line). (Note that in the plot a decrease in normal stress is presented as a positive contribution and an increase in normal stress is presented as a negative contribution to Coulomb stressing, see also the equations in section 6.2.5). Coulomb stresses on the fault increase gradually, reaching a value +1.8 bar end of August 2018 (point 5).

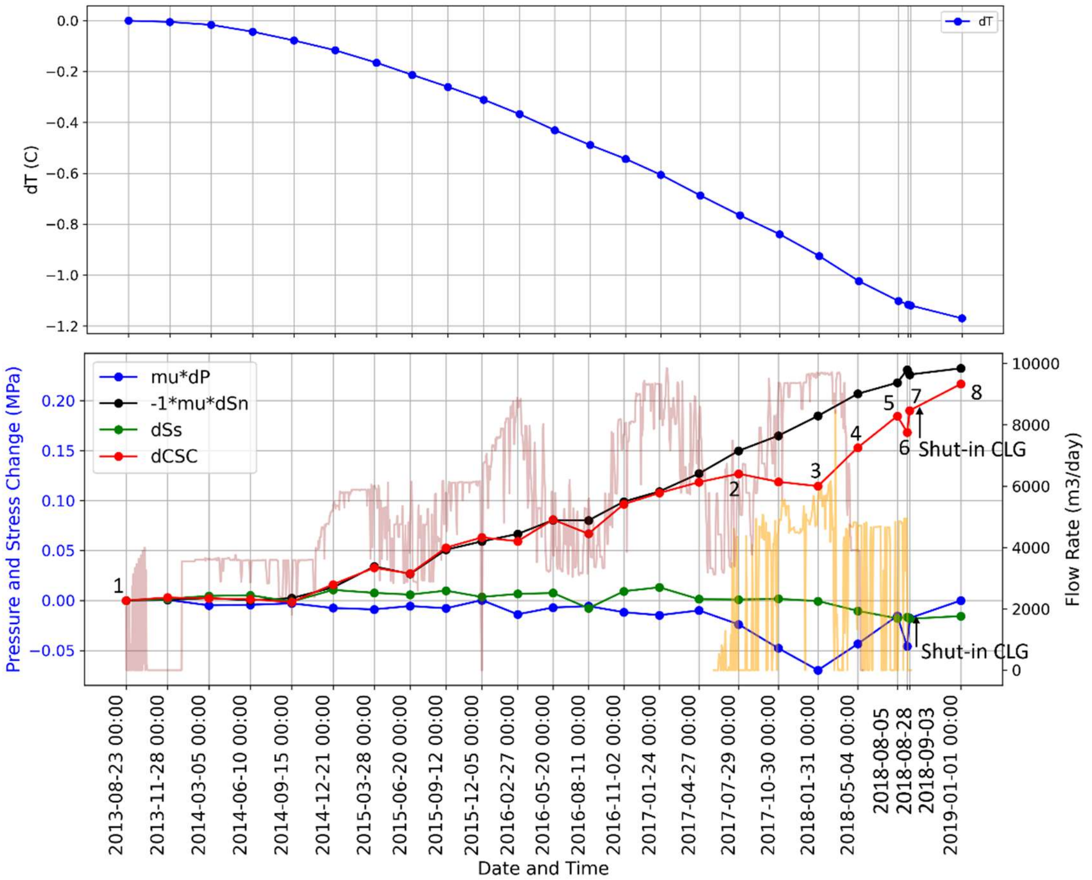

Figure 6-6. Temporal evolution of pressure, temperature and stress on the Tegelen Fault, at three-monthly resolution: a) maximum temperature change versus time (monitored at location of maximum temperature change, see also Figure 6-5c for spatial distribution), b) contributions of pore pressure (blue line), total normal stress (black line) and shear stress (green) to Coulomb stressing at the Tegelen Fault. Light brown and grey line in the background presents flow rates at CWG (well GT-03), light orange line at the background represents flow rates at CLG (well GT-05). Effect of shut-in on pressure and Coulomb stress indicated. meaning of points 1-8 explained in the text above.

Figure 6-6b shows that after start of the CWG-doublet in August 2013 (1) pressure in the fault (blue line) decreases and stabilizes relatively quickly. In June 2017 the CLG doublet is started (just before point 2). As the production well of CAL-GT-04 produces from the Tegelen Fault zone, the pressure in the fault further reduces, resulting in a reduction of the Coulomb stress and providing some stability to the fault - especially in winter 2018, when production rates are relatively high (point 3). May 2018 (just before point 4) the CWG-doublet is shut-in and pressure increases (abruptly, though this doesn't show in the current plot due to the sampling interval).

Production rates in the CLG doublet are relatively low between 4-5 (August 5, 2018). Both effects result in an increase of Coulomb stresses. At the end of August (5-6) production rates in the CLG doublet are relatively high again for a short period, and pressure decreases, resulting in a decrease of the Coulomb stresses, providing some additional stability to the fault. August 28, 2018 (6) the CLG-doublet is shut-in; due to the sudden shut-in an abrupt pressure increase occurs, resulting in a sudden, though minor, rise in Coulomb stresses (~+0.3 bar) (7). In January 2019 pressure (and before – but not visible because of the sampling interval) is back to the initial value (8). The increase of the Coulomb stress between 3 September, 2018 and January 2019 (7-8) can be attributed to the increase of pressure back to initial pressures and the equilibration of temperatures between fractures and the matrix rocks.

The general trend of the Coulomb stress in Figure 6-6 is primarily dominated by cooling and closely follows the temperature trend, though small variations are caused by pressure variations and associated poroelasticity (expressed as the small variations in the normal and shear stress).

6.2.8 Coulomb stressing on the Carboniferous Normal Fault

In a similar manner, the spatial and temporal evolution of pressure, temperature and Coulomb stress was analysed for the Carboniferous Normal Fault.

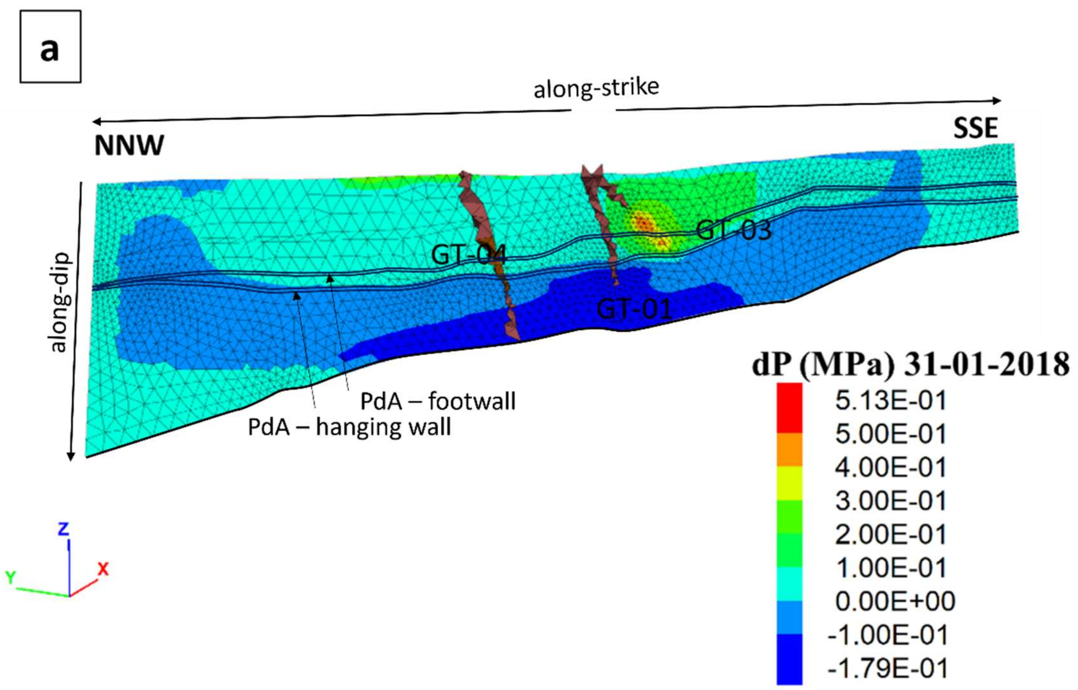

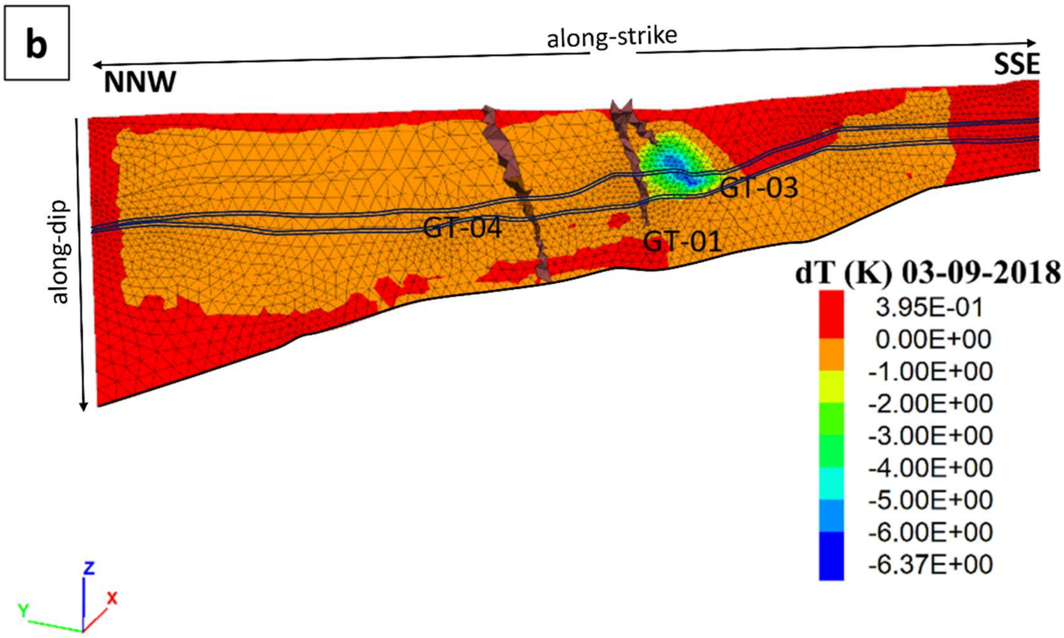
b
along-strike
NNW
SSE
along-dip
GT-04
GT-03
GT-01
dT (K) 03-09-2018
3.95E-01
0.00E+00
-1.00E+00
-2.00E+00
-3.00E+00
-4.00E+00
-5.00E+00
-6.00E+00
-6.37E+00
Z
Y
X

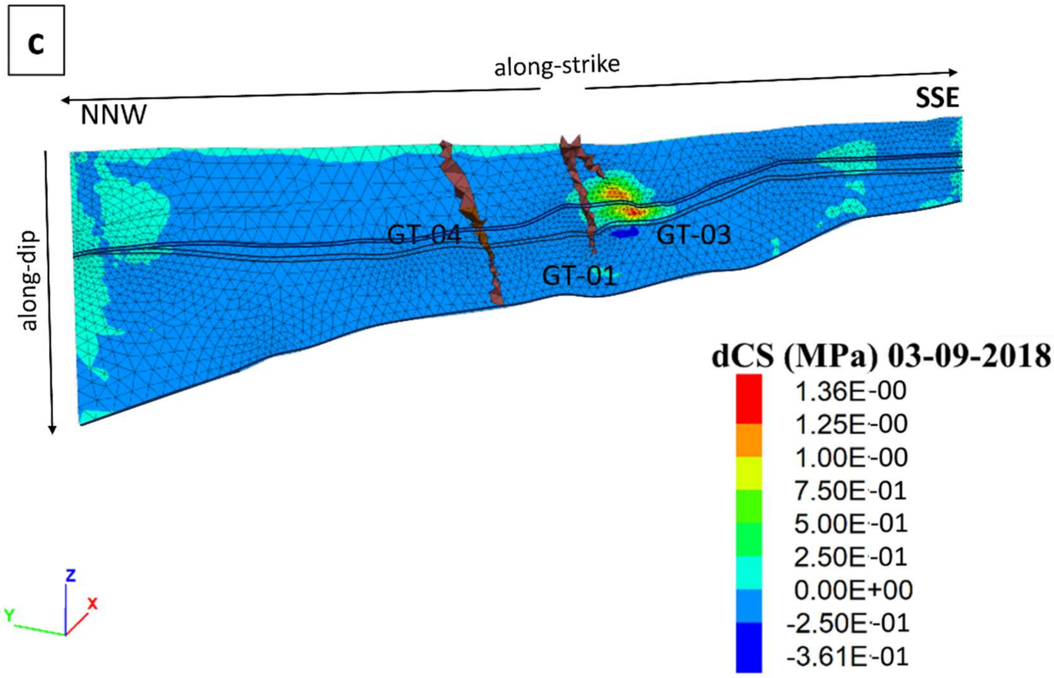
c
along-strike
NNW
SSE
along-dip
GT-04
GT-03
GT-01
dCS (MPa) 03-09-2018
1.36E-00
1.25E-00
1.00E-00
7.50E-01
5.00E-01
2.50E-01
0.00E+00
-2.50E-01
-3.61E-01
Z
Y
X

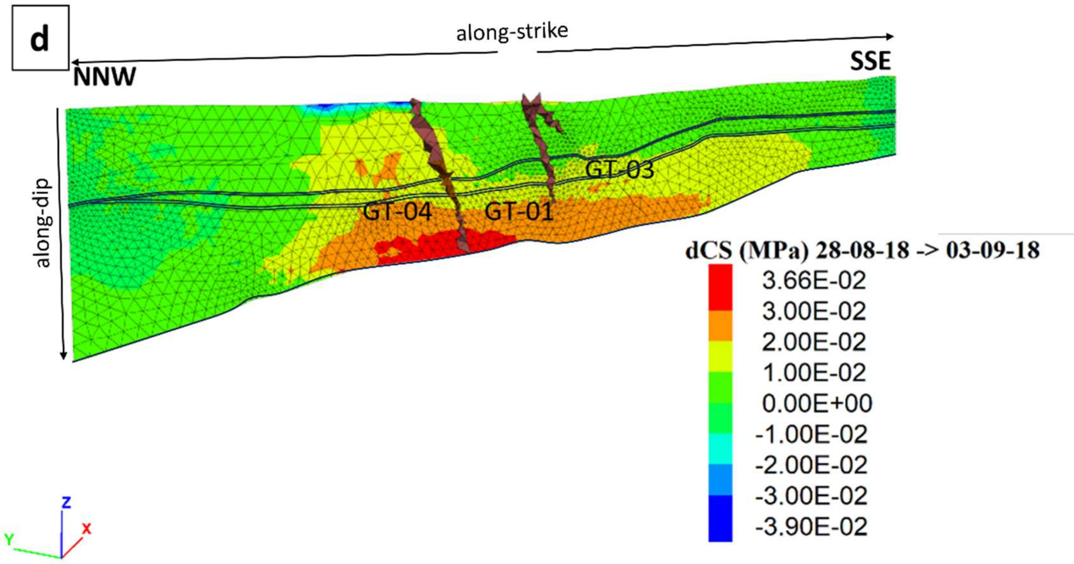

Figure 6-7. Pressure and stress on the Carboniferous Normal Fault (CNF). a) Pressure change in the fault 31-01-2018 as compared to initial conditions, b) temperature change at the fault 03-09-2018 as compared to initial conditions, c) Coulomb stress change on the fault at 03-09-2018 as compared to initial conditions, d) Coulomb stress change between 28-08-2018, just before the final shut-in of the CLG doublet and the time of the Ml 1.7 seismic event at 03-09-2018. Dark blue lines indicate depth of intersection with the Pont d'Arcole Formation. The bottom of the fault intersects with the Tegelen Fault.

Figure 6-7 illustrates the spatial changes in pore pressure, temperature and stress on the Carboniferous Normal Fault, derived from scenario HM8 of the dynamic reservoir model. Figure 6-7a shows a maximum pressure increase of approximately 5 bar on January 31, 2018, near injection well CAL-GT-03, while the lower section of the fault experiences a pressure drawdown of up to 2 bar due to fluid extraction from wells CAL-GT-01 and CAL-GT-04. Figure 6-7b indicates a local temperature decrease of over 6°C resulting from the cold fluid injection at CAL-GT-03.
Figure 6-7c demonstrates a maximum change in Coulomb stress of up to 1.3 MPa (13 bar) on September 3, 2018, shortly after the CLG doublet shut-in (with an additional increase in Coulomb stress due to temperature equilibration between fractures and matrix after shut-in of the CLG doublet). Figure 6-7d compares Coulomb stress at shut-in (August 28, 2018) to September 3, 2018, the time of the Ml 1.7 event. The shut-in of well GT-04 leads to a rapid increase in Coulomb stresses, with a maximum increase of approximately 0.4 bar at deeper fault segments and changes of +0.1 to +0.2 bar in the shallower sections affected by prior cooling.

Figure 6-8 depicts the temporal evolution of temperature, pressure, and stress at the fault, sampled at three-month intervals at the location of maximum cooling (Figure 6-8a) and Coulomb stress increase (Figure 6-8b). The injection into well CAL-GT-03 raises pressures in the shallow fault segment until May 2018 (point 1 to just after point 4), when the CWG doublet is shut in (Figure 6-8b, blue line). Temperatures in Figure 6-8a show continuous cooling until late summer 2018, with a continuation of matrix cooling due to equilibration of temperatures after shut-in (point 6-8).

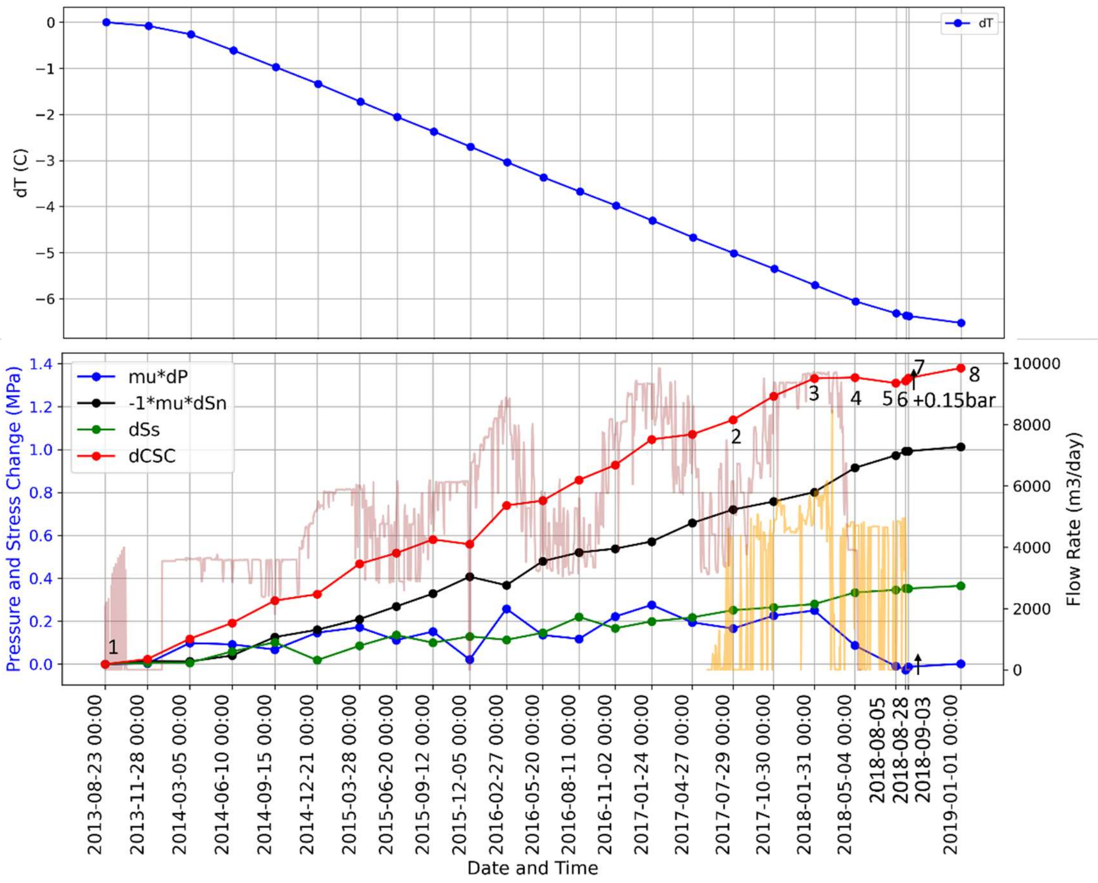

Figure 6-8. Temporal evolution of pressure, temperature and stress on the Carboniferous Normal Fault, at three-monthly resolution: a) maximum temperature change versus time (monitored at location of maximum temperature change, see also Figure 6-7b for spatial distribution), b) contributions of pore pressure (blue line), total normal stress (black line) and shear stress (green) to Coulomb stressing (red line). Light brown line in the background presents flow rates at CWG (well GT-03), light orange line at the background represents flow rates at CLG (well GT-05). Effect of shut-in on pressure and stress indicated as small circles. Meaning of points 1-8 is mentioned in the text. Small black arrrows show moment of shut-in CLG-doublet.

The evolution of normal, shear, and Coulomb stress is primarily influenced by cooling and follows the temperature trend, with deviations attributed to poroelastic effects and direct pressure changes. After operations of CWG were stopped, Following the shut-in of CAL-GT-04 on August 28, 2018 (point 6), there is a sudden, though small, rise in pore pressure (from point 6-7) leading to a minor, but rapid increase in total Coulomb stresses (at this specific location +0.15bar), at deeper locations somewhat larger – up to +0.4 bar (see Figure 6-7d).

6.2.9 Coulomb stressing on the Western Pop-up Fault

Figure 6-9 illustrates the spatial changes in the pore pressure, temperature and stress on the Western Pop-Up Fault, derived from scenario HM8 of the dynamic reservoir model. Figure 6-10 presents the temporal evolution of the pressure and stress on the Western Pop-Up Fault at the location of maximum cooling (a) and maximum Coulomb stress changes (b).

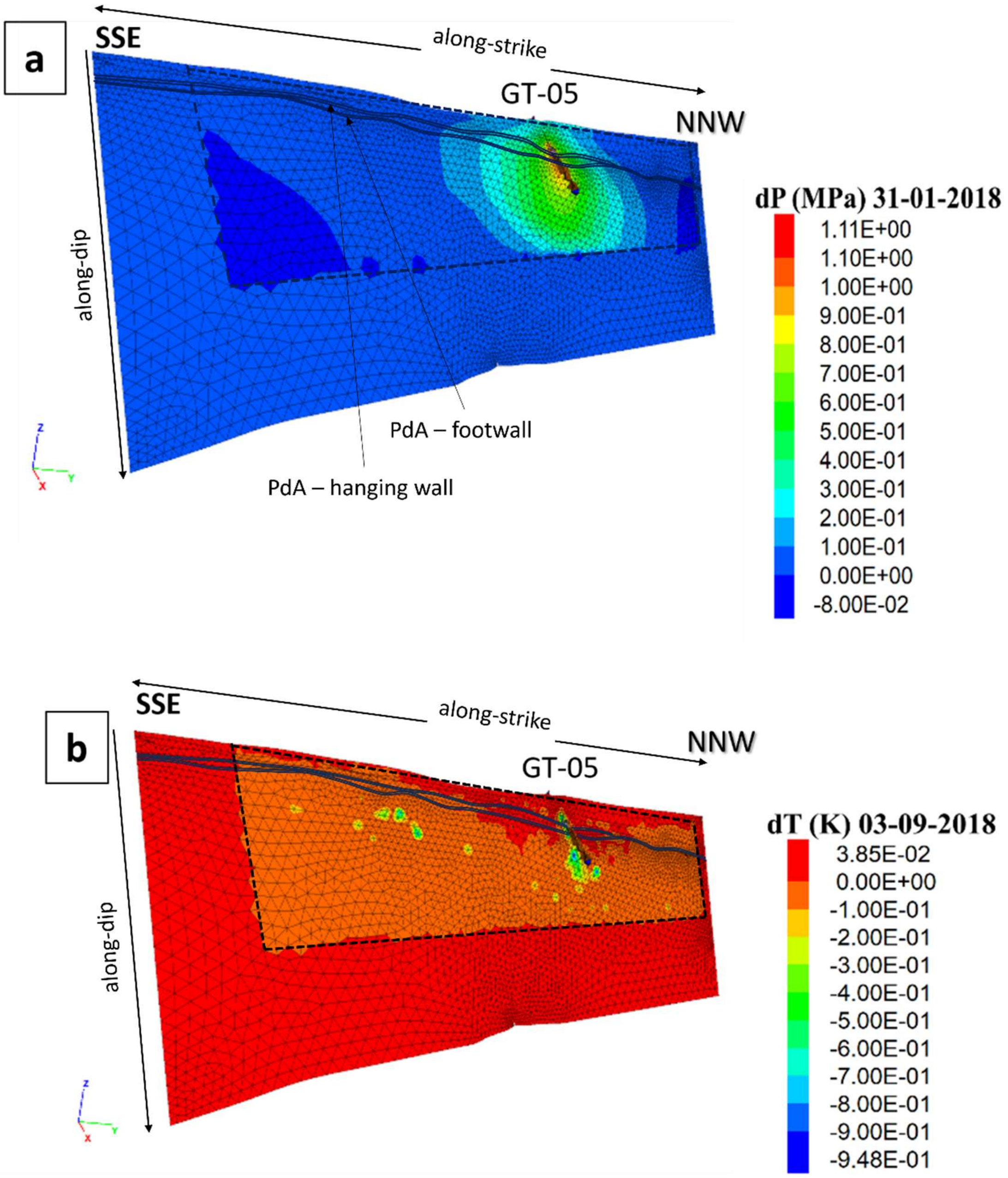
a
SSE
along-strike
GT-05
NNW
along-dip
PdA – footwall
PdA – hanging wall
dP (MPa) 31-01-2018
1.11E+00
1.10E+00
1.00E+00
9.00E-01
8.00E-01
7.00E-01
6.00E-01
5.00E-01
4.00E-01
3.00E-01
2.00E-01
1.00E-01
0.00E+00
-8.00E-02
b
SSE
along-strike
NNW
GT-05
along-dip
dT (K) 03-09-2018
3.85E-02
0.00E+00
-1.00E-01
-2.00E-01
-3.00E-01
-4.00E-01
-5.00E-01
-6.00E-01
-7.00E-01
-8.00E-01
-9.00E-01
-9.48E-01

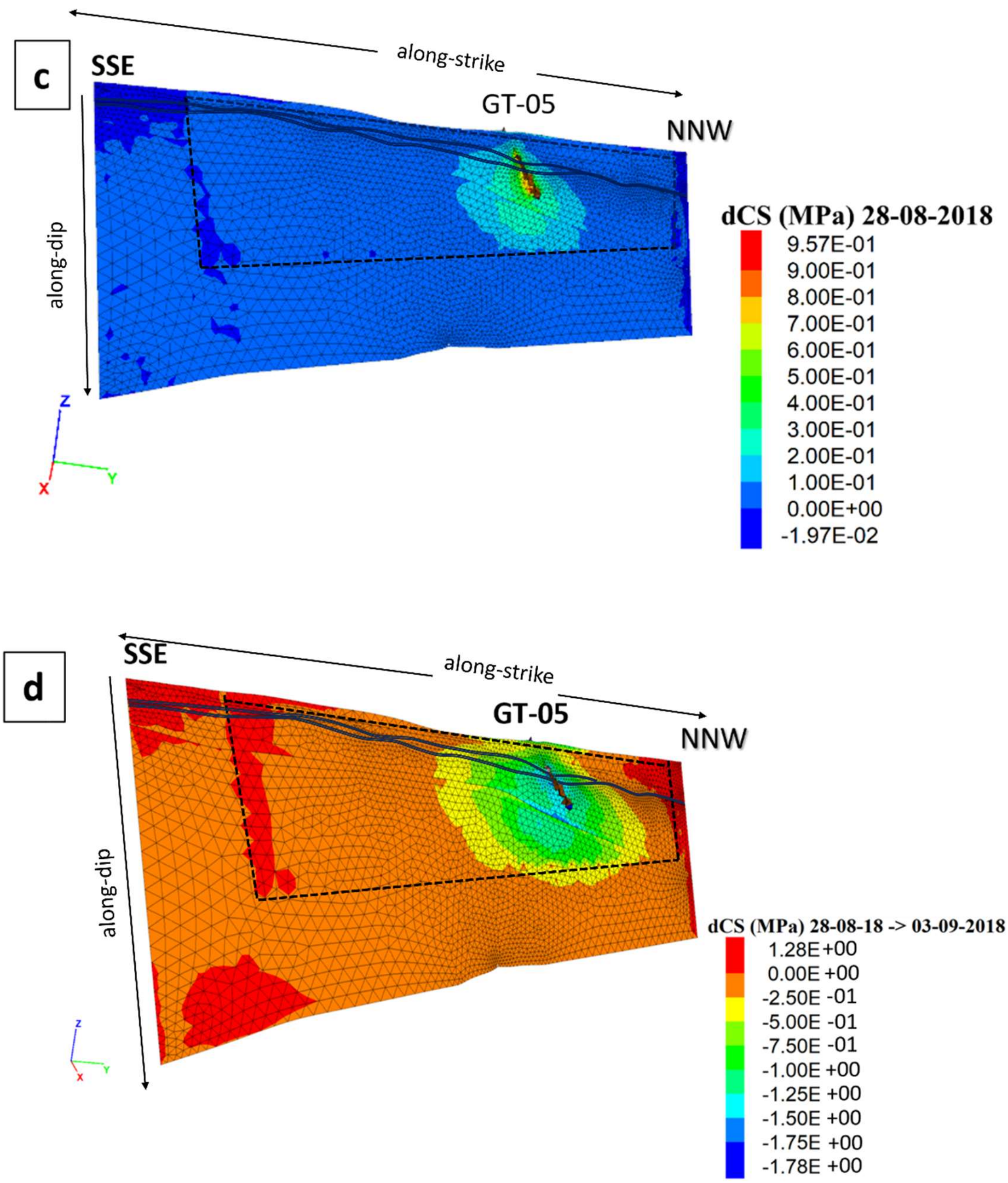

Figure 6-9. Pressure and stress on the Western Pop-Up Fault (WPF). a) Pressure change in the fault 31-01-2018 as compared to initial conditions, b) temperature change at the fault 03-09-2018 as compared to initial conditions. Coulomb stress change on the fault at 28-08-2018 as compared to initial conditions, c) Coulomb stress change on the fault at 28-08-2018 as compared to initial conditions, d) Coulomb stress change between 28-08-2018, just before the final shut-in of the CLG doublet and the time of the Ml 1.7 seismic event at 03-09-2018. Dark blue lines indicate depth of intersection with the Pont d'Arcole Formation. Black dashed line indicates dimensions of dynamic reservoir model.

From the moment the CLG doublet starts operations (Figure 6-10b just before point 2), Coulomb stresses on the fault increase, at first (from point 2-3) mainly driven by pressure diffusion into the fault (direct pressure effect). Figure 6-10b shows a significant pressure increase on January 31, 2018, with a maximum of around 11 bar near injection well CAL-GT-

05. Figure 6-10b illustrates the effect of poroelastic stresses due to expanding rock volumes, as normal stresses (black line) clamp and slightly stabilize the fault during the first injection period (negative contribution to Coulomb stress – point 2-3). As production rates decline (end of winter – beginning August 2018) pressure effects and associated poroelastic effects reduce (point 3-5). Figure 6-9 indicates cooling of the bulk matrix resulting from the cold fluid injection at CAL-GT-05 is limited to less than 1°C. Cooling specifically affects stability during later stages, causing the gradient of the Coulomb stress change to be less steep from end of January 2018 to beginning of August 2018 than during the first period of injection, and keeping Coulomb stress at a relatively high level (point 3-5). Coulomb stresses increase rapidly during a short period of high injection rates and pressure increase before the end of August (point 5-6), reaching values of almost 1 MPa (point 6) – and then rapidly reduce after shut-in of the CLG doublet (point 6-7). Note that this is the same high rate period that caused the reduction in Coulomb stress on the Tegelen fault just before the shut-in of the CLG operations.

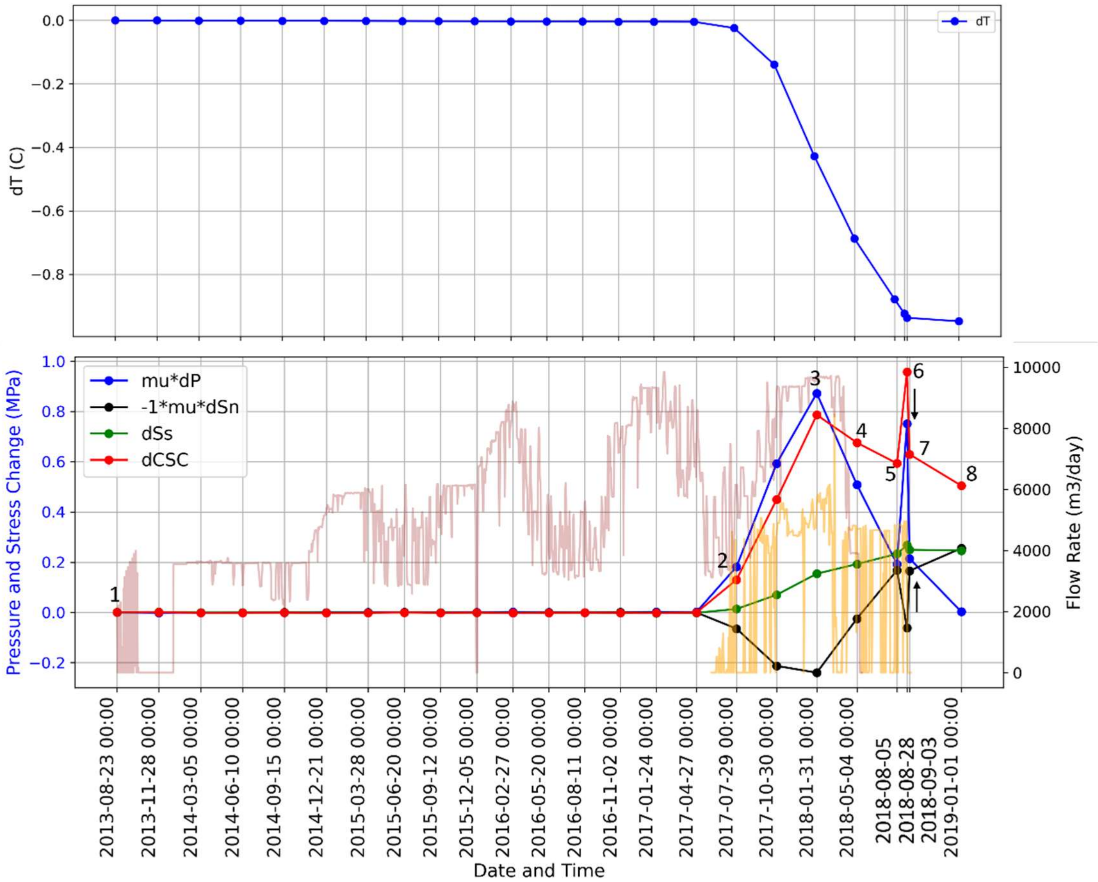

Figure 6-10. Temporal evolution of pressure, temperature and stress on the Western Pop-up Fault, at three-monthly resolution: a) maximum temperature change versus time (monitored at location of maximum temperature change, see for spatial distribution, b) contributions of pore pressure (blue line), total normal stress (black line) and shear stress (green) to Coulomb stressing (red line). Light brown line in the background presents flow rates at CWG (well GT-03), light orange line at the background represents flow rates at CLG (well GT-05). Meaning of numbers 1-8 are explained in the text. Black arrows present timing of shut-in of the CLG-doublet.

The positive Coulomb stresses change of 5 bar that remains after shut-in of the CLG-doublet can be attributed to cooling and thermal stressing (point 8).

Figure 6-9d compares pressures and stress at shut-in (August 28, 2018) and on September 3, 2018, showing a stabilisation of the Western Pop-Up Fault after shut-in of the CLG doublet. The positive Coulomb stresses change of 5 bar that remains after shut-in of the CLG-doublet can be attributed to cooling and thermal stressing.

6.2.10 Coulomb stressing on the Eastern Pop-up Fault

Figure 6-11 illustrates the spatial changes in pore pressure, temperature and stress on the Eastern Pop-Up Fault, derived from scenario HM8 of the dynamic reservoir model. Figure 6-12 presents the temporal evolution of the pressure and stress on the Eastern Pop-Up Fault at the location of maximum cooling (a) and maximum Coulomb stress changes (b). Trends simulated are similar to those observed for the Western Pop-Up Fault, with a predominant effect of pressure changes to fault loading at the early stages, and a delayed additional effect of cooling.

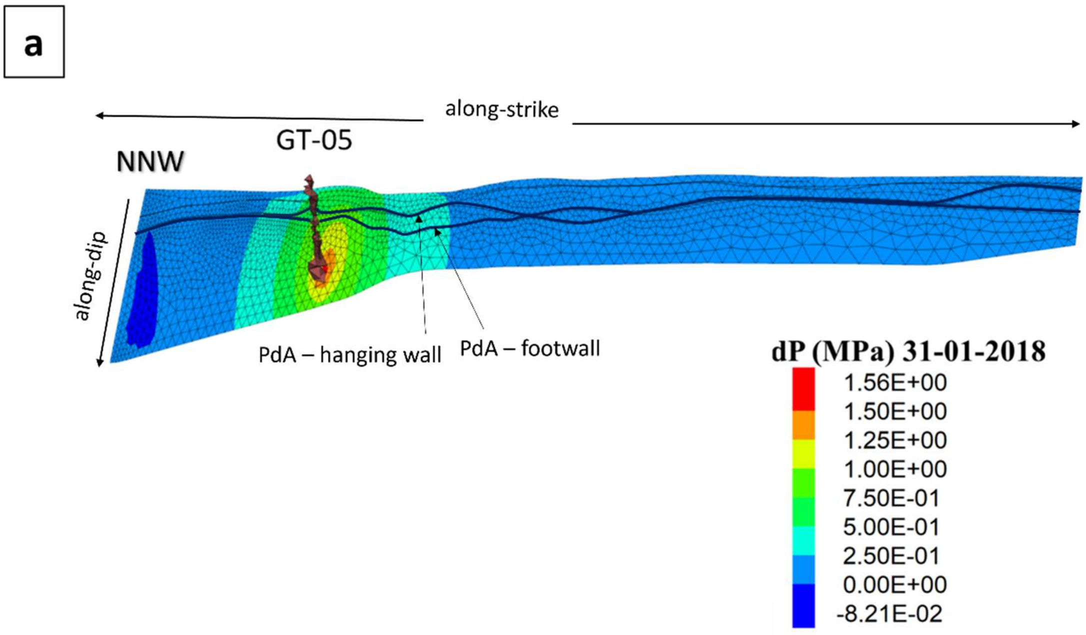

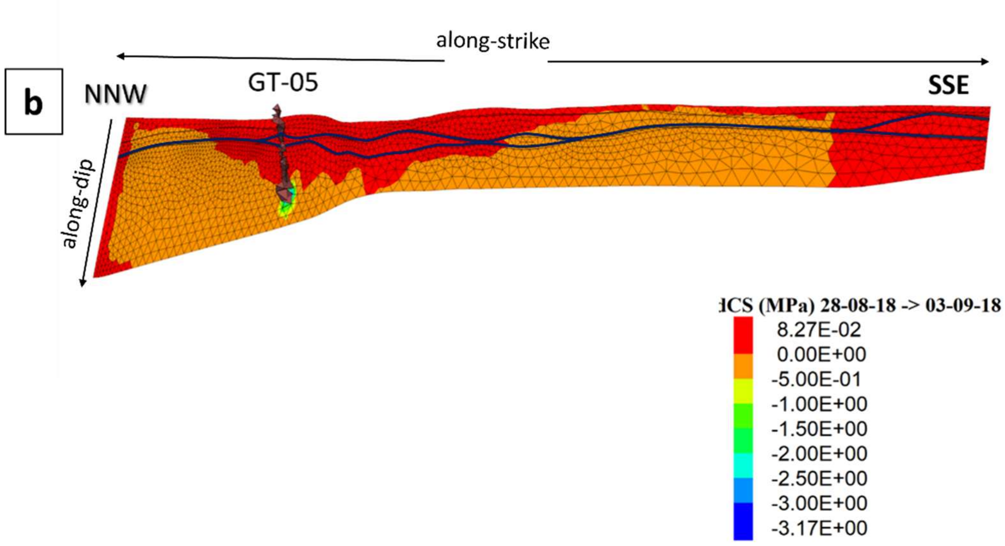
b
along-strike
NNW
GT-05
SSE
along-dip
dCS (MPa) 28-08-18 -> 03-09-18
8.27E-02
0.00E+00
-5.00E-01
-1.00E+00
-1.50E+00
-2.00E+00
-2.50E+00
-3.00E+00
-3.17E+00

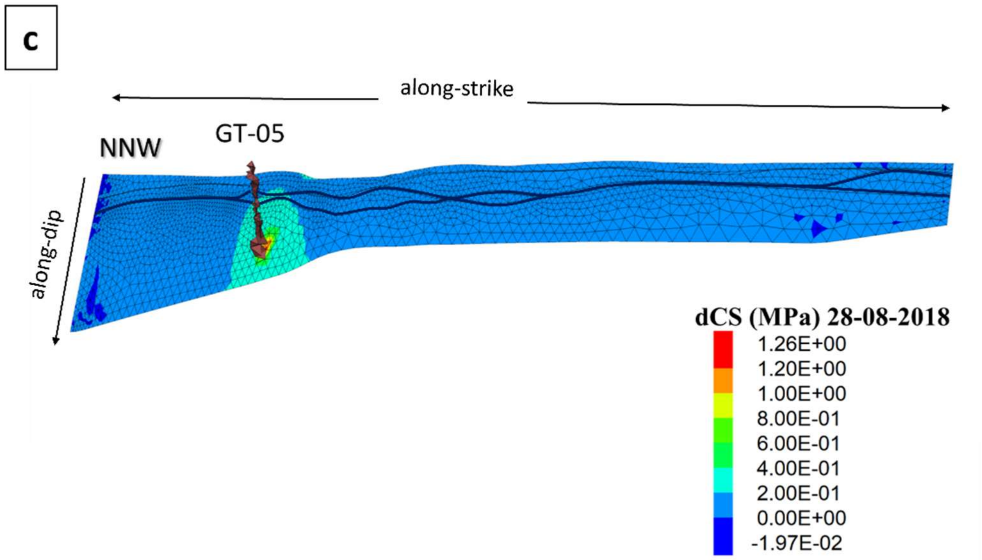
c
along-strike
NNW
GT-05
along-dip
dCS (MPa) 28-08-2018
1.26E+00
1.20E+00
1.00E+00
8.00E-01
6.00E-01
4.00E-01
2.00E-01
0.00E+00
-1.97E-02

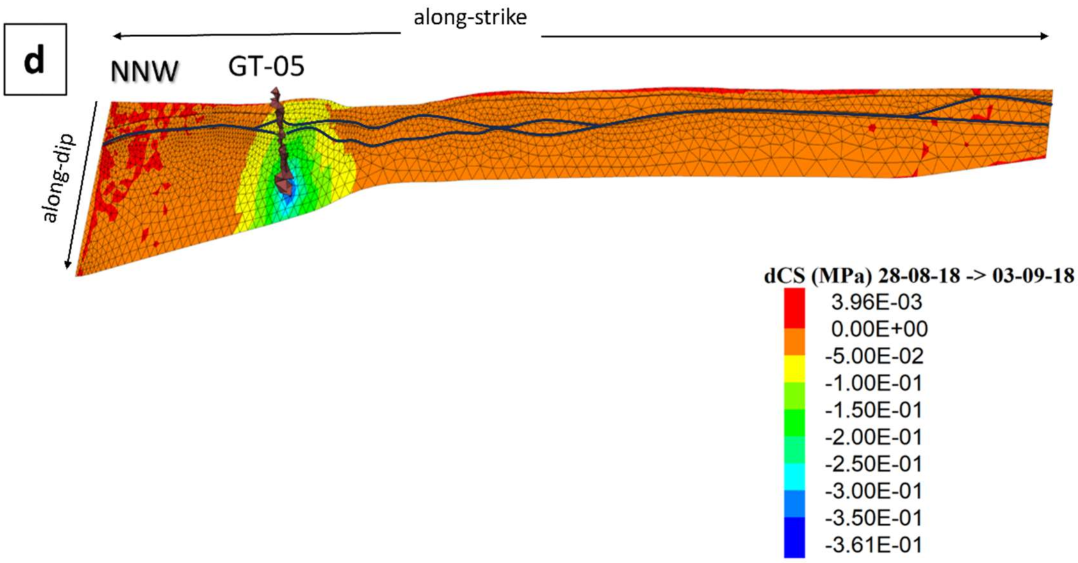

Figure 6-11. Pressure and stress on the Eastern Pop-Up Fault (WPF). a) Pressure change in the fault 31-01-2018 as compared to initial conditions, b) temperature change at the fault 03-09-2018 as compared to initial conditions Coulomb stress change on the fault at 28-08-2018 as compared to initial conditions, c) Coulomb stress change on the fault at 28-08-2018 as compared to initial conditions, d) Coulomb stress change between 28-08-2018, just before the final shut-in of the CLG doublet and 03-09-2018, some days after shut-in of the doublet. Dark blue lines indicate depth of intersection with the Pont d'Arcole Formation.

Total Coulomb stress changes (up to 1.26 MPa) are higher than for the Western Pop-Up Fault, as the amount of cooling simulated in this scenario on the eastern Pop-Up fault is higher than for the Western Pop-Up Fault (up to -3°C). Largest Coulomb stress changes are simulated for the end of August 2018, during the period of increased injection just before the shut-in of the CLG-doublet point (during the period point 5 -6) . Similar to the Western Pop-Up Fault, the fault shows a stabilisation after shut-in of the CLG doublet. The positive Coulomb stresses change of 5 bar that remains after shut-in of the CLG-doublet can be attributed to cooling and thermal stressing (point 8).

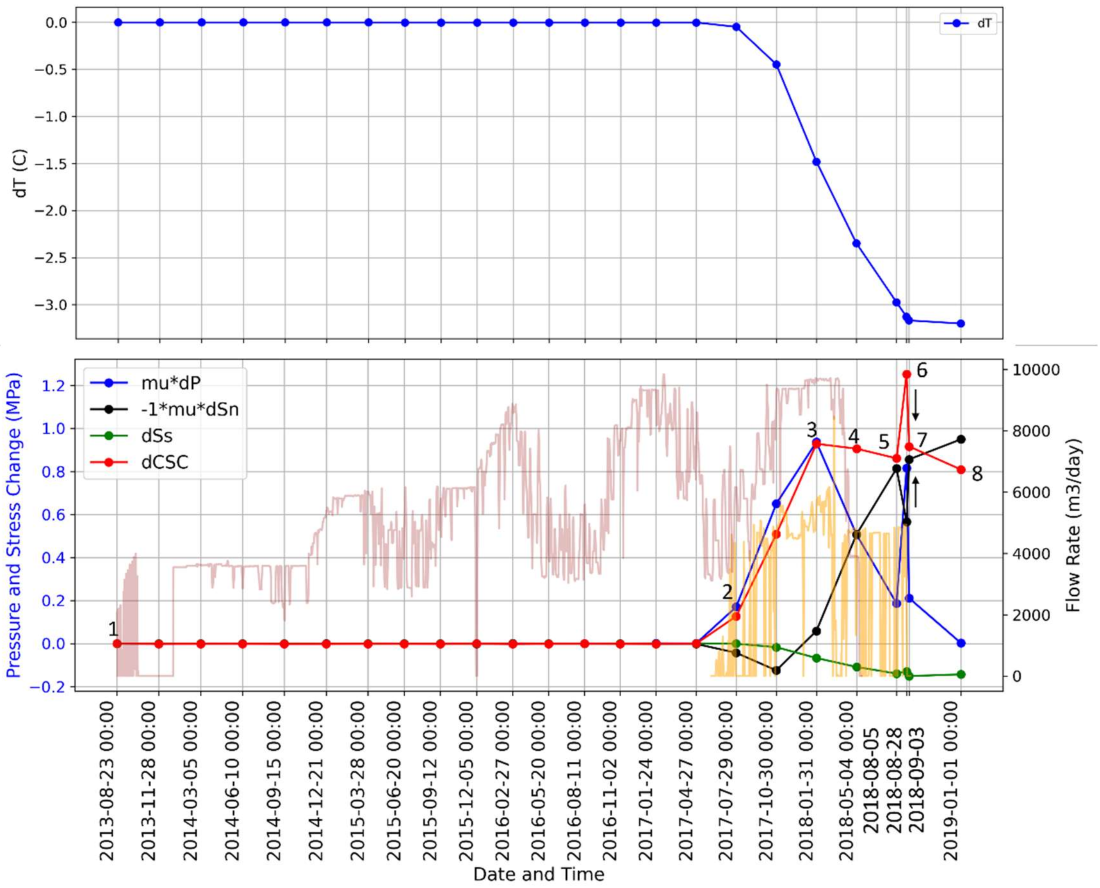

Figure 6-12. Temporal evolution of pressure, temperature and stress on the Eastern Pop-up Fault, at three-monthly resolution: a) maximum temperature change versus time (monitored at location of maximum temperature change, see also Figure 6-11b. b) contributions of pore pressure (blue line), total normal stress (black line) and shear stress (green) to Coulomb stressing (red line). Light brown line in the background presents flow rates at CWG (well GT-03), light orange line at the background represents flow rates at CLG (well GT-05). Meaning of numbers 1-8 are explained in the text.

6.3 Discussion on potential mechanisms of induced seismicity

Although there are various uncertainties associated to (the parametrisation of) the models, general observations and trends from the simulations allow to gain insights into the contributing mechanisms that are playing a role in historical seismicity and their relative impacts. The discussion below is based on the results of the three different scenarios (for results of scenarios HM1 and HM5, see Appendix G). Though magnitudes of pressure, temperature and Coulomb stress changes for the three scenarios vary (see Appendix G), the overall trends in the scenarios is similar and support the hypotheses for the mechanisms driving the seismicity at the geothermal site (Figure 6-19).

Based on image logs and production logging tests, flow near CAL-GT-03 and CAL-GT-01 is interpreted as fracture-dominated and preferentially occurring through a limited number of widely spaced large fractures in the damage zones of the Tegelen and Carboniferous Normal faults.

The thermal drawdown associated with flow through large, widely-spaced fractures is expected to be gradual and continuous over space and time, lacking a distinct thermal front (Gan and Elsworth, 2014). The cold water in the faults and fractures slowly cools the walls of the faults and fractures. Simulation results show that this results in a very gradual cooling of the rock matrix, as shown in Figure 6-8a, which causes an increase in Coulomb stresses (Figure 6-8b) on the Carboniferous Normal Fault near injection well CAL-GT-03. The thermal front simulated near CAL-GT-03 is diffuse, with fracture fluids cooling more and over larger distances than the rock matrix. Figure 6-13 shows cooling of the fracture fluids and rock matrix of the Carboniferous Normal Fault in September 2015 (approximately one month after the first induced seismic event near the CWG doublet) and September 3, 2018. The model computes thermal stresses based on temperature changes in the matrix, as it represents the bulk of the volumetric thermal deformation, and does not account for the local effects of cooling in the fracture network. This is a simplification, though, as locally around the fractures cooling and thermal deformation can take place of the fracture wall, which is not captured, due to the resolution of the reservoir and geomechanical model. This may lead to an underestimation of the effect of thermal stresses and may affect larger depths and distances from the injection well than simulated.

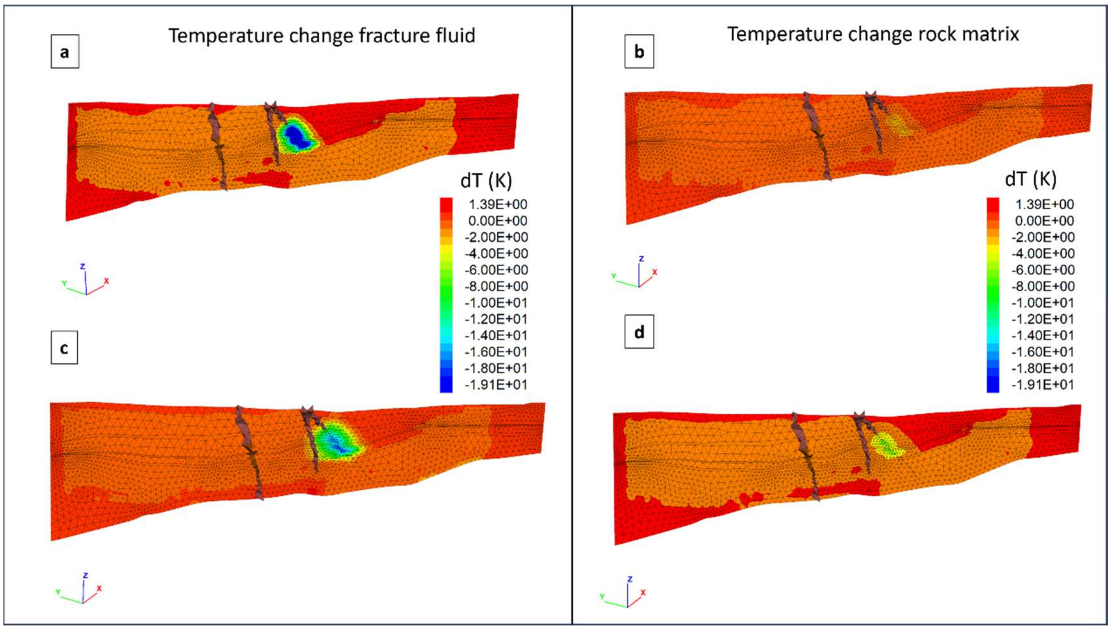

Figure 6-13. Temperature changes in fracture fluid and rock matrix September 2015 and in September 2018, a) fracture fluid, September 2015, b) rock matrix, September 2015, c) fracture fluid, September 2018, d) rock matrix, September 2018. Maximum temperature change of the fracrure fluid close to the well is -29.4°C in September 2015 and -19.1°C in September 2018.

Observations of induced seismicity indicate a correlation between reduced flow rates and the occurrence of seismic events for the early events that occurred when only the CWG doublet was active. The April 2018 event that occurred during the simultaneous operation of the CWG and CLG doublet also shows a potential correlation with reduction of flow rates in the CWG doublet. The main Ml 1.7 event occurred approximately six days after the shut-in of the CLG doublet, preceded by two small events on the same day. Both the absolute locations derived in this study, and the former (including relative) locations derived by Q-con (Vörös and Baisch, 2022) of the majority of the seismic events indicate that the events are located relatively close to the CAL-GT-03 injection well of the CWG doublet (see Table 4-2 for new hypocenter locations derived in this study and Figure 4-8 and Figure 4-9 for mean hypocenter locations and confidence ellipses). The mean hypocenter locations of the seismic events that occurred during the CWG doublet operations, the April event and the main event are located to the east of the Carboniferous Normal Fault and the part of the Tegelen Fault that lies below the intersection with the Carboniferous, close to well CAL-GT-03. Mean hypocenter depths are located below 2 km in the Devonian sandstones; uncertainty in hypocenter depths is significant (Figure 4-7), with a standard deviation (marginalized in the z-direction) between 882 – 1088m. Figure 4-8 gives distance of mean hypocenter locations to the closest fault. In section 3.4.1 it was discussed that the intersection depth of the Carboniferous Normal Fault with CAL-GT-03 is uncertain and can potentially be located at 230 m lower level. A repositioning to a deeper level would move the Carboniferous Normal fault closer to the seismic cloud.

Notably, the Ml 0.2 event on August 25, 2018 appears to fall outside this cluster (Figure 4-8 and Figure 4-9). Additionally, there is a discrepancy in the hypocenter locations interpreted by Q-con and TNO for the Ml 0.2 event of August, 25, 2018, with the new interpretation placing the hypocenter approximately 800 m to the east and 1.5 km to the north, closer to injection well CAL-GT-05. See also discussion at the end of this paragraph.

The gradual thermal stressing of the Carboniferous Normal fault does not account for the observed correlation between reductions in flow rate and seismicity during CWG operations. Several hypotheses may clarify this correlation:

- <u>Thermal stress accumulation:</u> Deeper segments of the Carboniferous Normal Fault near injection well CAL-GT-03, which undergo cooling and pressure depletion during CWG operations (attributed to production from CAL-GT-01, see also Figure 6-7b and c) become gradually more critically-stressed due to thermal stresses. A sudden decline in flow rates can lead to an abrupt pressure increase within the fault, further destabilizing it and inducing / triggering seismicity on or near the area that was already affected by cooling (Figure 6-7d).
- <u>Aseismic reactivation:</u> Fault segments of the Carboniferous Normal Fault near CAL-GT-03 may be reactivated and slip aseismically during gradual cooling, thereby loading asperities or surrounding segments. In addition to aseismic stress transfer, fault segments can be loaded by stress transferred due to earlier seismic events. A sudden decrease in flow rates would then cause an immediate rise in pressure on previously depleted fault segments which have been loaded by the stress transfer, potentially resulting in seismic events.
- <u>Poroelastic stress effects:</u> Fault segments close to injection well CAL-GT-03 experiencing poroelastic stresses from injection (due to volumetric changes in the rock) may undergo a near-instantaneous reduction in normal stresses that clamp the fault when flow rates are reduced. This reduction could occur alongside a sudden increase in shear stresses when injection rates decrease. Since pore pressure diffusion is typically slower than the propagation of poroelastic effects, there may be a brief window during which pore pressures remain high while poroelastic (normal) stresses drop due to contraction of the surrounding rock. If critical stress levels are reached, seismicity may occur, especially if the fault has already been cooled or loaded by stress transfer. This mechanism was first described by Segall and Lu (2015) for single-porosity media. Its contribution to seismicity at the Californië geothermal site remains uncertain, as it depends on the interplay between flow and fracture mechanics, including delays in pressure changes in the matrix and fractures, effects of fracture closure on permeability and diffusivity, and the effect of fracture density and orientation on the Biot coeffients of the carbonates and Devonian sandstones. This interplay cannot be analysed with the current one-way

coupled model and model resolution. This mechanism would preferentially affect faults and fractures with a low hydraulic connectivity to the injection well that are still influenced by the cooling front and/or loaded by stress transfer.

These mechanisms may explain the observed correlation between decreasing flow rates and seismicity during the operation of the CWG doublet. Moreover, the first two mechanism may also explain the occurence of seismicity in September 2018, culminating in a Ml 1.7 events some days after the shut-in of the CLG-doublet. As shown in Figure 6-7 and Figure 6-8, production from CAL-GT-04 affects the pressures at the location of the CWG-site. While CAL-GT-04 has a stabilizing effect on the deeper fault segments (both of the Carboniferous Normal Fault and the Tegelen Fault) when it is producing, this stabilising effect is lost at the shut-in of the well. The combination of a gradual destabilisation and loading of the fault by thermal stressing and potential loading of deeper segments by (a)seismic stress transfer in combination with a rapid increase of the pressures within the fault as CAL-GT-04 was shut-in seems a plausible mechanisms for the Ml 1.7 seismic event.

We note though that the pressure changes and associated Coulomb stress changes after reduction of flow rates or shut-in of the wells are very small (generally << 1 bar). Rates of stress changes associated to reduction in flow rates however are large as compared to the rate of stress changes associated to thermal loading. Rate-and-state friction theory supports the likelihood of earthquake triggering to be largely dependent on the rate of pore pressure changes rather than its magnitude (Alghannam and Juanes, 2020). The correlation between the occurrence of seismicity and the reduction of flow rates might indicate that rate-effects play a role.

As mentioned above, the Ml 0.2 seismic event on August 25, 2018 appears to fall outside the cluster of seismic events close to the CAL-GT-03 injection well. In both the former interpretation of Q-con (Vörös and Baisch, 2022) and the new hypocenter location derived in this study, this event is localized further to the north. The new interpretation of the mean hypocenter location and its confidence ellipse is shown in Figure 4-9. The mean hypocenter of this seismic event and its 68% confidence ellipse plots close to the CAL-GT-05 injection well and the Western Pop-Up Fault. The mean hypocenter depth of this event is estimated at -2575 m, in the Devonian sandstones, with a standard deviation (marginalized) in the z-direction of 963m.

Figure 6-14a and b show the spatial distribution of pore pressures around the CAL-GT-05 injection well at a depth between -1850m and -1875m and at a deeper level between -2500m and -2600m which corresponds to the hypocenter depth of the Ml 0.2 event on August 25, 2018. Pressure changes caused by the injection into CAL-GT-05 are significant (up to ~5 bar) and 'felt' up to hundreds of meters from CAL-GT-05. Pressure increase at the TNO-hypocenter location at a depth between 1850 – 1875m is approximately 10 bar, whereas pressure increase at the (mean / maximum likelihood) hypocenter depth still reaches several bars.

Figure 6-9 and Figure 6-10 and results for scenario HM1 and HM5 in Appendix H already showed that Coulomb stress changes on the Western Pop-Up Fault (due to pressure and temperature changes are significant (1-2 MPa). Figure 6-15c and d below show the spatial distribution of Coulomb stress changes around the CAL-GT-05 injection well at a depth between -1850m to -1875m and at a deeper level between -2500m and -2600m, where Coulomb stress changes are computed for potential locations of subseismic faults. Here it is assumed that the orientation of the structures is aligned with the general orientation of the major fault structures in the region. This figure shows that injection activities in CAL-GT-05 increase Coulomb stresses on (sub-seismic) faults and fractures up to a distance of hundreds of meters from CAL-GT-05.

The consistency between the newly determined hypocenter location of the M0.2 seismic event on August 28, 2018, and the relatively high Coulomb stress changes near well CAL-GT-05, as shown in the figures above, makes it plausible that this event is directly linked to injection activities in CAL-GT-05.

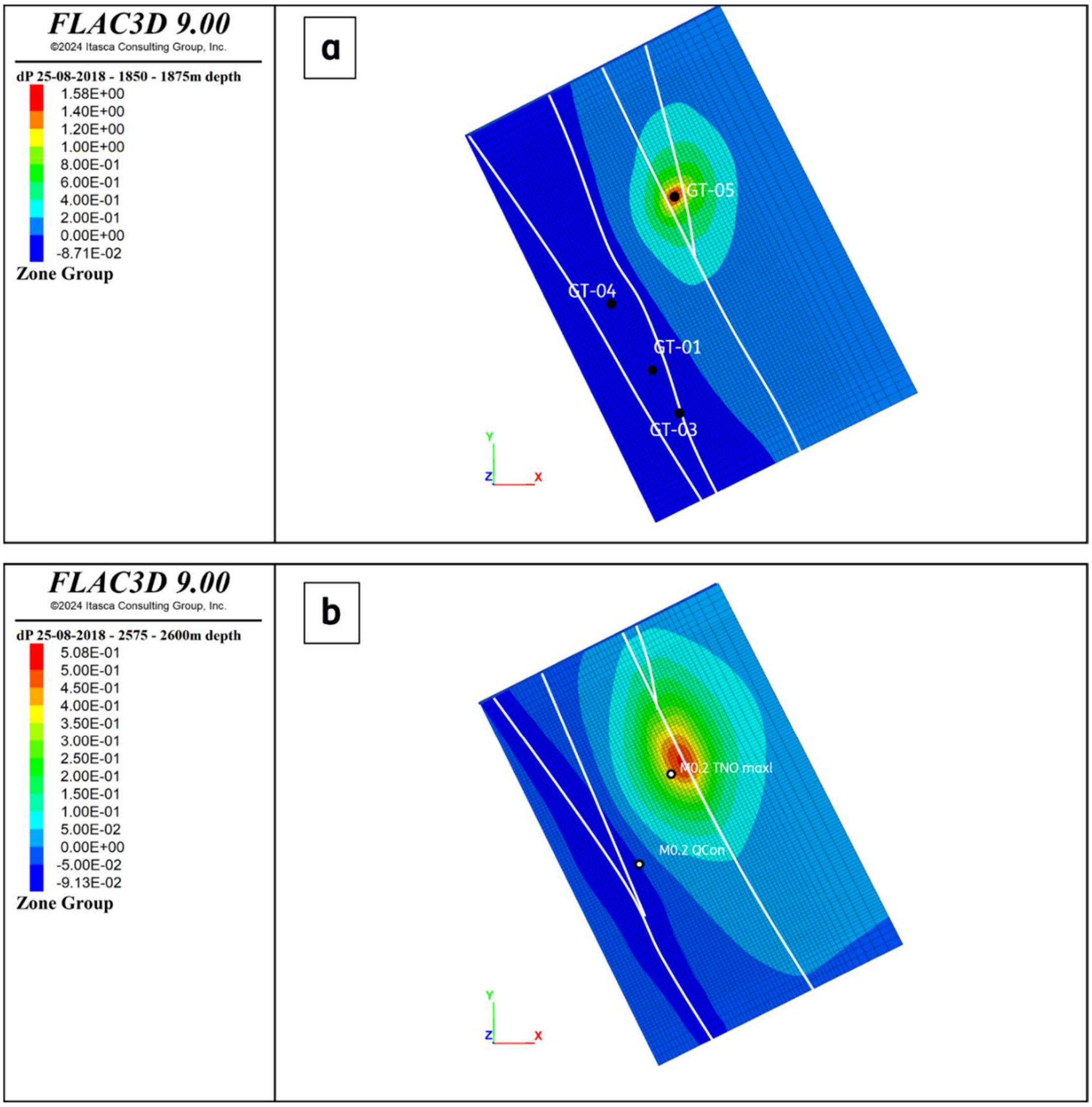

Figure 6-14 a). Pressure change (MPa) at 25-08-2018, during production from doublet CLG, depth 1850 – 1875m, b) pressure change at 25-08-2018, during production from doublet CLG, depth 2575 – 2600m, d) Coulomb stress change (MPa) at 25-08-2018, during production from doublet CLG, depth 2575 – 2600m. White lines indicate position of large faults, small white dots indicate location of M0.2 seismic event, black dots indicate position of the wells. Coulomb stress changes have been calculated for subseismic faults with strike 152° and dip 67°, conform the predominant strike and dip of the major faults. Based on HM8-scenario.

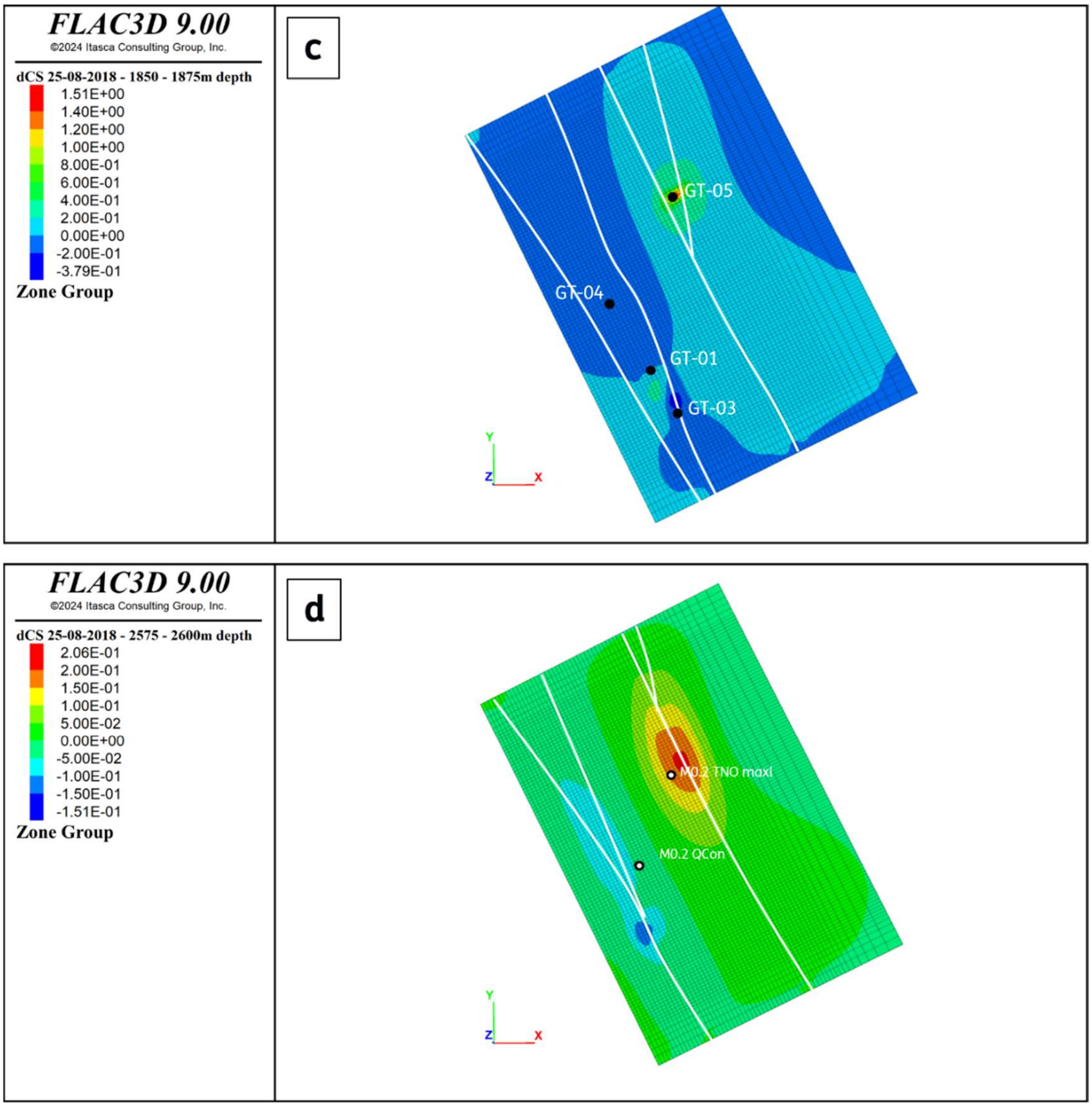

Figure 6-15. c) Coulomb stress change at 25-08-2018 caused by operation of doublet CLG, depth 1850 – 1875 m, d) Coulomb stress change at 25-08-2018, during production from doublet CLG, depth 2575 – 2600m. White lines indicate position of large faults, small white dots indicate location of M0.2 seismic event, black dots indicate position of the wells. Coulomb stress changes have been calculated for subseismic faults with strike 152° and dip 67°, conform the predominant strike and dip of the major faults. Based on HM8 scenario.

6.4 Operational scenario for the pilot phase

In section 5.4 a possible test scenario for a long-term injection & production test is described, consisting of two stages: Stage 2 ramp-up warm operation and Stage 3 ramp-up cold operation. A longer test-period is proposed in which a doublet is slowly started up with low rates and a temperature that is close to the reservoir temperature and slowly increasing rates from 180 to 210 and 240 m^3/hr, with long (> 2 weeks) flow periods per rate. This will allow to fully stabilize the pressure in the flow periods and allow for monitoring of potential (micro-)seismicity associated to pressure change. The ramp-up warm operation is then followed by a similar ramp-up of rates, but now with cooling of the injected fluid to 40°C. In this phase, the impact of the cooling on the injectivity and potential (micro-)seismicity in the vicinity of the well can be evaluated. Because the cooling of the matrix is expected to be more important for seismicity than the cooling of the fractures, this phase can potentially last quite long. To enable the analysis of relations between operations and the seismic response a dedicated seismic monitoring network is required, which has a sufficiently low detection limit and is optimised for localisation of seismic events. Options for seismic network configurations and their performance are described in Chapter 8.

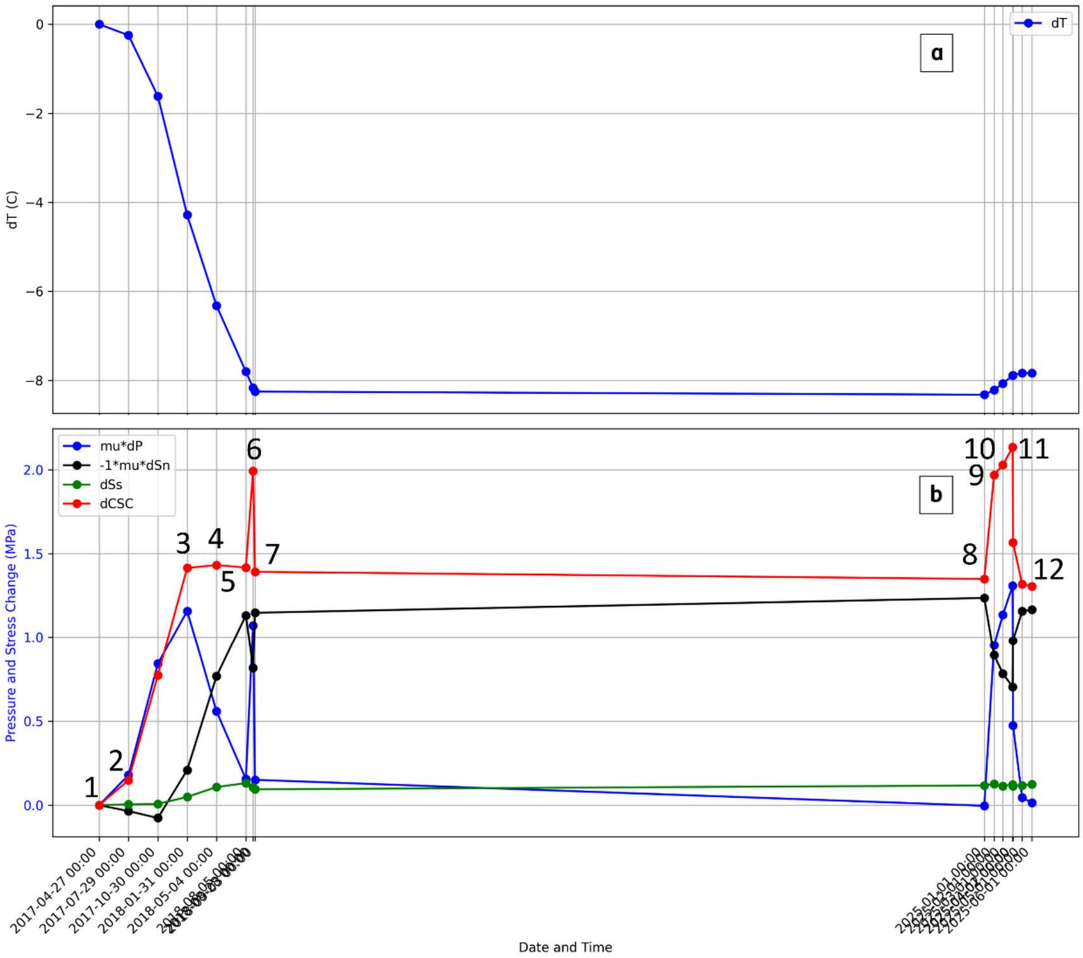

Figure 6-16. Evolution of temperature at location of maximum temperature change at the Western Pop-Up Fault during the <u>warm</u> long injection test for the pilot phase. The period between April 2017 and August 2018 represents the operational period of the CLG doublet. The doublet is assumed to be shut-in from September 1018 till January 1, 2025. The injection test is assumed to take place between January 1, 2025 and June 1, 2025. b) Evolution of pressures and stresses during warm long term injection test for the pilot phase, sampled at the location of maximum Coulomb stress change. For description of test see section 5.4.

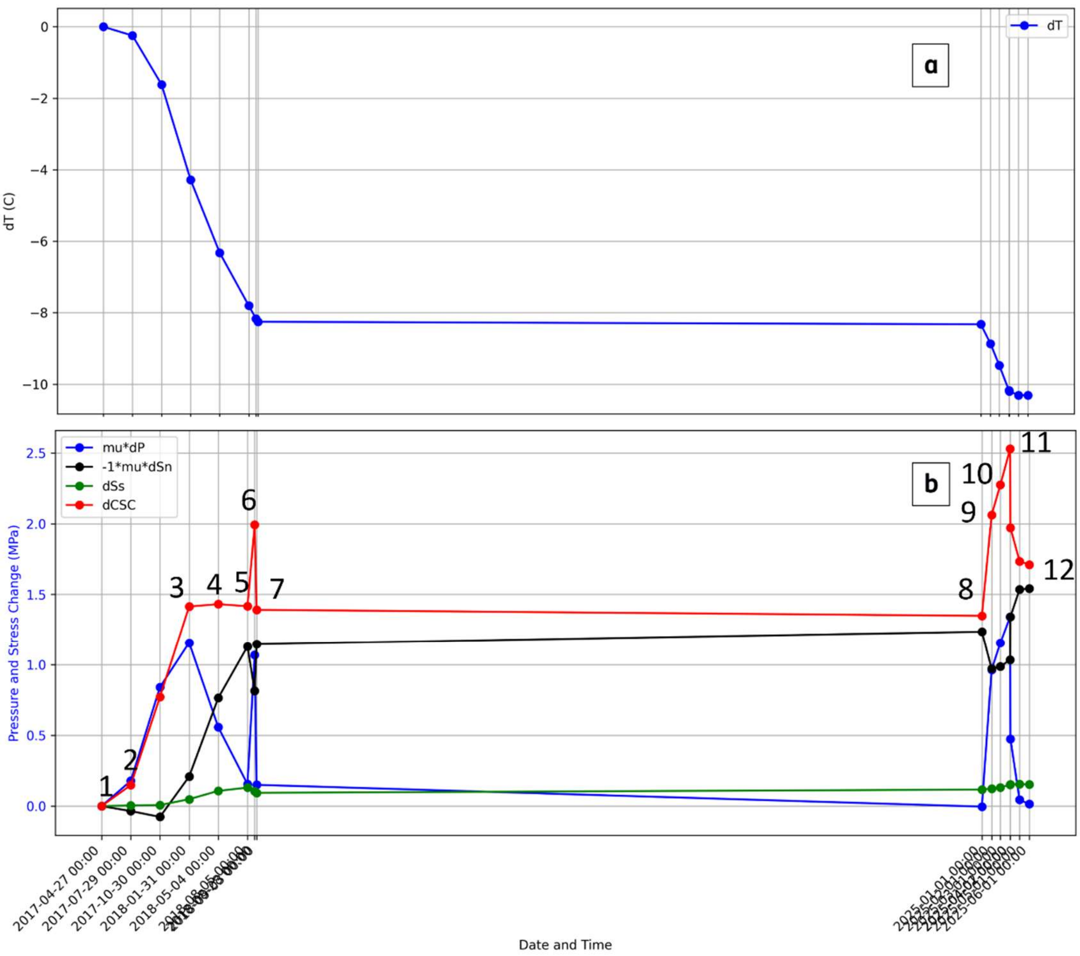

Figure 6-17. Evolution of temperature at location of maximum temperature change at the Western Pop-Up Fault during the cold long injection test for the pilot phase. The period between April 2017 and August 2018 represents the operational period of the CLG doublet. The doublet is assumed to be shut-in from September 1018 till January 1, 2025. The injection test is assumed to take place between January 1, 2025 and June 1, 2025. b) Evolution of pressures and stresses during warm long term injection test for the pilot phase, sampled at the location of maximum Coulomb stress change. For description of test see section 5.4.

Figure 6.16 presents the evolution of stress and temperature with time on the Western Pop-Up Fault for the warm ramp-up test. Note that for the pilot phase scenario HM5 is used here as base scenario. Although magnitudes of temperature, pressure and stress changes differ from those in HM8, the general trends observed in the evolution of temperature, pressure and stress during the operational period of the CLG doublet (point 1-7) are similar to scenario HM8 and have been described in section 6.2.9.

Operations of the CLG doublet start in June 2017 (between point 1 and 2). After shut-in of the doublet at the end of August 2018 (7) a small decrease of temperatures in the rock matrix is observed, which can be attributed to the equilibration of fracture and matrix temperatures.

The ramp-up warm injection test is assumed to start on January 1, 2025 (8) and injection rates are step-wise increased from 180 m3/hr, to 210 m3/hr (9) and 240 m3/hr (10). April 1, 2025 injection stops (11) and pressures and temperatures are monitored till June 1, 2025 (12). After start of the warm injection test, a rapid pressure increase of ~1.0 MPa is observed, followed by a slower rate of pressure change during the second and third injection rate-step. Total pressure change as compared to initial reservoir pressures at this specific location is ~1.3MPa. Total normal stress on the fault increases due to a combination of poro- and thermoelastic effects (increased clamping), resulting in stabilisation of the fault. Coulomb stress change (as compared to the initial stress before the start of operations in CLG) during the warm injection test follows the same trend as the pressure changes, with a maximum Coulomb stress change of 2.2 MPa (point 11). It is noted that Coulomb stress exceeds the past Coulomb stress (6) at the end of the second rate step (10). After shut-in of the injection well (11), pressures rapidly decline to initial reservoir pressures. Coulomb stresses reduce quickly until June 1, 2025 (12) remaining slightly below Coulomb stresses at the beginning of the test. The latter can be explained by the increase of temperatures and thermal stresses (increased clamping) due to the injection of the warm water.

Figure 6.17 shows the effect of the cold injection test. In 6.16 it is again assumed that injection starts at January 1, 2025. Maximum Coulomb stress changes (11) on the fault is ~3 bar higher than in the warm injection test, which can be attributed to the effect of additional cooling on the normal stresses, reducing the clamping of the fault. Coulomb stresses at the end of the test period are higher than at the start of the test, due to additional cooling of the rock matrix near the fault.

It is noted that in the current simulation the warm and cold injection test both are assumed to start at January 1, 2025. In reality the cold injection phase starts after the warm injection phase and maximum Coulomb stress changes reached will be slightly lower, due to the slight increase in temperatures at the end of the warm injection.

Figure 6.18a shows the spatial distribution of the Coulomb stress changes (as compared to the values at the start of the pilot) on the Carboniferous Normal Fault at the end of the third rate step of the cold ramp-up phase, just before shut-in on April 1, 2025. The production in CAL-GT-04 has a temporarily stabilising effect on the Carboniferous Fault. Figure 6.18b and c show the Coulomb stress changes (as compared to the values at the start of the pilot) on the Western Pop-Up Fault (injection CAL-GT-05) at the end of the third rate step, just before shut-in on April 1, 2025, respectively at the end of the test, June 1, 2025. The cold injection test results in a very local additional loading of the Western Pop-Up Fault (0.3 MPa) due to the injection of the cold fluids.

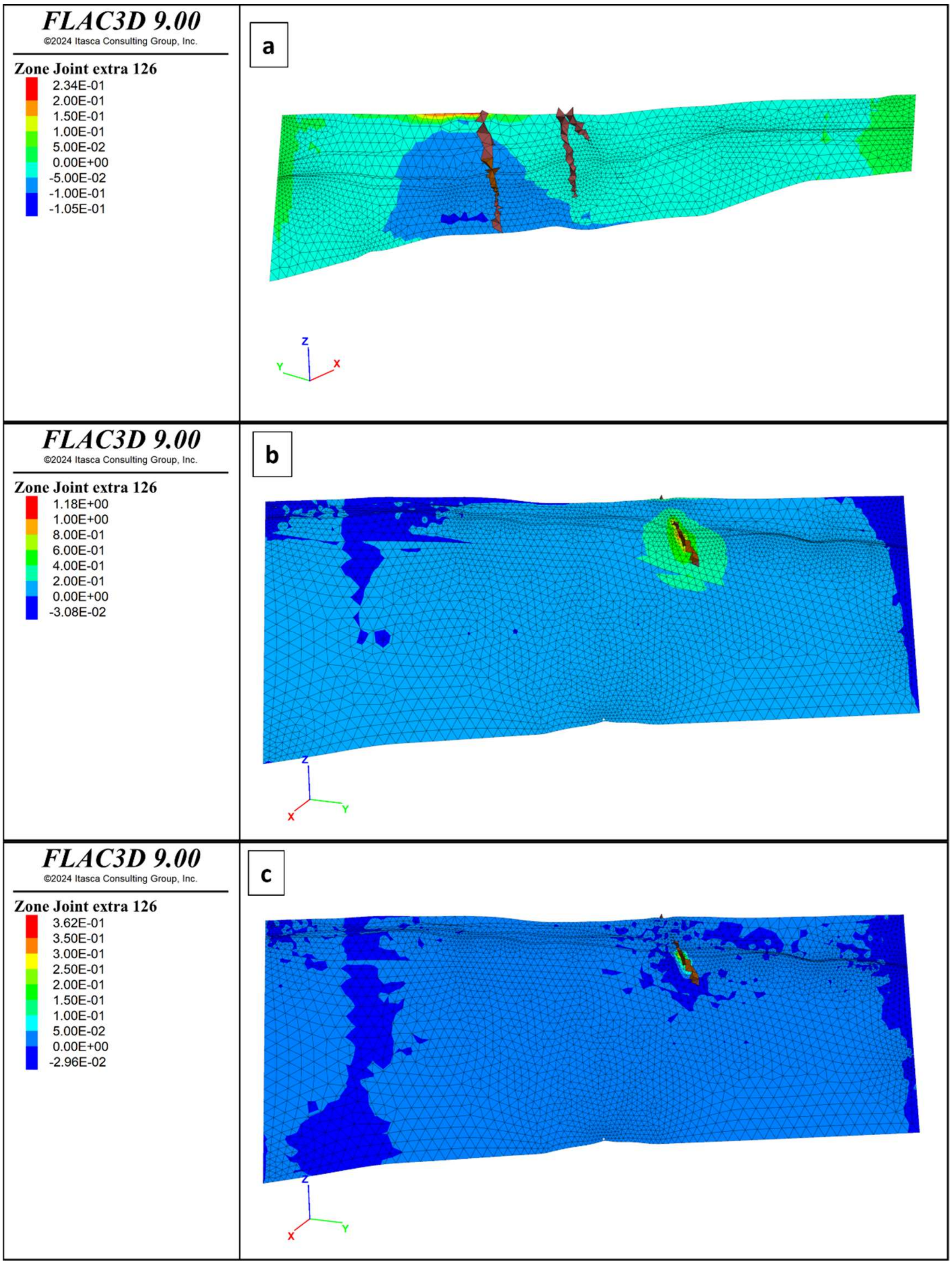

Figure 6-18. Coulomb stress changes during the pilot phase a) on the Carboniferous Normal Faul – at the end of the third rate-step, April 1, 2025 as compared to the Coulomb stress at the beginning of the pilot test. Cold injection, b) on the Western Pop-Up Fault– at the end of the third rate-step, April 1, 2025 as compared to the Coulomb stress at the beginning of the pilot test. Cold injection, c) on the Western Pop-Up Fault,– at the end of the pilot phase, Junel 1, 2025 as compared to the Coulomb stress at the beginning of the pilot test. Cold injection.

.

A long-term injection-production test in combination with a local seismic monitoring network is regarded as a key element of the pilot phase. New data on the relation between production/injection parameters such as temperature, pressure and rate on seismicity rates, hypocenters and magnitudes can be used to test the hypotheses on the mechanisms driving seismicity, and to validate and calibrate model forecasts with observations. Such data can greatly help the understanding of processes driving induced seismicity at the Californië site and in the Dinantian fractured carbonate/Devonian sandstone reservoirs in general. Moreover data on total seismicity rates and frequency magnitude relations and how they relate to operational parameters like pressure, temperature and rates is crucial information for seismic hazard assessment. Additionally, fast models (fully stochastic, semi-analytical or a combination of both) can possibly be developed that capture the key processes, are fast enough to account for (geological) uncertainties and can be used in probabilistic seismic hazard and risk assessment. As these kind of models are robust and efficient, they might be used in near real-time to forecast seismic hazard and in adaptive traffic light systems.

6.5 Conclusion geomechanical modelling

Focus of the geomechanical analysis is on understanding the mechanisms driving induced seismicity and validation of the geomechanical model against the main characteristics of historical induced seismicity.

Apart from the uncertainties related to the geological and flow model, described in the former chapters, uncertainty in the input data for the geomechanical model is specifically related to:

- (thermo)elastic properties of the rocks, frictional properties of the faults
- magnitude of the in-situ stresses are unknown, so the focus of the analysis is on Coulomb stress <u>changes</u>

Figure 6-19 gives an example of the effect of the choice of the history-matched flow scenario on model outcome. It compares maximum Coulomb stress evolution for the three history-match scenarios on the Carboniferous Normal Fault and Western Pop-Up Fault. It shows absolute magnitude of maximum Coulomb stress differs with a factor of 2 depending on choice of flow scenario, but shows consistent trends in the evolution of Coulomb stresses in time for all three scenarios. It is noted that uncertainties in elastic and fault strength parameters have not been accounted for in Figure 6-19. For example, the thermoelastic response of the rocks to temperature changes is linearly dependent on Young's modulus (and thermal expansion coefficient), and thermal stress changes scale linearly with both parameters. Ranges for Young's modulus reported for the Dinantian carbonates are 20 to 70 GPa, so this range would result in a difference of a factor 3.5 for the thermal stresses. The effect of all parameter uncertainties on model outcome should be assessed in a sensitivity analysis, which has not been conducted and is beyond the scope of this study.

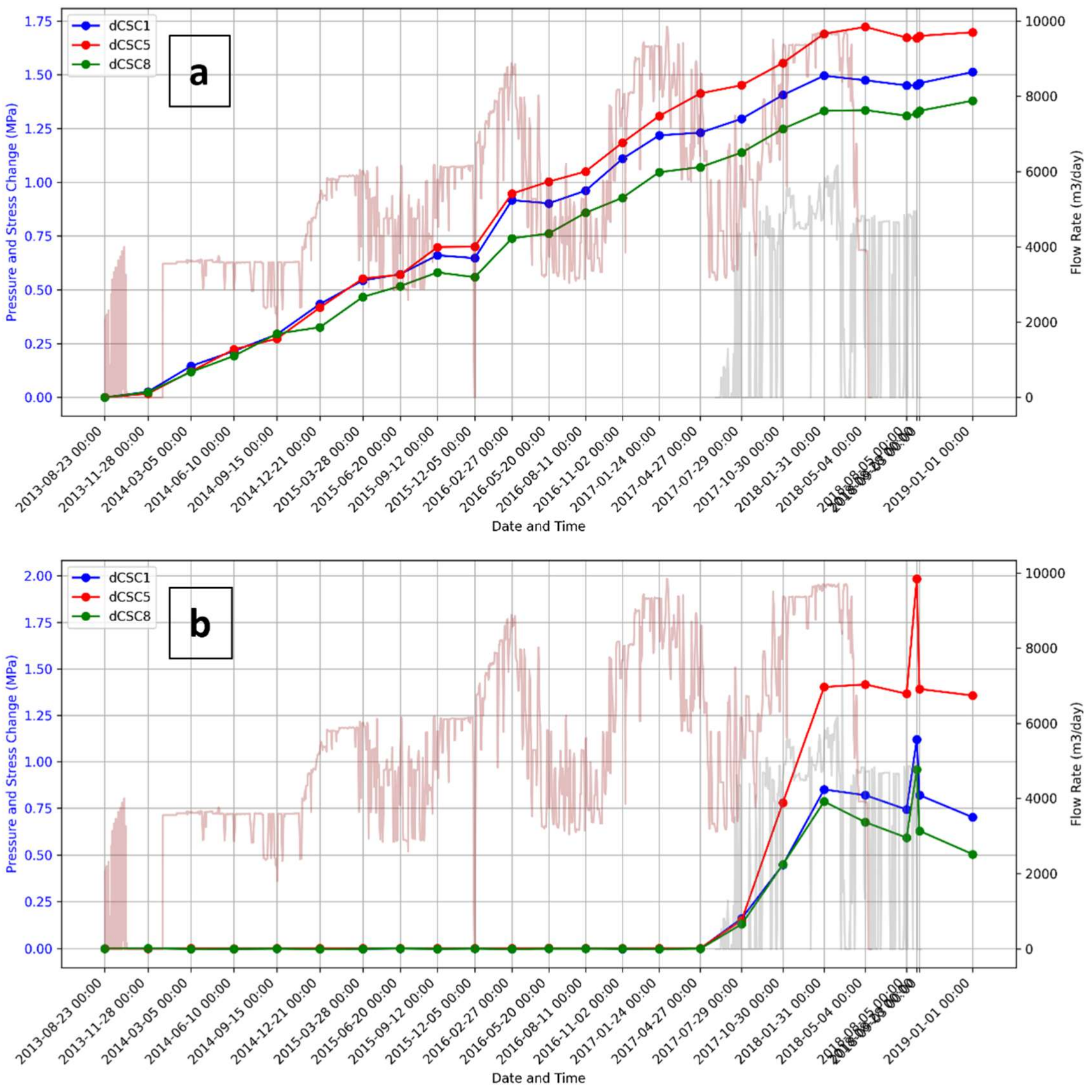

Figure 6-19 Comparison of Coulomb stress evolution with time for history-match scenarios HM1, HM5 and HM8, a) Carboniferous Normal Fault, b) Western Pop-Up Fault.

In Chapter 9 we give an overview of additional data-acquisition, tests and measurements that can be performed in the pilot phase to reduce the above uncertainties.

Despite these uncertainties, general observations and trends from the simulations allow us to gain insights into the contributing mechanisms and their relative impacts.

Results from the geomechanical simulations indicate that:

- Gradual but significant Coulomb stress changes (~1.4 – 1.7 MPa) occur on the Carboniferous Normal Fault due to injection in- and cooling near CAL-GT-03, which destabilizes the fault and promotes fault reactivation between ~1300 and 1800m depth
- Coulomb stress changes are larger on the Carboniferous Normal fault than on the Tegelen Fault (e.g. HM8: 0.2 MPa versus 1.4 MPa), mainly due to the short distance between the Carboniferous Normal Fault and injection well CAL-GT-03 and because

the Tegelen Fault is ‘shielded’ from the CAL-GT-03 injection well by the Carboniferous Normal Fault

- Temperatures on the Carboniferous Normal Fault gradually decrease over time – simultaneously leading to a gradual decrease of normal stresses (unclamping the fault) and an increase of Coulomb stresses on the fault. In terms of magnitudes of stress changes, the effect of pressure fluctuations and poroelastic fluctuations is of a second order. Though the thermal stresses caused by injection in CAL-GT-03 most likely ‘drive’ the reactivation of the fault, they cannot explain the observed relation between the reduction of flow rates and the occurrence of seismicity.

- The correlation between the reduction in flow rates and seismicity observed during the CWG production phase may be explained by the following mechanisms:

    - Mechanism 1: thermal stressing promotes fault reactivation at the Carboniferous Normal Fault close to CAL-GT-03, abrupt small pressure increases due to reduction in flow rates induce seismicity on fault sections which are close-to-critically stressed due to thermal stresses and ‘feel’ the pressure drawdown of the CAL-GT-01 and CAL-GT-04 well.

    - Mechanism 2: aseismic fault slip occurs due to thermal stressing of the Carboniferous Normal Fault close to CAL-GT-03, which causes stress transfer to other (particularly deeper) fault sections. Abrupt small pressure increases due to reduction in flow rates induce seismicity on (deeper) fault sections affected by stress transfer, both on the Carboniferous Normal Fault and the Tegelen Fault (below the intersection with the Carboniferous Normal Fault)

    - Mechanism 3: reduction of flow rates causes an abrupt poroelastic decrease in normal stress at reduced flow rates or shut-in. This mechanism is most likely for faults (segments) with a reduced hydraulic connectivity to well GT-03 (and have been cooled and/or loaded by stress transfer due to the injection in CAL-GT-03)

- The occurrence of the main event is most probably related to a pressure increase in the Carboniferous Normal Fault after shut-in of well CAL-GT-04, which induces seismicity on segments affected and critically-stressed by thermal stresses or (deeper) segments that experienced additional loading due to stress transfer (mechanism 1 / mechanism 2)

- Significant positive Coulomb stress changes (~1-2 MPa) can occur on the Western and Eastern Pop-Up Fault , if these faults are present, or on subseismic faults in the area close to injection well CAL-GT-05. Coulomb stressing caused by pressure diffusion (direct pressure effect) and thermal stresses promote fault reactivation on the Western and Eastern Pop-Up Fault or potential sub-seismic faults in this region. The seismic event with Ml 0.2 on August 25, 2018 occurred during relatively high injection rates in CAL-GT-05 and is probably related to injection activities in well CAL-GT-05.

- The latter mechanism is consistent with the location of the M0.2 event close to CAL-GT-05, but not consistent with the location of the M0.2 event close to the Carboniferous Normal fault. An alternative mechanism, such as stress transfer along the Carboniferous Normal Fault from prior seismic events or aseismic creep, would be needed to explain its location near the Carboniferous Normal Fault.

7 General approach for seismic hazard assessment in Dinantian reservoirs

7.1 Introduction

Seismic Hazard Analysis (SHA) is aimed at providing a description of future ground shaking at a specific site, or for a specific region. This is typically done for one of two reasons:

1) To serve as input for earthquake engineering analyses. Such an analysis is performed to ensure that a given structure can withstand a certain level of ground motion intensity while maintaining a specified level of integrity or performance.
2) To serve as input for Seismic Risk Analysis (SRA). SRA is typically performed to assess the expected damage/causalities/repair costs for a given system in the future. This can for instance be for insurance purposes, or from a regulatory/governmental perspective.

Regardless of whether the SHA is used for an engineering analysis for a specific structure, or for a risk analysis for an entire portfolio of existing buildings/structures/infrastructure, today's best-practice approach to SHA is probabilistic in nature. Probabilistic Seismic Hazard Analysis (PSHA) aims to account for the inherent uncertainty in future earthquake size, location, and resulting shaking intensity (Baker et al., 2021).

Baker and colleagues (2021) describe a PSHA framework in its most basic form (see also Figure 7.1):

1. *Identify all earthquake sources capable of producing damaging ground motions.*
2. *Characterize the distribution of earthquake magnitudes (the rates at which earthquakes of various magnitudes are expected to occur).*
3. *Characterize the distribution of source-to-site distances associated with potential earthquakes.*
4. *Predict the resulting distribution of ground motion intensity as a function of earthquake magnitude, distance, etc.*
5. *Combine uncertainties in earthquake size, location and ground motion intensity, using a calculation known as the total probability theorem.*

This approach essentially boils down into 2 main components:

A. Describing the earthquake source(s) in terms of their magnitude-frequency relation, including the spatial and temporal variability thereof (Steps 1, 2, 3 in the framework)
B. Describing the ground motion intensity distribution, given the occurrence of a seismic event of magnitudes M and distances r. (Step 4 in the framework)

The seismic hazard can then be calculated by the multiplication of A and B (Step 5 in the framework)

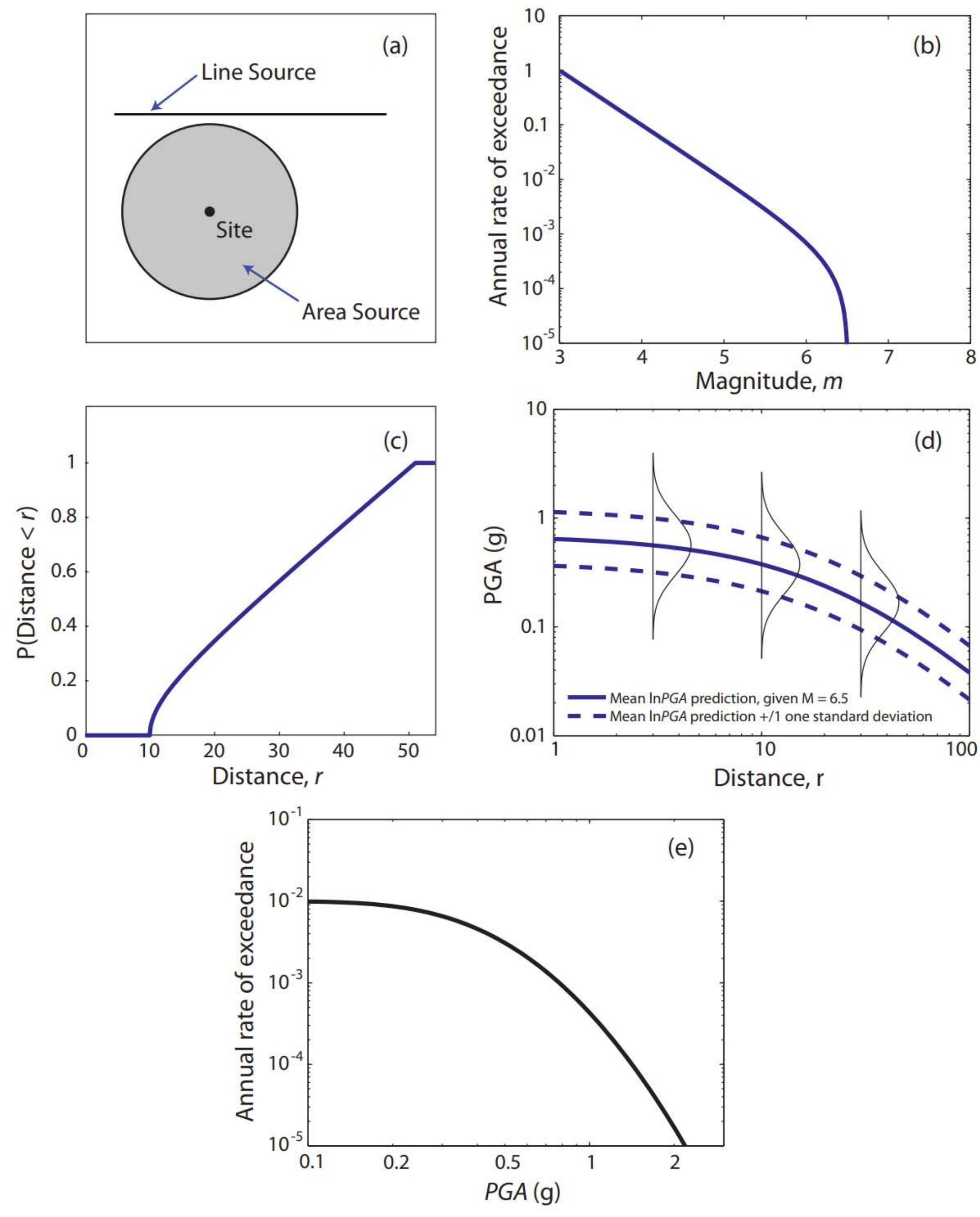

Figure 7-1. From Baker et al. (2013). A schematic description of PSHA, directly corresponding to the on the 5 steps. a) Identify all earthquake sources capable of producing damaging ground motions, b) Characterize the distribution of earthquake magnitudes (the rates at which earthquakes of various magnitudes are expected to occur). c) Characterize the distribution of source-to-site distances associated with potential earthquakes. d) Predict the resulting distribution of ground motion intensity, e) Combine information from parts a-d to compute the annual rate of exceeding a given ground motion intensity.

Optionally, in order to also include a risk assessment on top of the hazard assessment, one could add:

C. Describing the building response in terms of damage or collapse, given the occurrence of a ground motion.
D. Describe the probability of loss of human life, given the occurrence of a damage/collapse state.

Multiplying the hazard by C would yield the risk of damage, and multiplying the hazard by C and D would yield the safety risk.

7.2 PSHA in the Dutch geothermal context

As stated in the introduction, seismic hazard analysis is typically performed to either aid in the design of a single structure, or to assess the risk that a given portfolio of existing structures is exposed to. There are many possible risks metrics that could be assessed in theory, such as safety risk, risk of damage of a certain level occurring, risk in terms of financial loss, etc. Which ones are relevant to explore depends on the local situation.

In the Netherlands, geothermal operations are governed by the Mining Law. This law also governs other operations such as oil and gas extraction, CO2 storage, salt dissolution mining, and natural gas storage. All these types of projects have to show that the safety risk they pose for inhabitants in the vicinity of the project is acceptable, and that they will not cause unacceptable damage to buildings or infrastructure. As such, performing a SHA is required as a first step to assess the damage risk and safety risk for the building and infrastructure stock in the area of influence of the project.

As described above, both hazard and risk are described in rates/probabilities of occurrence of either ground motions of a given severity (hazard) or casualties, building damage or financial consequences (risk). It is crucial to realize that these *probabilities* which are integral to the way we describe hazard and risk are directly tied to the *probabilities of occurrence* of earthquakes of different magnitudes. A main difficulty in the context of geothermal operations in the Netherlands, and in fact for many sub-surface operations in the Netherlands, lies exactly in this step: describing the earthquake source in terms of its magnitude-frequency relation, without having any pre-operational knowledge about the system in terms of its seismicity potential. Without this, a hazard and risk assessment is not possible.

Recently, a new approach (Mijnlieff et al., 2023) for seismic hazard and risk assessment for geothermal operations in the Netherlands was published by TNO-AGE and EBN. In it, the source model is based on the concept of a ‘maximum credible earthquake’ occurring once during the operational lifetime of the geothermal project. The authors of the method describe why this is considered to be a conservative assumption (one that is expected to overestimate the true hazard/risk), and hence why it can be used to assess the seismic hazard and risk of geothermal projects in the context of a license application. However, they also describe that geothermal systems based on fracture permeability and/or in tectonically active areas (such as the projects included in SafeGeo) need a ‘custom’ approach since the standard method for calculation of the ‘maximum credible earthquake’ with the new approach (Mijnlieff et al., 2023) is only suited for matrix-permeable systems in areas without aberrant stress conditions (aberrant conditions due to either prior mining activities or, as is the case for the SafeGeo projects, the tectonic setting that is associated with natural seismicity).

The challenge for such projects that need to perform a 'custom' SHRA, becomes finding a different source model that can be considered to be fit-for-purpose. In general, the following should be kept in mind:

- Different parts of the magnitude-frequency distribution will influence different possible risk metrics and/or norms. For example, small but noticeable earthquakes will impact a metric like 'annual number of felt events' much more than rare but large events. Conversely, the safety risk will likely be much more impacted by those rare but large events and not at all by the smaller events. Risk of light non-structural damage may be more impacted by the magnitudes in between these two. Consequently, depending on the norms that are applied, the magnitude range considered may be narrowed without impacting the resulting hazard/risk calculation (e.g. for a calculation aimed at determining safety risk, defining the rate of occurrence of small earthquakes on the edge of human perceptibility is generally not required).

- In risk calculations in general (also outside of SHRA), it is quite common to apply a so-called logic tree to represent epistemic uncertainty and/or lack of knowledge. This involves incorporation of multiple plausible forecasting models with associated weights. The weight assignment is typically done through a process of expert elicitation. The result of such an expert elicitation and the resulting logic tree is often considered 'the best we can do given the current amount (or lack) of knowledge'. This implies two things:
    - The result is not a representation of 'the truth'. It should not be considered to be set in stone, but rather as something to be updated with some regular interval to reflect a changing state-of-the-art and (hopefully) a larger availability of data.
    - The result is a representation of the state-of-the-art. It is therefore the best, and perhaps only, way to describe the system of interest (in this case the earthquake source) without somehow gathering more data.

Gathering data that is relevant for updating our understanding of the seismic source would require actually performing geothermal operations, for which it is a prerequisite to perform a hazard and risk assessment and test the outcomes against the applicable norms. This does not pose a barrier to either performing geothermal operations, nor to performing a hazard and risk assessment, as long as it is accepted that the results reflect the current state of knowledge to the best of our collective ability.
It becomes problematic when the hazard and risk assessment is expected to provide guarantees or certainties, while by its very nature it is an *assessment* of the hazard and risk.

7.3 Potential way forward

As described in the introduction of this section, state-of-the-art seismic hazard and risk assessment essentially boils down into 2 main components for hazard (A, B) and 3 components for risk of building damage (A, B, C), and 4 components for safety risk (A, B, C, D):

A. Describing the earthquake source(s) in terms of their magnitude-frequency relation, including the spatial and temporal variability thereof
B. Describing the ground motion intensity distribution, given the occurrence of a seismic event of magnitudes M and distances r
C. Describing the building response in terms of damage or collapse, given the occurrence of a ground motion.
D. Describe the probability of loss of human life, given the occurrence of a damage/collapse state.

It is important to notice that B, C, and D are independent of whether an earthquake occurs and also, to a large extent, of its causal mechanism . Consequently, these descriptions of *conditional* ground motion intensity (hazard), and *conditional* risk (both relating to building damage and personal safety) can be determined in a project-independent, subsurface technology-independent manner. Furthermore, these descriptions/conditional probability distributions could be made publicly available (for example as a report or software tool). Performing a seismic hazard and risk assessment for a specific project would then consist of describing the earthquake source and applying these standard descriptions/conditional probability distributions to obtain a ground motion distribution (describing the hazard), buildings damage distribution (describing the building damage risk) and loss of life distribution (describing the safety risk). These quantified risks could then be compared to the applicable norms for license applications.

This brings us to the matter of describing the earthquake source (component A) for any given (geothermal) project. Earthquake hazard and risk are determined by *both*:

1) the probability of seismic events occurring over a range of magnitudes (i.e. component A, a description of the earthquake source).
2) the impact of the effects of these seismic events (i.e. components B, C and D, the conditional hazard and risk)

Since the probability of seismic events occurring (number 1 above / component A) is an integral part of a hazard/risk assessment, it needs to be described, even if there is no observational data to base this description on. In other, non-subsurface applications (for example when building a bridge, or when transporting nuclear waste) similar difficulties often exist in quantifying probability of occurrence of events. It is therefore sensible to see if the methodology applied in these cases could also be applied to geothermal projects.

In these non-subsurface contexts, a conservative (overestimated) expert-estimated probability is often sufficient because it is relatively simple and cheap to take additional safety measures that reduce both the probability of occurrence and/or the magnitude of the effect, leading to an overall acceptable risk level. In contrast, it is much more difficult to assess the effects of any potentially mitigating measures related to subsurface projects. In the case of geothermal, subsurface stress changes can be limited in magnitude by reducing injection/production rates or reinjecting at higher temperatures. However, these directly impact the power/heat generation of the project and therefore the project's (often already marginal) business case. Furthermore, it is unclear what such a decreased stress change would imply for the probability of occurrence of damaging/dangerous earthquakes. Their probability will likely go down, but by how much? This is much more difficult to quantify than the effect of safety measures for nuclear waste transport (e.g. transporting nuclear waste only with clear weather, at night when there is little traffic, driving in a convoy at low speeds in a heavily armoured vehicle and in relatively small quantities at a time). We therefore conclude that the approach of taking a conservative estimate of the probability of occurrence cannot be applied to geothermal projects and a different approach for describing the probability of occurrence is needed.

In the context of seismic hazard/risk assessment, the description of the probability of occurrence of earthquakes over a range of magnitudes is done in using a seismic source model. It goes beyond the scope of this project to develop a generic seismic source model for geothermal systems in fractured reservoirs. However, just as for the components B, C, and D, we believe that there is much opportunity for harmonization between different subsurface application in the seismic source model. Induced seismicity happens due to temperature and or pressure-induced stress changes on pre-existing faults leading to (local) exceedance of the fault's strength, followed by rapid fault movement. This basic physical understanding of earthquake nucleation should underpin any seismic source model. In addition, it is important to continuously calibrate the model's forecasts with observations, which requires sufficient monitoring. Finally, a generic approach consisting of multiple plausible source models in a logic-tree with weights based on expert elicitation is recommended, since this is the current state-of-the-art method to assess the risk for these projects.

Specifically for the matter of defining magnitude-frequency relations for fractured-dominated systems in tectonically active areas, some of the key questions that need to be answered relate to the probability of impacting the release of tectonically accumulated stress (impacting the rate/probability of large magnitude earthquakes and Mmax) , the expected ratio between smaller and larger events (Gutenberg-Richter b-value), and the relation between production/injection parameters such as temperature and rate on the total seismicity rate. Since much of the expert knowledge is likely applicable on a national/regional scale, it is expected that expert elicitation of this kind should not be needed on a project-by-project basis. E.g., it could be valid for the entire Dinantian play in this particular tectonic setting, instead of for a single project in this region. However, in the end, the scope and applicability of the expert assessment should be provided by the experts whose input is used.

Finally, even if the methodology relating to the earthquake source description remains undescribed/up to the individual project owner, there is immense value in harmonizing steps B, C and D. Not only from the perspective of creating a scientifically state-of-the art, nationally applicable, subsurface technology-independent methodology, but also for the simplification this would bring compared to the complex existing workflows and for the improvement this would have on the explainability of decisions regarding license applications, and creating a fair and level playing field for different operators in different types of subsurface projects.

It goes without saying that although there is much inherent value in having an explainable, easy-to-use, publicly maintained, state-of-the-art methodology for seismic risk assessment, the true potential of such a methodology would only be realized if there is a legal framework in which to apply it. Defining norms that give quantitative meaning to the legal requirements contained in Dutch law is a pre-requisite to a successful role of the subsurface in the Dutch energy transition. For general recommendations also see general recommendations in Chapter 9.

8 Seismic monitoring network

8.1 Introduction

Seismicity monitoring data is of great value for improving insight into processes occurring during geothermal operations and their effects on local stresses and seismicity. Improving the link between monitoring data and modelling forecasts will help improve understanding of relations between operations and seismicity. Moreover, a dedicated seismic monitoring network is a key component for risk mitigation if longer injection and production tests are performed. The seismic monitoring network during the operational period of the CWG and CLG systems in 2014-2018 provided essential data for this TKI-study, advancing the understanding of the geomechanical behaviour of the Dinantien in the Californië area. This chapter provides a guideline and possible method for determining the optimum configuration of a monitoring network using the Californië case history as a reference. The actual design depends on the specific geological, technical and non-technical conditions of a project and therefore can vary per case, while alignment and consensus between the objectives and required capabilities of the monitoring network is important.

The accuracy of hypocenter locations is mainly dependent on the geometry of the station network and the type of seismic sensors. Specifically, the spatial arrangement of stations that record an earthquake with a sufficient signal-to-noise ratio is important. The accuracy tends to improve with the use of more stations closer to the epicenter and by placing the seismic sensors below ground. To convert the signals to magnitude and location, a good velocity model of the subsurface is essential, which emphasizes the need for checkshots or VSP. Additionally, the network's detection threshold (magnitude of completeness, MoC) can be enhanced by reducing seismic background noise, which can be achieved through careful site selection or the use of downhole instrumentation. Moreover, seismic signal amplitude is stronger when the recording instrument is closer to the source, so placing instruments near the seismic source can further improve the detection threshold.

In document SGEO-002 – October 30, 2024 by Q-con (Appendix H) a number of options for seismic network configurations are described, including a surface station network, a network based on shallow monitoring wells, a network combining shallow monitoring wells and surface stations and a network including a deep observation well. The seismic monitoring system that is evaluated focuses on detecting and locating earthquakes within an area of approximately 4 km by 6 km, which includes regions of previous seismic activity as well as the vicinity of the CAL-GT-05 injection well. The previous network at the Californië site, consisting of the stations K01 to K05 is used as a baseline configuration. The summary below is largely based on the network configurations described in Q-con in Appendix H. For a more detailed description of network configurations, coordinates, station characteristics, advantages and disadvantages we refer to Appendix H.

Four layouts have been evaluated by KNMI in terms of their magnitude of completeness (MoC) and location error according to the methodology defined in Ruigrok et al. (2023). The location errors are assessed for a local magnitude Ml = 0.5 event at 3 km depth, as this is the depth assumed in Ruigrok et al. (2023). The MoC and error assessments are based on the station configurations (with a number of small adjustments) and noise conditions provided by Q-con (Appendix H).

It should be noted that the magnitude of completeness is expressed in terms of local magnitude Ml, rather than Mw as mentioned in the Q-con report. The method to derive MoC in the Netherlands is based on local magnitude M_L, because this is the magnitude type that is reported in the earthquake catalogue by KNMI. Mw is determined by a different method, the values are not necessarily equivalent. There is no conversion available between ML and Mw for the region of Limburg. Incidentally, e.g. during quiet noise conditions, earthquakes below the MoC can be detected, but the catalogue will not be complete below the MoC. Q-con and KNMI use different percentiles of the noise power spectral density to define the local noise conditions: P95 and P90 respectively. The P95 values from the table in the Q-con report were converted to P90 using P90 = P95 * 0.8457. In addition, an average factor of 6.5 better noise conditions was assumed for the 200 m borehole geophones relative to the surface stations according to Ruigrok et al. (2023).

The KNMI station configuration of 2024 was used (i.e. all stations in the Netherlands for which KNMI receives real-time data) and 4 additional layouts based on the configurations described by Q-con) were considered:

1. 5 original surface stations (§ 8.2)
2. 5 original surface stations with 3 additional surface stations (§ 8.2)
3. All 8 surface stations changed to borehole stations with geophones to a depth of 200m at the same locations as layout 2 (§ 8.3)
4. Combination of 3 borehole stations at 200m depth and 2 surface stations at 5 of the 8 locations of layout 2 (§8.3)

In Section 8.4 the added value of monitoring in deep boreholes is briefly discussed.

8.2 Surface station network: Baseline and extended configuration

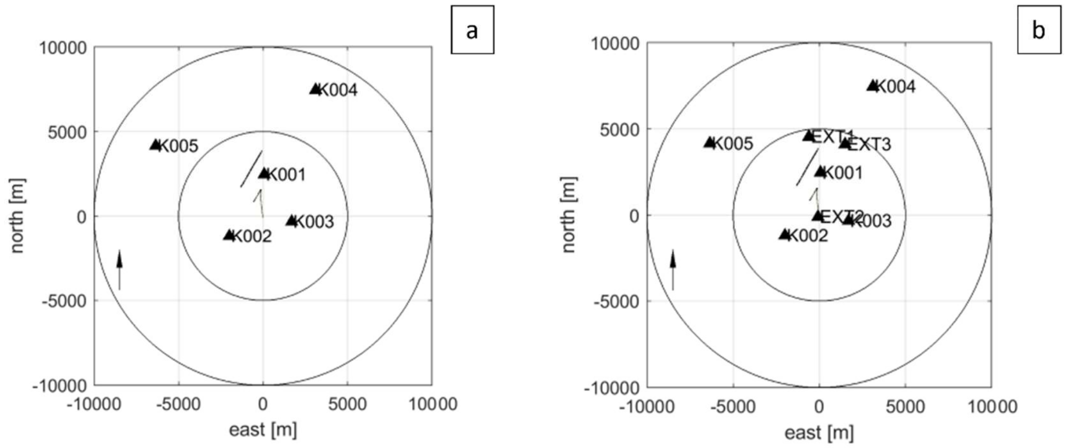

Figure 8-1. a) baseline configuration of previous monitoring network of surface stations K001 – K005. B) extended configuration– with three additional surface stations EXT1 – Ext3. Source: SGEO-002, 2024, Appendix .. Note that station coordinates are shown in a local coordinate system.

The previous network configuration with surface stations K001 – K005 is shown Figure 8-1a. Figure 8-1b shows the extended network configuration comprising three additional surface stations EXT1-EXT3. The surface stations are added to the baseline to improve location accuracy and detection limits near the region of past seismic activity (near the CAL-GT-03 injection well) and near injection well CAL-GT-05. By extending the previous network with additional stations, artificial bias from changes in the network geometry are avoided and a comparison to previous earthquakes can be made more easily.

The MoC, horizontal and vertical location uncertainty (sigma1 and sigmaz) for the baseline configuration with 5 surface stations is shown in Figure 8-2. The MoC for this configuration varies between 0.5 and 1.1 in the area of interest. The MoC is smaller than 0.5 in only a very small region. The location uncertainty in this small area varies between 400 m and 1200 m in horizontal direction and between 800 and 1200 m in vertical direction.

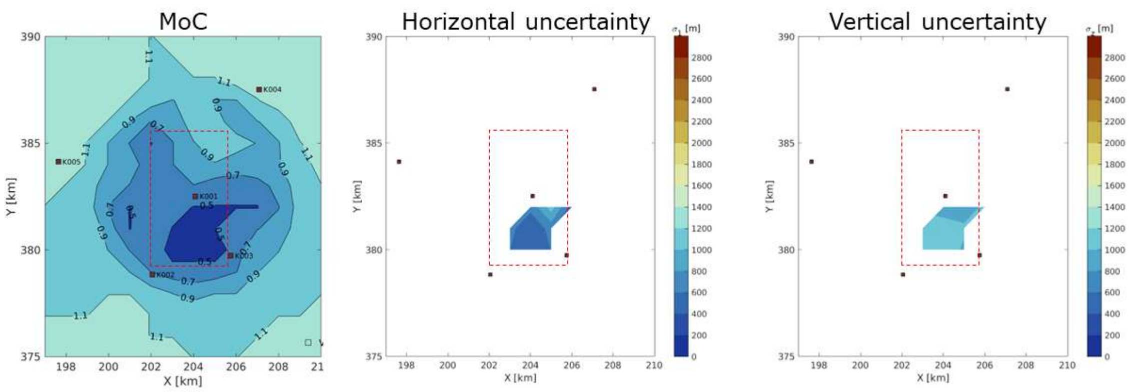

Figure 8-2. Baseline configuration of five surface stations. Left: MoC; middle: horizontal location uncertainty sigma1 for MoC = 0.5; right: vertical location uncertainty sigmaz for MoC = 0.5. This MoC is only detected in the coloured area of the location uncertainty maps. The MoC in the white area is higher than 0.5. The red dashed box approximately indicates the area of interest. Square symbols represent surface stations.

Adding three surface stations (Figure 8-3) improves the MoC a lot. An MoC of 0.5 is reached in almost the entire area of interest..

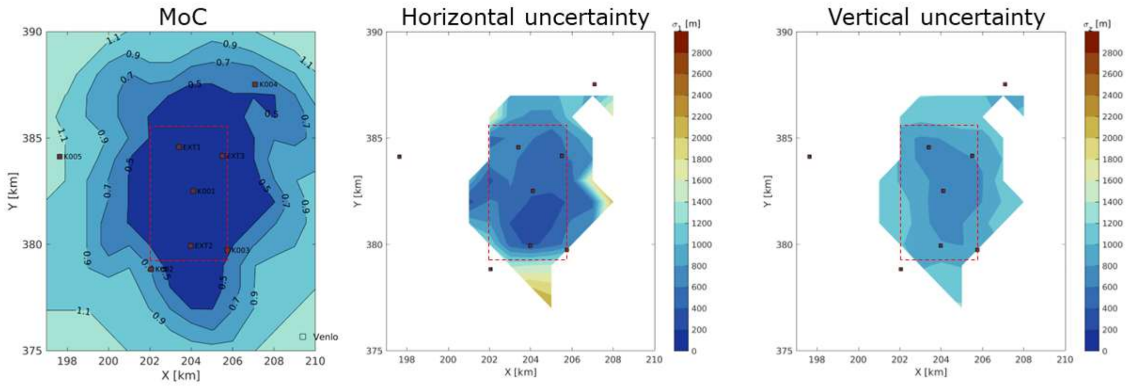

Figure 8-3. Configuration with eight surface stations. Left: MoC; middle: horizontal location uncertainty sigma1 for MoC = 0.5; right: vertical location uncertainty sigmaz for MoC = 0.5. This MoC is only detected in the coloured area of the location uncertainty maps. The MoC in the white area is higher than 0.5. The red dashed box approximately indicates the area of interest. Square symbols represent surface stations.

The main advantages of a surface station network are the relatively low costs of installation and maintenance, as well as the multi-purpose use of measurements. The surface measurements can be used both to locate earthquakes and assess the amplitudes surface ground motions due to the earthquakes in the context of damage assessment. To improve the signal-to-noise ratio, however, and to lower the completeness threshold, placement of sensor in (shallow) boreholes is worth considering. This is done in the next section.

8.3 Shallow monitoring wells: Extended configuration & combined with shallow stations

Detection capabilities of the seismic monitoring network can be improved by deploying monitoring instruments in shallow observation wells. Here we assume geophones are employed at four different levels in observation wells of 200m depth, like generally used by KNMI. As the deepest geophone yields the largest signal-to-noise ratio (SNR), performance is assessed for the deepest geophone. The extended network configuration is evaluated based on Figure 8-1b, where all surface stations are replaced by the 200 m deep shallow monitoring wells. A combination of surface and borehole stations results in a cost-effective network with good location uncertainty and magnitude of completeness. One example of a combined network has been considered.

Replacing the eight surface stations by 200 m borehole stations results in an MoC of 0.5 for a large area, way outside the area of interest (Figure 8-4). The effect on horizontal location uncertainty is also large. The location uncertainty improved to 200-400 m in horizontal direction. In vertical direction the location uncertainty is slightly better: between 400 and 800 m.

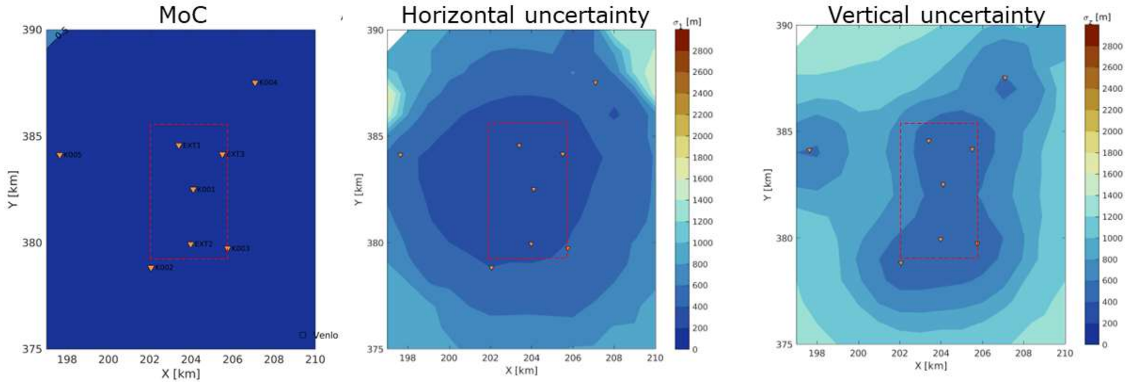

Figure 8-4. Configuration with eight 200 m borehole stations. Left: MoC; middle: horizontal location uncertainty sigma1 for MoC = 0.5; right: vertical location uncertainty sigmaz for MoC = 0.5. This MoC is only detected in the coloured area of the location uncertainty maps. The MoC in the white area (top left corner) is higher than 0.5. The red dashed box approximately indicates the area of interest. Triangle symbols represent borehole stations.

The advantages of shallow borehole stations relative to surface stations include an increased signal-to-noise ratio and, in the current standard setup, some redundancy because of the multiple sensors per borehole. The cost of installation, however, is somewhat higher, and upon failure, the sensors cannot be retrieved and repaired. In the standard KNMI setup, the shallow boreholes are combined with a surface station to also be able to assess the surface ground motions.

Some of the disadvantages can be overcome by installing a network consisting of a mix of surface stations and borehole stations. The locations of the three boreholes were chosen so that the area that is spanned by them includes the area of interest. The two surface stations in the epicentral area will help to constrain the location. With this layout the MoC is 0.5 everywhere in the area of interest, apart from a very small corner (Figure 8-5). The location uncertainty varies between 200 and 600 m in horizontal direction and between 600 and 1400 in vertical direction. This network can be improved by moving the two surface stations more to the north.

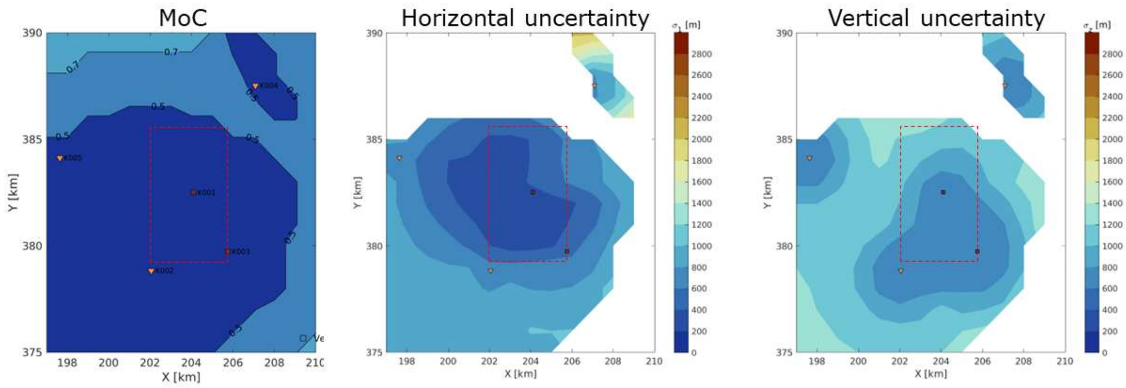

Figure 8-5. Configuration with three 200 m borehole stations and two surface stations. Left: MoC; middle: horizontal location uncertainty sigma1 for MoC=0.5; right: vertical location uncertainty sigmaz for MoC = 0.5. This MoC is only detected in the coloured area of the location uncertainty maps. The MoC in the white area is higher than 0.5. The red dashed box approximately indicates the area of interest. Square symbols represent surface stations, triangle symbols are borehole stations.

8.4 Deep observation well: single geophone and geophone string

The magnitude detection threshold in a deep well is significantly lower compared to the (near-) surface monitoring networks, for two reasons. First the seismic noise related to human activity and weather conditions at the surface is strongly suppressed at depth. Second, if a subsurface sensor is well placed, it may be in a much closer proximity to the source, translating to a lower amount of geometrical spreading and higher amplitudes. Both effects lead to a higher signal to noise ratio and therefore a lower detection threshold.

It should be noted, however, that a reduced detection threshold does not automatically lower the MoC to the same extent, as according to Ruigrok et al. (2023) the MoC is limited to events that are not only detectable, but also locatable. According to Ruigrok et al. (2023) the requirement for MoC is that an event is to be detected at a minimum of 3 spatially distinct stations to allow for a location assessment. A single downhole sensor, or even a single downhole array cannot fully accommodate that.

On the other hand, lowering the detection threshold does improve the statistics of event counts, which is of interest to hazard and risk assessments. Also, when low magnitude events are part of clusters that include events with higher magnitudes, it may still be a possible to locate them with appreciable accuracy. This may include, for example, also the orientation of the seismic motions.

Since the KNMI analysis tools of Ruigrok et al. (2013) currently do not provide completeness and location error assessments for downhole stations, a formal analysis was not performed. Experience from downhole monitoring at the Bergermeer site, however, shows that events with magnitudes down to -2 are regularly detected and located (TAQA, 2023).

For a detailed description and advantages and disadvantages of the different seismic network configurations, we refer to the original Q-con document in Appendix H.

9 Conclusions and recommendations

9.1 Conclusions from subsurface models

In the previous chapters the findings from the geological, velocity, reservoir and geomechanical modelling, along with the associated uncertainties were discussed. The pressure and temperature evolution in the reservoir rocks throughout the historical operational period of the CWG and CLG doublet were modelled and the effect on fault stress changes was assessed. Based on the results of the subsurface models hypotheses regarding the mechanisms contributing to induced seismicity at the Californië geothermal site were formulated.

The key outcomes of the subsurface modelling are:

Four main fault structures have been interpreted at the Californië geothermal sites from the seismic lines, from west to east:

- The main Tegelen Fault structure
- The Carboniferous Normal Fault, i.e. an antithetic fault to the Tegelen Fault
- A possible Western Pop-up Fault, part of a pop-up structure at the eastern part of the sites
- A possible Eastern Pop-up Fault, also part of this pop-up structure

The final 3D geological interpretation presents a logic integration of two end-member interpretations. In the first end-member the Dinantian carbonates are characterised by approximately the same thickness throughout the region, with the observed differences in Dinantian thickness in the wells being attributed to faulting. In the second end-member the Dinantian is characterised by a rapid stratigraphic thickening towards the southwest, combined with components of syn-depositional fault activity, erosion and karstification. The final model contains all faults and a certain amount of stratigraphic thickening. The presence and extent of the pop-up structure in the east and the depth of the Carboniferous Normal Fault are uncertain, due to uncertainty associated to interpretation of the seismic lines. The current 3D- model is a new geological model, based on the information from the wells and seismic lines, including the new SCAN-lines. It is noted that the Carboniferous Normal Fault and the pop-up structure were not included in the former geological interpretations of the site.

A revised velocity model for the Californië sites was constructed consistent with the geological model. This was achieved by populating the interpreted stratigraphy from the revised geological model with P- and S-wave velocities based on separate velocity data, amongst others from the sonic log in CAL-GT-01 and other wells with similar layers and TNO's regional velocity model VELMOD-3.2. The revised velocity model was used for the time-depth conversion of the seismics and to estimate the earthquake hypocenters.

From the velocity modelling it was concluded that:

- New mean hypocenter locations generally lie in the vicinity of the former Q-con locations, but are located more eastward compared to the Q-con locations and have a larger depth spread amongst the 17 events (mean hypocenter depths ~2200-3400 m versus ~2200-2500 m, with the former Q-con locations more closely confined around reservoir depth).

- The new hypocenter of the Ml 0.2 event that occurred on August 25, 2018 in the SafeGeo interpretation is located relatively close to the Western Pop-Up Fault and well CAL-GT-05. In contrast, the original hypocenter interpreted by Q-con for this event is located relatively close to the Carboniferous Normal Fault.

- Error ellipses, and particularly the vertical component, show that the hypocenter location uncertainties are significant. (Standard deviations (marginalized) for the z- direction are between 882m-1088m)

Simulation of the flow and temperature behaviour was done using a dual porosity approach. Three history matched scenarios were created based on different concepts of the distribution of the fracture permeability. The fracture permeability was assumed to be mainly related to the faults from the geological interpretation. The history matching did improve our understanding of the reservoir behaviour on the following points:

- From the PLT information, which shows zones of little to no inflow in both CAL-GT-03 and CAL-GT-05, it is clear that the background permeability in many areas is low. The PLT information in CAL-GT-03 suggests flow is dominated by a small number of highly permeable faults. In CAL-GT-05, the PLT information shows flow in a fracture network over a larger area with thin, low-permeable fractures.

- Satisfactory history matches were achieved with the assumption that there is little permeability in most areas outside the fault zones.

- Some form of fracture flow or dual-porosity is necessary to match the temperature decrease in CAL-GT-01. A single porosity medium would result in the cooling of the entire rock volume, with a cooling front that stays (too) close to the injection well CAL-GT-03.

- Some inflow, either from the bottom or from the sides, appears to be necessary to match the limited drawdown that CAL-GT-04 causes in CAL-GT-01, unless the permeability distribution is very different from what has been assumed here. This could be possible due to permeability related to karst outside of the fault damage zones. In particular this would require much more connectivity between CAL-GT-04 and -05 and much less between CAL-GT-04 and -01, neither of which is supported by the currently available information.

- The pressure behaviour during production appears to be dominated by fracture permeability. The exchange with the matrix is very important for the progress of the thermal front and transient behaviour during well tests.

All three history matched scenarios showed that:

- Cooling is largest in the Carboniferous Normal Fault, because the well CAL-GT-03 intersects this fault and runs parallel to it for a large part. Pressure increase on the Carboniferous Normal Fault is limited to ~5 bar due to the high permeability, and mainly occurs close to the injection well. The models show that deeper sections of the Carboniferous Normal Fault experience a pressure decrease of a few bars, due to production from CAL-GT-01 and CAL-GT-04.

- Cooling on the Tegelen Fault is probably limited, as it is 'shielded' from the injection well CAL-GT-03 by the presence of the Carboniferous Normal Fault. Some cooling is observed in the models, driven by the extraction of cold water by CAL-GT-01 from shallower levels and, to a lesser extent, breakthrough of the cold water injected in CAL-GT-03. A pressure decrease is observed in the Tegelen fault, due to production from wells CAL-GT-01 and CAL-GT-04, which both target the damage zone of the Tegelen Fault. Pressure changes are limited, because of the high permeability of the fault zone.

- The model results showed that the proximity of CAL-GT-05 to the probable Western and Eastern Pop-Up faults causes cooling on these faults. Due to the assumption that the fracture distance is relatively small (smaller than near the Tegelen Fault and Carboniferous Normal Fault), the cooling of the matrix is larger but occurs in a smaller area. The high injection pressure in CAL-GT-05 causes relatively large pressure changes on the pop-up faults (up to ~10-20 bar).

Focus of the geomechanical analysis was on understanding the mechanisms driving induced seismicity and validation of the geomechanical model against the main characteristics of historical induced seismicity. Pressure and temperature evolutions derived from the three different history-matched dynamic reservoir scenarios were used to compute Coulomb stress changes on the four main fault structures. Results from the geomechanical simulations indicate that:

- Positive Coulomb stress changes simulated are largest on the Carboniferous Normal Fault (HM8: ~1.4MPa). These stress changes are significantly larger than on the Tegelen Fault (HM8: ~0.2 MPa), mainly due to the short distance between the Carboniferous Normal Fault and injection well CAL-GT-03 and because the Tegelen Fault is 'shielded' from the CAL-GT-03 injection well by the Carboniferous Normal Fault

- Gradual but significant Coulomb stressing occurs on the Carboniferous Normal Fault, which is mainly caused by a reduction of normal stresses and 'unclamping' of the fault, due to injection in- and cooling near CAL-GT-03. This promotes fault reactivation between 1300 and 1800m depth.

- In terms of magnitudes of stress changes on the Carboniferous Normal Fault, the effect of pressure fluctuations and poroelastic fluctuations is of a second order. Though the thermal stresses most likely 'drive' the reactivation of the fault, they cannot explain the observed rapid seismic response of the system to a reduction of the flow rates.

- The correlation between the reduction in flow rates and seismicity observed during the CWG production phase may be explained by the following mechanisms; the three hypotheses for the causal mechanisms during this phase are summarized below:

- Mechanism 1: thermal stressing promotes fault reactivation at the Carboniferous Normal Fault close to CAL-GT-03, abrupt small pressure increases due to reduction in flow rates induce seismicity on fault sections which are close-to-critically stressed due to thermal stresses
- Mechanism 2: aseismic fault slip occurs due to thermal stressing of the Carboniferous Normal Fault close to CAL-GT-03, which causes stress transfer to other deeper fault sections, either on the Carboniferous Normal Fault or (deeper) sections of the Tegelen fault. Abrupt small pressure increases due to reduction in flow rates induce seismicity on deeper fault sections affected by stress transfer.
- Mechanism 3: reduction of flow rates or shut-in causes an abrupt poroelastic decrease in normal stress. This mechanism is most likely for faults (segments) with a reduced hydraulic connectivity to well CAL-GT-03

- The fault segment on the Carboniferous Normal fault has become (near-)critically stressed due to cooling as a result of injection in well CAL-GT-03, stress transfer and aseismic slip. The pressure decrease caused by production from wells CAL-GT-01 and later well CAL-GT-04 was affecting both the Tegelen Fault and the deeper part of the Carboniferous Normal Fault, providing a stabilizing effect on (deeper) sections of the fault system. During reductions of flow rates and after shut-in of the production wells (first CAL-GT-01, then CAL-GT-04) the stabilising effect disappears. After shut-in of CAL-GT-04 pressure in the Tegelen Fault and the Carboniferous Normal Fault increases to initial reservoir pressure. Coulomb stress increased due to the pressure rise and induced seismicity, including the Ml 1.7 main event, on a segment of the Carboniferous Normal Fault affected by thermal stresses or on a (deeper) segment of the Carboniferous Normal fault and/or Tegelen Fault that experienced additional loading due to stress transfer (mechanism 1 / mechanism 2).

- The simulated pressure changes – and thus also the associated positive Coulomb stress changes – after reduction of flow rates or shut-in of the wells are very small (generally << 1 bar). Rates of stress changes associated to reduction in flow rates however are large as compared to the rate of stress changes associated to thermal loading. Rate-and-state friction theory supports the likelihood of triggering earthquakes to be largely dependent on the rate of pore pressure changes rather than its magnitude (Alghannam and Juanes, 2020).

- Positive Coulomb stress changes (simulated values 1-2 MPa) can occur on the Western and Eastern Pop-Up Faults (i.e. if it is assumed that the pop-up structure is present), or on subseismic faults in the area close to injection well CAL-GT-05. This Coulomb stressing is caused by pressure diffusion (direct pressure effect) in combination with thermal stressing and promotes fault reactivation on the Western and Eastern Pop-Up Fault (i.e. if it is assumed that the pop-up structure is present) or any potential sub-seismic faults in this region.

- The new mean hypocenter locations of seismic events during the CWG doublet operations, the April event and the main event after shut-in of the CLG-doublet are located predominantly to the southeast of CAL-GT-01, close to injection well CAL-GT-

03. Laterally they are located nearby the cooled and stressed fault segment on the Carboniferous Normal Fault, but at a larger depth in the Devonian sandstones. The majority of the locations within the hypocenter location confidence ellipse lie within the Devonian sandstones. The difference between the hypocenter depths and fault segment with highest Coulomb stress can (partially) be related to the uncertainty of the exact position of the Carboniferous Normal Fault, but may also indicate that stress transfer due to aseismic slip plays a role (mechanism 2).

- The seismic event with Ml 0.2 on August 25, 2018 occurred during relatively high injection rates in CAL-GT-05. The new mean hypocenter of this seismic event is located close to CAL-GT-05 and the Western Pop-Up Fault. The combination of high pressures and thermal stressing due to cooling may have caused positive Coulomb stress changes on the Western Pop-Up Fault (assuming it is present) and caused this event (alternatively on the Eastern Pop-Up Fault or a sub-seismic fault near CAL-GT-05).

- The latter mechanism is consistent with the location of the Ml 0.2 event close to CAL-GT-05, but not consistent with a location of the Ml 0.2 event close to the Carboniferous Normal fault as interpreted by Q-con. An alternative mechanism, such as stress transfer along the Carboniferous Normal Fault from prior seismic events or aseismic creep, would be needed to explain its location near the Carboniferous Normal Fault.

Overall, the hypotheses for the mechanisms driving induced seismicity are consistent with the hypocenter locations of the induced events.

Some of the model results are subject to remaining uncertainty, due to the complex geological structure of the fractured, faulted and karstified reservoir, the sparse availability and the quality of the data. In summary, the main uncertainties in the subsurface models are related to:

- The structure of the local geology, including the position and orientation of the different intervals, as well as the presence, position and orientation of the main faults, in particular the presence and extent of the large-scale pop-up structure in the east near the injection well CAL-GT-05 and well CAL-GT-02, and the uncertainty about the depth of the intersection of the Carboniferous Normal Fault with well CAL-GT-03.
- The locations of the hypocenters and in particular the depths of the hypocenters of the seismic events. Uncertainties in hypocenters are strongly related to uncertainties in the P- and particularly the S-wave velocity model.
- The spatial distribution of the permeability which cannot be constrained based on the pressure and temperature in the wells only. Moreover, the reservoir models are based on one single geological interpretation in the final geological model and do not include the possible impact of karst features. This results in uncertainties associated to reservoir flow, particularly the connectivity in the reservoir and in-between the wells.
- Magnitudes of the in-situ stresses and static frictional properties and cohesion of the faults define the initial criticality of the faults. Dynamic frictional properties determine if fault slip will be seismic or aseismic. Little information is available on the magnitudes of the in-situ stress field; no site-specific data on static or dynamic frictional properties are available.
- (Thermo)elastic properties of the rocks, which define the magnitude of the thermo- and poroelastic response of the rock to changes in pressure and temperature. The

thermoelastic and poroelastic responses scale linearly with the Youngs modulus and thermal expansion coefficients of the rocks.

Though it will be impossible to resolve all uncertainties related to the subsurface, additional data acquisition can help to reduce some of these uncertainties, to enable further validation of the models and to 'narrow down' the most likely hypothesis for the induced seismicity at the Californië sites.

9.2 Test phase: data acquisition & testing

Data acquisition during the test phase should focus on reduction of the above uncertainties to further improve our understanding of the subsurface, and on generating data to support relations between operations and seismic response of the system. This would help to provide input for- and enable assessment of the hazards associated to the operations.

Table I.1 in Appendix I gives a general overview of possible tests and measurements that could be performed to reduce the above mentioned uncertainties. The list is based on an inventory of tests and measurements that could be performed during a pilot phase as described in document AGE 22-10/109, dd 21 December 2022. Below, options for data acquisition and tests are highlighted that can offer valuable information in a pilot phase at the Californië site. It is described how data acquisition and test options can contribute to reducing uncertainties in the different models and can serve as input to the seismic hazard assessment.

It is emphasized that the list below summarizes *options* for data acquisition and a practical test phase. The final definition of the pilot phase and the data acquisition, practical injection & production test and monitoring network that are part of it, depends on various operational and non-technical aspects and needs to be approved by the regulator. This definition is outside the defined scope of the TKI-SafeGeo study.

A total of five wells are available for testing, measurements, and monitoring. In an optimal pilot phase, one well is used for injection and another for production, allowing simultaneous monitoring and testing in the other wells. The suitability of the wells should be considered for the pilot phase, especially for the injection/production test. Currently, CAL-GT-05 is the only operational injector since CAL-GT-02 is inaccessible at reservoir level and CAL-GT-03 is not recommended due to its intersection with the Carboniferous Normal Fault and proximity to the Tegelen Fault. One obvious option is to inject into CAL-GT-05 and produce from CAL-GT-04, using the other wells for testing, data acquisition and monitoring. Alternatively, drilling of a new well or a sidetrack for CAL-GT-02 as injector could be considered. However, cooling of the fault sections near the wells GT-03 and GT-01 should be avoided, due to previous seismic reactivation and potential critically-stressed conditions. Production from CAL-GT-01 (and from CAL-GT-04, but to a much smaller extent, as its distance from the cold front is much larger) could further propagate the thermal front along the fault. Additionally, wells GT-02 and GT-05 may be located near a potential eastern pop-up structure (with its presence and extent still uncertain). These factors must be carefully considered when designing the test phase.

Data obtained from the data-acquisition and test options for the pilot phase are site-specific, but information and 'lessons-learned' are also valuable for the future development of fractured and faulted Dinantian / Devonian reservoirs in other parts of the Netherlands.

A practical injection & production test is considered as the ‘core’ of the technical test phase and is described in section 9.2.1. It is important to recognize that injection & production operations during such a test phase can induce (micro-)seismicity. Therefore, it is crucial to define what constitutes an acceptable level of seismicity before the start of the test phase. This definition cannot be established within the scope of the TKI SafeGeo project alone, as collaboration and discussion with additional parties is necessary to address this issue.

Data acquisition and tests that could be considered to further constrain the geological, velocity, reservoir and geomechanical model are described in the subsequent paragraphs 9.2.2 to 9.2.4. These sections summarize the various options for data acquisition and testing, organized by subsurface model type. Options are listed (where possible) based on costs, time investment and degree of complexity. In some instances, data acquisition serves multiple purposes and may therefore be categorized under several headings. For example, 3D data contributes to both the geological and SHA models, as it enables a more detailed mapping of the extent and architecture of the fractures. To avoid repetition, such tests are described once, with a note that they can be applied to other areas as well. Additionally, some data acquisition and testing methods are most effective when used in conjunction with other measurements.

9.2.1 Data acquisition and tests as input for seismic hazard assessment

Injection / production test with continuous seismic monitoring
Aim: To test and monitor the relations between production and injection activities / strategies and seismicity, see also below for seismicity monitoring
An injection/production test, combined with seismic monitoring can be used to test the relations between operations and seismicity, and how operational strategies affect the seismic response of the system. This provides essential information for the seismic hazard assessment and risk mitigation, to evaluate if safe geothermal operations at the Californië site using a Traffic Light System are possible, and to further calibrate the subsurface models. In section 6.4 an example is given of a test-phase of approximately a year, with a ramp up of flow rates, starting with a phase of warm injection and followed by cold injection to test the response of the system. It is noted that the duration of 1 year and the operational strategy described in section 6.4 is an example used to model and analyse the response of the faults.
A phased, iterative approach is recommended to ensure flexibility in adjusting plans and operational strategies as new data becomes available. The expected duration of such a test will exceed that of a standard well test, amongst others because reservoir cooling (leading to fault reactivation) is a gradual process. To gather sufficient data on the relationship between operations and seismicity, it may be necessary to extend the test phase over several years. The actual rates, strategy and duration for such a test should be decided upon by the operator considering requirements and boundary conditions set by the regulator, but will in practice also depend on the site's behaviour during the test. Based on the (seismic) response of the site and learnings/knowledge built up during the test phase, a regular update of the test design may be needed. As injection/production operations may induce (micro-)seismicity it will require an assessment of the seismic hazard, the incorporation of a risk management protocol, a communication plan and the establishment of a seismic monitoring network, which must ultimately be approved by the regulator.

Seismicity monitoring:
Aim: Seismicity monitoring data is of great value for improving insight into processes occurring during geothermal operations and their effects on local stresses and seismicity. Better linking monitoring data to modelling forecasts will help to improve understanding of relations between operations and seismicity. Moreover, a dedicated seismic monitoring network is a key component for risk mitigation for an injection and production test to be performed.
<u>Seismic monitoring during short-term and long-term injection/production test.</u> As mentioned above, a long-term injection/production test will need establishment of a seismic monitoring network. The accuracy of hypocenter locations is mainly dependent on the geometry of the station network—specifically, the spatial arrangement of stations that record an earthquake with a sufficient signal-to-noise ratio. To convert the signals to magnitude and location, a good velocity model of the subsurface is essential, which emphasizes the need for a checkshot or VSP. Additionally, the network's detection threshold (magnitude of completeness) can be enhanced by reducing seismic background noise, which can be achieved through careful site selection or the use of downhole instrumentation. Moreover, seismic signal amplitude is stronger when the recording instrument is closer to the source, so placing instruments near the seismic source can further improve the detection threshold.

Several options for network configurations, their magnitude of completeness and location errors have been described in Chapter 8. For a method to identify an optimum network configuration and detailed description and advantages and disadvantages of the different seismic network configurations, the reader is referred to this chapter.

The design and specifications of the seismic monitoring network must align with the requirements of the risk management system, such as the Traffic Light System (TLS), which should be discussed with- and approved by the regulatory authorities. Furthermore, a seismic monitoring network with a low detection threshold and low magnitude of completeness (MoC) will enable the analysis of the frequency-magnitude relationship and changes in this relation, associated to the operational activities. Reduction of the hypocenter location error, in particular the vertical component is important to further constrain the area that is reactivated – providing valuable information to test and validate the model outcomes, thereby enhancing our understanding of the underlying mechanisms driving seismicity. The actual design of a monitoring system can also depend on local, technical and non-technical considerations. In this perspective consensus among the stakeholders regarding the objectives of the measurements and the capabilities of the system is required.

A <u>null-measurement</u> of seismicity refers to the situation before the start of the geothermal operations. In practice, reference to the past situation is not feasible anymore, as the subsurface conditions have already changed due to the past operations at the Californië site. Fault reactivation potential has been altered (and will remain so for a considerable time) as rocks and fault segments have been locally cooled during past operations. The template matching by Qcon (Q-con report SGEO001, December 6, 2023, see Appendix F) did reveal one single micro-seismic event with magnitude Ml that occurred on February 7, 2022, after the shut-in of the CLG-doublet. This event was detected on the two seismic stations (K01 and K03) remaining at that time, which limited the accuracy with which the event could be located. If the original design of the monitoring network is chosen, monitoring before restart of injection/production is not necessary. If the monitoring network is adapted to a new configuration with lower detection limits, additional monitoring before restart of injection/production could be useful, as it would enable detecting any changes in the seismicity rate due to the restart of injection operations.

A long-term injection-production test in combination with a local seismic monitoring network is regarded as a key element of the pilot phase. New data on the relation between production/injection parameters such as temperature and rate on seismicity rates and magnitudes can be used to test the hypotheses on the mechanisms driving seismicity, and to validate and calibrate model forecasts with observations. Such data can greatly help the understanding of processes driving induced seismicity at the Californië site and in the Dinantian fractured carbonate/Devonian sandstone reservoirs in general. Moreover data on total seismicity rates and frequency magnitude relations and how they relate to operational parameters like pressure, temperature and rates is crucial information for seismic hazard assessment. Additionally, fast models (fully stochastic, semi-analytical or a combination of both) can possibly be developed that capture the key processes and are fast enough to account for (geological) uncertainties and could then be used in probabilistic seismic hazard and risk assessment. As these kind of models are robust and efficient, they might be used in near real-time to forecast seismic hazard and in adaptive traffic light systems.

9.2.2 Data acquisition related to geology and hypocenter locations of seismic events

Petrographic analysis of cuttings
Aim: to reduce uncertainties associated to the vertical position of the Carboniferous Normal Fault
Petrographic analysis of cuttings of the Pont d'Arcole interval at well CAL-GT-03. The depth interval in well CAL-GT-03 that in the current model is interpretated as the Pont d'Arcole is characterised by a deviating Gamma-Ray log signature. An explanation could be that the Pont d'Arcole is (partly) faulted out in this well and that the relatively high GR-values, which are now observed below the Dinantian, are in fact part of the damage zone of the Carboniferous normal fault. This could add certainty to the position of the Carboniferous Normal fault. Though the analysis might not give absolute clarity on the presence of a fault damage zone, it is worth to give it a try, as it would be relatively cheap.

Checkshot or Vertical Seismic Profiling (VSP) and / or density-sonic log
Aim: to reduce uncertainties in geological model and hypocenter locations
At the moment the acoustic velocities of the rocks are uncertain. A better quantification of the velocities will lead to more certainty in the seismic interpretation, both in terms of fault presence, orientation and dip of faults, as orientation and dip of geological layers as well as hypocenter locations. A checkshot or Vertical Seismic Profile (VSP) study could be considered to get better constraints on the interval velocities of the Paleozoic and Mesozoic strata. This could be combined with a dipole-sonic-density log over the entire borehole-interval to obtain better constraints on the interval velocities of the reservoir layers and overburden. Dipole sonic well log data can provide compressional and shear wave velocities (shear wave velocities are mostly lacking). Acquiring and accommodating new S-wave velocity data can further enhance the S-wave velocity model, which can be used to constrain hypocenter locations of seismic events. Additional information on heterogeneities in the velocity structure could be gathered if these tests were performed at several well locations.

Additional seismic data
Aim: Reduce uncertainties in geological framework, improve velocity model and localization of events
New seismic data (a 2.5D and particularly a 3D seismic survey) can help increase the certainty of the seismic interpretation and would help to further scrutinize the actual geological models. It will give additional information on the location, orientation and particularly the extent and 3D-architecture of the faults (e.g. the presence and size of the possible pop-up structure in the east, which is located close to the injection well CAL-GT-05 and well CAL-GT-02) and the depths of the geological layers. It may also allow delineation of karstified areas. The presence and size of the faults is important information for the seismic hazard assessment. Based on this information, the velocity model can be updated, which will lead to less uncertainty when calculating/estimating the hypocenter locations. Focus should be on the imaging of the Paleozoic interval. For the current 2D seismic data available, this interval is often not well imaged. We note that even on 3D-seismics sub-seismic faults will not be detected (e.g. the Ml 1.7 seismic event can be induced on a fault structure of several tens of meters – which would not be visible on 3D seismics). In practice, it is often the case that these subseismic fault structures are only highlighted by the occurrence of the seismic events itself. For the Dinantian / Devonian geothermal play in general, a 3D seismic campaign would give insight into the added value of 3D seismics for the geological characterisation complex reservoirs

9.2.3 Data acquisition and tests related to reservoir characterisation

Measurements and tests to characterise the flow and temperature characteristics of the reservoir
Aim: reduce the uncertainty on the dual porosity behaviour, faults and connectivity between the wells
Because of the historical production, the uncertainty in the bulk flow properties at the wells is relatively low. For the seismicity modelling however, the temperature distribution is very important, which depends strongly on the fracture network and dual porosity behaviour, as well as on flow through karstified zones.

Well tests with down hole sensors, of sufficient duration and with possible packers limiting the well bore storage and possibly also limiting the length of the inflow zone, could provide more information on dual porosity behaviour and possibly reservoir boundaries. The required duration depends on the set-up of the test and can be estimated using a model tuned based on earlier well tests. Results from the current models suggest at least a shut-in period of several days to weeks for the 4-day injection test. It is unlikely that the presence of faults can be identified from well tests because most faults appear to be permeable. It will probably be a challenge to achieve sufficient accuracy in the well tests due to the thickness of the inflow zones. For wells CAL-GT-03 and CAL-GT-04 which both can have flow behind the casing, well tests will always be difficult to interpret.

Interference tests (with downhole pressure sensors) could provide useful information on the connectivity between the wells. Such tests could provide evidence of high-permeability flow paths related to larger fault structures such as WPF and EPF between CAL-GT-02 and CAL-GT-05. Also a better estimate of the connectivity between CAL-GT-04 and 05 could help constrain the permeability distribution. Optionally, adding monitoring of the production temperature could possibly provide additional information, in particular between CAL-GT-01 and 04 and between CAL-GT-02 and 05.

Temperature surveys in the producers can reduce the uncertainty in reservoir temperature and surveys in the injectors can provide additional information for history matching. Reduced uncertainty in the temperature gradient will help constrain the flow properties.

Additional test in the wells: thermal back-production test and tracer test
Aim: reduce the uncertainty about the (near-well) fracture network architecture
A thermal back production test or push-and-pull tracer test can both provide information about the permeability distribution and fracture network around the well. These tests require monitoring along the length of the inflow zone (e.g. DAS for temperature). For the injectors, a back production test can be performed to test the cooled area around the well. Additionally salinity can also be monitored during a back production test, because in both injection wells, the injected brine had a different salinity compared to the in-situ brine.

9.2.4 Data acquisition and tests related to geomechanical characterisation

In-situ stress measurements
Aim: Reduce uncertainties related to the in-situ stress field, affecting initial criticality of the faults

Density logs in the wells to compute vertical stress.

Advanced well testing such as described for CAL-GT-05 in section 6.2.3 could be considered to constrain the in-situ stress field, as a sudden increase in flow rates can be indicative of fracture opening and exceedance of Shmin. It is noted that low gradients for Shmin were obtained for CAL-GT-05 (resulting in (more than)-critically stressed faults, which may indicate the method provides a lower bound for Shmin.

A dedicated minifrac test with packers in one of the boreholes could be considered, conducted not too close to a fracture, to determine the magnitude of the minimum horizontal stress Shmin, can help constrain the in-situ stress field and give insight into the initial criticality and reactivation potential of the different faults. The minifrac test would ideally be combined with an (already existing) image log, density log, sonic, caliper. Stress tests at multiple intervals could provide information on decoupling of the stress field, e.g. with depth or between formations. It is noted here that it is generally more difficult to constrain Shmax- which would require information on the size of the break-outs and detailed information on the strength of the rocks at the tested depth interval. Moreover, initial criticality and fault reactivation potential depend on the combination of in-situ stress and fault strength (defined by the static friction and cohesion of the fault).

Geomechanical measurements on core samples of the Dinantian carbonates and Devonian sandstones
Aim: Reduce uncertainty related to the (thermo-)elastic properties of the rocks, in particular for the Dinantian carbonates and Devonian sandstones
The Dinantian and Devonian sections of the wells at the California sites have not been cored, and as such, there is limited site-specific information on the hydrological and

geomechanical properties of these rocks. Experiments on core samples (specifically) from the Dinantian carbonates and Devonian sandstones would provide valuable input for the dynamic reservoir and geomechanical models. E.g. magnitudes of thermo- and poroelastic stress changes scale linearly with elastic Young's modulus and thermal expansion coefficient. Currently, the only available site-specific geomechanical data comes from sonic velocity measurements. While these measurements can be used to assess dynamic elastic parameters, no local empirical relations are available to derive static elasticity parameters, which is important input for geomechanical modelling. Soustelle (2023) demonstrated that general empirical relations from literature, such as those used for the Balmatt site, differ significantly (by a factor of almost 2) from the empirical relations derived in the lab from Dinantian samples. Site-specific (thermo-)elastic parameters (Young's modulus, Poisson's ratio, Biot coefficient, thermal expansion coefficient) can be derived from experiments of core samples. Moreover, through combining information from sonic logs with experimental data, local empirical relations between static and dynamic parameters can be established, which could be of added value for other geothermal sites in similar Dinantian and Devonian sandstone reservoirs.

Additionally, understanding the frictional and strength behaviour of the rocks and faults in the Devonian and Dinantian formations, including their differences, is important. Dinantian rock samples from other locations are currently used in a PhD-study at Delft University of Technology for testing of fault frictional behaviour. Core samples could possibly be tested in this PhD-study.

Additionally, core samples could be tested to derive hydrological and thermal parameters, in particular for the Devonian sandstones.

To conduct these experiments, sidewall samples or sidetrack cores are necessary, or alternatively, analogue samples from other sites with similar geological characteristics could be used for comparison.

9.3 General recommendations for geothermal projects in fractured reservoirs in a tectonic setting

- Thorough data acquisition prior to projects in fractured reservoirs in a natural tectonic setting is essential to ensure that well trajectories relative to larger fault structures can be properly assessed to enable more accurate modelling with reduced uncertainties and to allow for better analysis of the causes of seismicity and potential mitigation strategies. Furthermore, it is essential to establish a local seismic monitoring network prior to the project, including baseline measurements. This network ensures continuous monitoring of developments, timely intervention if necessary, generates data as input to seismic hazard assessment and the possibility to assess and implement mitigation measures.

- Injection wells need to be placed at sufficient distance (based on modelling or practical experience) of major fault structures. Injection in CAL-GT-03 into the Carboniferous Normal Fault caused significant cooling and thermal stress changes on this fault and this is likely one of the driving mechanisms of fault reactivation. Moreover, this study emphasizes the need for injection wells to be placed sufficiently far from the production well and the fault zone from which it produces, to prevent cooling of the fault. Without this separation, the fault may experience both thermal stress and rising pressure upon shut-in, eliminating the possibility of mitigation. Therefore, it is also important to monitor for thermal breakthrough.

- Model results and observations indicate that there is interference between the geothermal operations at the CWG and CLG geothermal sites, particularly via the fault zone of the Tegelen and Carboniferous Normal Fault. It is important to account for potential interference between different geothermal sites when planning geothermal operations in faulted and fractured reservoirs.

- A correlation is observed between reduction of flow rates and the occurrence of seismicity. Model results suggest that rate-effects may play a role and relatively rapid changes in pore pressures, and potentially rapid changes in poroelastic stresses, can cause a seismic response. It is recommended to avoid instantaneous shut-in of the wells and rapid changes in flow rates, to reduce the rate of pressure rise and poroelastic unloading.

- Recommendations for seismic hazard assessment:

    - A general framework for seismic hazard assessment for geothermal in the Dinantian carbonates in areas with natural seismicity is proposed. This framework is based on a widely accepted approach for probabilistic seismic hazard assessment. A key component of the seismic hazard assessment is a site-specific seismic source model, which relies on a physical understanding of the mechanisms driving seismicity at the geothermal site. The multiple causal mechanisms identified in this study provide crucial input for this seismic source model. It is recommended to use a logic-tree with multiple plausible source models, weighted based on expert elicitation. Continuous calibration of model forecasts with observations is essential, requiring sufficient monitoring, and emphasizing the importance of practical injection/production test phases and a robust monitoring network. For defining magnitude-frequency relations for fracture-dominated systems in tectonically active areas, key questions include the probability of impacting the release of tectonically accumulated stress (affecting the rate/probability of large magnitude earthquakes and Mmax), the expected ratio between smaller and larger events (Gutenberg-Richter b-value), and the relation between production/injection parameters such as temperature and rate on the total seismicity rate.
    - Harmonization of SH(R)A across sub-surface applications is possible and useful. A large part of seismic hazard assessment (and seismic risk assessment) is independent of whether an earthquake occurs and what its source is. Descriptions of *conditional* ground motion intensity (hazard), and *conditional* risk (both relating to building damage and personal safety) can be determined in a project-independent, subsurface technology-independent manner.

10 References

- Alghannam, Maryam & Juanes, Ruben. (2020). Understanding rate effects in injection-induced earthquakes. Nature Communications. 11. 3053. 10.1038/s41467-020-16860-y.
- Anselmetti, F. S., & Eberli, G. P. (1999). The velocity-deviation log : A tool to predict pore type and permeability trends in carbonate drill holesfrom sonic and porosity or density logs. AAPG Bulletin, 83(3), 450–466. https://doi.org/10.1306/00aa9bce-1730-11d7-8645000102c1865d
- Baisch, S. & Vörös, R., 2019. Earthquakes near the californie geothermal site: August 2015 – November 2018 (No. CLGG005). 50.
- Baisch, 2023. Californië Seismicity – Template Matching. Report SGEO001, December 6, 2023.
- Baker, J., & Bradley, B., Stafford, P. (2021). Seismic Hazard and Risk Analysis. 10.1017/9781108425056.
- Bakx, E., Wassing, B., Buijze., B. Formation, lithology and region-specific minimum horizontal stress field in the Netherlands. Implications for fault stability in geothermal doublets.
- Batzle, M., & Z. Wang, 1992. Seismic properties of pore fluids. Geophysics, Vol. 57, 1396-1408.
- Billi, A., F. Salvini and F. Storti, 2003. The damage zone-fault core transition in carbonate rocks: implications for fault growth, structure and permeability. *J. of Structural Geology*, vol. 25, p. 1779-1794.
- Bless, M.J.M., Bouckaert, J., Bouzet, Ph., Conil, R., Cornet, P., Fairon-Demanet, M., Groessens, E., Longerstaey, P.J., Meessen, J.P.M.Th., Paproth, E., Pirlet, H., Streel, M., Van Amerom, H.W.J. &Wolf, M., 1976. Dinantian rocks in the subsurface North of the Brabant and Ardenno-Rhenish massifs in Belgium, the Netherlands and the Federal Republic of Germany. Mededelingen Rijks Geologische Dienst 27: 81–195.
- Bless, M.J.M., Bouckaert, J., Conil, R., Groessens, E., Kasig, W., Paproth, E., Poty, E., van Steenwinkel, M., Streel, M., Walter, R., 1980. Pre-Permian depositional environments around the Brabant Massif in Belgium, The Netherlands and Germany. Sediment. Geol. 27, 1–81.
- Bouckaert, J., Dusar, M., 1987. Arguments géophysiques pour une tectonique cassante en Campine (Belgique), active au Paléozoique supérieur et réactive depuis le Jurassique supérieur. Ann. Soc. Geol. Nord 106, 201–208.
- Bouroullec, R., Nelskamp, S., Kloppenburg, A., Abdul Fattah, R., Foeken, J., ten Veen, J., Geel, K., Debacker, T., Smit, J., 2019. Burial and Structural Analysis of the Dinantian Carbonates in the Dutch Subsurface. Report by SCAN.
- Broothaers M. & Laenen B. (2010). Geologisch onderzoek term geothermie Californië. Studie uitgevoerd in opdracht van Wijnen Groep c.s. 2010/SCT/R/096.
- Broothaers, M. and H. Ferket, 2011, Toelichting Geologie voor de Boringen van Californië Wijnen Geothermie, tussentijds rapport Vito, 34pp.
- Buijze, L., van Bijsterveldt, L., Cremer, H., Paap, B., Veldkamp, H., Wassing, B., and Ter Heege, J. (2019) Review of worldwide geothermal projects: mechanisms and occurrence of induced seismicity. TNO-report 2019 R100043. https://www.nlog.nl/scan.
- Burghout, L., Vorage, R., and Broothaers, M. (2019). Koepelnotitie Aardwarmtewinning en Seismiciteit Californie Lipzig Gielen Geothermie BV.

- Carlson, T., 2019. Petrophysical Report of the Dinantian Carbonates in the Dutch subsurface. Report by SCAN.
- Choi, J., Edwards, P., Ko, K., Kim, Y., 2016. Definition and classification of fault damage zones: A review and a new methodological approach. Elsevier, 70-87.
- Deckers, J., Rombaut, B., van Noten, K., Vanneste, K., 2021. Influence of inherited structural domains and their particular strain distributions on the Roer Valley Graben evolution from inversion to extension. Solid Earth, 12, 345–361. https://doi.org/10.5194/se-12-345-2021
- Deckers, J., Rombaut, B., Broothaers, M., Dirix, K., Debacker, T., 2023. New 3D fault model for eastern Flanders (Belgium) providing insights on the major deformation phases in the region since the late Paleozoic. Journal of Structural Geology 166, 104779. https://doi.org/10.1016/j.jsg.2022.104779
- De Simone, S., Darcel, C., Kasani, H. A., Mas Ivars, D., and Davy, P.: Equivalent Biot and Skempton coefficients for fractured rocks , EGU General Assembly 2023, Vienna, Austria, 24–28 Apr 2023, EGU23-14955, https://doi.org/10.5194/egusphere-egu23-14955, 2023.
- Doornenbal, J.C., Middelburg, H., de Haan, H., and Botz M., 2020, VELMOD-4, TNO 2020 R10558
- Duin, E.J.T., Doornenbal, J.C., Rijkers, R.H.B., Verbeek, J.W., Wong, Th,E., 2006. Subsurface structure of the Netherlands – results of recent onshore and offshore mapping.
- Fetkovich, M. J. “A Simplified Approach to Water Influx Calculations - Finite Aquifer Systems,” Journal of Petroleum Technology, (1971) 23, No. 7, 814-828.
- Fraser, A.J., Gawthorpe, R.L., 1990. Tectono-stratigraphic development and hydrocarbon habitat of the Carboniferous in northern England. In: R.F.P. Hardman, Brooks, J., (eds.). Tectonic Events Responsible for Britain’s Oil and Gas Reserves. Geological Society London, Special Publications, V. 55, pp. 49-86.
- Geluk, M., Dusar, M., de Vos, W., 2007. Pre-Silesian. In: T. Wong, D. Batjes & J. de Jager (eds.). Geology of the Netherlands. Royal Netherlands Academy of Arts and Sciences, Amsterdam, 27-42.
- George, G.T., Berry, J.K., 1997. Permian (Upper Rotliegend) synsedimentary tectonics, basin development and palaeogeography of the Southern North Sea. Geological Society, London, Special Publications, Volume 123, Pages 31 – 61, https://doi.org/10.1144/GSL.SP.1997.123.01.04
- Goense, T., 2018. Physical characterization of the Lower Carboniferous Limestone as a potential Geothermal Reservoir. MSc.-thesis Delft University of Technology.
- Grunberg, L. 1970. Properties of sea water concentrates. 3rd Int. Symp on Fresh Water from the Sea. Vol. 1, p 31-39.
- Hance, L., Poty, E., 2022. Biostratigraphic revision of the Dinantian (Mississippian) of the Campine Basin. Internal VITO publication.
- Harings, M. J. (2014). CAL-GT-01 - Implications for the Distribution of the Early Namurian Geverik Member in the Netherlands. In 76th EAGE Conference and Exhibition (p. 5). Amsterdam.
- Heege Ter, J., Bijsterveldt Van, L., Wassing, B., Osinga, S., Paap, B., Kraaijpoel, D., 2020. Induced seismicity potential for geothermal projects targeting Dinantian carbonates in the Netherlands. SCAN-Dinantian report.
- Hinzen, K., 2003. Stress field in the Northern Rhine area, Central Europe, from earthquake fault plane solutions,Tectonophysics,Volume 377, Issues 3–4,2003,Pages 325-356,ISSN 0040-1951, https://doi.org/10.1016/j.tecto.2003.10.004.
- Houben, S., Bouroullec, R., Nelskamp, S., de Haan, H., Geel, K., Ventra, D., Janssen, N., Verreussel, R., Peeters, S., Veenstra, F., 2020. Paleo-Five Project - Paleozoic petroleum potential of the five countries area, Southern-Central North Sea. TNO Report 2020 R10231. https://doi.org/10.1029

- Jeppson, T. N., & Kitajima, H. (2022).Velocity-porosity relations in carbonateand siliciclastic subduction zone inputmaterials. Geochemistry, Geophysics,Geosystems, 23, e2021GC010074. https://doi.org/10.1029/2021GC01004
- Juez-Larré, J., & van Kempen, B. (2017). Well test evaluation CAL-GT-05. Utrecht, The Netherlands: TNO. (unpublished TNO report)
- Kazemi, H., Merrill JR., L. S., Porterfield, K. L., and Zeman, P. R. "Numerical Simulation of Water- Oil Flow in Naturally Fractured Reservoirs," paper SPE 5719, Society of Petroleum Engineers Journal (1976) 16, No. 6, 317-326.
- Kombrink, H., Leever, K.A., van Wees, J.D., van Bergen, F., David, P., Wong, T.E., 2008. Late Carboniferous foreland basin formation and Early Carboniferous stretching in Northwestern Europe: inferences from quantitative subsidence analyses in the Netherlands. Basin Research. Doi: https://10.1111/j.1365-2117.2008.00353.x
- Kombrink, H., van Lochem, H., van der Zwan, K.J., 2010. Seismic interpretation of Dinantian carbonate platforms in the Netherlands; implications for the palaeogeographical and structural development of the Northwest European Carboniferous Basin. Journal of the Geological Society, London, Vol. 167, pp.99-108. https://doi.org/10.1144/0016-76492008-149
- Kombrink, H., Doornenbal, J.C., Duin, E.J.T., den Dulk, M., van Gessel, S.F., ten Veen, J.H., Witmans, N., 2012. New insights into the geological structure of the Netherlands; results of a detailed mapping project. Netherlands Journal of Geosciences – Geologie en Mijnbouw, 91-4, 419-446.
- Laloux, M., Geukens, F., Ghysel, P., Hance, L. & Servais, T. 2000: Notice explicative, feuilles Gemmenich - Botzelaar (35/5-6), Henri-Chapelle - Raeren (43/1-2), Petergensfeld - Lammersdorf (43/3-4), Carte géologique de Wallonie, 1:25.000. Service géologique de Belgique
- Laenen, B. and M. Broothaers (2016) Pump Tests on Geothermal Well CAL-GT-05: Execution, Interpretation, and Impact on the Performance of the Geothermal Doublet and Update of Calculation for RNES. Interim report VITO. ENES/1310289/2016-0003.
- Leverink, D., Geel, K., 2019. Fracture characterization of the Dinantian carbonates in the Dutch subsurface. Report by SCAN.
- Michie, E., Haines, T., Healy, D., Neilson, J., Timms, N., Wibberley, C., 2014. Influence of carbonate facies on fault zone architecture. Elsevier, 82-99.
- Mijnlieff, H., de Vries, S., Jaarsma, B., Vogelaar, B. (2023). Seismic Hazard and Risk Assessment for geothermal projects in the Netherland. Available at: https://www.nlog.nl/sdra-geothermie-integriteit-afdichtend-pakket
- Mozafari, M., Gutteridge, P., Riva, A., Geel, C. R., Garland, J., and Dewit, J., 2019. Facies analysis and diagenetic evolution of the Dinantian carbonates in the Dutch subsurface. Report by SCAN.
- Oncken, O., von Winterfeld, C., Dittmar, U., 1999. Accretion of a rifted margin: the late Paleozoic Rhenohercynian fold and thrust belt (Middle EuropeanVariscides). Tectonics, 18, 75-91.
- Osinga, S. and Buik, N., 2019. Report by SCAN. Stress field characterization in the Dinantian carbonates in the Dutch subsurface
- PanTerra Geoconsultants, 2012. Description and microscopic analysis of 2 cutting samples, Well CAL-GT-01. Unpublished report EBN B.V.
- Paap, B.F., Doornenbal, J.C., den Dulk, M., Hettelaar, J.M.M., 2024. VELMOD-3.2-TNO report R12557.
- Paap, B.F. and Kraaijpoel, D., 2022, Seismic monitoring network performance assessment tool for geothermal operations
- PanTerra, 2023. Sedimentological reconstruction of the Campine Basin during the Dinantian. Vlaams Planbureau voor Omgeving, 123 pp.v

- Patruno, S., Reid, W., Jackson, C.A-L. and Davies, C., 2017. New insights into the unexploited reservoir potential of the Mid North Sea High (UKCS quadrants 35-38 and 41-43): a newly described intra-Zechstein sulphate-carbonate platform complex. In: Petroleum Geology of NW Europe: 50 Years of Learning – Proceedings of the 8th Petroleum Geology Conference. Geological Society, London.
- Peeters, S.H.J., Geel, C.R., Garland, J., Bouroullec, R., 2023. Seismic and petrographic characterisation of the Zechstein Hauptdolomit platforms around the Elbow Spit High, Dutch Offshore. Journal of Petroleum Geolog, Vol.46(3), pp 361-382.
- Poty, E. 2014. Report on cuttings from the CAL-GT-01S borehole. Unpublished report EBN B.V.
- PRESEIS software, https://github.com/TNO/PRESEIS-source-location
- Pykonal software, https://github.com/malcolmw/pykonal
- Reijmer, J.J.G., ten Veen, J.H., Jaarsma, B., Boots, R., 2017. Seismic stratigraphy of Dinantian carbonates in the southern Netherlands and northern Belgium. Netherlands Journal of Geosciences – Geologie en Mijnbouw, 96-4, 353-379. https://doi.org/10.1017/njg.2017.33
- Reith, D., 2018. Dynamic simulation of a geothermal reservoir. Case study of the Dinantian carbonates in the Californië geothermal wells, Limburg, NL. MSc. thesis, TU Delft-EBN.
- Rombaut B., Deckers J., Dirix K., Van Baelen K. (in prep). Nieuwe inzichten en geologische 3D modellen van het Dinantiaan in het Bekken van de Kempen. Studie uitgevoerd in opdracht van: VLAKO / VLAANDEREN, referentie: 2021/RMA/R/2477.
- Ruigrok, E., Kruiver, P. P., & Dost, B. (2023). *Construction of earthquake location uncertainty maps for the Netherlands* (Technical Report No. TR-405) (p. 160). De Bilt: KNMI.
- Segall and Lu, 2015. Injection-induced Seismicity:Poroelastic and Earthquake Nucleation Effects. J. *Geophys. Res. Solid Earth 102*, 5082-5103. https://doi:10.1002/2015jb012060
- Smit, J., van Wees, J-D., Cloetingh, S., 2018. Early Carboniferous extension in East Avalonia: 350 My record of lithospheric memory. Marine and Petroleum Geology 92, 1010-1027. https://doi.org/10.1016/j.marpetgeo.2018.01.004
- Soustelle, V. and Heege Ter, J., 2023. Relationship Between Static and Dynamic Elastic Moduli in Carbonates. https://doi.org/10.56952/arma-2023-0331.
- Spetzler, J., Ruigrok, E., Dost, B., Evers, L., 2018, Hypocenter Estimation of Detected Event near Venlo on September 3rd, KNMI, De Bilt, Technical report, 369
- Spetzler, J., Ruigrok, E. & Bouwman, D. Hypocenter uncertainty analysis of induced and tectonic earthquakes in the Netherlands. J Seismol 28, 555–577 (2024). https://doi.org/10.1007/s10950-024-10205-8
- Sun, H., R. Feistel, M. Koch and A. Markoe (2008) New equations for density, entropy, heat capacity, and potential temperature of a saline thermal fluid. *Deep-Sea Research I*, vol. 55, p 1304-1310.
- Tarantola, A. and Valette, B., 1982. Inverse Problems = Quest for Information. Journal of Geophysics, 1982, 50, p. 159–170. 159.
- TAQA (2023) Gasopslag Bergermeer Microseismische Monitoring Jaarrapportage 2023, Jaarrapportage 2023
- Ten Veen, J.H., den Dulk, M., Nelskamp, S., Houben, A.J.P., Kaliar, A.L., Witteman, T.T., Altenburg, R.J. H3O-Diep Zuid-NL – De ondergrond van de provincies Noord-Brabant en Zeeland in meer detail. *in press*
- Ter Borgh, M.M., Eikelenboom, W., Jaarsma, B., 2018. Hydrocarbon potential of the Visean and Namurian in the northern Dutch offshore. In: Monaghan, A.A., Underhill, J.R.,

Hewett, A.J., Marshall, J.E.A. (eds). Paleozoic Plays of NW Europe. Geological Society, London, Special Publications, 471, https://doi.org/10.1144/SP471.5

- Ter Borgh, M.M., Jaarsma, B., Rosendaal, E.A., 2018b. Structural development of the northern Dutch offshore: Paleozoic to present. In: Monaghan, A. A., Underhill, J. R., Hewett, A. J. & Marshall, J. E. A. (eds). Paleozoic Plays of NW Europe. Geological Society, London, Special Publications, 471, https://doi.org/10.1144/SP471.4
- Thomas, C.W., Woodcock, N.H., 2015. The kinematic linkage of the Dent, Craven and related faults of Northern England. Proc. Yorks. Geol. Soc. 60 (4), 258–274. https://doi.org/10.1144/pygs2015-358
- Total E&P UK, 2007. A regional review of the Dinantian carbonate play: southern North Sea & onshore UK. Total E&P UK.
- TNO – GDN (2019) DGM-diep v5.0. TNO - Geologische Dienst Nederland
- Van Buggenum, J.M., den Hartog Jager, D.G., 2007. Silesian. In: Wong, T.E., Batjes, D.A.J. & De Jager, J. (eds). Geology of the Netherlands. Royal Netherlands Academy of Arts and Sciences, Amsterdam, 43-62.
- Van der Voet, E., Laenen, B., rombaut, B., Kourta, M., Swennen, R., 2020. Fracture chracteristics of Lower Carboniferous carbonates in northern Belgium based on FMI log analyses. Netherlands Journal of Geosciences, Volume 99, e8. https://doi.org/10.1017/njg.2020.6
- Van der Voet, E., Laenen, G., Muchez, P., Lagrou, D., Claes, H., Verbiest, M., Swennen, R. Controls of dolomitization and bed thickness on fracture networks in Lower Carboniferous carbonates in southern Belgium. Journal of Structural Geology, 164, 104729. https://doi.org/10.1016/j.jsg.2022.104729
- Van de Sande, J.M.M., Reijers, T.J.A. and Casson, N., 1996. Multidisciplinary exploration strategy in the northeast Netherlands Zechstein 2 Carbonate play, guided by 3D seismics. In: Rondeel, H.E., Batjes, D.A.J. & Nieuwenhuijs, W.H. (Eds), Geology of Gas and Oil under the Netherlands. Kluwer Academic Publishers, pp 125-142.
- Van Hulten, F.F.N., 2012. Devono-Carboniferous carbonate platform systems of the Netherlands. Geologica Belgica 15/4: 284-296
- Veldkamp, H., Arndt, M., Broothaers, M., Dezayes, C., Lacquement, F., Laurent, A., Vanbrabant, Y., ten Veen, J. 2023. Updated Transnational harmonized depth and thickness map of the Dinantian in North-West Europe. Interreg North-West Europe DGE-Rollout.
- Vörös R and Baisch S. Induced seismicity and seismic risk management – a showcase from the Californië geothermal field (the Netherlands). Netherlands Journal of Geosciences, Volume 101, e15. https://doi.org/ 10.1017/njg.2022.12
- Wassing, B., Broothaers, M., Candela, C., Cremer, H., Heege, ter, J. Laenen, B., Pogacnik, J., Soustelle, V., Tsopela, A., 2022. Seismicity Potential Dinantian geothermal reservoirs – implications of case study Balmatt for projects in the Netherlands – SeiMoD. TKI Project SeiMoD (TKI2021-02-GE), Public results report | September 3, 2022.
- Wennberg, O.P., Azizzadeh, M., Aqrawi, M., Blanc, E., Brockbank, P., Lyslo, K.B., Pickard, N., Salem, L.D., Svånå. 2007. The Khaviz Anticline: an outcrop analogue to giant fractured Asmari Fromation reservoirs in SW Iran. Geological Society, London, Special Publications. Volume 270, pp 23 – 42. https://doi.org/10.1144/GSL.SP.2007.270.01.02
- Wilson, J. L. (1997). Carbonate depositional environments and diagenesis. In I. Palaz, & K. J. Marfurt (Eds.), Carbonate seismology (pp. 9–28).Society of Exploration Geophysicists. https://doi.org/10.1190/1.9781560802099.ch2
- Ziegler, P.A., 1990. Tectonic and palaeogeographic development of the North Sea Rift system. In: Blundell, D.J., & Gibbs, A.D. (eds): Tectonic evolution of the North Sea rifts. Oxford Science Publications (Oxford): 1-36.

11 Signature

Authorization release:

G.P. (Paul) Wyers
Research Manager Geoscience and Technology

12 Appendices

APPENDIX A - Well Logs

APPENDIX_A_Well_logs - high-resolution figure

Appendix A

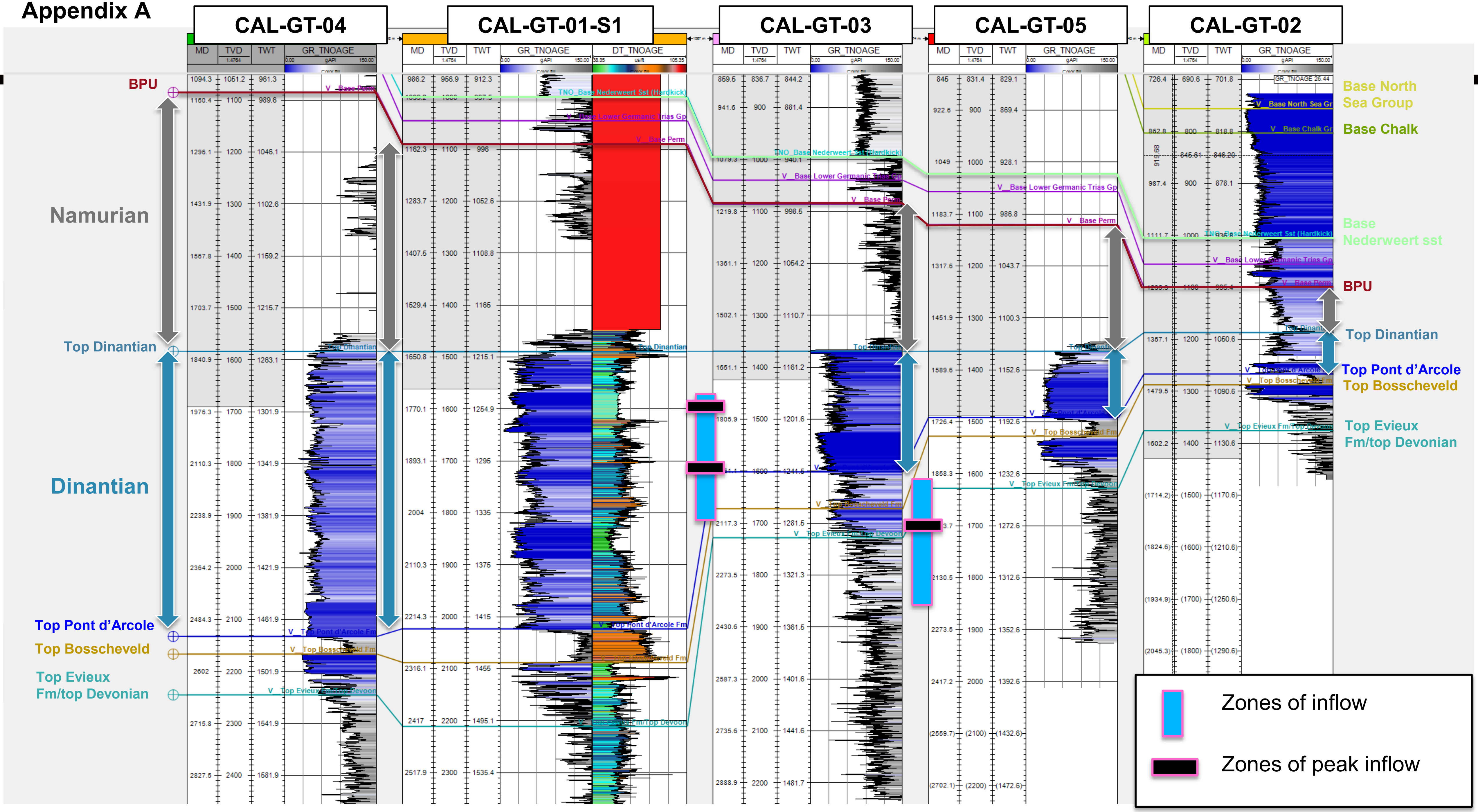

CAL-GT-04
CAL-GT-01-S1
CAL-GT-03
CAL-GT-05
CAL-GT-02
MD
TVD
TWT
GR_TNOAGE
DT_TNOAGE
BPU
Namurian
Top Dinantian
Dinantian
Top Pont d'Arcole
Top Bosscheveld
Top Evieux Fm/top Devonian
Base North Sea Group
Base Chalk
Base Nederweert sst
Zones of inflow
Zones of peak inflow

Appendix A

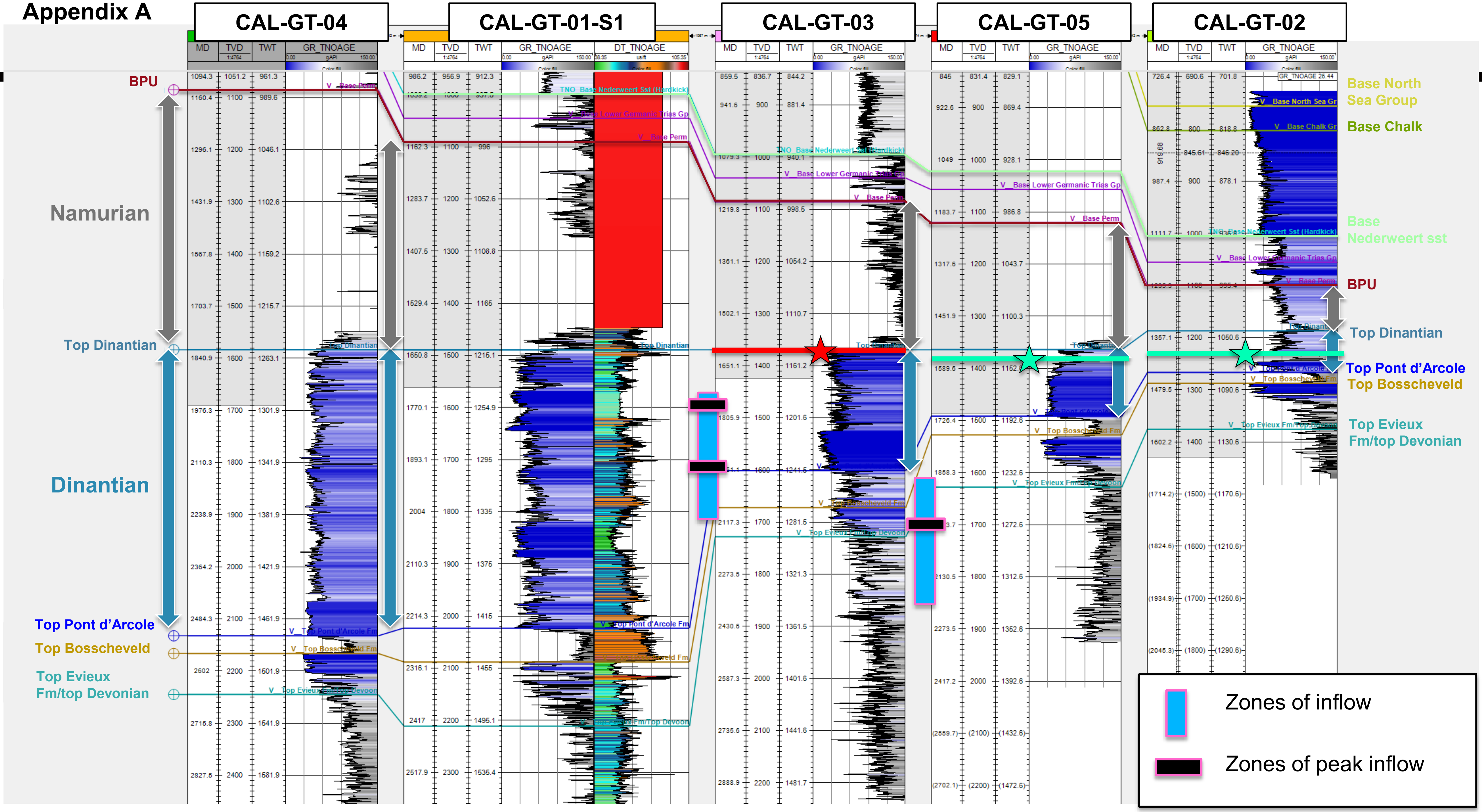

CAL-GT-04
CAL-GT-01-S1
CAL-GT-03
CAL-GT-05
CAL-GT-02
MD
TVD
TWT
GR_TNOAGE
DT_TNOAGE
BPU
Namurian
Top Dinantian
Dinantian
Top Pont d'Arcole
Top Bosscheveld
Top Evieux Fm/top Devonian
Base North Sea Group
Base Chalk
Base Nederweert sst
BPU
Top Dinantian
Top Pont d'Arcole
Top Bosscheveld
Top Evieux Fm/top Devonian
Zones of inflow
Zones of peak inflow

APPENDIX B - Seismic Interpretation Hybrid Model

Appendix B

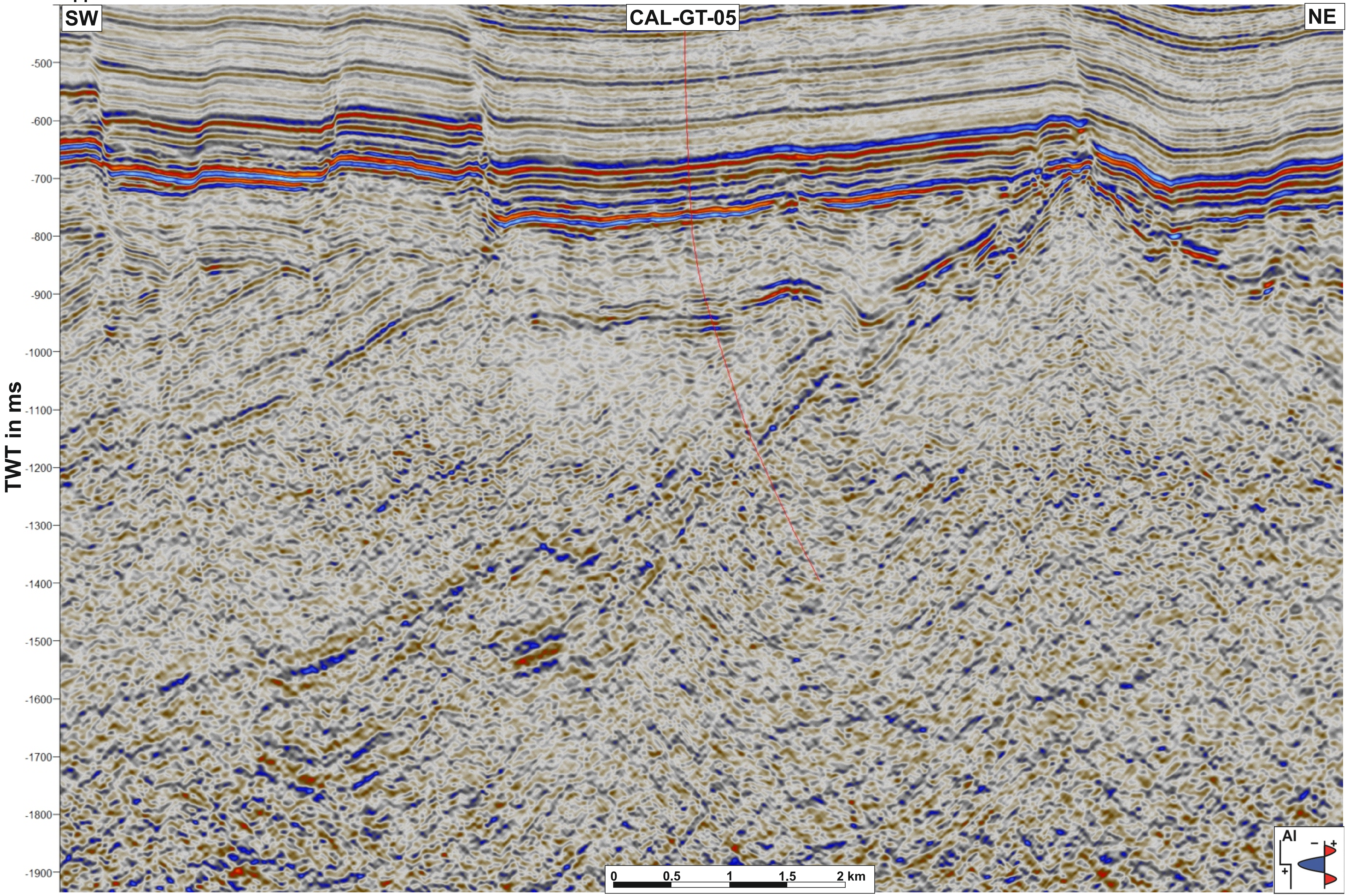

SW
CAL-GT-05
NE
TWT in ms
-500
-600
-700
-800
-900
-1000
-1100
-1200
-1300
-1400
-1500
-1600
-1700
-1800
-1900
0
0.5
1
1.5
2 km
AI
−
+
+

Appendix B

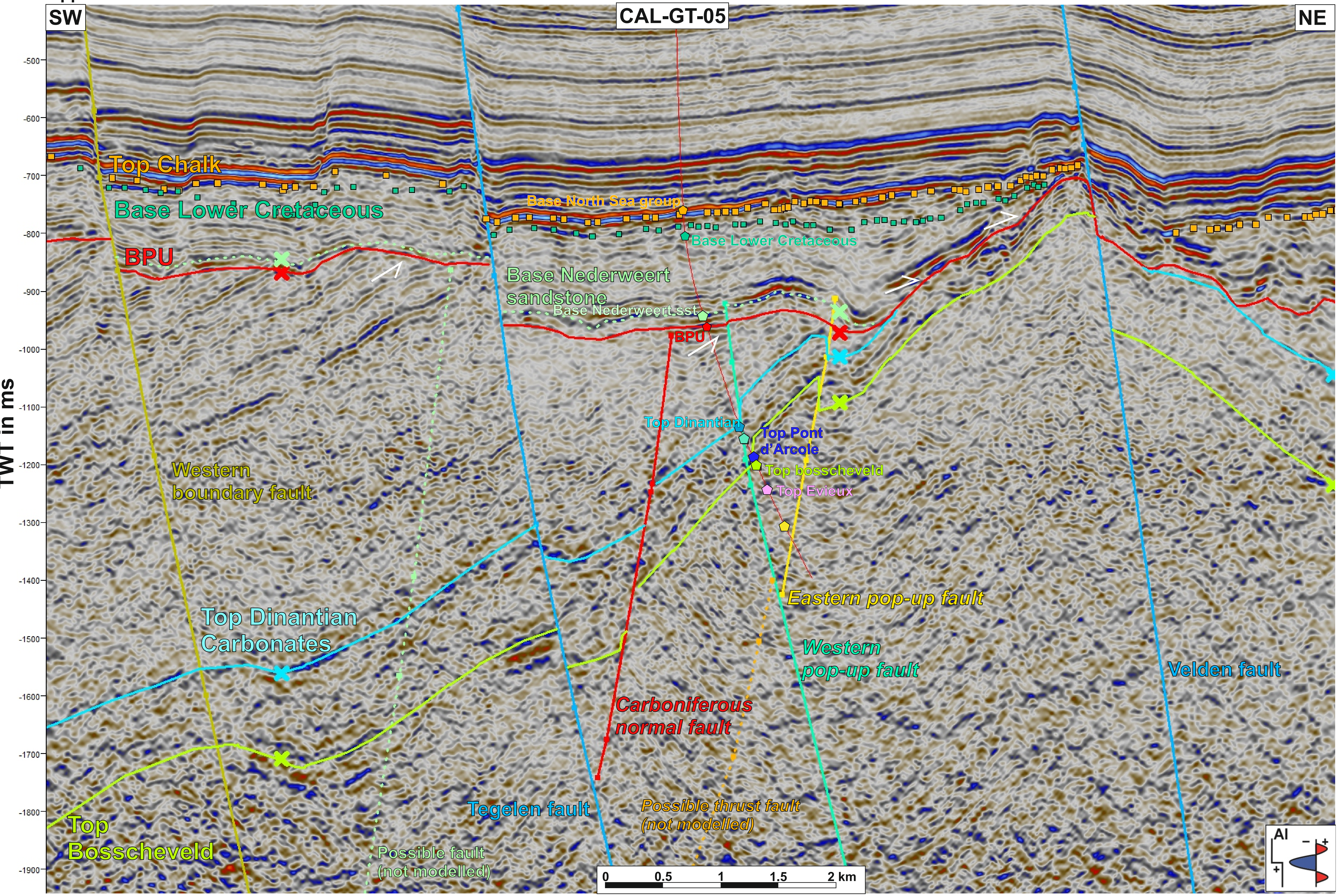

SW
CAL-GT-05
NE
-500
-600
-700
-800
-900
-1000
-1100
-1200
-1300
-1400
-1500
-1600
-1700
-1800
-1900
TWT in ms
Top Chalk
Base Lower Cretaceous
BPU
Base North Sea group
Base Lower Cretaceous
Base Nederweert sandstone
Base Nederweert sst
BPU
Top Dinantian
Top Pont d'Arcole
Top bosscheveld
Top Evieux
Western boundary fault
Eastern pop-up fault
Western pop-up fault
Velden fault
Top Dinantian Carbonates
Carboniferous normal fault
Top Bosscheveld
Tegelen fault
Possible thrust fault (not modelled)
Possible fault (not modelled)
0 0.5 1 1.5 2 km
AI

Appendix B

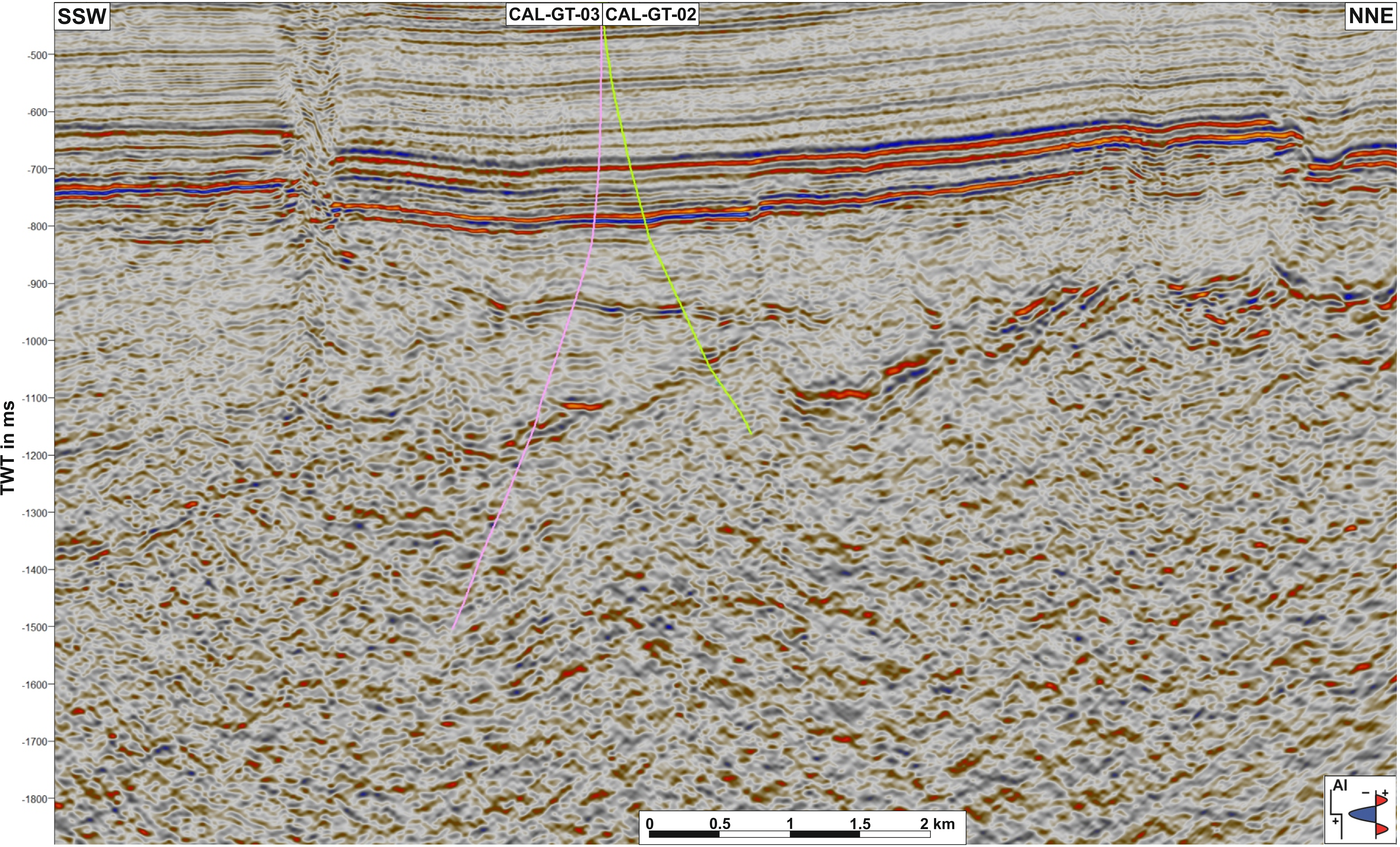

SSW
CAL-GT-03
CAL-GT-02
NNE
-500
-600
-700
-800
-900
-1000
-1100
-1200
-1300
-1400
-1500
-1600
-1700
-1800
TWT in ms
0
0.5
1
1.5
2 km
AI

Appendix B

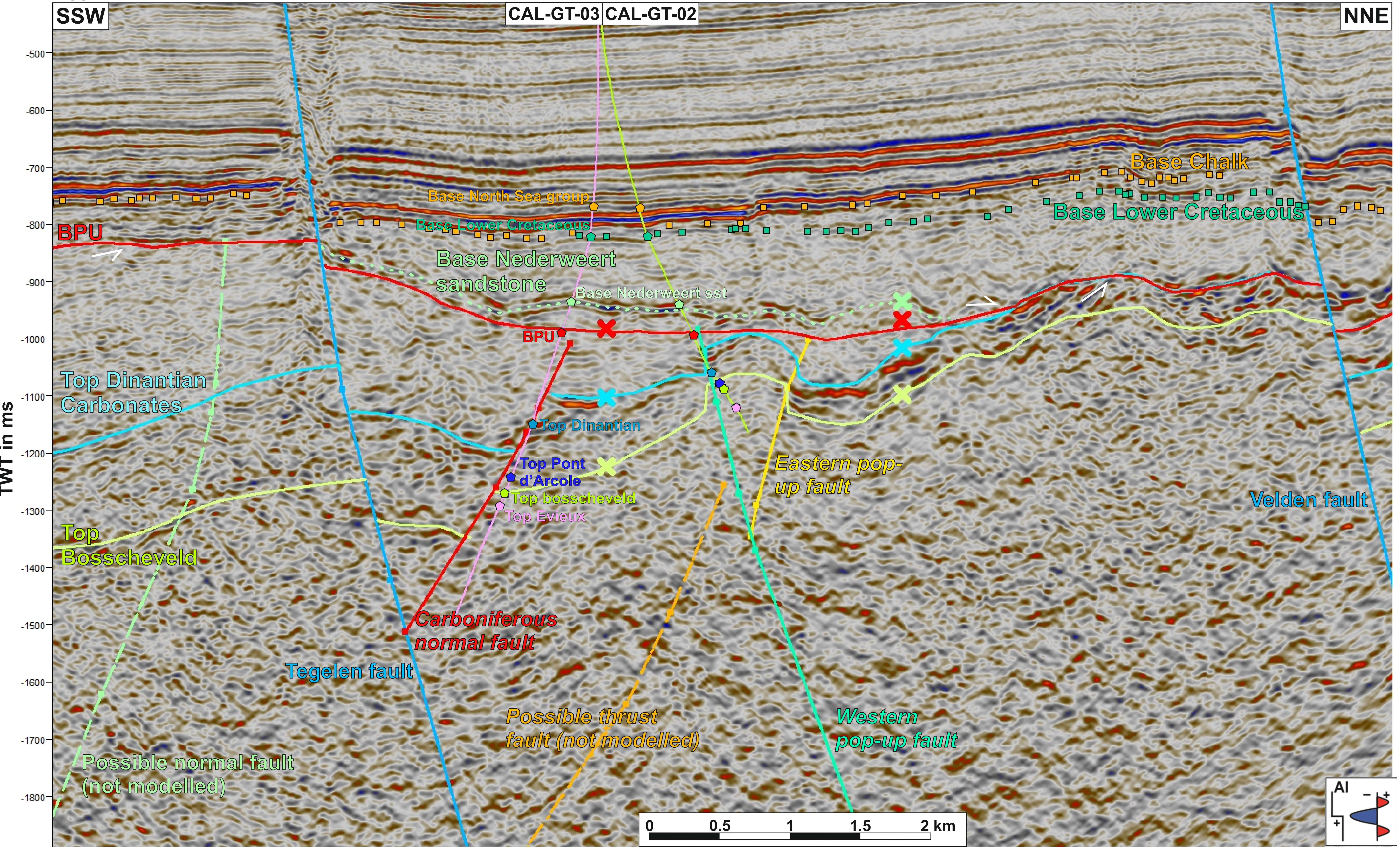

SSW
CAL-GT-03
CAL-GT-02
NNE
-500
-600
-700
-800
-900
-1000
-1100
-1200
-1300
-1400
-1500
-1600
-1700
-1800
TWT in ms
Base Chalk
Base North Sea group
Base Lower Cretaceous
Base Lower Cretaceous
BPU
Base Nederweert sandstone
Base Nederweert sst
BPU
Top Dinantian Carbonates
Top Dinantian
Top Pont d'Arcole
Top bosscheveld
Top Evieux
Eastern pop-up fault
Velden fault
Top Bosscheveld
Carboniferous normal fault
Tegelen fault
Possible thrust fault (not modelled)
Western pop-up fault
Possible normal fault (not modelled)
0
0.5
1
1.5
2 km
AI

Appendix B

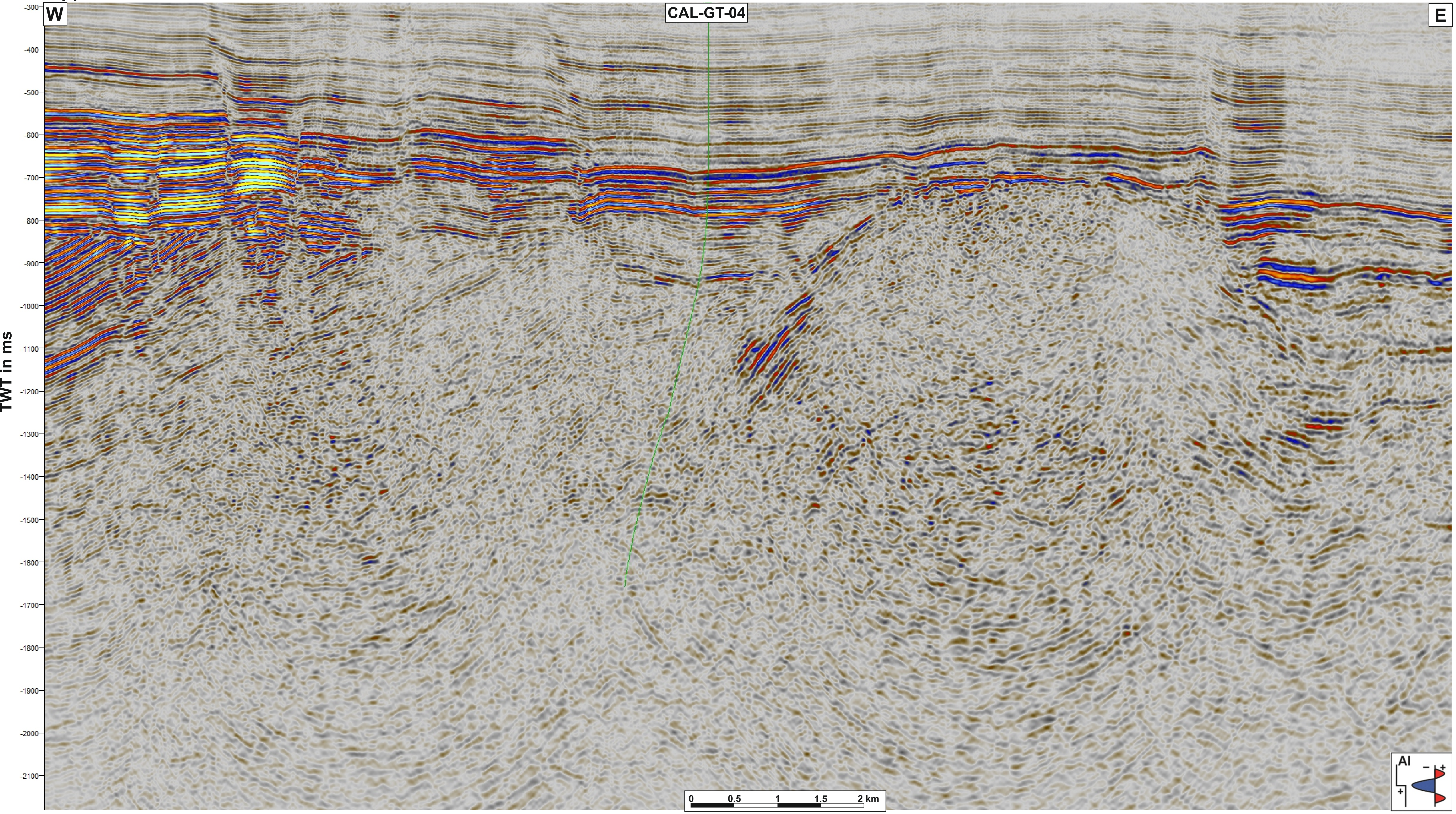
W
CAL-GT-04
E
TWT in ms
-300
-400
-500
-600
-700
-800
-900
-1000
-1100
-1200
-1300
-1400
-1500
-1600
-1700
-1800
-1900
-2000
-2100
0 0.5 1 1.5 2 km
AI
-
+
+

Appendix B

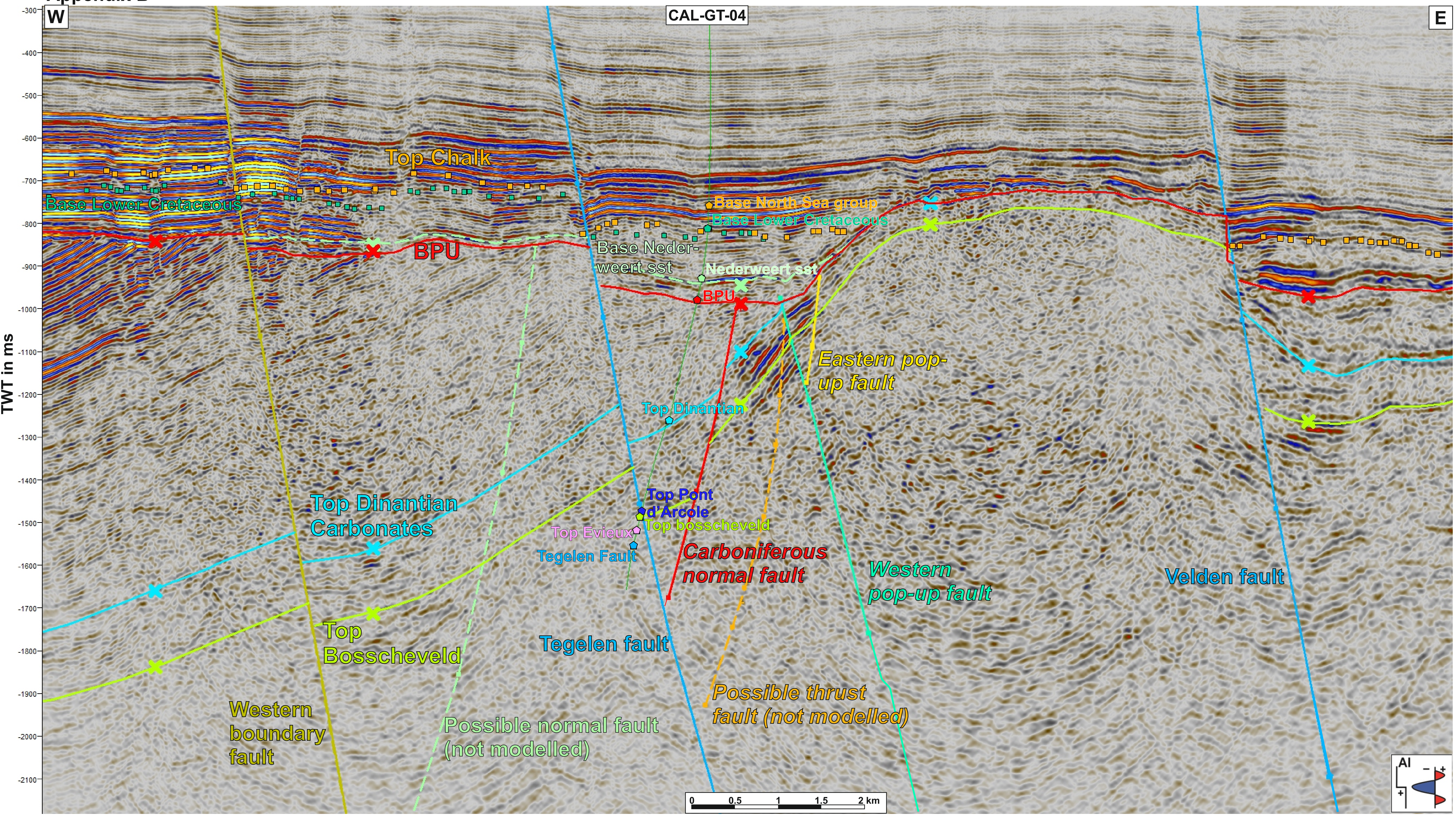

W
E
CAL-GT-04
TWT in ms
-300
-400
-500
-600
-700
-800
-900
-1000
-1100
-1200
-1300
-1400
-1500
-1600
-1700
-1800
-1900
-2000
-2100
Top Chalk
Base Lower Cretaceous
BPU
Base North Sea group
Base Lower Cretaceous
Base Neder-
weert sst
Nederweert sst
BPU
Eastern pop-
up fault
Top Dinantian
Top Pont
d'Arcole
Top bosscheveld
Top Evieux
Tegelen Fault
Top Dinantian
Carbonates
Carboniferous
normal fault
Western
pop-up fault
Velden fault
Top
Bosscheveld
Tegelen fault
Possible thrust
fault (not modelled)
Western
boundary
fault
Possible normal fault
(not modelled)
0 0.5 1 1.5 2 km
AI

APPENDIX C - Seismic Interpretation I

APPENDIX_C_Seismic Interpretation I - high-resolution figure

Appendix C

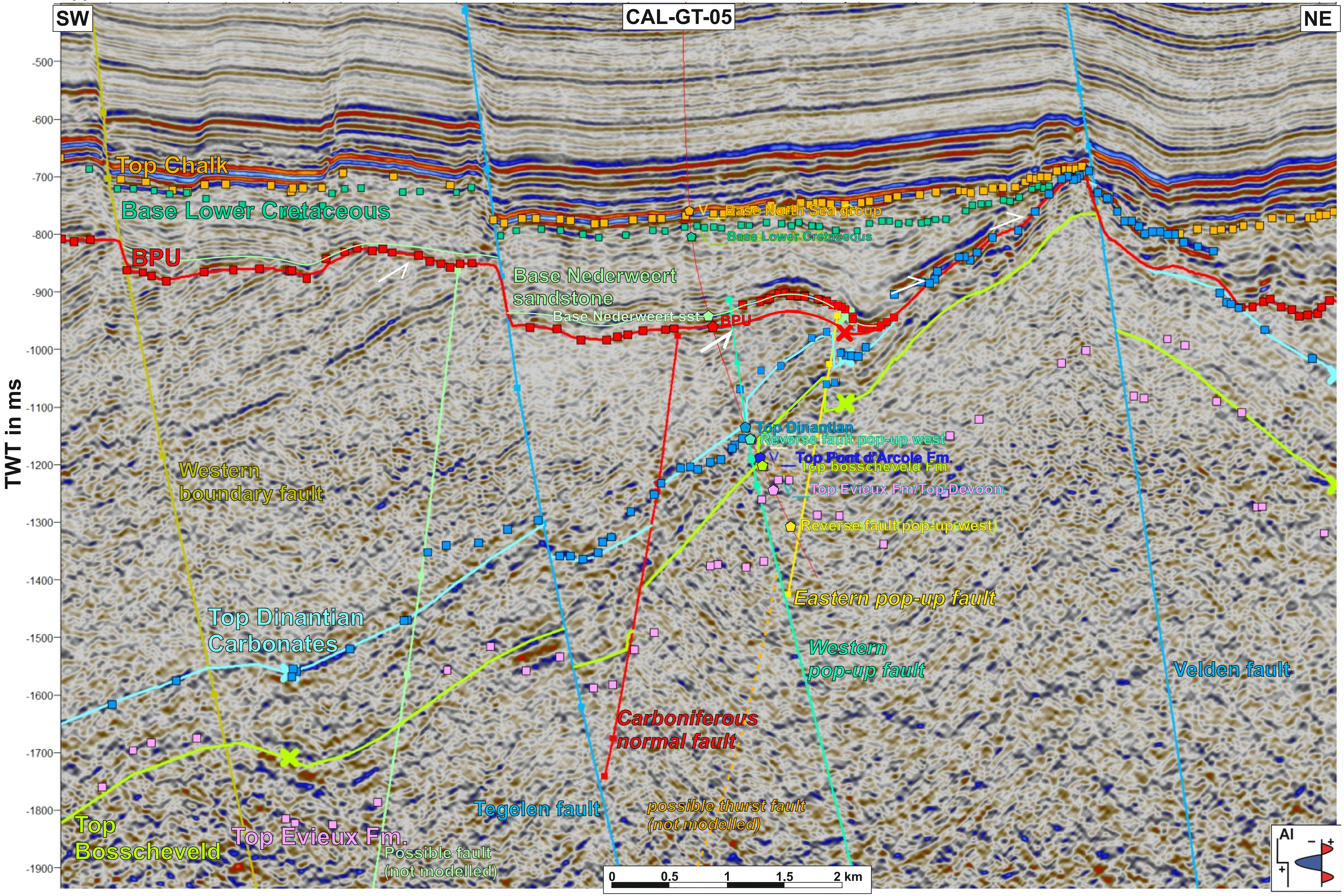
SW
CAL-GT-05
NE
TWT in ms
-500
-600
-700
-800
-900
-1000
-1100
-1200
-1300
-1400
-1500
-1600
-1700
-1800
-1900
Top Chalk
Base Lower Cretaceous
BPU
Base North Sea group
Base Lower Cretaceous
Base Nederweert sandstone
Base Nederweert sst
BPU
Top Dinantian
Reverse fault pop-up west
Top Pont d'Arcole Fm.
Top bosscheveld Fm
Top Evieux Fm/Top Devoon
Reverse fault pop-up west
Western boundary fault
Top Dinantian Carbonates
Eastern pop-up fault
Western pop-up fault
Velden fault
Carboniferous normal fault
Tegelen fault
possible thurst fault (not modelled)
Top Bosscheveld
Top Evieux Fm.
Possible fault (not modelled)
0
0.5
1
1.5
2 km
AI

Appendix C

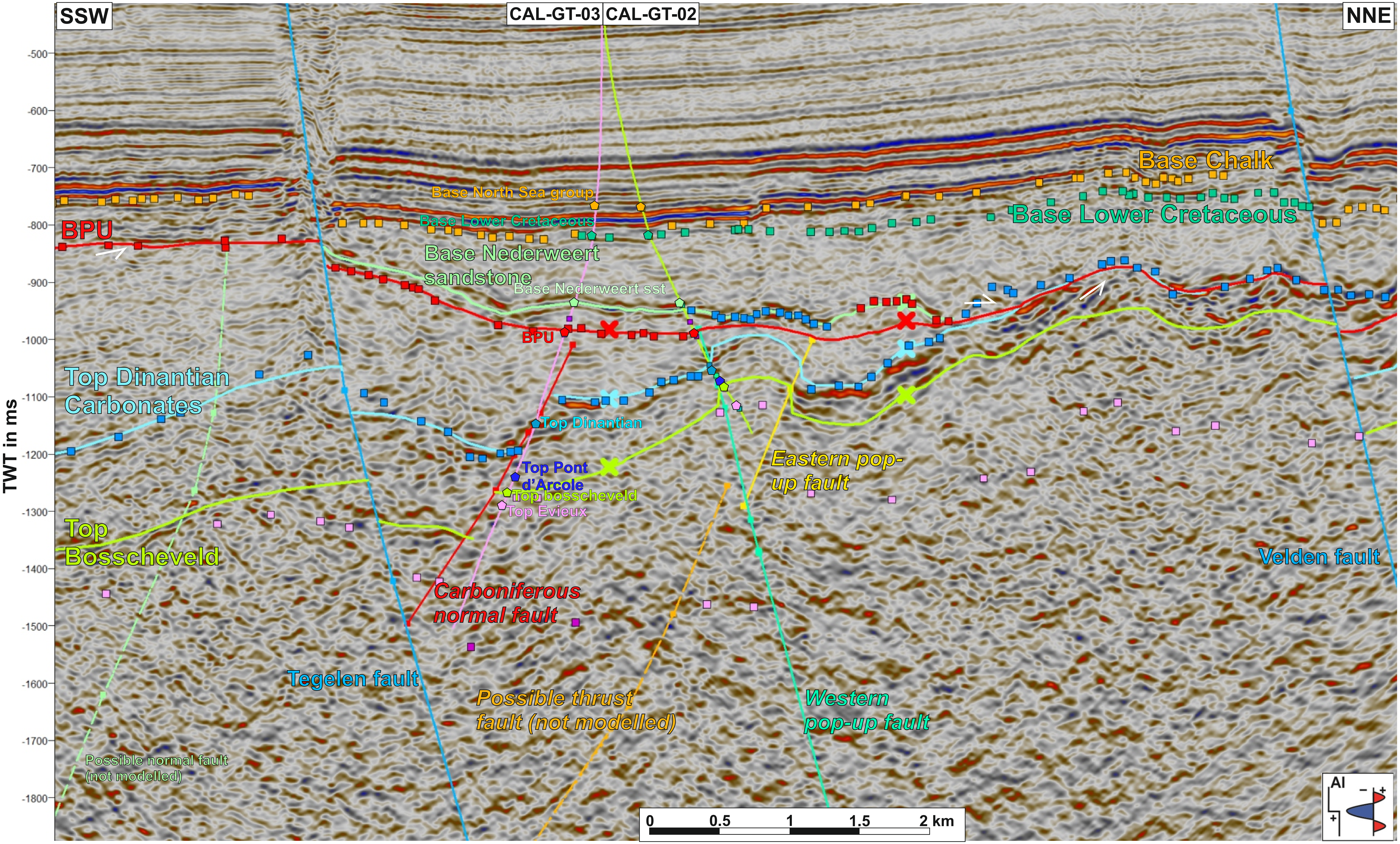
SSW
CAL-GT-03
CAL-GT-02
NNE
TWT in ms
-500
-600
-700
-800
-900
-1000
-1100
-1200
-1300
-1400
-1500
-1600
-1700
-1800
BPU
Base North Sea group
Base Lower Cretaceous
Base Nederweert sandstone
Base Nederweert sst
BPU
Base Chalk
Base Lower Cretaceous
Top Dinantian Carbonates
Top Dinantian
Top Pont d'Arcole
Top bosscheveld
Top Evieux
Top Bosscheveld
Eastern pop-up fault
Velden fault
Carboniferous normal fault
Tegelen fault
Possible thrust fault (not modelled)
Western pop-up fault
Possible normal fault (not modelled)
0
0.5
1
1.5
2 km
AI
-
+
+

Appendix C

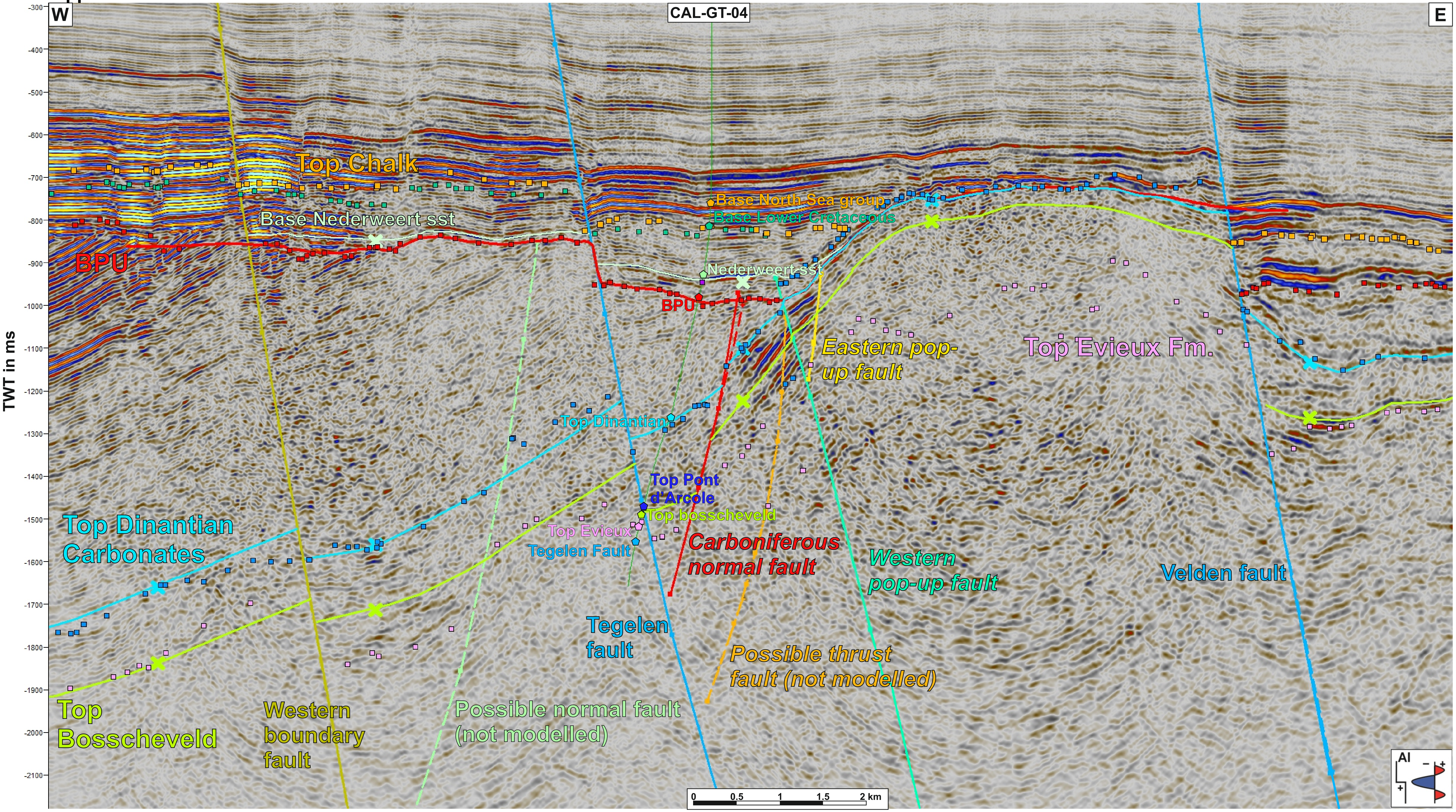
W
E
CAL-GT-04
TWT in ms
-300
-400
-500
-600
-700
-800
-900
-1000
-1100
-1200
-1300
-1400
-1500
-1600
-1700
-1800
-1900
-2000
-2100
Top Chalk
Base Nederweert sst
BPU
Base North Sea group
Base Lower Cretaceous
Nederweert sst
BPU
Eastern pop-up fault
Top Evieux Fm.
Top Dinantian
Top Pont d'Arcole
Top bosscheveld
Top Evieux
Tegelen Fault
Top Dinantian Carbonates
Carboniferous normal fault
Western pop-up fault
Velden fault
Tegelen fault
Possible thrust fault (not modelled)
Top Bosscheveld
Western boundary fault
Possible normal fault (not modelled)
0
0.5
1
1.5
2 km
AI

APPENDIX D - Seismic Interpretation II

APPENDIX_D_SeismicInterpretation_II - high-resolution figure

Appendix D

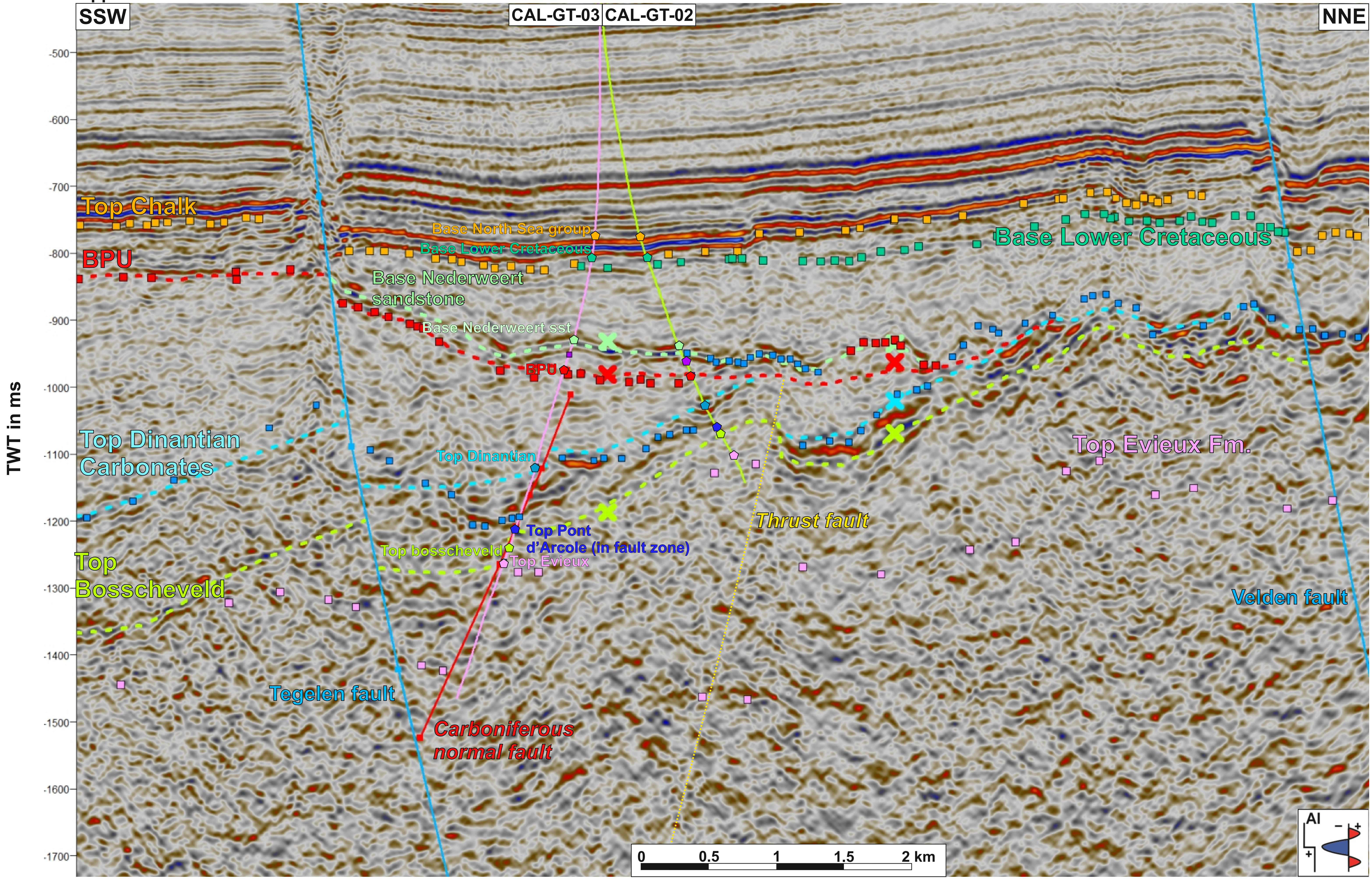

SSW
CAL-GT-03
CAL-GT-02
NNE
TWT in ms
-500
-600
-700
-800
-900
-1000
-1100
-1200
-1300
-1400
-1500
-1600
-1700
Top Chalk
BPU
Base North Sea group
Base Lower Cretaceous
Base Nederweert sandstone
Base Nederweert sst
BPU
Base Lower Cretaceous
Top Dinantian Carbonates
Top Dinantian
Top Evieux Fm.
Thrust fault
Top Pont d'Arcole (in fault zone)
Top bosscheveld
Top Evieux
Top Bosscheveld
Velden fault
Tegelen fault
Carboniferous normal fault
0
0.5
1
1.5
2 km
AI

Appendix D

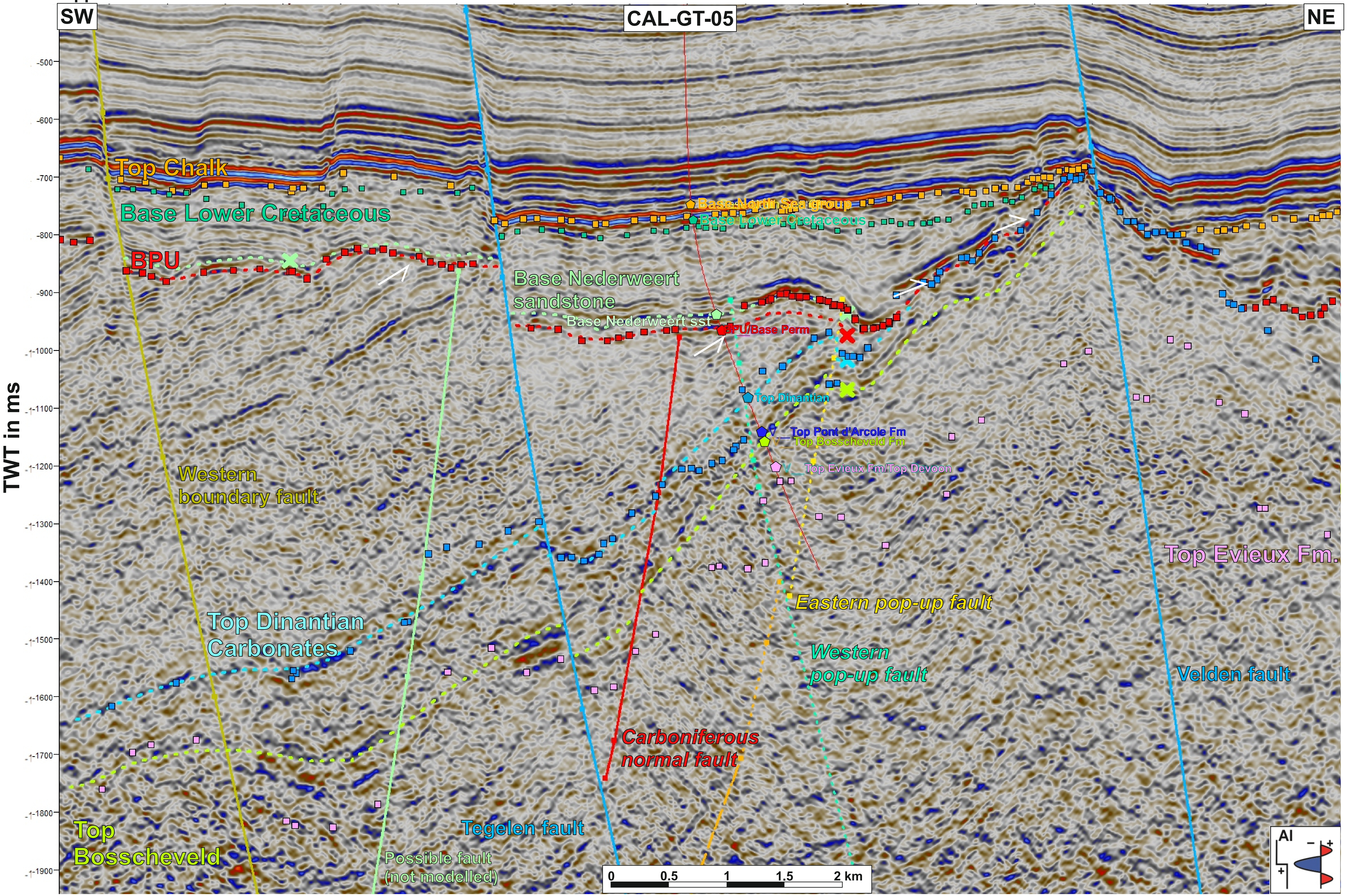

SW
CAL-GT-05
NE
TWT in ms
-500
-600
-700
-800
-900
-1000
-1100
-1200
-1300
-1400
-1500
-1600
-1700
-1800
-1900
Top Chalk
Base Lower Cretaceous
BPU
Base Nederweert sandstone
Base Nederweert sst
Base North Sea group
Base Lower Cretaceous
BPU/Base Perm
Top Dinantian
Top Pont d'Arcole Fm
Top Bosscheveld Fm
Top Evieux Fm/Top Devoon
Western boundary fault
Top Evieux Fm.
Eastern pop-up fault
Top Dinantian Carbonates
Western pop-up fault
Velden fault
Carboniferous normal fault
Top Bosscheveld
Tegelen fault
Possible fault (not modelled)
0 0.5 1 1.5 2 km
AI
–
+

APPENDIX E - Pogacnik, 2024. Report SafeGeo: Well Test Analysis

SafeGEO: Well Test Analysis

Justin Pogacnik
2024

Vision on technology
for a better world

vito.be

SafeGEO: Well Test Analysis

VITO
Boeretang 200
2400 MOL
Belgium
VAT No: BE0244.195.916
vito@vito.be – www.vito.be
IBAN BE34 3751 1173 5490 BBRUBEBB

Ben Laenen
Project Manager
ben.laenen@vito.be

Justin Pogacnik
Reservoir Engineering Researcher
justin.pogacnik@vito.be

TABLE OF CONTENTS

LIST OF FIGURES

LIST OF TABLES

1 OVERVIEW

The overall goal of this analysis was to see if any new information could be obtained from old data at the Californië site and to provide an overview of the production/injection performance of the wells CAL-GT-01, CAL-GT-03, CAL-GT-04 and CAL-GT-05. To that end, we attempt to estimate formation permeability values and link those to the newly interpreted geologic structures to serve as starting points for numerical reservoir modelling.

In this report, we summarize the production data available that can also be used to estimate total well performance. Then the data for each well specifically is analyzed in turn. Every well had at least one production/pump test or injection test performed after drilling at multiple rates. Wells CAL-GT-03 and CAL-GT-05 have downhole PLT measurements which are invaluable for feedzone description and quantification. Even poor PLT data can be used to gain understanding. We also summarized the relevant available data and previous analysis performed for each well.

2 GENERAL PRODUCTION DATA

The general production data for each site (CLG and CWG) were available as history excel files with the data expressed every 5 minutes. For the CLG dataset, the tags available were ESP inlet pressure and temperature; temperature and flow measured at various points; and injection wellhead temperature and pressure. The first datapoint was timestamped 2017-06-01 00:05:00 and the last datapoint was timestamped 2018-09-10 00:00:00. The CWG dataset included the ESP parameters of temperature, flow, pressure, voltage, and current. Production temperature was also reported in the data set. The entire timestamp range of the dataset was from 2014-02-03 to 2018-05-16. However, flow data was only reported from 2016-11-30 until the end. Eventually, Q-Con Gmbh supplied flow data for the SafeGEO project for CAL-GT-03, but it was not available at the time of this analysis. The summary of the relevant tags for well performance indicators can be seen in Figure 1. The lack of historical flow data for the CWG dataset made it difficult to evaluate performance from 2014-2017. However, some flow data from well tests were available at earlier times.

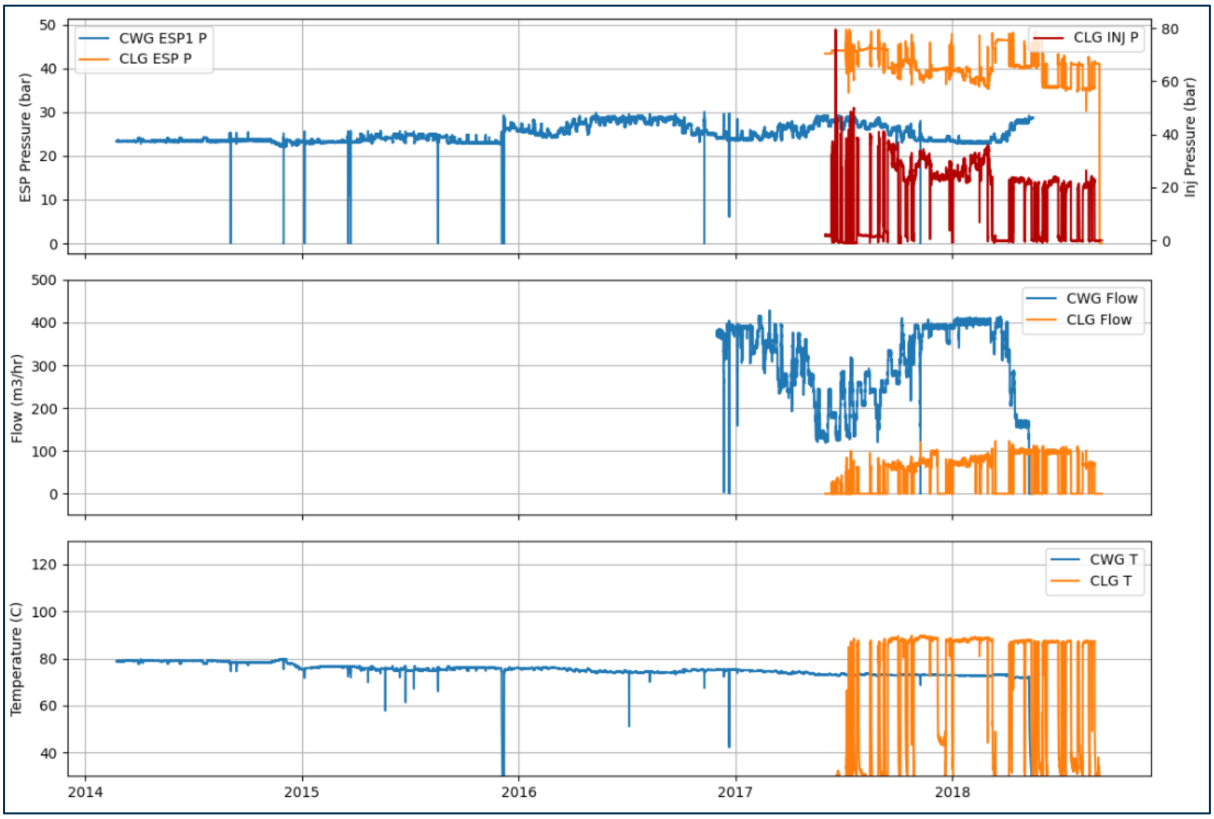

Figure 1: Well performance production parameters available in the production history dataset for both CWG and CLG.

3 CAL-GT-01 S1

As a note, we only analyzed data and performance of the sidetrack of CAL-GT-01. Any reference to CAL-GT-01 in the well performance section refers to CAL-GT-01 S1.

3.1 Well Test Data and Previous Analysis

A multi-rate production well test was performed on CAL-GT-01 on 6-7 August 2012. The data is available in an excel file. Previous analysis was performed by VITO and reported (Broothaers & Laenen, Execution and Interpretation of the Pump Tests on Geothermal Well

CAL-GT-01 (S02): Report for the SEI Application., 2012). The cleaning of the well began on 4 August 2012 and lasted 34 hours. Immediately after cleaning, the production test began. The test was run at 6 different flowrates each lasting approximately 3 hours with a 1-hour pressure recovery period between tests. As can be seen in the figure, the pressure changes are small for flowrate changes. The production index (PI) of the well can be estimated as the slope in the line connecting flow periods. That value was around 40-85 m^3/hr/bar. There is some uncertainty because the flow rate was decreasing over time for some fixed pump frequency values. For permeability estimates, the thickness of the productive zone in the well was not known. The total permeability thickness was determined to be about 16.2 D-m. This gives permeability values of 162 mD or 20 mD for reservoir thicknesses of 100 m or 800 m respectively. Both values were mentioned in the report as examples.

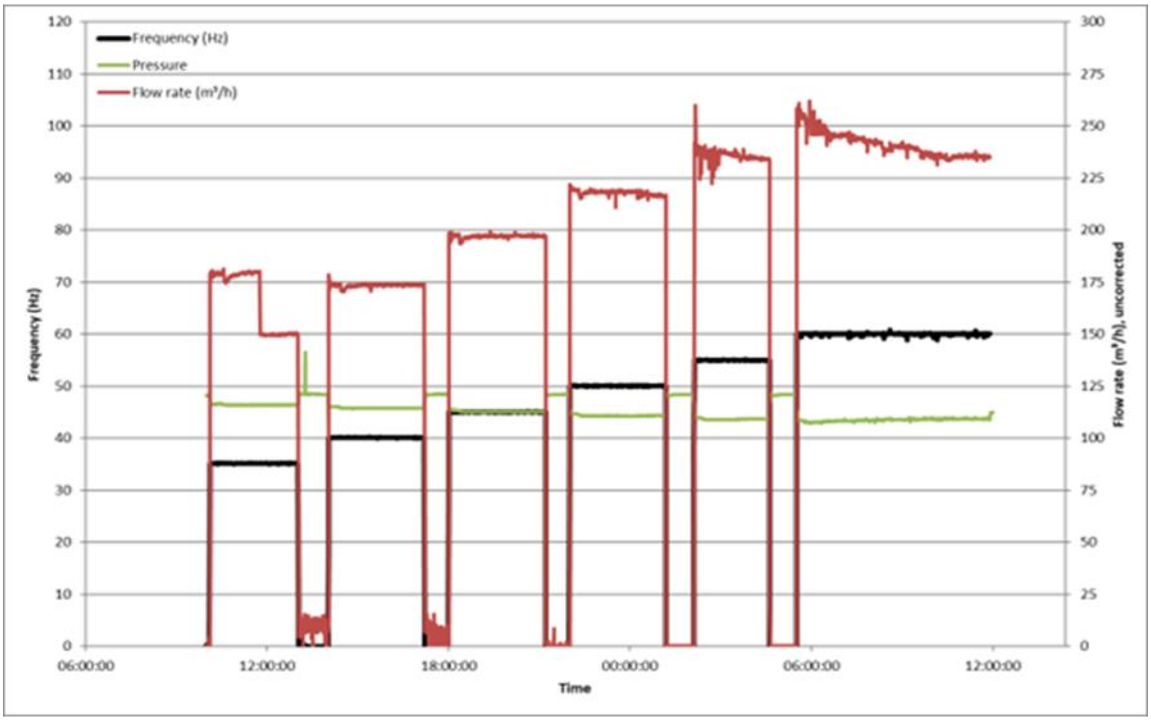

Figure 2: Multi-rate pump test data from CAL-GT-01 (Broothaers & Laenen, 2012).

3.2 New Analysis

As no new data was acquired, there was little new work to be done for CAL-GT-01. A plot of the well performance for the two production data sets can be seen in Figure 3. The 2014-2015 dataset is colored by date with blue data being the early times and red being the later times. The 2017/2018 dataset is also colored by time, but there was minor change in that period in well behavior. The pump pressure monitor was deepened by about 50 m from the 2014/2015 dataset to the 2017/2018 dataset. The original data from Figure 1 was corrected to the depth of the 2014/2015 dataset (295 mVD). A rough estimate of the slope of the performance curve indicates a productivity index (PI) of about 70 m^3/hr/bar. This value is consistent with what was previously obtained.

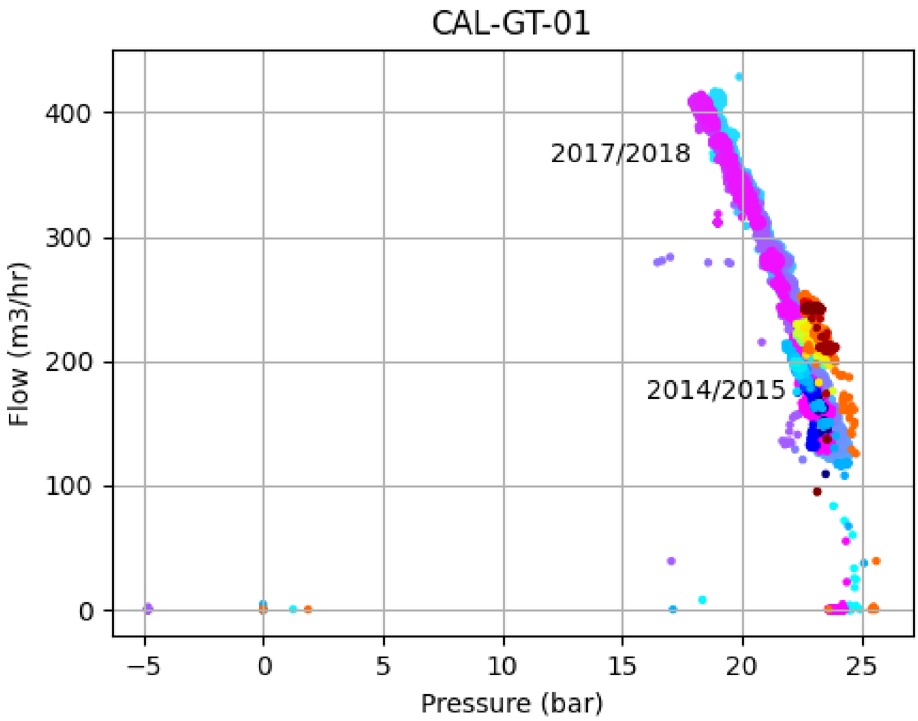

Figure 3: CAL-GT-01 well performance curve based on production data (colored by date).

The multirate test was also re-analyzed using a simple radial Darcy flow model of the transient linesource solution. The simplified linesource solution can be expressed as:

$$p(r,t) = p_i - \frac{1}{2}p_c\left[ln(4\eta\frac{t}{r^2}) - \gamma\right]$$

Where *p*(*r*,*t*) is the pressure at a radius (r) and a time (t), p_i is the original reservoir pressure, and $\gamma = 0.5772$ is the Euler constant arriving out of the original exponential integral term. η is the hydraulic diffusivity and is defined as:

$$\eta = \frac{k}{\mu\phi C_t}$$

Where k is permeability, μ is viscosity, ϕ is porosity, and C_t is the fluid compressibility. The p_c term is defined:

$$p_c = \frac{Q\mu}{4\pi kh}$$

Where Q is the volumetric flow rate (m^3/s) and h is the reservoir height.

The fitting of the radial Darcy linesource solution with the multirate test data can be seen in Figure 4. The parameters chosen were the flowrate data from Figure 2; 6” well radius; $\mu = 0.001$ Pa-s; $\phi = 0.02$ (though the porosity effect is small on the final result); and $C_t = 1 \times 10^{-9}\ \mathrm{Pa}^{-1}$; $p_i = 49$ bar. The best fit k-h value was found to be 204 Dm.

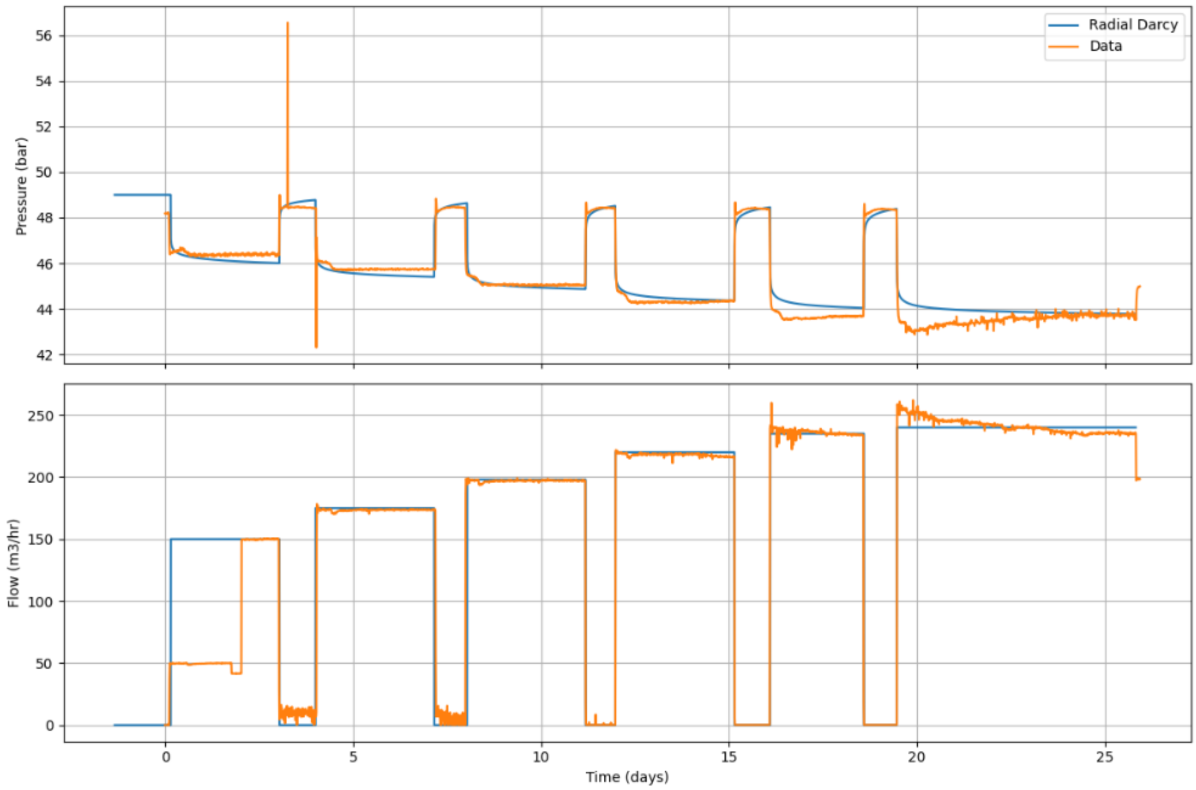

Figure 4: Radial linesource solution fit with multirate test data for CAL-GT-01 S1.

Based on drilling geology reports and discussions with the geologist, the most likely inflow zones (from drilling mud losses) are about 100 m below the top of the carbonate limestone reservoir and a potential faulted zone around -2070 m (elevation). The total thickness of those two zones is likely less than 100 m. So, as two bounds for permeability estimation if each zone is 50 m (total 100 m), then the average permeability would need to be 20.4e-13 m^2 (2.04 Darcy). If the faulted zone is larger, an absolute upper limit could be 400 m height, meaning an average permeability of 5.1e-13 m^2 (0.51 Darcy).
These values simply serve as examples. For numerical models, permeability thickness is often the better estimator as reservoir model blocks may be relatively thick (10-100 m) and the k-h is the parameter that needs to be accurately captured for history matching purposes in the numerical model.

4 CAL-GT-02

CAL-GT-02 was intended as the injection well. After completion in 2013, the well turned out to have limited injection capacity (Broothaers, 2019). After a production test, the well eventually ceased to flow. It was determined that the well was inaccessible below the 9 5/8” casing shoe. Eventually, CAL-GT-03 was used for injection pending the possible repair of CAL-GT-02.

4.1 Well Test Data and Previous Analysis

A multirate test was run over 4 days from 16-20 September 2012 in CAL-GT-02 before completion. The data of Figure 5 can be seen visualized as a well performance plot in Figure 6. The data show that the well performance was transient and best on the last day.

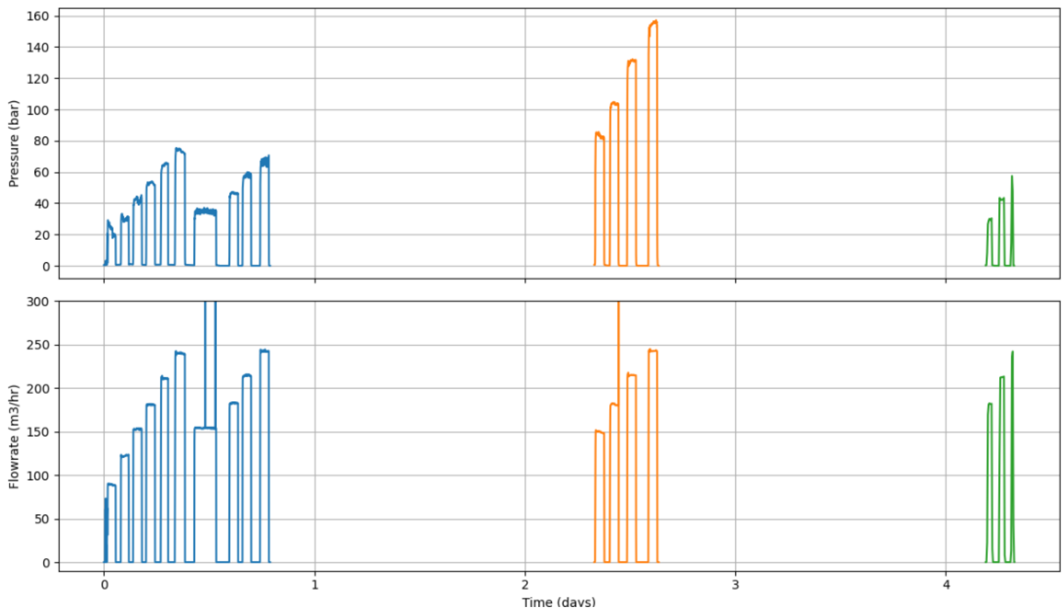

Figure 5: Multirate flow tests from September 2012 on CAL-GT-02.

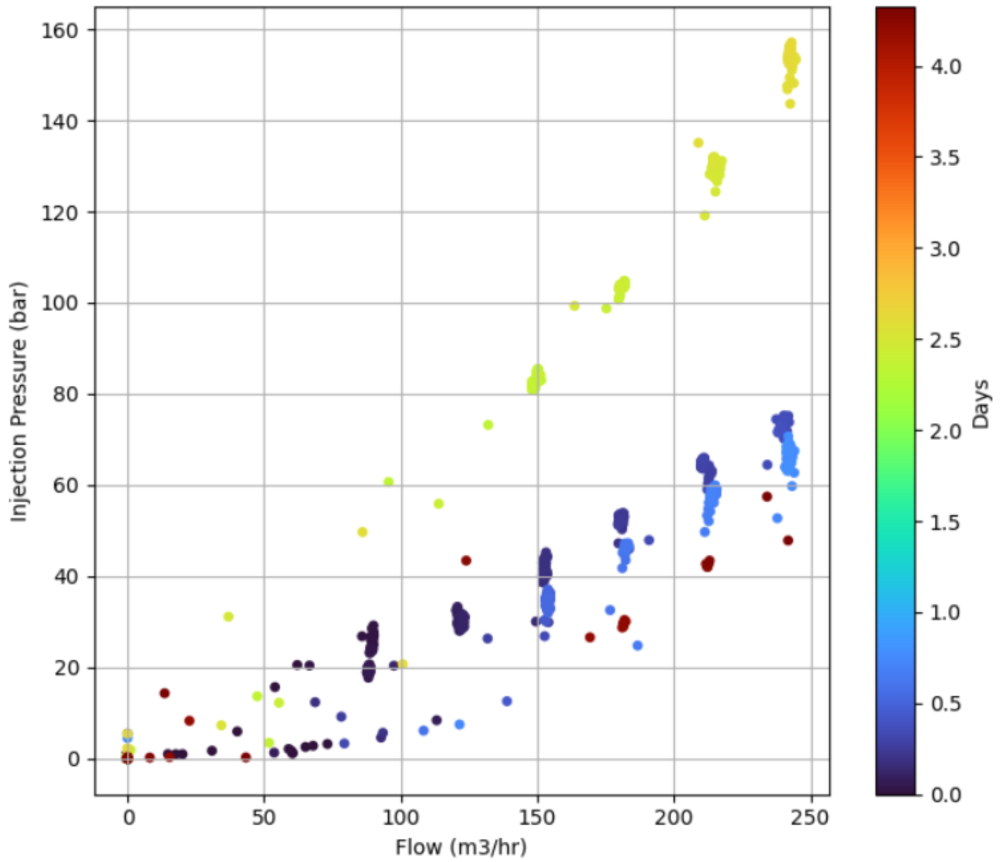

Figure 6: Well performance data from multirate injection test in September 2012 for CAL-GT-02.

4.2 New Analysis

From the injection performance plot of Figure 6, the injectivity index of the well was around 1.5-3.5 m^3/hr/bar. The first phase of the multirate test (blue data from Figure 5) was analyzed by the radial Darcy solution from CAL-GT-01. Using a kh value of 10 D-m provides a reasonable fit with the first 0.4 days. Afterward a kh value of 12.5 D-m provides a better fit. This indicates some stimulation or cleaning occurred. These values are reasonable values to begin for the reservoir numerical model.

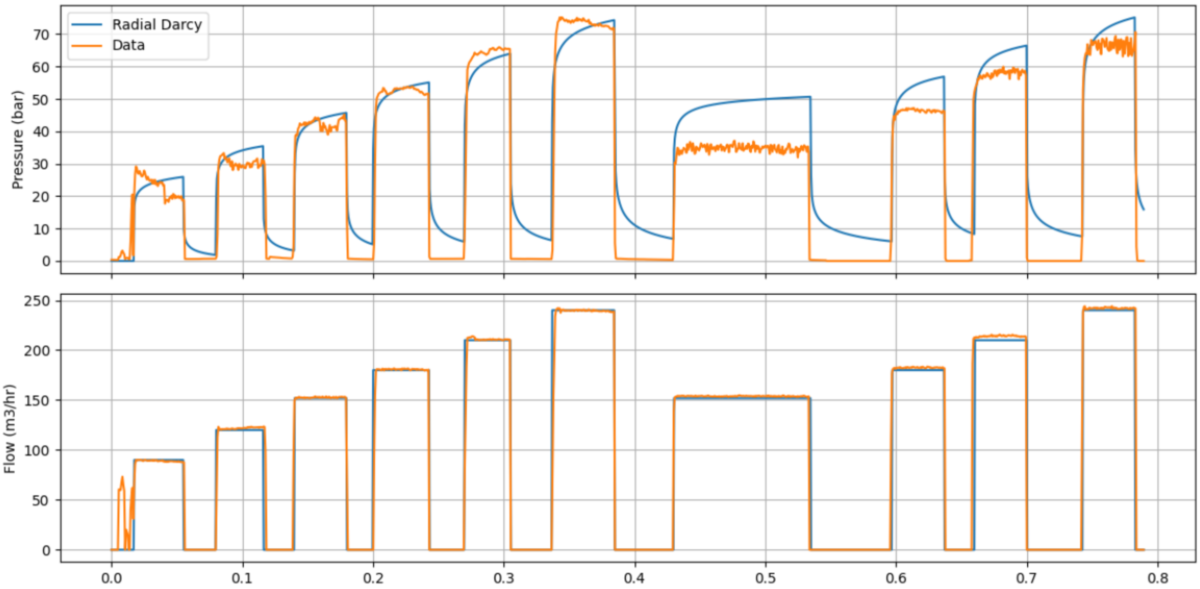

Figure 7: CAL-GT-02 Multirate test with radial Darcy flow fit for a permeability-thickness of 10 Dm.

5 CAL-GT-03

CAL-GT-03 was originally intended to be a production well but was used for injection due to the failure of CAL-GT-02. The well is nearby the production well CAL-GT-01 and located near the Tegelen fault structure.

5.1 Well Test Data and Previous Analysis

There has been a reasonable amount of previous work and available data on CAL-GT-03 as the well was used for some time. Production data exists in 5-minute intervals from November 2014 – March 2015 (See Figure 1). A production test occurred from 12-14 July 2013 with highly variable flowrates from the downhole ESP. A report over the tests is available (Laenen, 2013). The report determined a PI for the well of 7 m^3/hr/bar for lower discharge rates and 4.5 m^3/hr/bar for higher pump rates. Downhole pressure, temperature, spinner (PLT) measurements were made at a variety of flowrates in 2013, 2014, 2016, and 2017. The previous PLT analysis exists as an Excel file with percentage contributions determined for each 50 m (MD) well increment. No written report of the PLT analysis was located.

Table 1: Percentage of Total Flow for CAL-GT-03 depths from Excel workbook.

	Measurement	m3/h	MD											
			1770	1800	1850	1900	1950	2000	2050	2100	2150	2200	2300	2370
12+13 nov-13	1e	118	100%	37%	32%	24%	22%	0%	0%	0%	0%	0%	0%	0%
12+13 nov-13	4e	127	100%	44%	34%	27%	25%	15%	0%	0%	0%	0%	0%	0%
12+13 nov-13	2e	136	100%	41%	35%	27%	26%	16%	0%	0%	0%	0%	0%	0%
12+13 nov-13	3e	148	100%	44%	36%	27%	23%	16%	0%	0%	0%	0%	0%	0%
03-Oct-14	5e	148	100%	75%	61%	56%	56%	27%	13%	0%	0%	0%	0%	0%
03-Dec-15	6e	157	100%	74%	65%	59%	59%	23%	11%	0%	0%	0%	0%	0%
06-Oct-16	7e	156	100%	69%	58%	52%	52%	17%	0%	0%	0%	0%	0%	0%
06-Apr-17	8e	248	100%	68%	63%	58%	54%	22%	4%	0%	0%	0%	0%	0%
23-Oct-17	9e	248	100%	83%	75%	62%	59%	22%	9%	0%	0%	0%	0%	0%

5.2 New Analysis

5.2.1 Production Data

The well performance curve for the production data from November 2014 – March 2015 can be seen in Figure 8. The slope of the line of the data indicates an Injectivity Index (II) of about 10 m^3/hr/bar. This is slightly higher than the previous Productivity Index calculated (Laenen, 2013), but consistent in general, for geothermal wells to have a higher II vs PI.

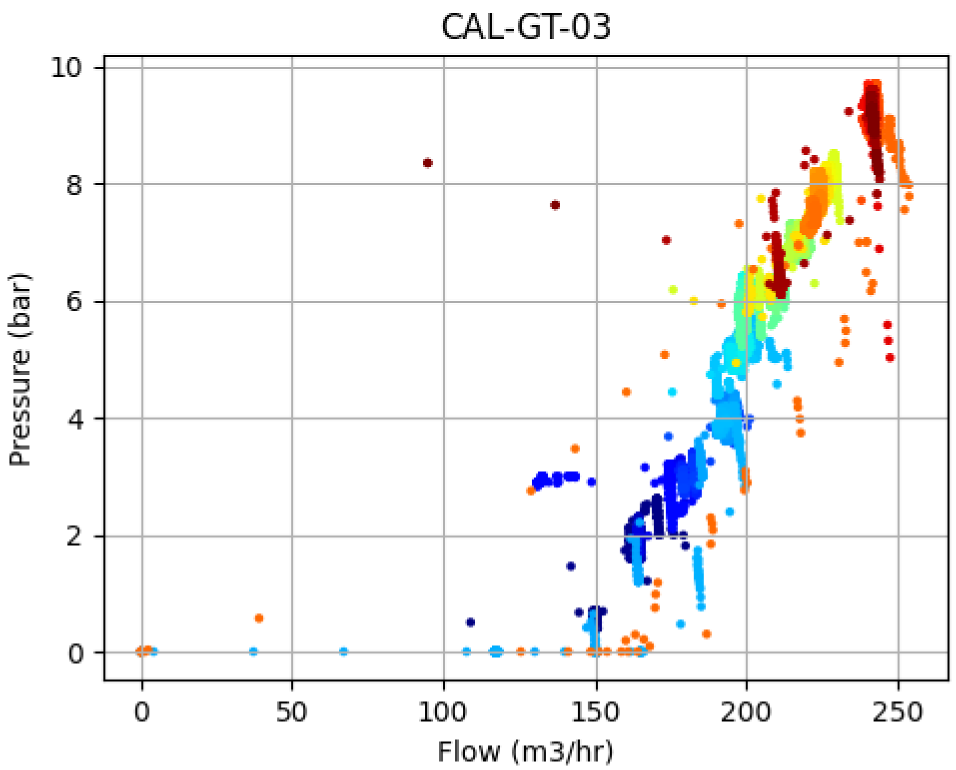

Figure 8: Performance curve for CAL-GT-03 for production dataset from 2014-2015.

5.2.2 PLT Data

Some data was available for the PLT tests run in November 2013, October 2014, and October 2017 at flowrates of 118 m^3/hr, 148 m^3/hr, and 248 m^3/hr, respectively. All spinner data was re-analyzed to evaluate the fluid velocity in the wellbore. In an ideal spinner test, the well is held at a consistent flowrate and the spinner tool will completely pass the feedzones both up and down at at least one consistent velocity. More than one tool velocity can help to provide more reliable velocity measurements as differences in the impellor response when the tool is moving with the fluid flow direction vs against the fluid flow direction can be seen. We followed the technique laid out in (Grant & Bixley, 2011) and separated the well in 5 m increments for flow analysis. In each interval, a “cross-plot” is constructed of spinner frequency (x) vs tool speed (y). The y-intercept of the line gives the fluid velocity in the well. The fluid velocity can then be used in a wellbore flow model to determine the flow and how the flow changes at different depths in the well.

The PLT data for CAL-GT-03 were incomplete. There was one complete up and down pass in 2013 and 2014 at about 12 m/min and 10 m/min, respectively. There was only one complete up pass in 2017. The main problems with the data were: the up/down tool speeds in 2013 were not consistent; the spinner response in 2013 is inconsistent between passes; there was only an up pass in 2017 (so it’s impossible to determine the actual fluid velocity); and the spinner seems to have been improperly chosen for the well. The issue with the spinner is that the spin seems to go to zero and not “positive” near the bottom of the well. It is especially visible in the 2013 up data but can be seen in nearly every dataset. So, the spinner response is not consistent across multiple passes and tool speeds/directions. Cross plots can be constructed from the 2014 dataset, but there will be some uncertainty/error below 2050 m MD. But that is near the bottom of the well and likely not essential.

At first inspection, major feedzones can be seen at around 1780 m MD in all data and around 1960 m MD in the 2014 dataset. There is also a more distributed feedzone around 2050 m MD over about 20-30 m. The pressure in the well also reduced for each test (in time) even though the flow rate was increasing. So, the well exhibited obvious signs of cleaning and stimulation.

For 2013, we use only the down-pass data set. For 2017, there is only an up-pass data set. Those data were simply scaled to the appropriate fluid velocity for the given recorded flowrates from the tests and analyzed in that way.

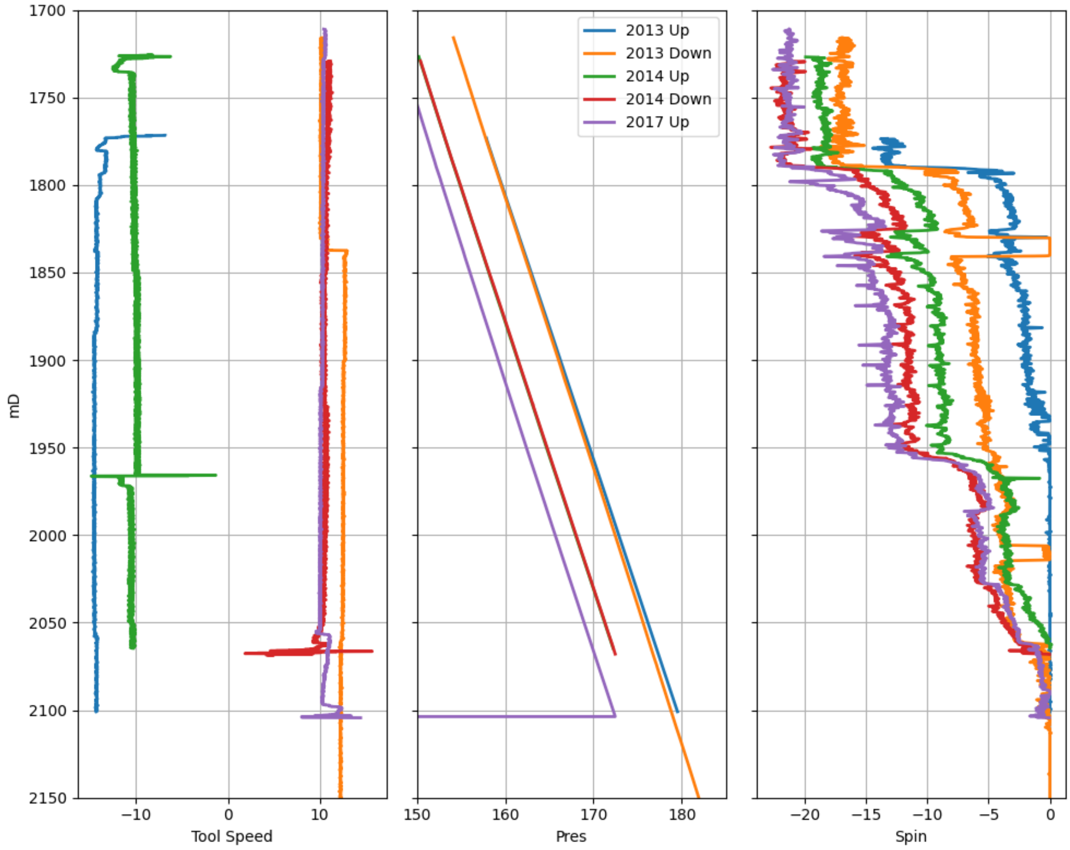

Figure 9: Raw PLT data for tool speed, pressure, and spin frequency for the CAL-GT-03 PLT measurements.

Figure 10 displays the analyzed pressure and fluid velocities for each PLT test. The reservoir pressure (black) was determined by a shut survey immediately before the 118 m^3/hr test in 2013.

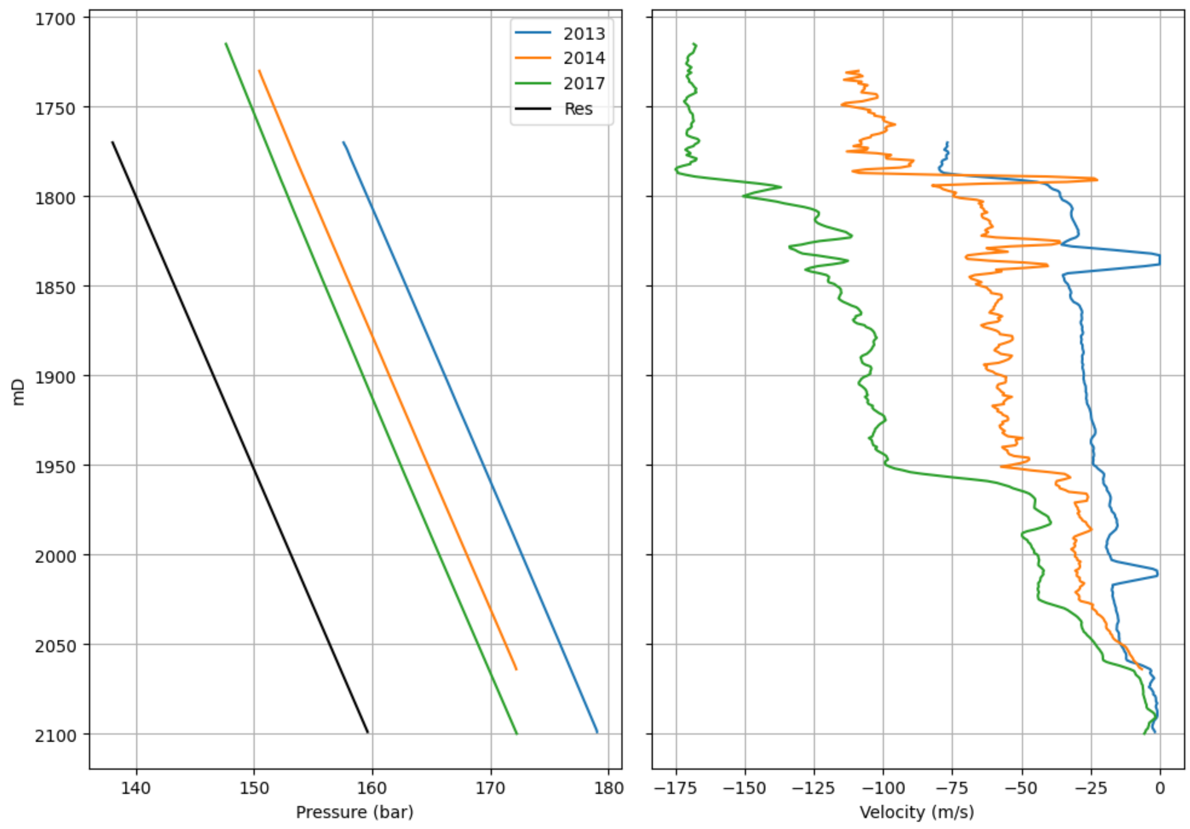

Figure 10: PLT pressure measurements and analyzed fluid velocity results (negative = downward flow) for CAL-GT-03 PLT tests.

Following from (Grant & Bixley, 2011), the Injectivity Index (II) of each feedzone can be determined by the flowrate decrease and subsequent fluid velocity drop at each zone. The injectivity index is defined as:

$$II_f = \frac{\pm W_f}{P_{Rf} - P_{wf}}$$

Where the subscripts *f* represents the *feedzone*, *R* the *reservoir*, and *w* the *well*. The variable *W* is the flow (in or out at the feedzone) and *P* is the pressure.

A wellbore flow model can be constructed to determine the pressure drop within the wellbore. The pressure drop over the elevation change can be expressed as:

$$\frac{dp}{dz} = \left(\frac{dp}{dz}\right)_{static} + \left(\frac{dp}{dz}\right)_{fric}$$

Where the static pressure change is:

$$\frac{dp}{dz_{static}} = \rho g$$

And the friction pressure drop is:

$$\frac{dp}{dl} = \frac{f_M \rho V^2}{2D}$$

Where D is the diameter of the wellbore, V^2 is the fluid velocity, l is the wellbore length (z if vertical), and f_M is the dimensionless “Moody friction factor”, which depends on Reynolds number and can be implicitly solved for.

Referring to the velocity plots from Figure 10, we determine feedzones to be located 1788 mD (-1436 mTVDSS, point source), 1801 mD (-1445 mTVDSS,105 m length), 1957 mD (-1551 mTVDSS, point source), 2028 mD (-1600 mTVDSS, 20 m length), and 2060 mD (-1622 mTVDSS, point source). The flow loss in each feedzone can be estimated to match the velocity drop over each zone. Then pressure, velocity, and flow were modelled by using the pressure drop equations above for the test flowrates. The results for pressure, fluid velocity, and mass flow can be seen for each test in Figure 11 - Figure 13.

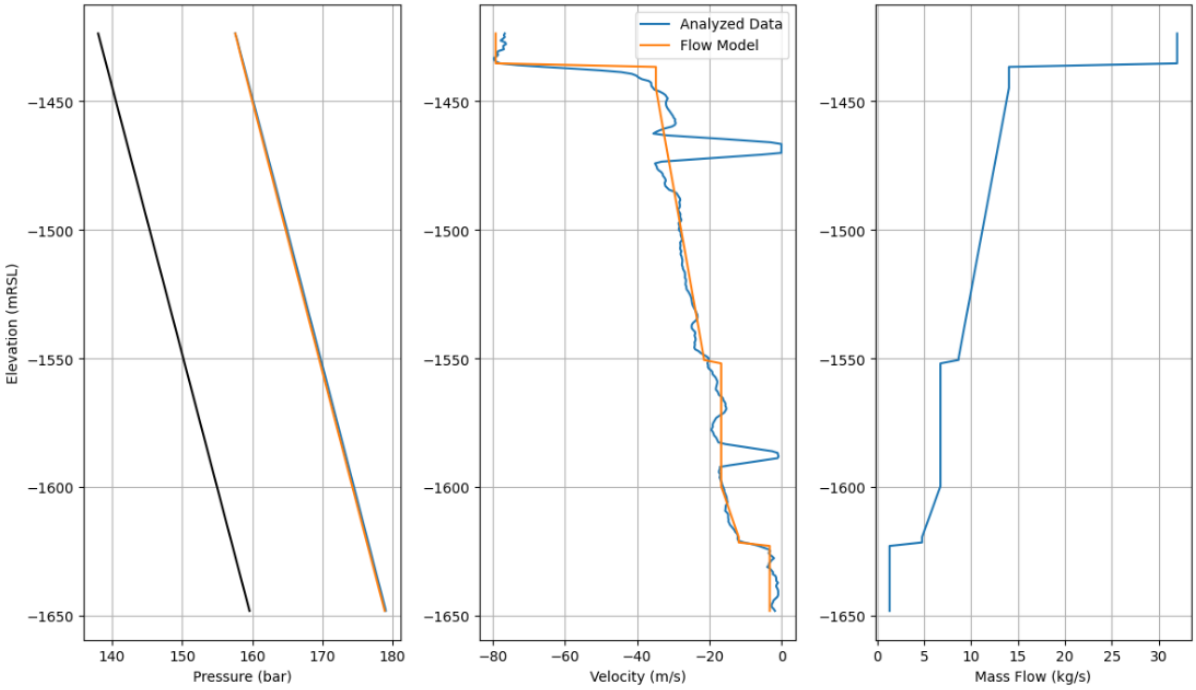

Figure 11: Wellbore model pressure (left), fluid velocity (center), and flow for CAL-GT-03 2013 PLT dataset.

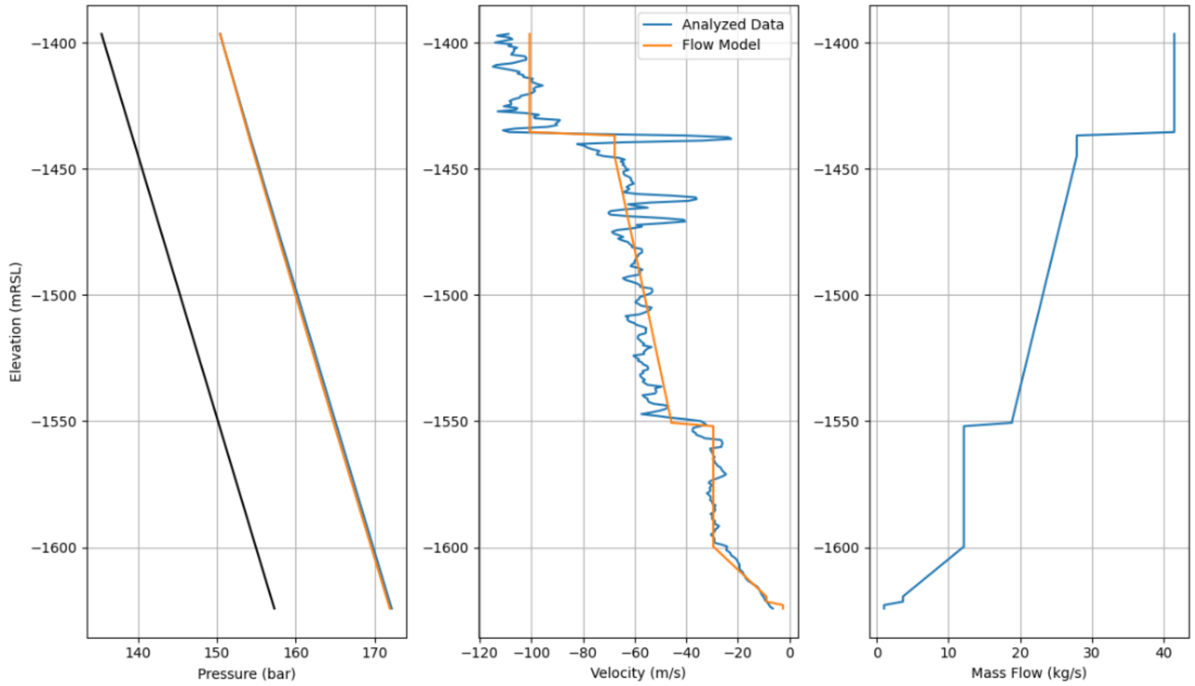

Figure 12: Wellbore model pressure (left), fluid velocity (center), and flow for CAL-GT-03 2014 PLT dataset.

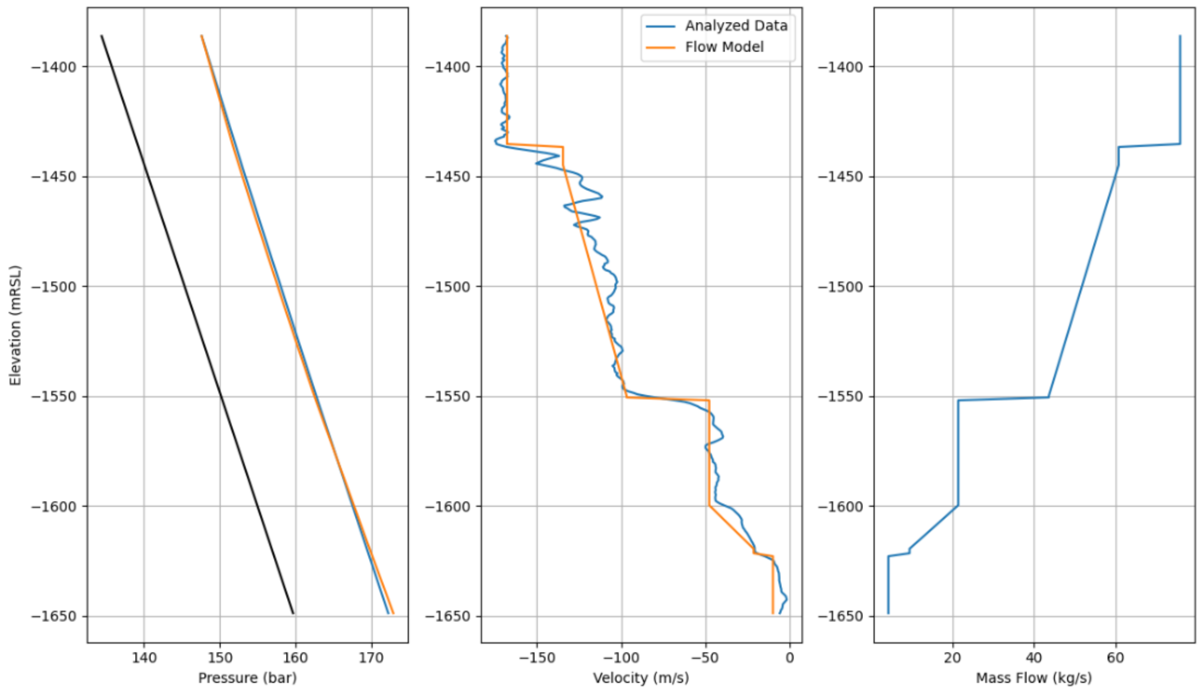

Figure 13: Wellbore model pressure (left), fluid velocity (center), and flow for CAL-GT-03 2017 PLT dataset.

As the well performance was stimulating, the injectivity indices of each feedzone had to increase in time to match the changes in flow loss at each zone over time. The results of each PLT test analysis for feedzone location, extent, and injectivity index can be seen in Table 2. The total injectivity index of the well increased from 3.09 to 5.76 to 11.8 m^3/hr/bar. The feedzone at -1550 mTVDSS showed the largest single increase in injectivity.

Table 2: Feedzone locations and injectivity indices for the PLT tests in CAL-GT-03.

Year	Flow [m3/hr]	FZ Z	MD	Length	II [m3/hr/bar]	Total II
2013	118	-1436	1788	1	1.656	3.092
		-1445	1801	105	0.68	
		-1551	1957	1	0.18	
		-1600	2028	20	0.252	
		-1622	2060	1	0.324	
2014	148	-1436	1788	1	1.656	5.76
		-1445	1801	105	1.512	
		-1551	1957	1	0.828	
		-1600	2028	20	1.44	
		-1622	2060	1	0.324	
2017	248	-1436	1788	1	2.16	11.826
		-1445	1801	105	3.402	
		-1551	1957	1	3.24	
		-1600	2028	20	2.304	
		-1622	2060	1	0.72	

To complete the analysis, the goal was to arrive at permeability estimations for each feedzone to provide appropriate values for the reservoir numerical model history match. To do this, we utilized the steady-state radial linesource solution equation with skin included:

$$p_r = p_w + \frac{Q\mu}{2\pi kh}\{\ln(\mathrm{r/r\_w}) + S\}$$

Where *r* is the radius of pressure evaluation (away from the well) and p_r is the pressure at that radius. In this case, that is the reservoir pressure from the feedzone analysis p_{Rf}. Additionally, *k* is the permeability, *h* is the reservoir height, *Q* is the mass flowrate (kg/s), μ is the fluid viscosity, and *S* is the skin factor.

The radial flow assumption may not be a perfect assumption for the fractured reservoir at the Californië site, but it is a reasonable estimation for beginning the history matching process in the numerical reservoir model. We assume that S=0 for the 2013 test, then allow skin to increase to match the equivalent increases in well injectivity. We tested reservoir radii of 500 m and 1000 m to determine that effect on the result and to provide a small range of permeabilities for testing. Summing up each feedzone, we can arrive at a total well k-h value (in D-m). We then fix that value and determine the skin that is required to maintain well injectivity increase over time. Table 3 shows the results of the wellbore modelling analysis for CAL-GT-03 for the 500 m reservoir radius and Table 4 shows the results for a 1000 m radius. The takeaway values are the feedzone kh values. These values can be placed in for appropriate kh values on the representative geologic structures in the numerical reservoir model.

Table 3: CAL-GT-03 results for Injectivity Index, kh, and skin for 500 m reservoir radius.

Year	Flow [m3/hr]	FZ Z	MD	Length	II [m3/hr/bar]	Total II	kh (D-m)	total kh (D-m)	Skin
2013	118	-1436	1788	1	1.656	3.092	6.322	11.806	0
		-1445	1801	105	0.68		2.597		
		-1551	1957	1	0.18		0.688		
		-1600	2028	20	0.252		0.962		
		-1622	2060	1	0.324		1.237		
2014	148	-1436	1788	1	1.656	5.76	3.394	11.806	-3.999
		-1445	1801	105	1.512		3.099		
		-1551	1957	1	0.828		1.697		
		-1600	2028	20	1.44		2.952		
		-1622	2060	1	0.324		0.664		
2017	248	-1436	1788	1	2.16	11.826	2.156	11.806	-6.377
		-1445	1801	105	3.402		3.396		
		-1551	1957	1	3.24		3.235		
		-1600	2028	20	2.304		2.3		
		-1622	2060	1	0.72		0.719		

Table 4: CAL-GT-03 results for Injectivity Index, kh, and skin for 1000 m reservoir radius.

Year	Flow [m3/hr]	FZ Z	MD	Length	II [m3/hr/bar]	Total II	kh (D-m)	total kh (D-m)	Skin
2013	118	-1436	1788	1	1.656	3.092	6.829	12.752	0
		-1445	1801	105	0.68		2.806		
		-1551	1957	1	0.18		0.742		
		-1600	2028	20	0.252		1.039		
		-1622	2060	1	0.324		1.336		
2014	148	-1436	1788	1	1.656	5.76	3.666	12.752	-4.32
		-1445	1801	105	1.512		3.348		
		-1551	1957	1	0.828		1.833		
		-1600	2028	20	1.44		3.188		
		-1622	2060	1	0.324		0.717		
Feb-17	248	-1436	1788	1	2.16	11.826	2.329	12.751	-6.889
		-1445	1801	105	3.402		3.668		
		-1551	1957	1	3.24		3.494		
		-1600	2028	20	2.304		2.484		
		-1622	2060	1	0.72		0.776		

Linking the feedzone locations to geology, the likely structures that host each feedzone are: 1788 mD (-1436 mTVDSS) – possibly permeable layer or fracture connected to nearby fault zone; 1801 mD (-1445 mTVDSS) – limestones (dolomites) with some distributed permeability; 1957 mD (-1551 mTVDSS) – possible permeable fracture or layer just above clays/shales (Pont d'Arcole formation); 2028 mD (-1600 mTVDSS) – Just below Pont d'Arcole formation; and 2060 mD (-1622 mTVDSS) – same general zone as distributed zone above.

6 CAL-GT-04

6.1 Well Test Data and Previous Analysis

A multirate pump test was performed on CAL-GT-04 in February 2016 after drilling. The well has a 7" perforated uncemented liner and about 200 m of open hole 8.5" well at the bottom. The pump test data was analyzed by VITO (Laenen & Broothaers, 2016a) and later TNO-AGE (Juez-Iarre & van Kempen, 2017). The data from the original pump test were available in an Excel file – the rates can be seen in Figure 14. The initial VITO analysis indicated a very high negative skin value (~-8) and a fairly high well transmissivity (7.8-10.8 m^2/hr). The permeability was estimated by VITO to be between 175 mD (480 m entire perforated + open hole section production) and 2 Darcy (50 m productive section). So a kh of around 84 – 100 Dm.

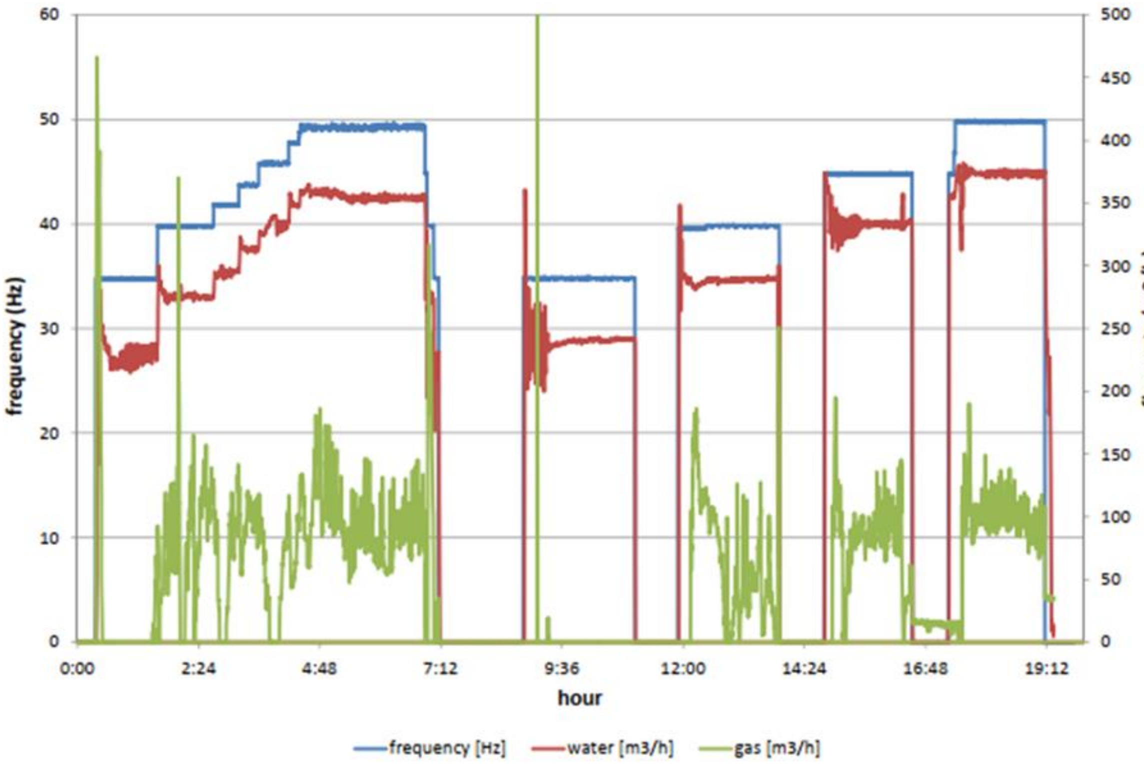

Figure 14: Pump test on CAL-GT-04.

A second analysis was performed by TNO-AGE in 2017. They also determined a high negative skin around the well of -8. Their analysis indicated a permeability thickness kh of 94 Dm, which indicated a permeability of 195 mD over the 480 m productive height of the well. No further analysis of CAL-GT-04 performance was performed during this project as no additional data was located.

7 CAL-GT-05

7.1 Well Test Data and Previous Analysis

The production data from the CLG site includes 5-minute interval data from July 2017 to September 2018 as seen in Figure 1. The data plotted as a well performance curve can be seen in Figure 15. The earliest data is colored in the teal-blue color and latest data in magenta. The data indicates a poorer well performance than CAL-GT-03 with well pressures often over 30 bar. The well did seem to stimulate in time though – showing an injection flow rate 100 m^3/hr at under 20 bar well head pressure in the later phases.

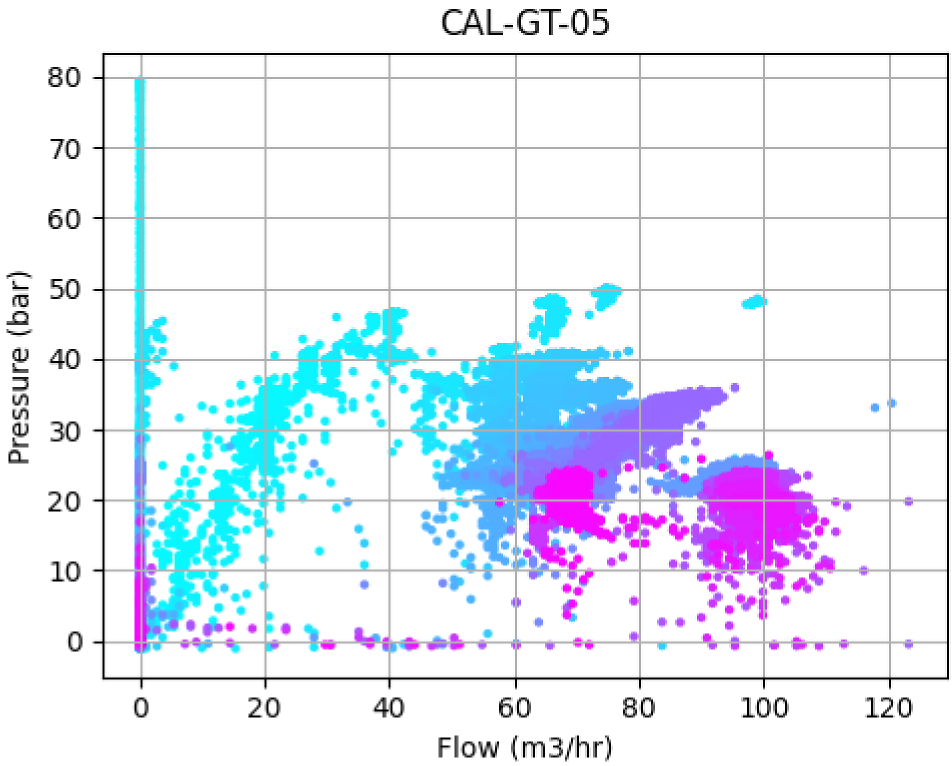

Figure 15: Performance of CAL-GT-05 for production data from July 2017 - September 2018. The data is colored by date where light blue colors are earlier dates and the purple/fuchsias are later dates.

There was a specific multi-rate production/buildup test on the well in March 2016. That test was analyzed by both VITO (Laenen & Broothaers, 2016b) and TNO-AGE (Juez-larre & van Kempen, 2017). The pressure, flowrate, and pump frequency from the test can be seen in Figure 16. VITO's analysis determined a total well permeability thickness kh of 1.8-3.5 Dm with a skin of -3. In the re-analysis by TNO-AGE, both the hypotheses of dual-porosity and homogenous porosity were tested. The results indicated a kh value of 1.6 Dm for the dua-porosity model and 9.3 Dm for the homogenous model. The skin was determined to also be about -3 (-3.5).

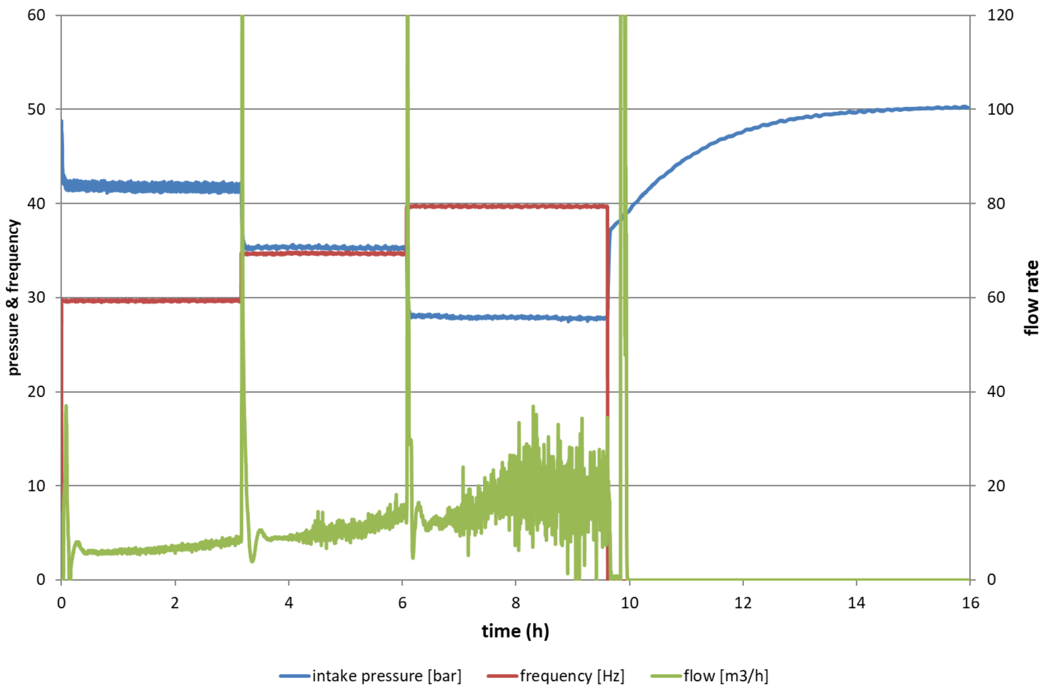

Figure 16: Pump test parameters from CAL-GT-05.

In addition, PLT tests were performed in 2016 and 2017 on CAL-GT-05. In 2016, PLT logs were run in the static (shut) position and at two flowrates: 30 m^3/hr and 120 m^3/hr. The flowing surveys were run at 3 different tool speeds (both up and down) – 15, 30, and 45 m/min. The raw data from 2016 can be seen in Figure 17 and Figure 18. The data is of exceptionally good quality. A few notes: the tool speed is consistent both in the up and down passes; the spinner response is also consistent across each pass; and the temperature results show clear heating from about 2220-2300 m MD. The heating indicates that most of the fluid has exited the well in that region. The consistent spinner data/tool speed allows for accurate flow estimations.

In 2017, PLT logs were run at two flowrates: 170 m3/hr and 250 m3/hr. Each survey was run at two different tool speeds (both up and down). The raw data can be seen in Figure 19 and Figure 20. Some data quality notes from 2017: the tool speeds are not as consistent as the 2016 dataset and the spinner data is also inconsistent and appears the pitch was perhaps incorrectly chosen (cutting out at low flowrates).

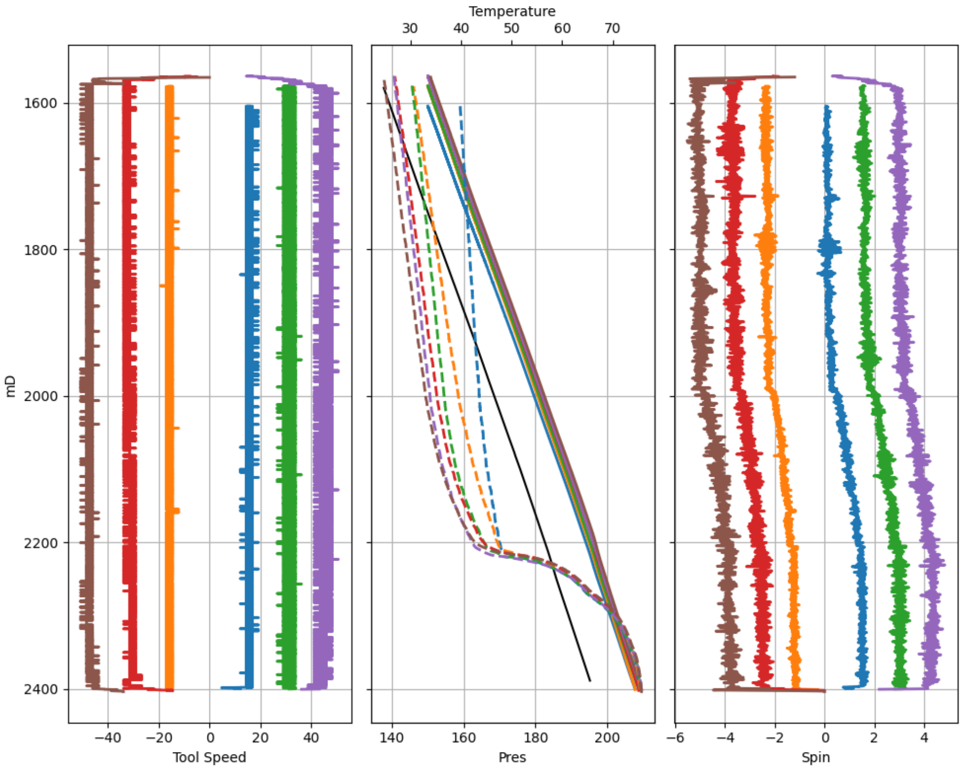

Figure 17: Raw PLT data for 2016 survey at 30 m^3/hr flowrate on CAL-GT-05. In the center image, temperatures are the dashed lines and pressures are the solid lines.

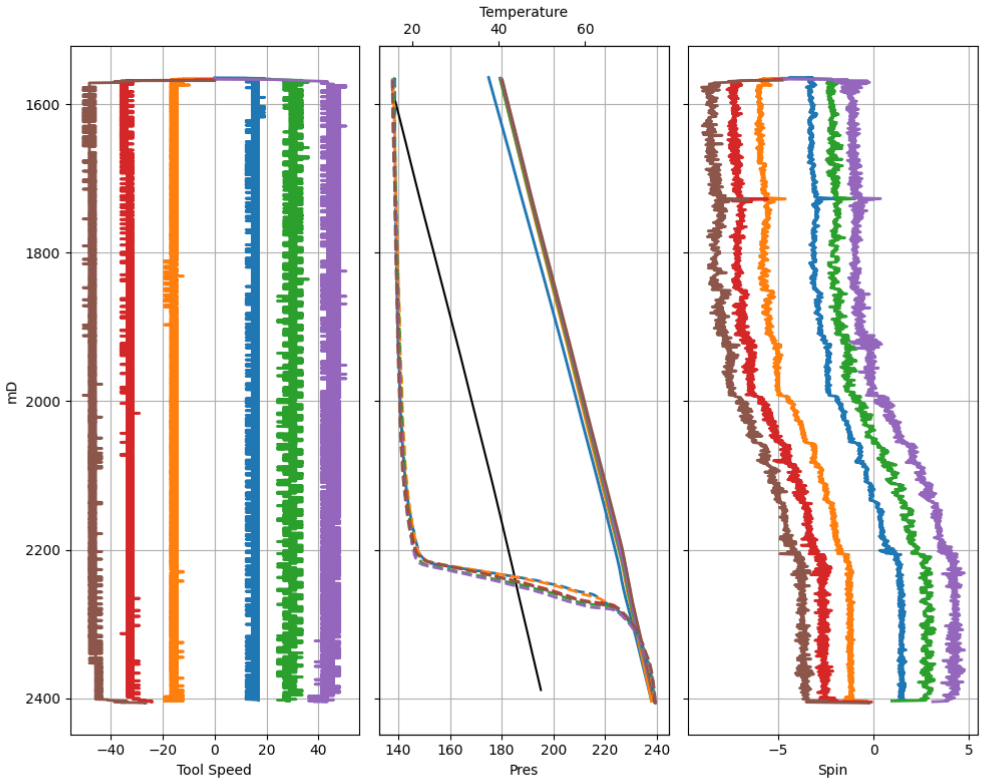

Figure 18: Raw PLT data for 2016 survey at 120 m^3/hr on CAL-GT-05 (pressure solid, temperature dashed lines)

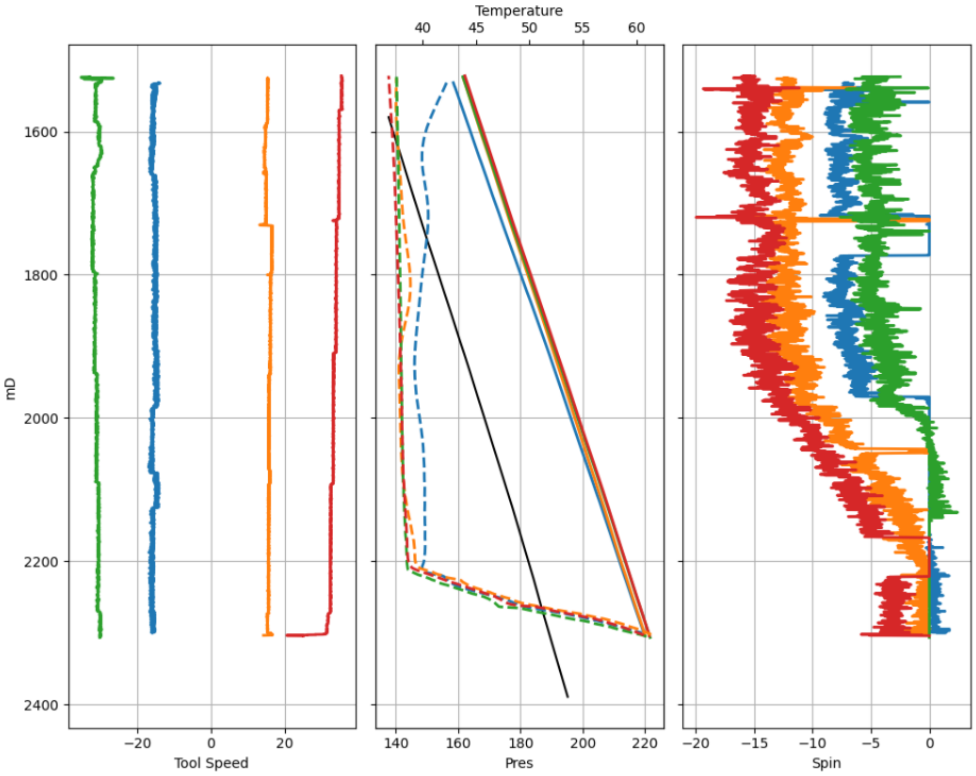

Figure 19: Raw PLT data for 170 m^3/hr test in 2017 on CAL-GT-05 (pressure solid, temperature dashed lines).

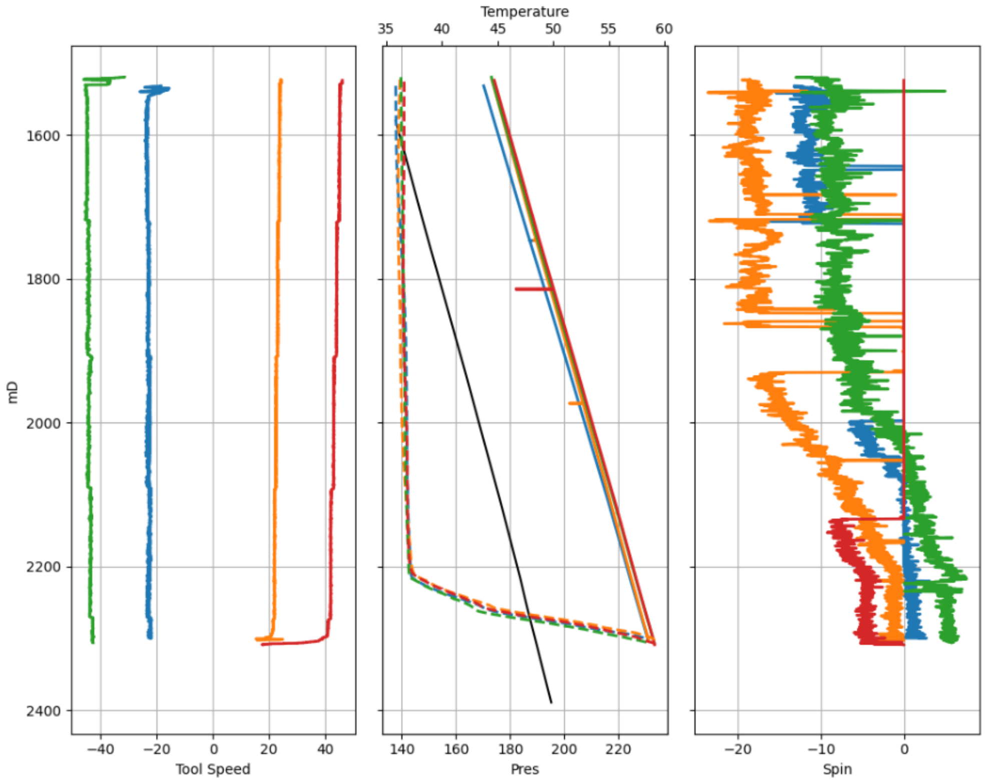

Figure 20: Raw PLT data for 250 m^3/hr test in 2017 on CAL-GT-05 (pressure solid, temperature dashed lines).

7.2 New Analysis

The new analysis was focused on the PLT data. Specifically, to gain additional insights into the permeability and injectivity indices of each feedzone as performed for CAL-GT-03. The data of 2016 was analyzed using cross plots for direct fluid velocity determination. The data of 2017 was best used by taking a single pass and scaling the velocity to the expected velocity for the flowrate and well diameter. The up pass at 15 m/min was used for the 170 m^3/hr dataset (orange data). For the 250 m3/hr dataset, we analyzed and scaled the data from the 40 m/min down pass (green data). These prove to be reasonable representations as the feedzone locations are consistent with the 2016 dataset which was indeed a clean dataset. There is some uncertainty around fluid velocity near the bottom of the well, but the location, extent, and injectivity of the feedzones can be estimated from the available data.

The analyzed velocities and pressures can be seen in Figure 21. By the velocity plots, we determine feedzone locations and lengths (vertical distance) to be: 1847 m MD (-1560 mTVDSS point source); 1927 m MD (-1620 mTVDSS, point source); 1982 m MD (-1660 mTVDSS, 40 m length); 2043 m MD (-1705 mTVDSS, 75 m length); 2168 m MD (-1795 mTVDSS, 25 m).

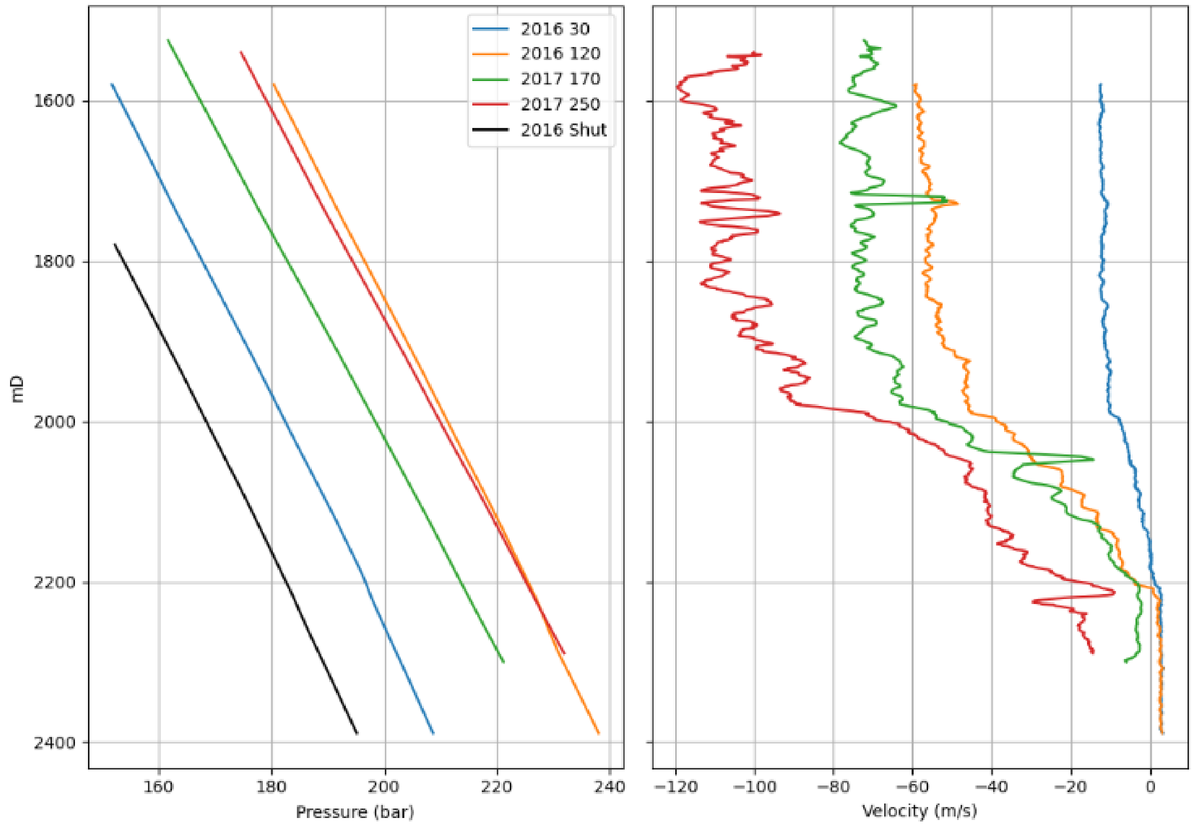

Figure 21: PLT pressure and analyzed velocities for 2016 and 2017 datasets on CAL-GT-05.

Figure 22 through Figure 25 display the wellbore modelled results from the PLT tests graphically. The same procedure as utilized for CAL-GT-03 was also performed here.

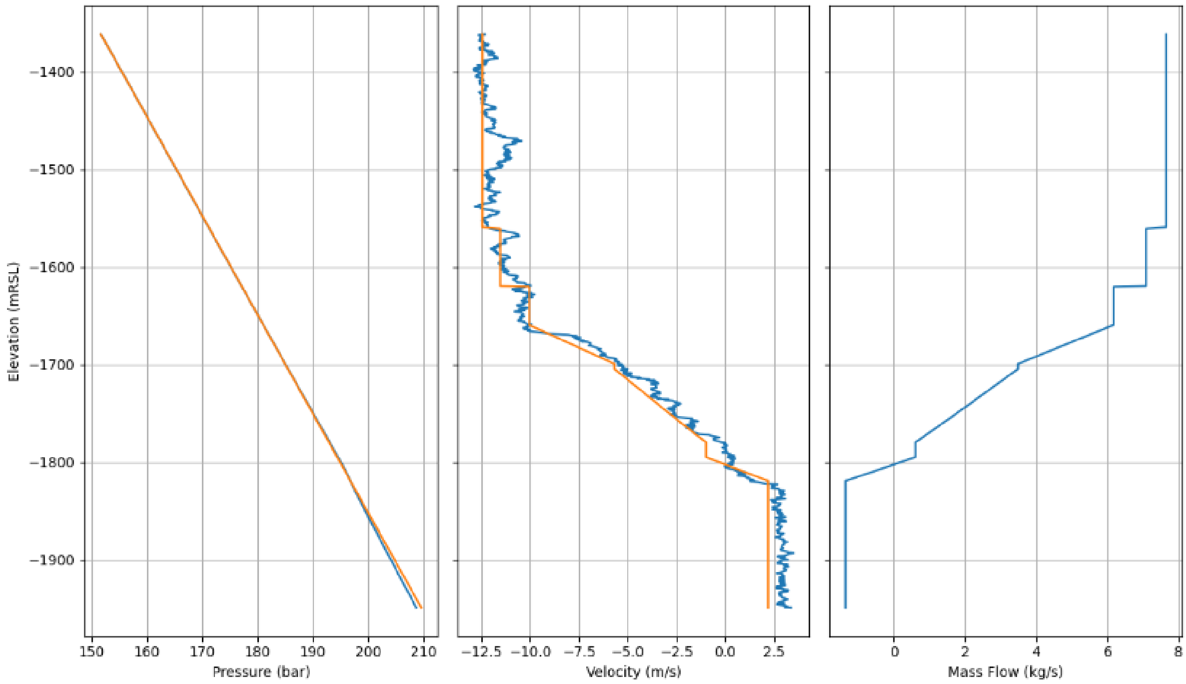

Figure 22: CAL-GT-05 wellbore model for 2016 dataset at 30 m³/hr.

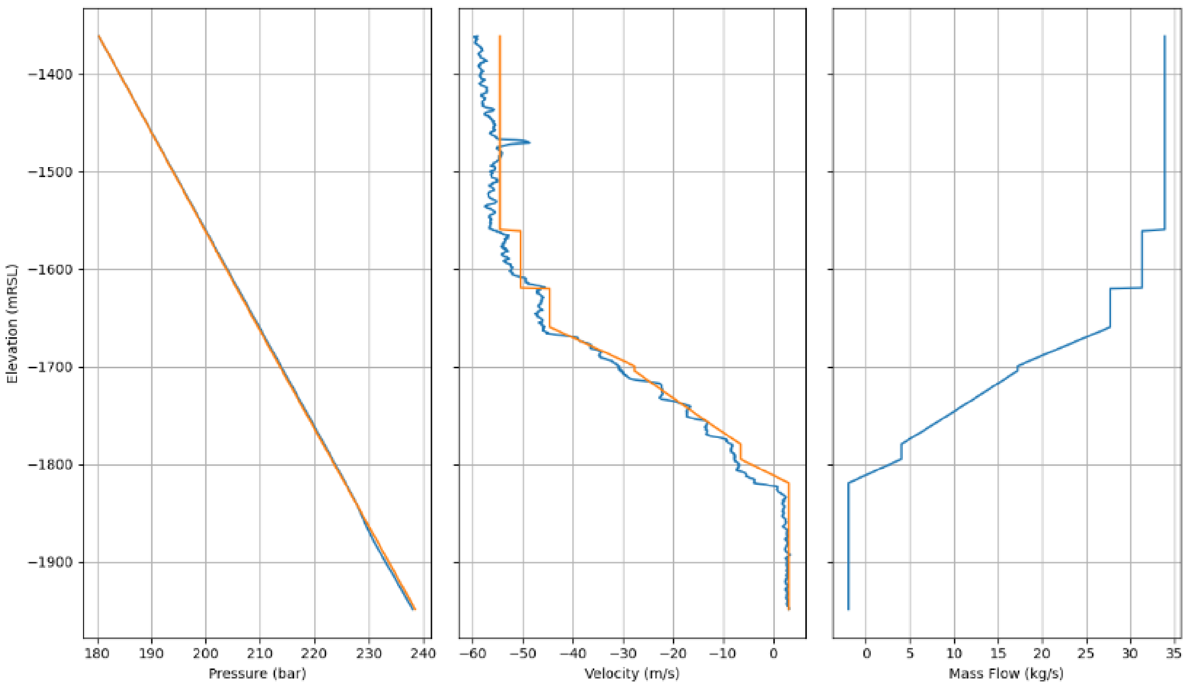

Figure 23: CAL-GT-05 wellbore model for 2016 dataset at 120 m³/hr.

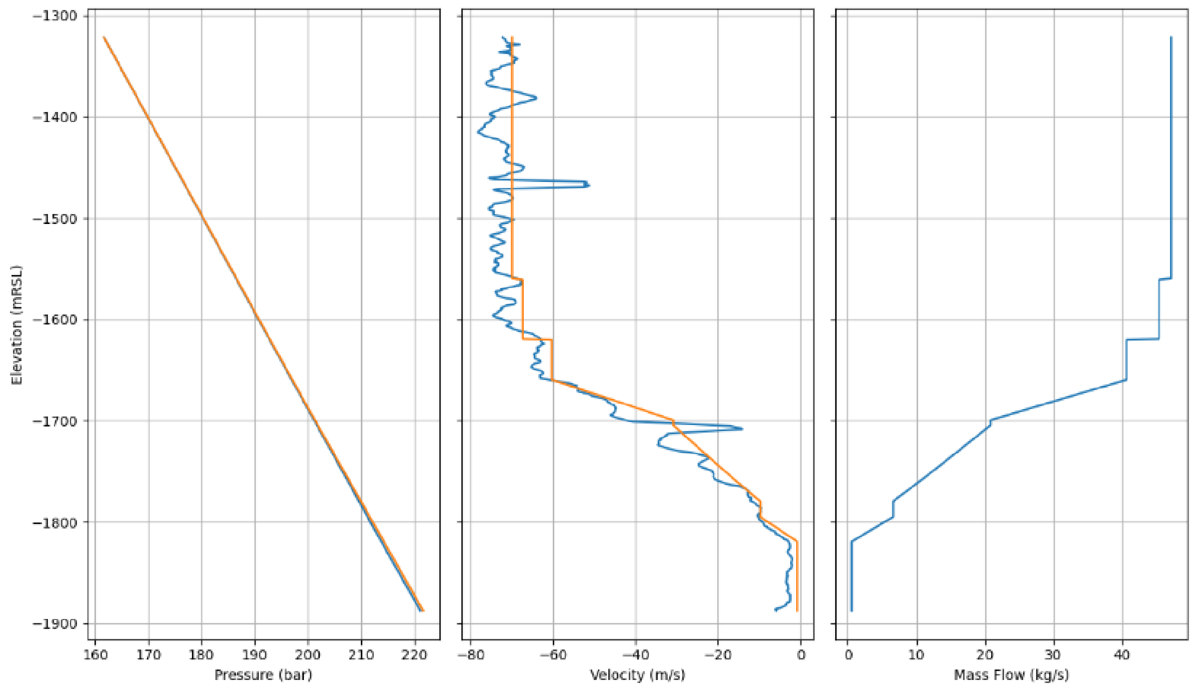

Figure 24: CAL-GT-05 wellbore model for 2017 dataset at 170 m^3/hr.

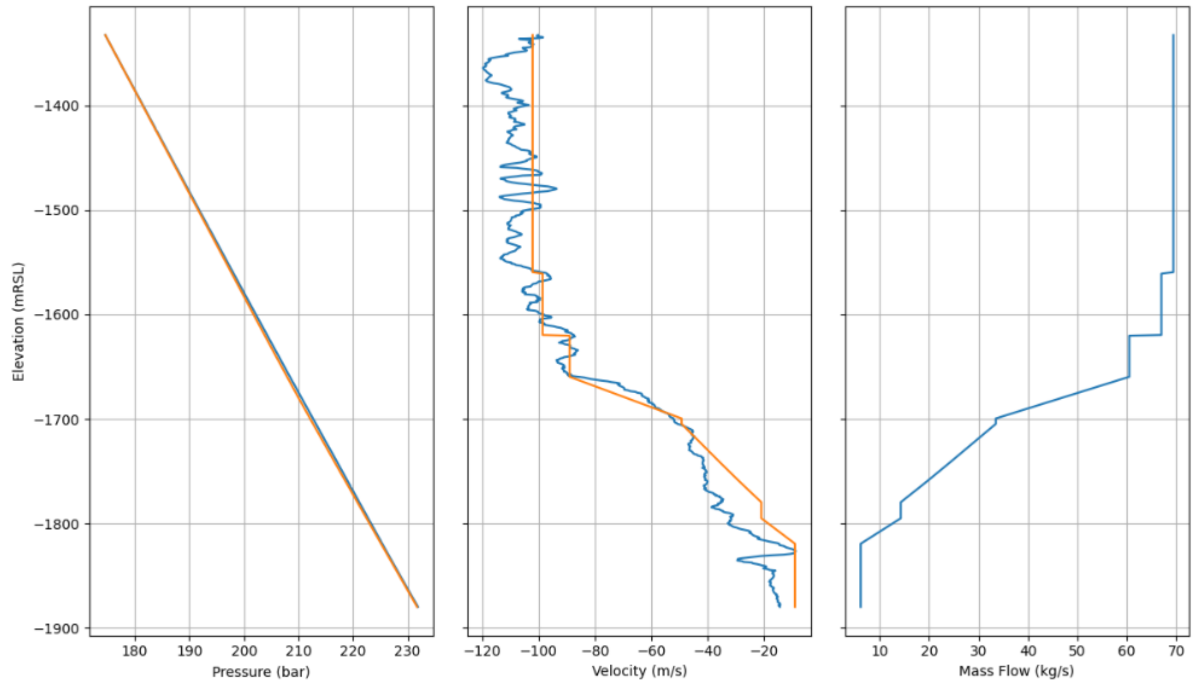

Figure 25: CAL-GT-05 wellbore model for 2017 dataset at 250 m^3/hr.

For injectivity index and permeability estimation, we again followed the procedure outlined for CAL-GT-03 and assumed reservoir radius values of 500 m and 1000 m. We assumed the initial skin around the well was -3.5 to correspond to previous analysis (Juez-Iarre & van Kempen, 2017). The well also showed clear signs of stimulation in time. In the analysis, this was expressed as an increase of the negative value of skin (-5.7 for 500 m radius and -6.1 for 1000 m radius). The results for the individual feedzone II and kh values are located in Table 5 and Table 6.

Table 5: PLT feedzone analysis summary for CAL-GT-05 at 500 m reservoir radius.

Year	Flow [m3/hr]	FZ Z	MD	Length	II [m3/hr/bar]	Total II	kh (D-m)	total kh (D-m)	Skin
2016	30	-1560	1847	1	0.072	1.71	0.157	3.735	-3.5
		-1620	1927	1	0.234		0.511		
		-1660	1982	40	0.504		1.101		
		-1705	2043	75	0.54		1.18		
		-1795	2168	25	0.36		0.786		
2016	120	-1560	1847	1	0.108	2.23	0.236	4.874	-3.5
		-1620	1927	1	0.306		0.668		
		-1660	1982	40	0.648		1.415		
		-1705	2043	75	0.81		1.769		
		-1795	2168	25	0.36		0.786		
2017	170	-1560	1847	1	0.108	4.12	0.128	4.874	-5.766
		-1620	1927	1	0.792		0.681		
		-1660	1982	40	1.728		2.043		
		-1705	2043	75	0.81		1.437		
		-1795	2168	25	0.72		0.585		
2017	250	-1560	1847	1	0.108	4.12	0.128	4.874	-5.766
		-1620	1927	1	0.792		0.681		
		-1660	1982	40	1.728		2.043		
		-1705	2043	75	0.81		1.437		
		-1795	2168	25	0.72		0.585		

Table 6: PLT feedzone analysis summary for CAL-GT-05 at 1000 m reservoir radius.

Year	Flow [m3/hr]	FZ Z	MD	Length	II [m3/hr/bar]	Total II	kh (D-m)	total kh (D-m)	Skin
2016	30	-1560	1847	1	0.072	1.71	0.179	4.259	-3.5
		-1620	1927	1	0.234		0.583		
		-1660	1982	40	0.504		1.255		
		-1705	2043	75	0.54		1.345		
		-1795	2168	25	0.36		0.897		
2016	120	-1560	1847	1	0.108	2.23	0.269	5.559	-3.5
		-1620	1927	1	0.306		0.762		
		-1660	1982	40	0.648		1.614		
		-1705	2043	75	0.81		2.017		
		-1795	2168	25	0.36		0.897		
2017	170	-1560	1847	1	0.108	4.12	0.146	5.56	-6.0833
		-1620	1927	1	0.792		0.777		
		-1660	1982	40	1.728		2.33		
		-1705	2043	75	0.81		1.639		
		-1795	2168	25	0.72		0.668		
2017	250	-1560	1847	1	0.108	4.12	0.146	5.56	-6.0833
		-1620	1927	1	0.792		0.777		
		-1660	1982	40	1.728		2.33		
		-1705	2043	75	0.81		1.639		
		-1795	2168	25	0.72		0.668		

The results provide kh values for different depths in the well that can be used as starting points in the numerical reservoir model. Regarding the geological connection to the feedzones, the first feedzone at 1847 m MD (-1560 mTVDSS) likely corresponds to the Dinantian/Devonian transition zone in the reservoir. The feedzone at 1927 m MD (-1620 mTVDSS) is described in the drilling as marlstone/crumbly and geologically may correspond to the edge of a faulted/damage zone. At 1982 m MD (-1660 mTVDSS) is the first distributed feedzone and is in the Devonian sandstones with a distributed fracture network of permeability. This is also clear of the feedzones below (2043 m MD/-1705 mTVDSS and 2168 m MD/-1795 mTVDSS). They are within the distributed fracture network of the damaged sandstones but show a variation in their local permeabilities. The kh values should give the reservoir model a starting point for the permeability value to assign to those regions.

8 REFERENCES

Broothaers, M. (2019). *Geologische onderbouwing voor de RNES Garantieregeling voor put CAL-GT-02.* VITO.

Broothaers, M., & Laenen, B. (2012). *Execution and Interpretation of the Pump Tests on Geothermal Well CAL-GT-01 (S02): Report for the SEI Application.* Mol, Belgium: VITO NV.

Grant, M., & Bixley, P. (2011). *Geothermal Reservoir Engineering.* Burlington, MA, USA: Elsevier.

Juez-Iarre, J., & van Kempen, B. (2017). *Well test evaluation CAL-GT-05.* Utrecht, The Netherlands: TNO.

Laenen, B. (2013). *Concise evaluation of the production test on CAL-GT-03.* Mol, Belgium: VITO.

Laenen, B., & Broothaers, M. (2016a). *Pump Tests on Geothermal Well CAL-GT-04: Execution, Interpretation, and Update of Calculation for RNES.* Mol, Belgium: VITO.

Laenen, B., & Broothaers, M. (2016b). *Pump Tests on Geothermal Well CAL-GT-05: Execution, Interpretation, and Impact on the Performance of the Geothermal Doublet and Update of Calculation for RNES.* Mol, Belgium: VITO.

vision on technology
for a better world

vito

APPENDIX F - Q-con report SGEO001, December 6, 2023. Californië Seismicity – Template Matching

REPORT

Californië Seismicity – Template Matching

Client: CWG/Nappa

Archive no.: SGEO001
Date: 06.12.2023

Q-con GmbH

Q-con GmbH
Marktstr. 39
76887 Bad Bergzabern
Germany

Email: info@q-con.de
Tel.: +49 (0) 6343 939699

Document title:	Californië Seismicity – Template Matching

Project:	safeGeo
Client:	CWG/Nappa
Archive no.:	SGEO001
Version:	231206
Date:	06.12.2023
Author(s):	Dr. S. Baisch
Checked by:	Dr. E. Rothert

Contents

1 BACKGROUND

1.1 Geothermal Operation and Seismic Monitoring at Californië

Earthquake activity near the Californië geothermal site has been continuously monitored by Q-con since September 2014. Seismic monitoring of the CWG doublet commenced with three monitoring stations in September 2014 (stations K01, K02, and K03). Two additional stations (K04 and K05) were deployed in November 2015 before drilling of the wells for the second geothermal doublet. Each monitoring station is equipped with a 3-C short-period surface seismometer (Lennartz LE3D) sampled at 100 Hz.

Routine data processing was performed using a highly sensitive STA/LTA detector combined with an amplitude threshold detector. Since the start of seismic monitoring in September 2014, a total number of 17 local earthquakes have been detected (Figure 1). The earthquakes occurred between Aug 2015 and Sep 2018. Using the magnitude definition by Dost et al. (2004), reported earthquake magnitudes range from $M_L = -1.2$ to $M_L = 1.7$. These magnitude values are sensitive to the earthquake depth, which was revised at a later stage after seismic velocities could be calibrated (Vörös & Baisch, 2022).

Operations at the CWG doublet stopped in May 2018, as no permit for continuous operation was granted by the regulator. Production from the CLG doublet was suspended in August 2018 following an $M_L = 0.0$ earthquake. Six days after stopping operations, a felt earthquake of magnitude $M_L = 1.7$ occurred within the previous cluster of reservoir seismicity. This was followed by eight additional earthquakes $M_L \leq 0.0$ within six days. No further earthquakes have been detected until March 2020.

In March 2020, one of the operators (Californie Lipzig Gielen Geothermie BV) terminated the monitoring contract. Seismic monitoring continued with a reduced station network consisting of the original stations K01, K02, and K03. Data processing was limited to running a relatively insensitive amplitude threshold detector designed for detecting perceptible earthquakes (PGV>0.3 mm/s). No earthquakes (exceeding the level of perceptibility) were detected in the time period March 2020 until today.

In September 2021 station K02 was shut-down and has not been replaced until now.

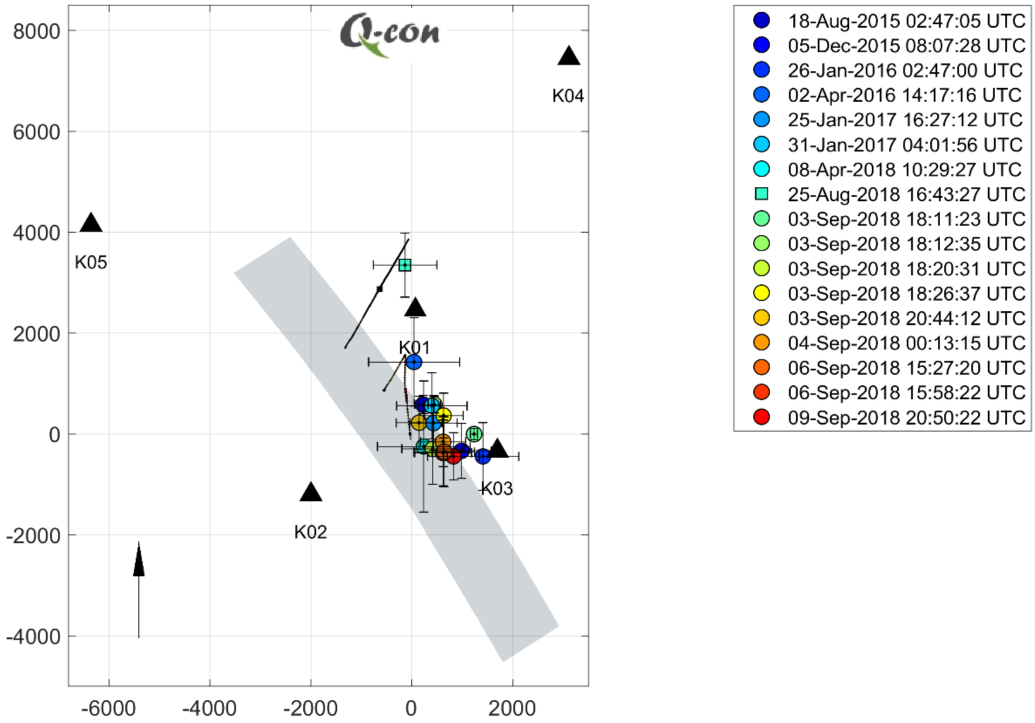

Figure 1: Absolute hypocentre location in map view. Error bars show the location accuracy with a 2σ confidence level (formal inversion error). Triangles denote the location of the seismic monitoring stations. Events were colour-coded according to the time of occurrence (see legend). The grey patch depicts the Tegelen fault. The black lines show the well trajectories of GT01, GT03, GT04 and GT05, respectively. Black arrow indicates Northern direction. Coordinates with respect to x = 204,042, y = 380,050 (RD). The first six events occurred prior to production start of the CLG doublet. Event hypocentres are depicted as determined for the SHA before seismic velocity model was calibrated. Figure from Baisch & Vörös (2019).

1.2 Scope of Study

For constraining geomechanical interpretations of the seismogenic processes at Californië, trailing earthquakes are of particular importance. At the level of perceptibility, no earthquakes were detected after March 2020. It is, however, unclear if seismicity at a lower magnitude level has occurred.

To answer this question, the time-continuous seismogram data shall be re-processed using a template detector.

2 TEMPLATE DETECTOR

2.1 Data Base

Time-continuous waveform data is available in data archives at Q-con. The original data was acquired for different operators using different data formats (cd11, miniSeed). Consequently, data copies in the Q-con archives are distributed over multiple hard drives (Figure 2).

In a first step, data from different sources was merged into a single data base using a homogeneous data format. Almost all data files exist for the period 2015-2023. In total, less than 1 day of data files is missing in the merged data base.

It should be noted, however, that the number of stations changed over time. After March 2020, only stations K01, K02, and K03 were operated. In 2021, station K02 had to be removed because new buildings were developed in the area. Therefore, an almost complete waveform data record for the period 2018-2023 is provided only by stations K01 and K03.

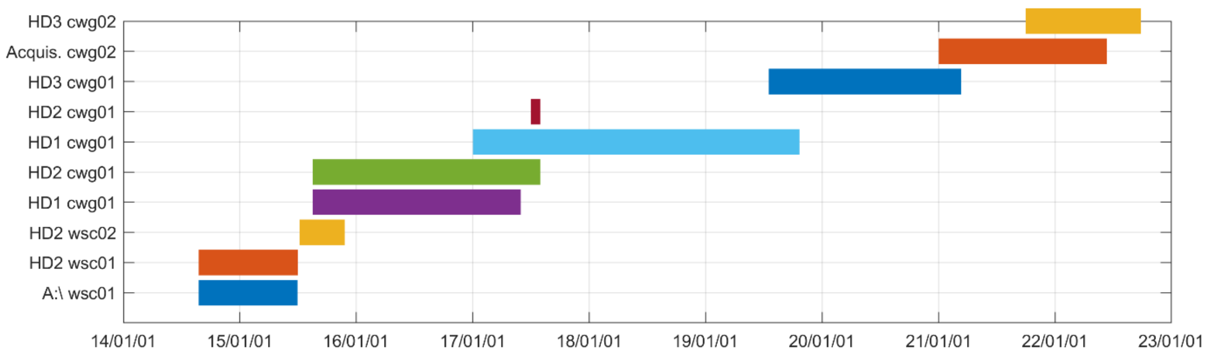

Figure 2: Raw data distribution on different hard drives.

2.2 Design of Detector

Initial tests have indicated that the 17 known earthquakes at Californië exhibit a comparatively low waveform similarity. For increasing the sensitivity of the template detector, multiple templates as well as a low similarity threshold have been used. In total, 12 earthquakes exhibit a sufficient signal-to-noise ratio at stations K01 and K03 for being used as templates. These 12 earthquakes define the set of templates. Figure 3 shows a waveform example of one of the templates.

For detection, each template is successively moved on a sliding window over the time-continuous waveform recordings of stations K01 and K03. All data is band-pass filtered in the range 1-30 Hz. In each time step, the multi-channel waveform cross correlation coefficient cc_{mult} is computed following Baisch et al. (2008). A detection is declared if cc_{mult} >0.3.

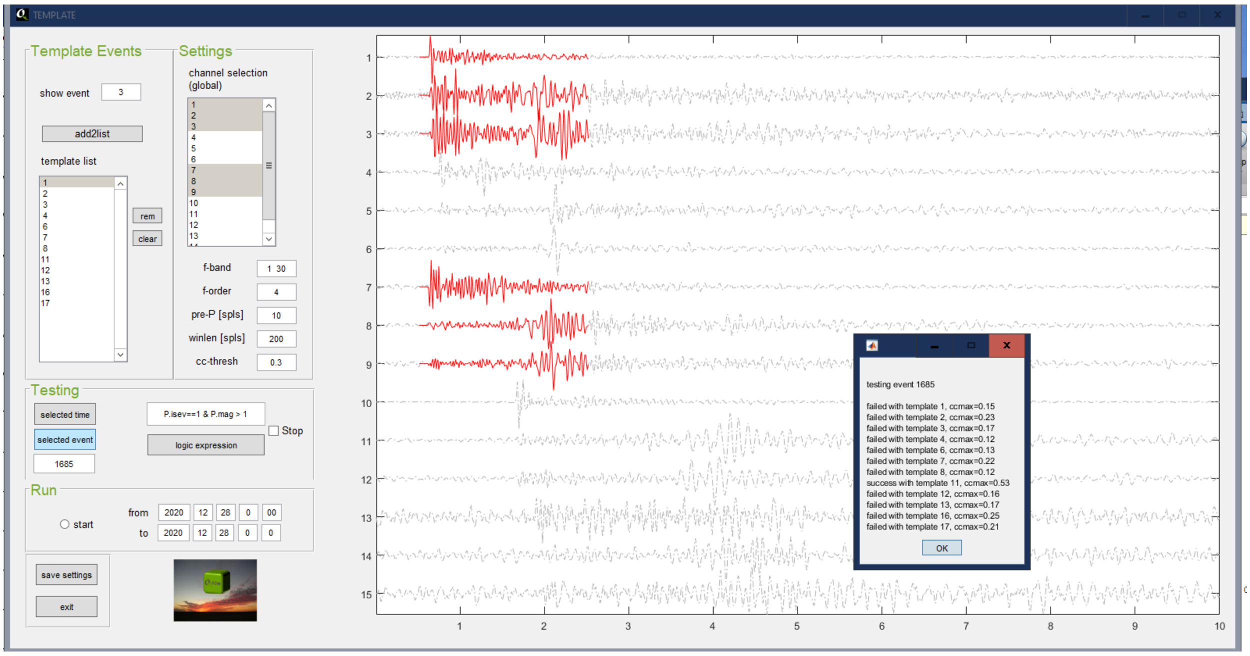

Figure 3: Snapshot of the configuration panel for the template detector. Waveforms of a template event are shown in light grey. The selected template is shown in red. It consists of 6 channels, each covering P- and S-wave onsets.

2.3 Test

The template detector has been operated on the time windows of the 17 known earthquakes. All known earthquakes were detected.

2.4 Template detection 2018-2023

The template detector has been operated from 10.09.2018 to 01.07.2023 yielding approximately 3.300 detections. Subsequently, each detection was visually inspected. All but one detection could be clearly identified as false triggers.

The remaining detection #1685 could be clearly identified as a reservoir earthquake. This earthquake occurred on 07.02.2022 19:57:52 UTC and was detected by the template of the M_L=1.7 main event (Figure 4) with a waveform similarity of cc_{mult} =0.53.

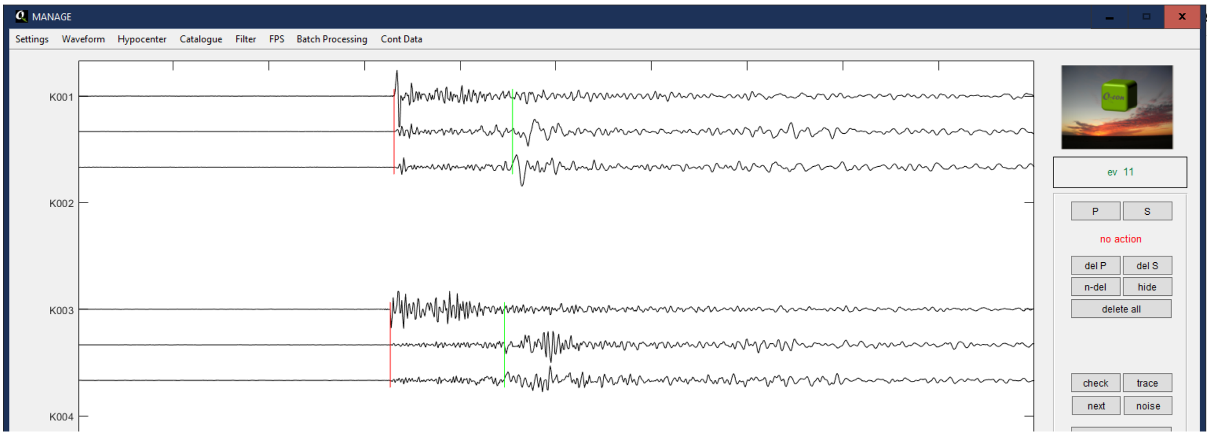

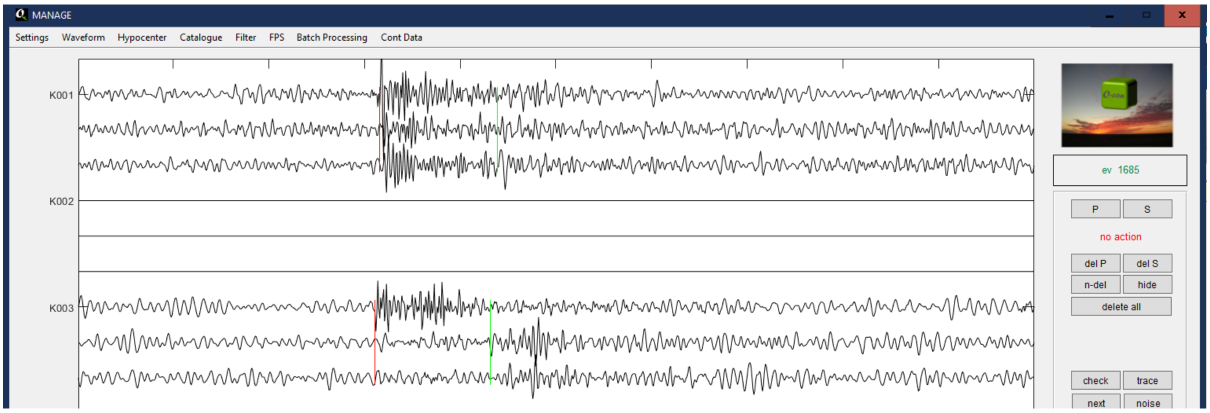

Figure 4: Top: Waveforms of the template event (M_L=1.7 main event). Bottom: Waveforms of the new detection. P- and S-phase onsets are marked by red and green lines, respectively.

3 EARTHQUAKE PROCESSING

3.1 Hypocenter

The earthquake occurring on 07.02.2022 was recorded by stations K01 and K03 only. With two stations, the absolute hypocenter location is not well constrained.

Instead, its relative hypocenter location with respect to the main event has been determined using the approach described in Baisch et al. (2006). Formally, the inversion is not well constrained, but the relative travel time differences compared to the main event are extremely small. Based on these travel time differences, the location of the new earthquake is well constrained. The earthquake is located in the immediate vicinity of the hypocenter of the main event (relative distance of ~10 m).

3.2 Magnitude

In previous reports on Californië seismicity (e.g., Baisch & Vörös, 2019), different magnitude scales were used. Reported magnitude values were generally depending on earthquake depth. After calibrating seismic velocities, earthquake depth changed considerably (compare Vörös & Baisch, 2022). The associated impact on earthquake magnitude has not been studied yet.

For providing a homogeneous magnitude scale for the entire catalogue of Californië seismicity, the local magnitude M_L^R of each earthquake has been determined relative to the M_L=1.7 main event (see subsequent section). This magnitude scale is based on the following assumptions:

1. The source-receiver paths for different earthquakes are approximately the same.
2. The magnitude of the calibration event (M_L=1.7 event) is correct.

Both assumptions appear to be justified: (1) Earthquake hypocenters are closely spaced (Vörös & Baisch, 2022) implying very similar source-receiver paths. (2) The main event is also assigned M_L=1.7 by the KNMI, who is the authoritative institution for earthquakes in the Netherlands.

3.3 Catalogue

date	time	lat	lon	depth [m]	M_L^R
18-Aug-2015	02:47:05	51.40991	6.0893466	-2192	0.1
05-Dec-2015	08:07:28	51.41001	6.0933441	-2445	0.5
26-Jan-2016	02:47:00	51.412404	6.0902309	-2434	0.1
02-Apr-2016	14:17:16	51.418007	6.0833162	-2536	-0.3
25-Jan-2017	16:27:12	51.408784	6.0917092	-2376	0.2
31-Jan-2017	04:01:56	51.415842	6.083939	-2366	-0.2
08-Apr-2018	10:29:27	51.409846	6.0893043	-2448	0.1
25-Aug-2018	16:43:27	51.425307	6.0802734	-2506	0.2
03-Sep-2018	18:11:23	51.410266	6.0893983	-2396	-0.2
03-Sep-2018	18:12:35	51.411083	6.0899763	-2368	0.1
03-Sep-2018	18:20:31	51.410368	6.0897539	-2441	1.7
03-Sep-2018	18:26:37	51.412097	6.0901977	-2205	0.3
03-Sep-2018	20:44:12	51.410382	6.0855934	-2435	-0.3
04-Sep-2018	00:13:15	51.409097	6.0906	-2418	-0.5
06-Sep-2018	15:27:20	51.410323	6.0884887	-2355	0
06-Sep-2018	15:58:22	51.410548	6.0884689	-2398	-0.1
09-Sep-2018	20:50:22	51.411986	6.086946	-2384	0.4
07-Feb-2022	19:57:52	51.410429	6.0896632	-2445	0

4 REFERENCES

Baisch, S., & Vörös, R. (2019). *Earthquakes Near the Californie Geothermal Site: August 2015 – November 2018* (Internal report prepared for Californie Lipzig Gielen Geothermie BV

No. CLGG005) (p. 50).

Baisch, S., Weidler, R., Vörös, R., Wyborn, D., & de Graaf, L. (2006). Induced Seismicity during the Stimulation of a Geothermal HFR Reservoir in the Cooper Basin, Australia. *Bulletin of the Seismological Society of America*, *96*(6), 2242–2256. https://doi.org/10.1785/0120050255

Baisch, S., Ceranna, L., & Harjes, H.-P. (2008). Earthquake Cluster: What Can We Learn from Waveform Similarity? *Bulletin of the Seismological Society of America*, *98*(6), 2806–2814. https://doi.org/10.1785/0120080018

Dost, B., van Eck, T., & Haak, H. (2004). Scaling peak ground acceleration and peak ground velocity recorded in The Netherlands. *Bolletino Di Geofisica Teorica Ed Applicata*, *45*(3), 153–168.

Vörös, R., & Baisch, S. (2022). Induced seismicity and seismic risk management – a showcase from the Californië geothermal field (the Netherlands). *Netherlands Journal of Geosciences*, *101*, e15. https://doi.org/10.1017/njg.2022.12

APPENDIX G – Geomechanical results of other history-match scenarios

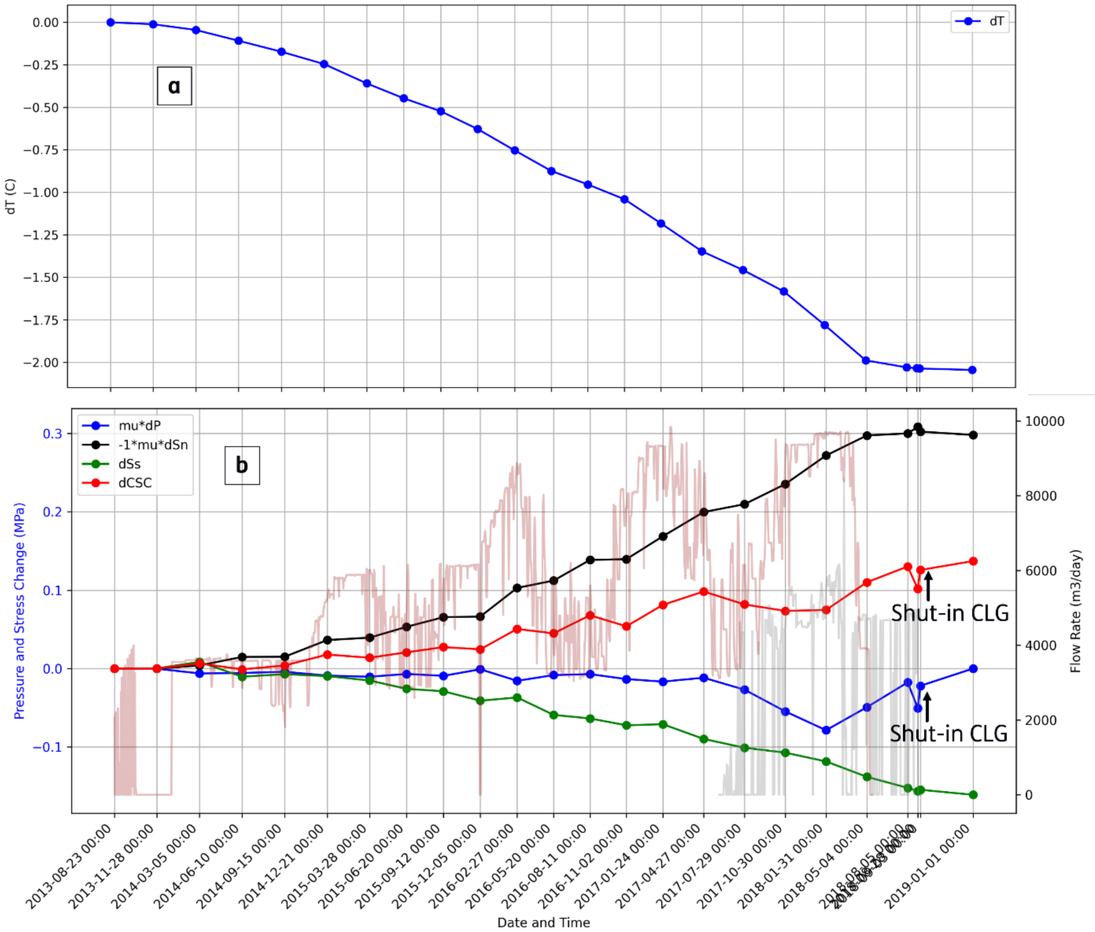

Figure G.1.Tegelen Fault – Scenario HM5. Temporal evolution of pressure, temperature and stress on the Tegelen Fault, at three-monthly resolution: a) maximum temperature change versus time (monitored at location of maximum temperature change, b) contributions of pore pressure (blue line), total normal stress (black line) and shear stress (green) to Coulomb stressing at the Tegelen Fault, at location of maximum temperature change. Light brown and grey line in the background presents flow rates at CWG (well GT-03), light grey line at the background represents flow rates at CLG (well GT-05). Effect of shut-in on pressure and Coulomb stress indicated.

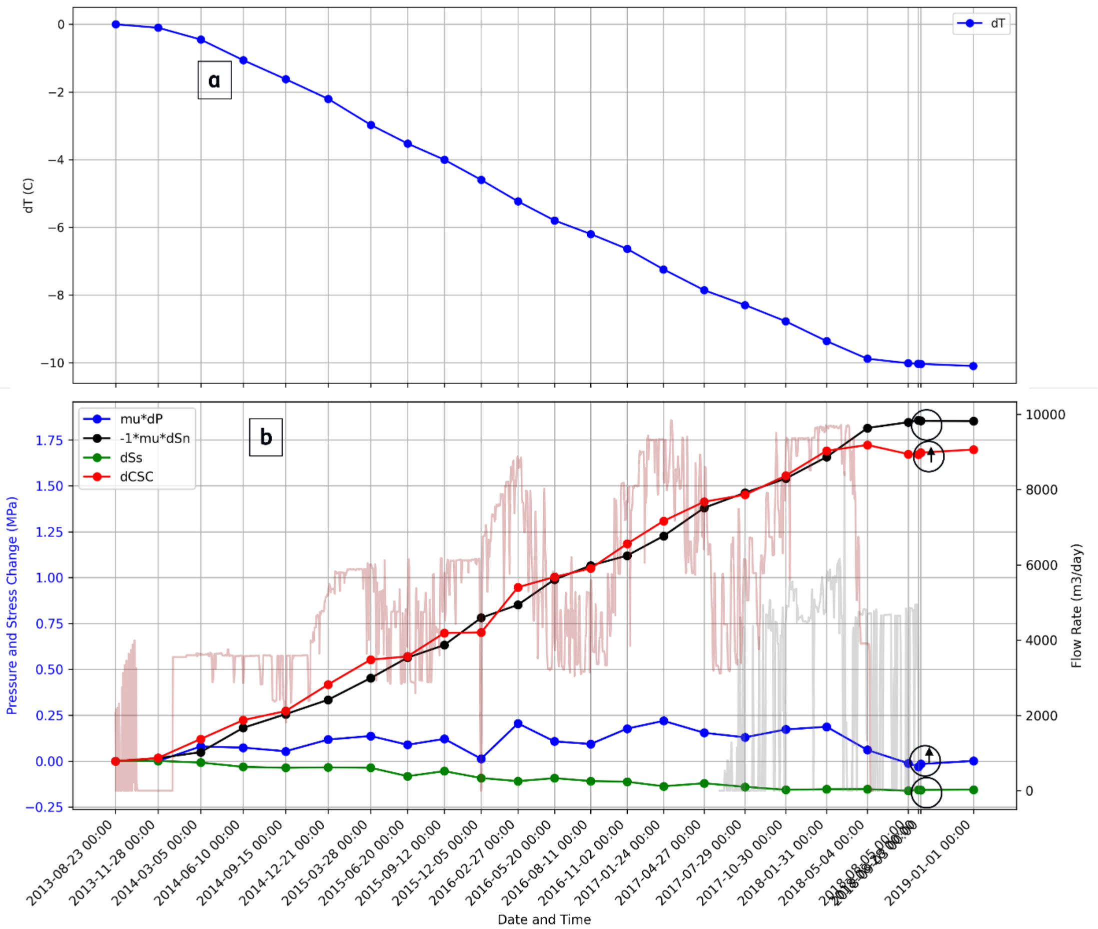

Figure G.2. Carboniferous Normal Fault – Scenario HM5. Carboniferous Normal Fault – Scenario HM5. Temporal evolution of pressure, temperature and stress on the Carboniferous Normal Fault, at three-monthly resolution: a) maximum temperature change versus time (monitored at location of maximum temperature change, b) contributions of pore pressure (blue line), total normal stress (black line) and shear stress (green) to Coulomb stressing at the Carboniferous Normal Fault. Light brown and grey line in the background presents flow rates at CWG (well GT-03), light grey line at the background represents flow rates at CLG (well GT-05). Effect of shut-in on pressure and Coulomb stress indicated.

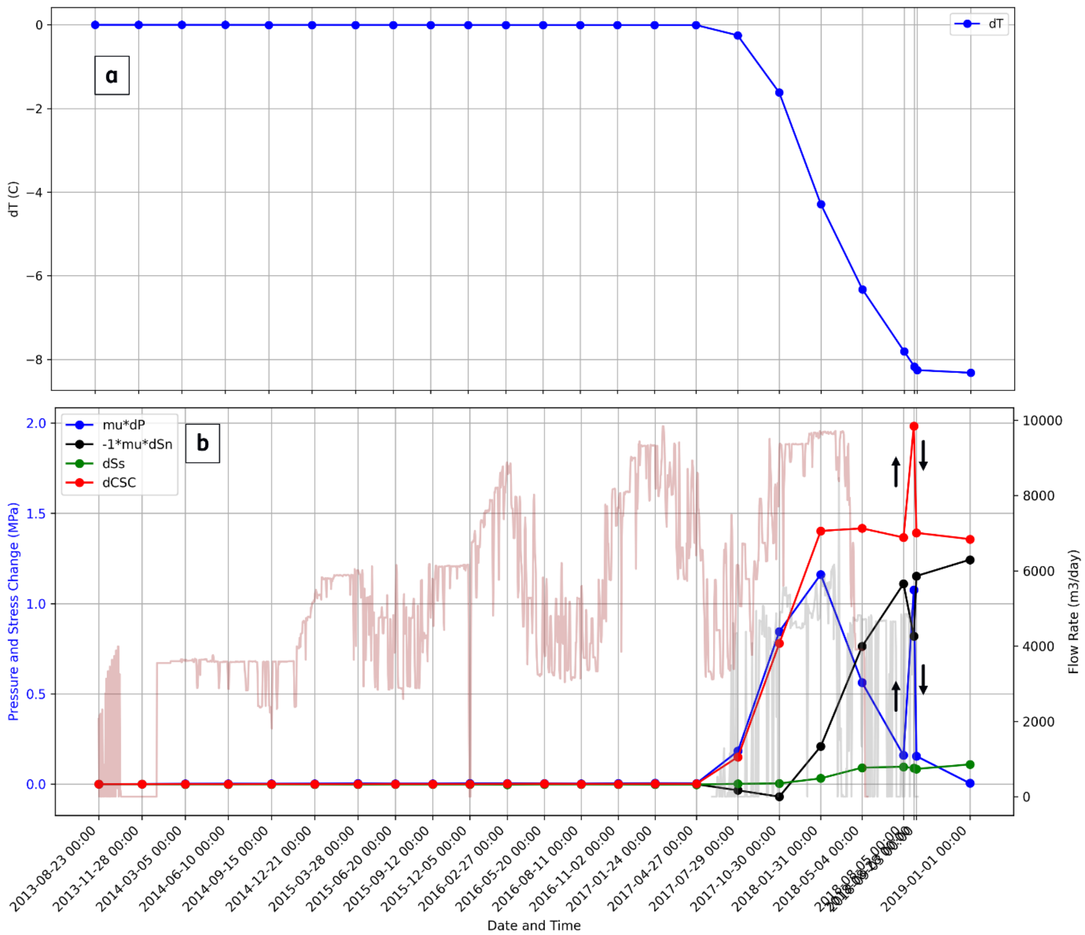

Figure G.3. Western Pop-Up Fault – Scenario HM5. Western Pop-Up Fault – Scenario HM5. Temporal evolution of pressure, temperature and stress on the Western Pop-Up Fault, at three-monthly resolution: a) maximum temperature change versus time (monitored at location of maximum temperature change, b) contributions of pore pressure (blue line), total normal stress (black line) and shear stress (green) to Coulomb stressing at the Western Pop-Up Fault. Light brown and grey line in the background presents flow rates at CWG (well GT-03), light grey line at the background represents flow rates at CLG (well GT-05). Effect of shut-in on pressure and Coulomb stress indicated.

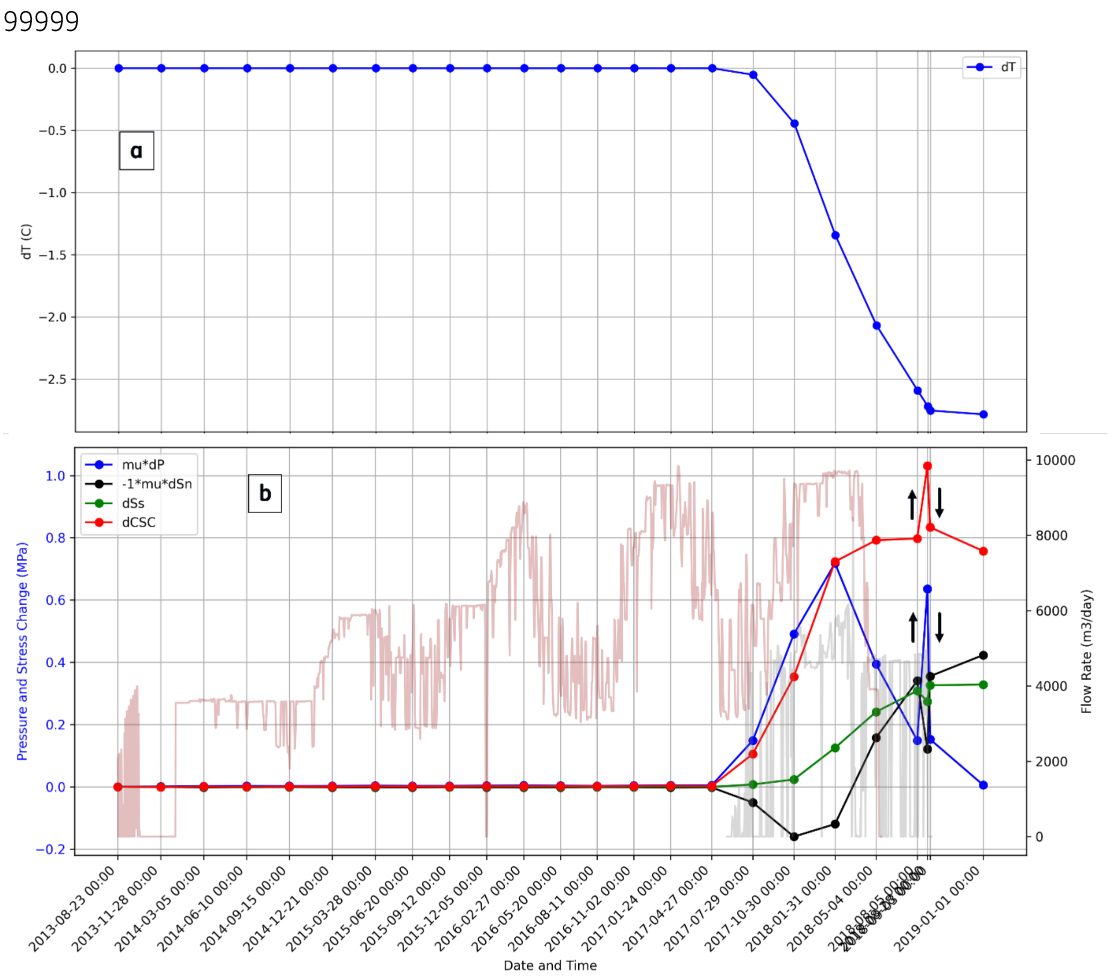

Figure G.4. Eastern Pop-Up Fault – Scenario HM5. Eastern Pop-Up Fault – Scenario HM5. Temporal evolution of pressure, temperature and stress on the Eastern Pop-Up Fault, at three-monthly resolution: a) maximum temperature change versus time (monitored at location of maximum temperature change, b) contributions of pore pressure (blue line), total normal stress (black line) and shear stress (green) to Coulomb stressing at the Eastern Pop-Up Fault. Light brown and grey line in the background presents flow rates at CWG (well GT-03), light grey line at the background represents flow rates at CLG (well GT-05). Effect of shut-in on pressure and Coulomb stress indicated.

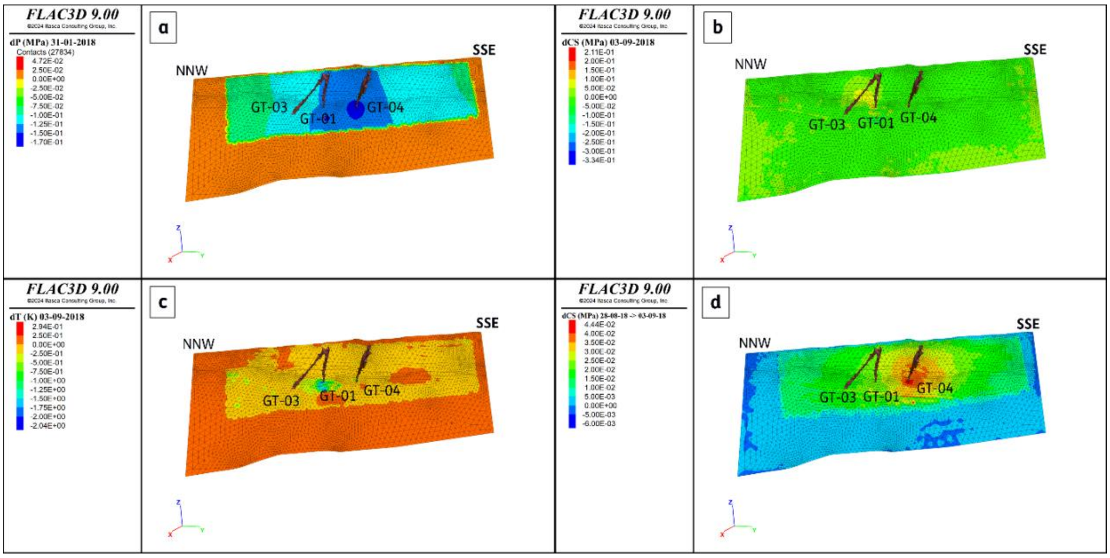

Figure G.5. Scenario HM5. Pressure and stress on the Tegelen Fault. a) Pressure change in the fault 31-01-2018 as compared to initial conditions, black dashed line indicates dimensions of dynamic reservoir model b) Coulomb stress change on the fault at 03-09-2018 as compared to initial conditions, c) temperature change at the fault 03-09-2018 as compared to initial conditions, d) Coulomb stress change between 28-08-2018, just before the final shut-in of the CLG doublet and the time of the Ml 1.7 seismic event at 03-09-2018.

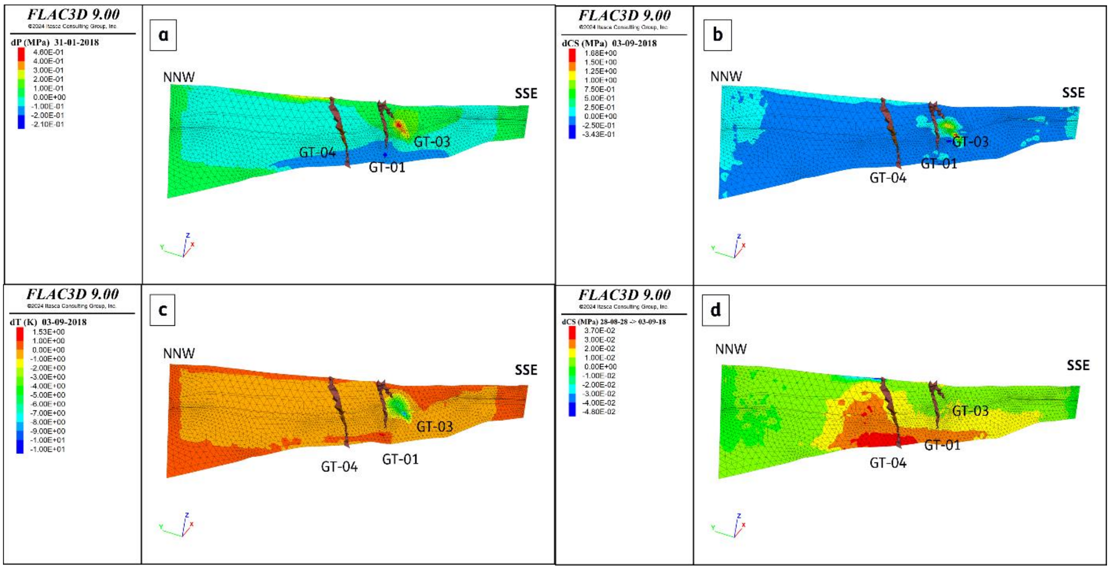

Figure G.6. Scenario HM5. Pressure and stress on the Carboniferous Normal Fault (CNF). a) Pressure change in the fault 31-01-2018 as compared to initial conditions, b) Coulomb stress change on the fault at 03-09-2018 as compared to initial conditions, c) temperature change at the fault 03-09-2018 as compared to initial conditions, d) Coulomb stress change between 28-08-2018, just before the final shut-in of the CLG doublet and the time of the Ml 1.7 seismic event at 03-09-2018.

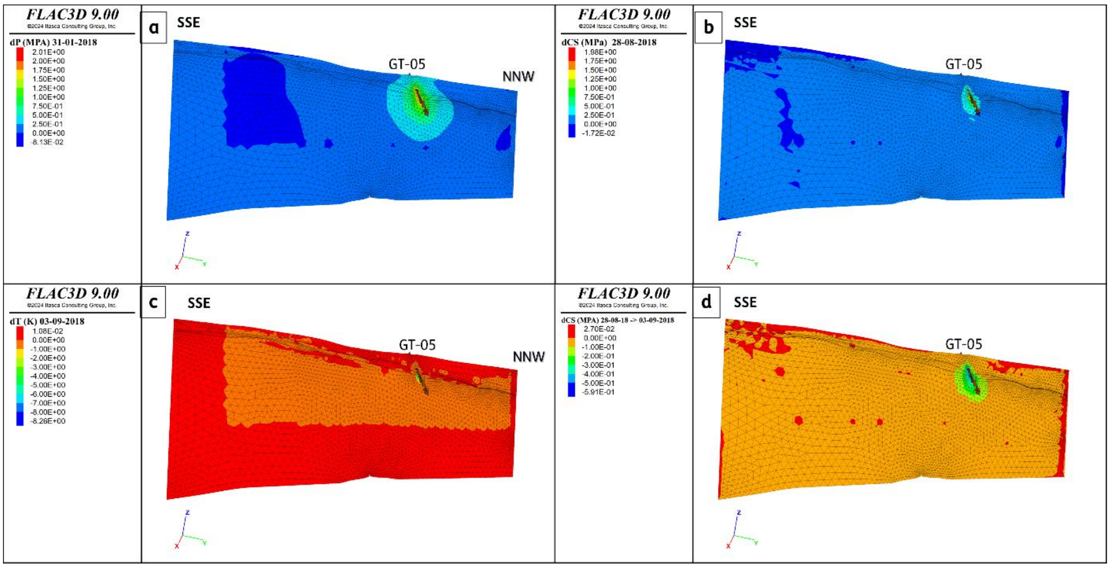

Figure G.7. Scenario HM5. Pressure and stress on the Western Pop-Up Fault (WPF). a) Pressure change in the fault 31-01-2018 as compared to initial conditions, b) Coulomb stress change on the fault at 28-08-2018 as compared to initial conditions, c) temperature change at the fault 03-09-2018 as compared to initial conditions, d) Coulomb stress change between 28-08-2018, just before the final shut-in of the CLG doublet and the time of the Ml 1.7 seismic event at 03-09-2018.

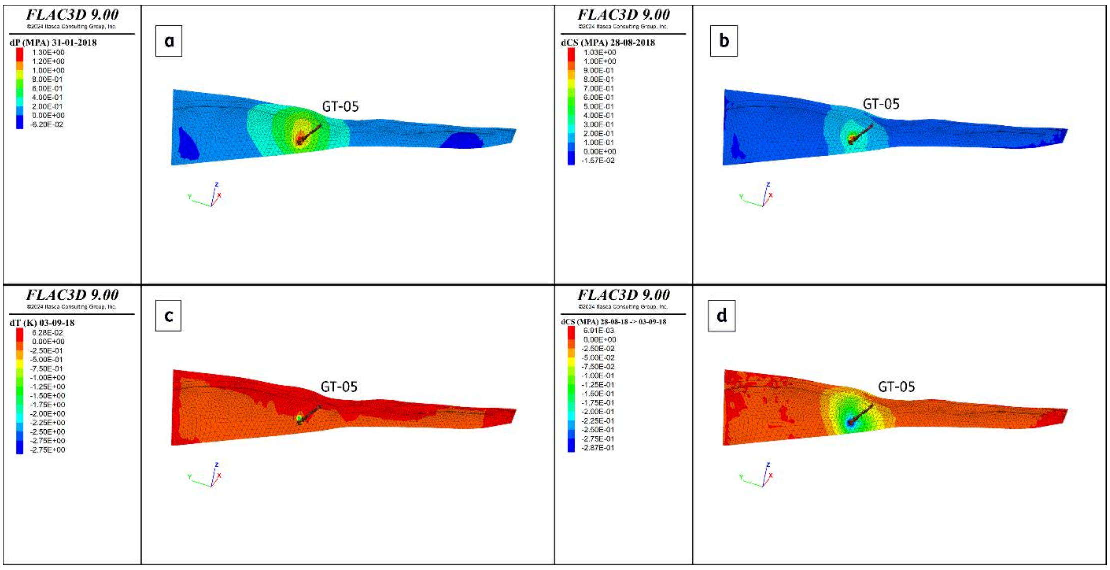

Figure D.8. Scenario HM5. Pressure and stress on the Eastern Pop-Up Fault (WPF). a) Pressure change in the fault 31-01-2018 as compared to initial conditions, b) Coulomb stress change on the fault at 28-08-2018 as compared to initial conditions, c) temperature change at the fault 03-09-2018 as compared to initial conditions, d) Coulomb stress change between 28-08-2018, just before the final shut-in of the CLG doublet and the time of the Ml 1.7 seismic event at 03-09-2018.

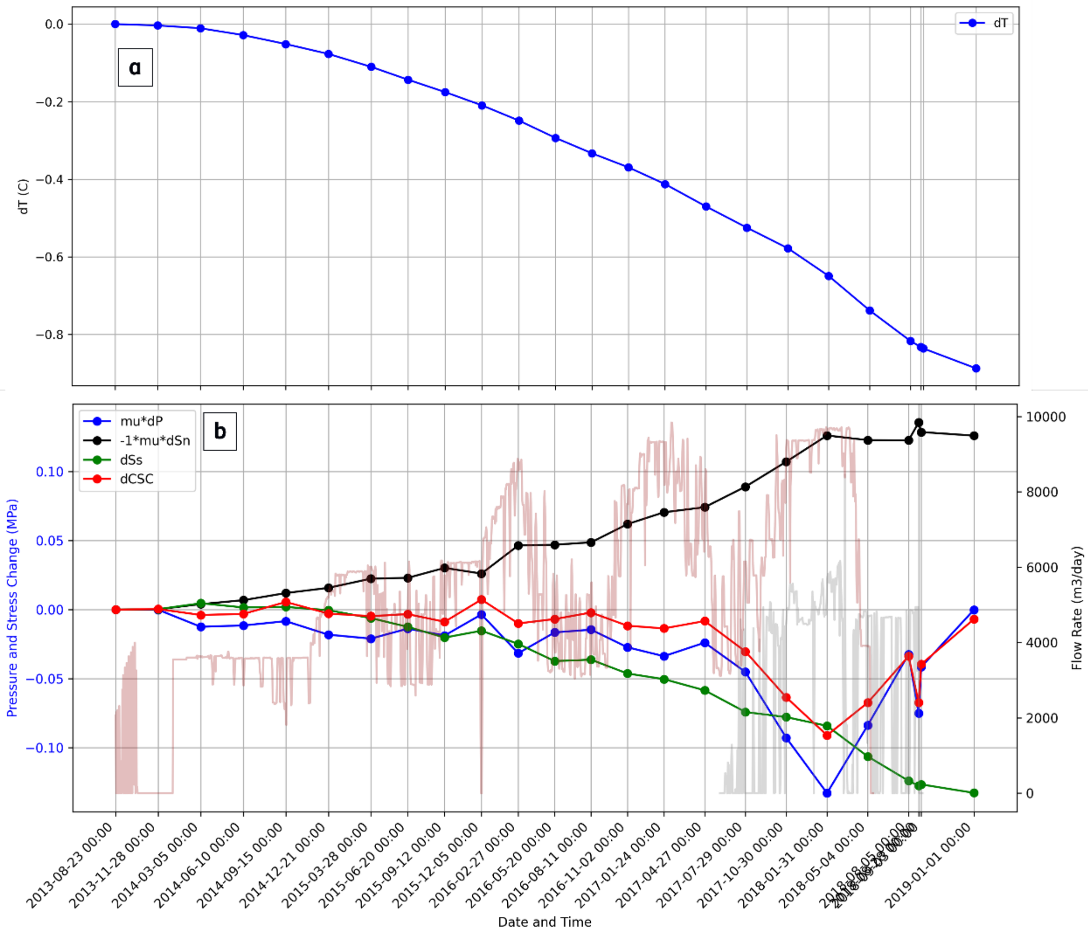

Figure G.9.Tegelen Fault – Scenario HM1. Temporal evolution of pressure, temperature and stress on the Tegelen Fault, at three-monthly resolution: a) maximum temperature change versus time (monitored at location of maximum temperature change, b) contributions of pore pressure (blue line), total normal stress (black line) and shear stress (green) to Coulomb stressing at the Tegelen Fault, at location of maximum temperature change. Light brown and grey line in the background presents flow rates at CWG (well GT-03), light grey line at the background represents flow rates at CLG (well GT-05). Effect of shut-in on pressure and Coulomb stress indicated.

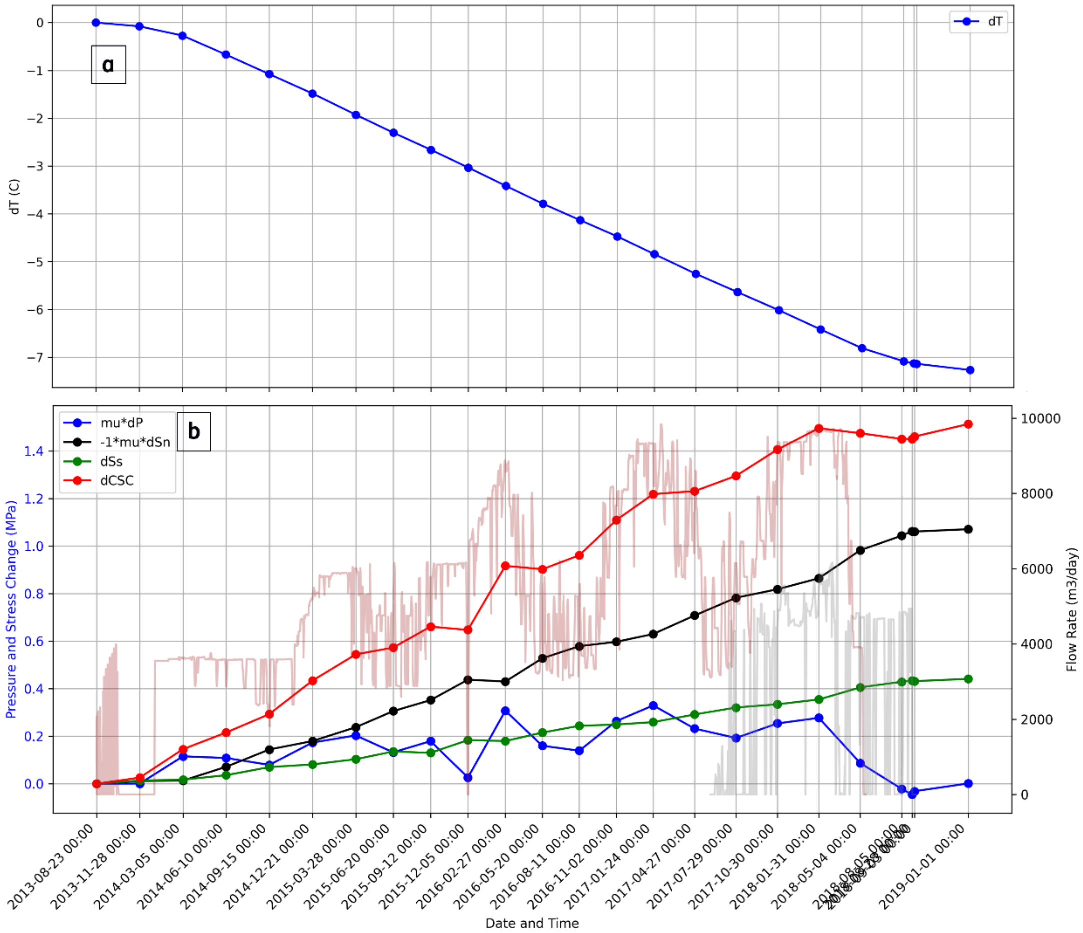

Figure G.10. Carboniferous Normal Fault – Scenario HM1. Temporal evolution of pressure, temperature and stress on the Carboniferous Normal Fault, at three-monthly resolution: a) maximum temperature change versus time (monitored at location of maximum temperature change, b) contributions of pore pressure (blue line), total normal stress (black line) and shear stress (green) to Coulomb stressing at the Carboniferous Normal Fault. Light brown and grey line in the background presents flow rates at CWG (well GT-03), light grey line at the background represents flow rates at CLG (well GT-05).

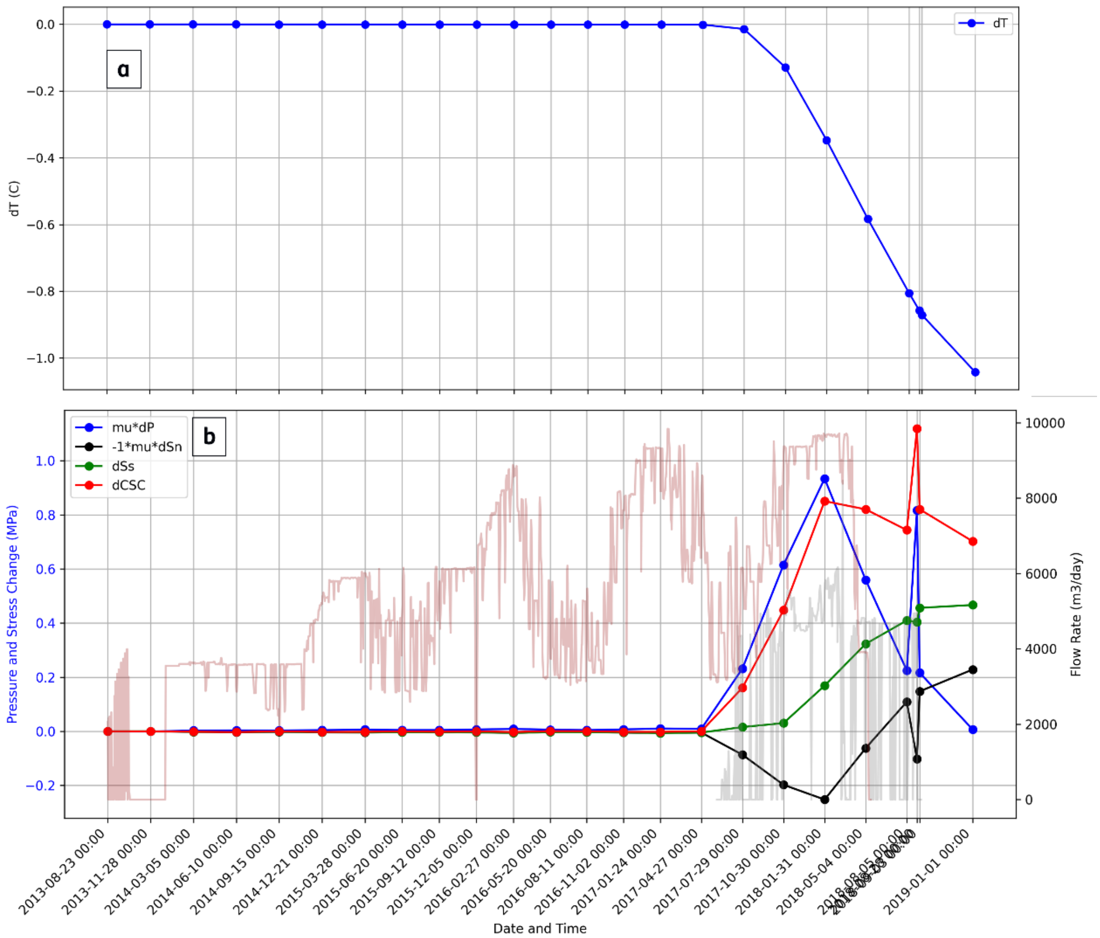

Figure G.11. Western Pop-Up Fault – Scenario HM1. Temporal evolution of pressure, temperature and stress on the Western Pop-Up Fault, at three-monthly resolution: a) maximum temperature change versus time (monitored at location of maximum temperature change, b) contributions of pore pressure (blue line), total normal stress (black line) and shear stress (green) to Coulomb stressing at the Western Pop-Up Fault. Light brown and grey line in the background presents flow rates at CWG (well GT-03), light grey line at the background represents flow rates at CLG (well GT-05).

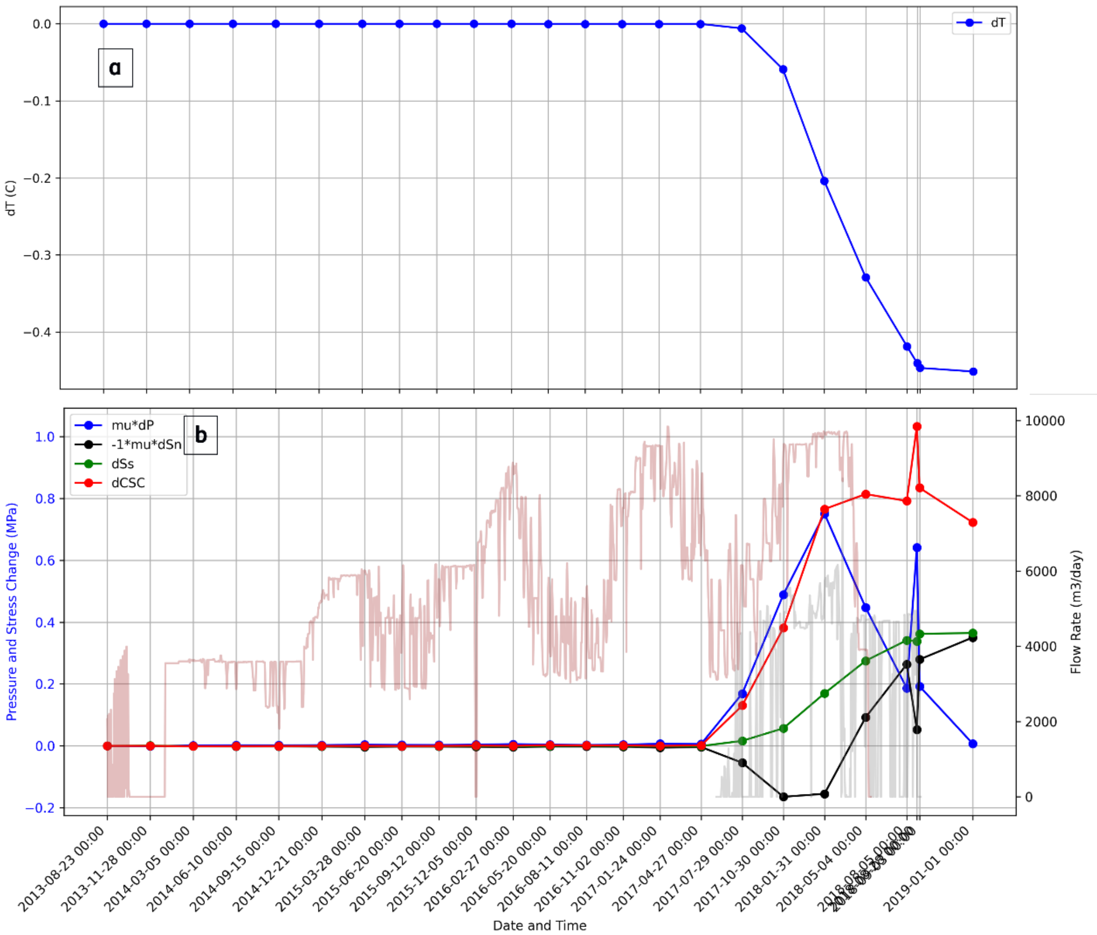

Figure G.12. Eastern Pop-Up Fault – Scenario HM1.Temporal evolution of pressure, temperature and stress on the Eastern Pop-Up Fault, at three-monthly resolution: a) maximum temperature change versus time (monitored at location of maximum temperature change, b) contributions of pore pressure (blue line), total normal stress (black line) and shear stress (green) to Coulomb stressing at the Eastern Pop-Up Fault. Light brown and grey line in the background presents flow rates at CWG (well GT-03), light grey line at the background represents flow rates at CLG (well GT-05).

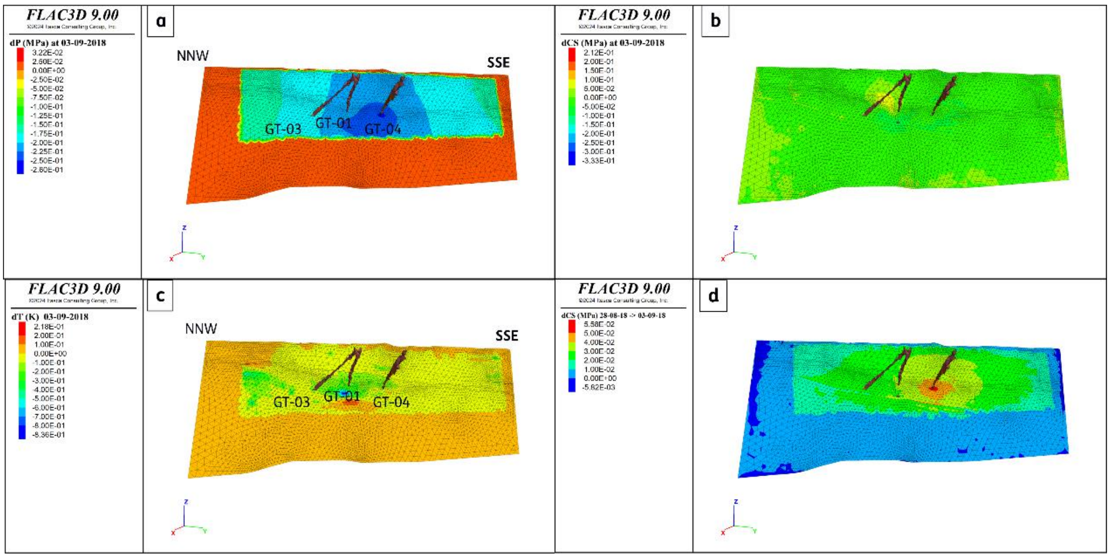

Figure G.13. Scenario HM1. Pressure and stress on the Tegelen Fault. a) Pressure change in the fault 31-01-2018 as compared to initial conditions, black dashed line indicates dimensions of dynamic reservoir model b) Coulomb stress change on the fault at 03-09-2018 as compared to initial conditions, c) temperature change at the fault 03-09-2018 as compared to initial conditions, d) Coulomb stress change between 28-08-2018, just before the final shut-in of the CLG doublet and the time of the Ml 1.7 seismic event at 03-09-2018.

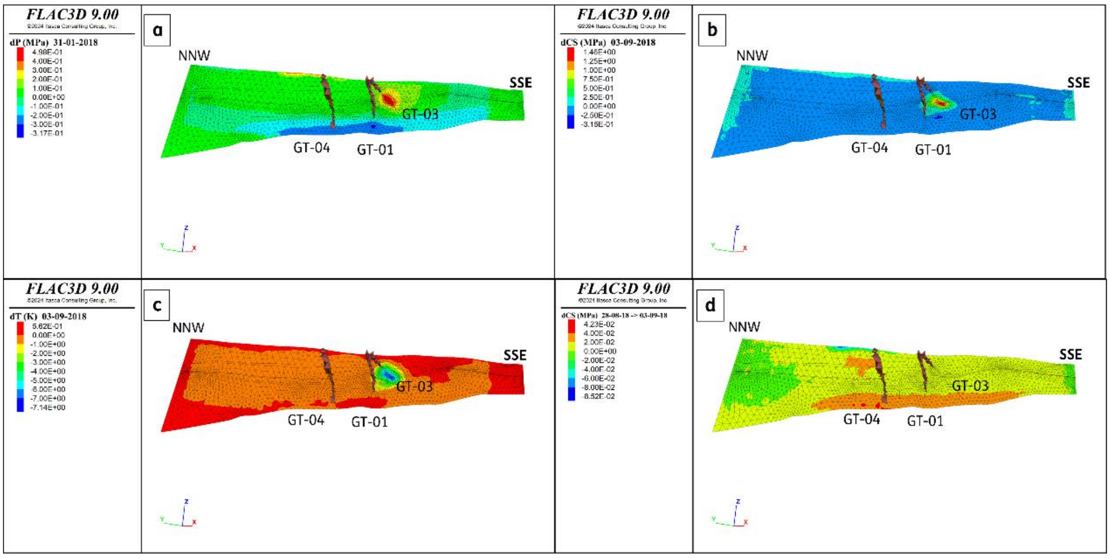

Figure G.14. Scenario HM1. Pressure and stress on the Carboniferous Normal Fault (CNF). a) Pressure change in the fault 31-01-2018 as compared to initial conditions, b) Coulomb stress change on the fault at 03-09-2018 as compared to initial conditions, c) temperature change at the fault 03-09-2018 as compared to initial conditions, d) Coulomb stress change between 28-08-2018, just before the final shut-in of the CLG doublet and the time of the Ml 1.7 seismic event at 03-09-2018.

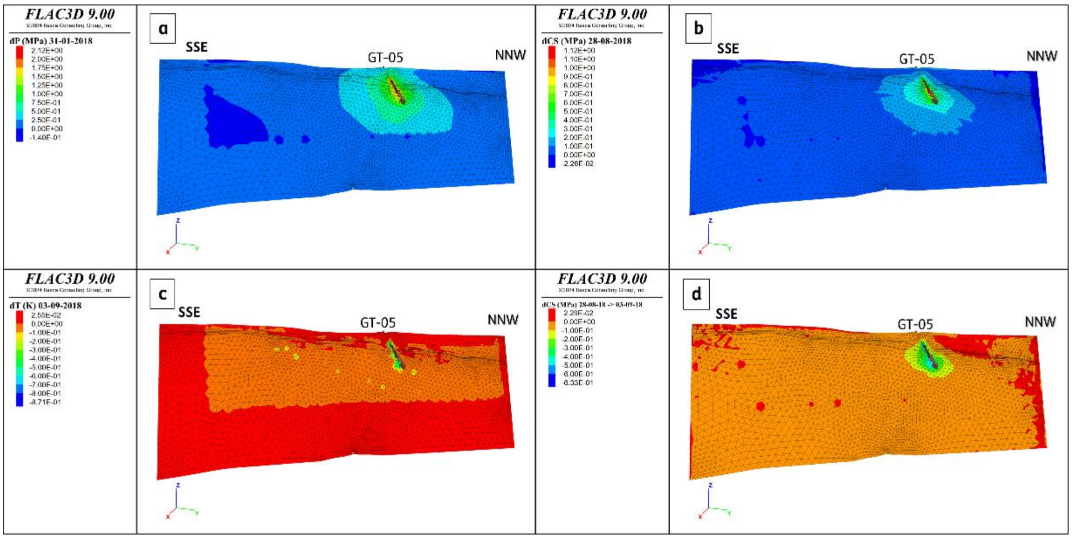

Figure G.15. Scenario HM1. Pressure and stress on the Western Pop-Up Fault (WPF). a) Pressure change in the fault 31-01-2018 as compared to initial conditions, b) Coulomb stress change on the fault at 28-08-2018 as compared to initial conditions, c) temperature change at the fault 03-09-2018 as compared to initial conditions, d) Coulomb stress change between 28-08-2018, just before the final shut-in of the CLG doublet and the time of the Ml 1.7 seismic event at 03-09-2018.

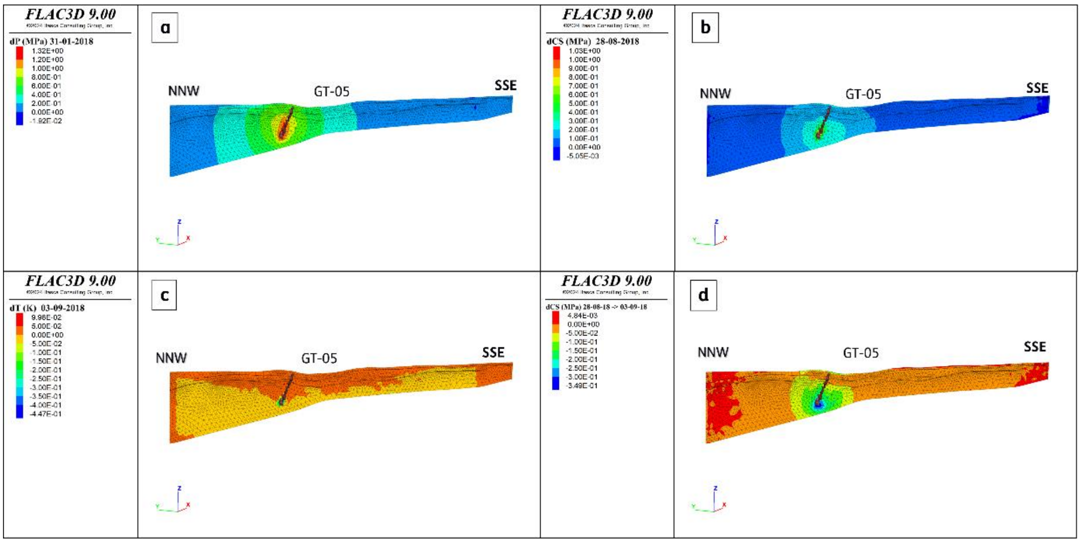

Figure G.16. Scenario HM1. Pressure and stress on the Eastern Pop-Up Fault (WPF). a) Pressure change in the fault 31-01-2018 as compared to initial conditions, b) Coulomb stress change on the fault at 28-08-2018 as compared to initial conditions, c) temperature change at the fault 03-09-2018 as compared to initial conditions, d) Coulomb stress change between 28-08-2018, just before the final shut-in of the CLG doublet and the time of the Ml 1.7 seismic event at 03-09-2018.

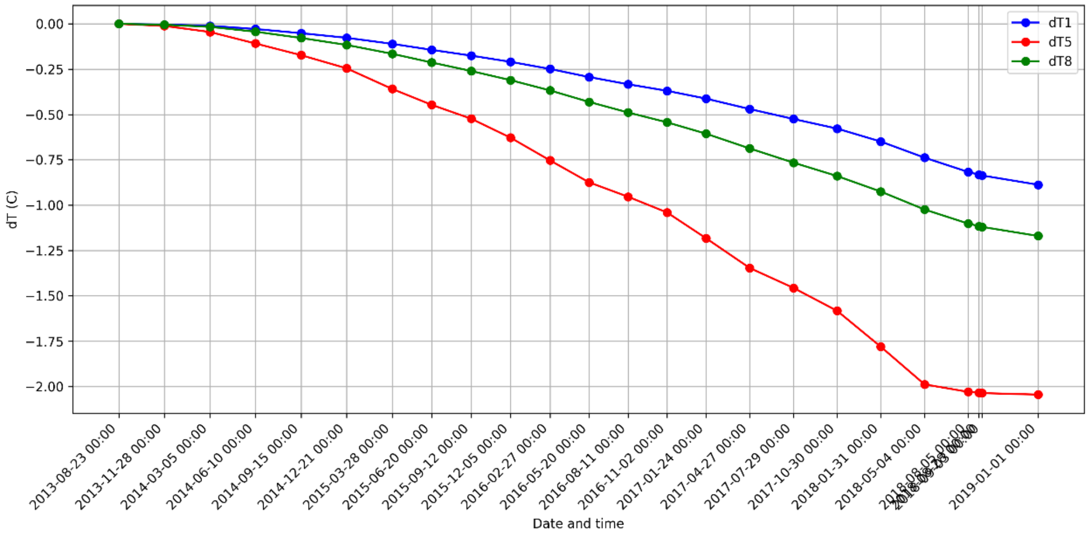

Figure D.17. Temperature evolution for the three history-match scenario's HM1,HM5 and HM8, at the location of maximum temperature decrease of the the Tegelen Fault.

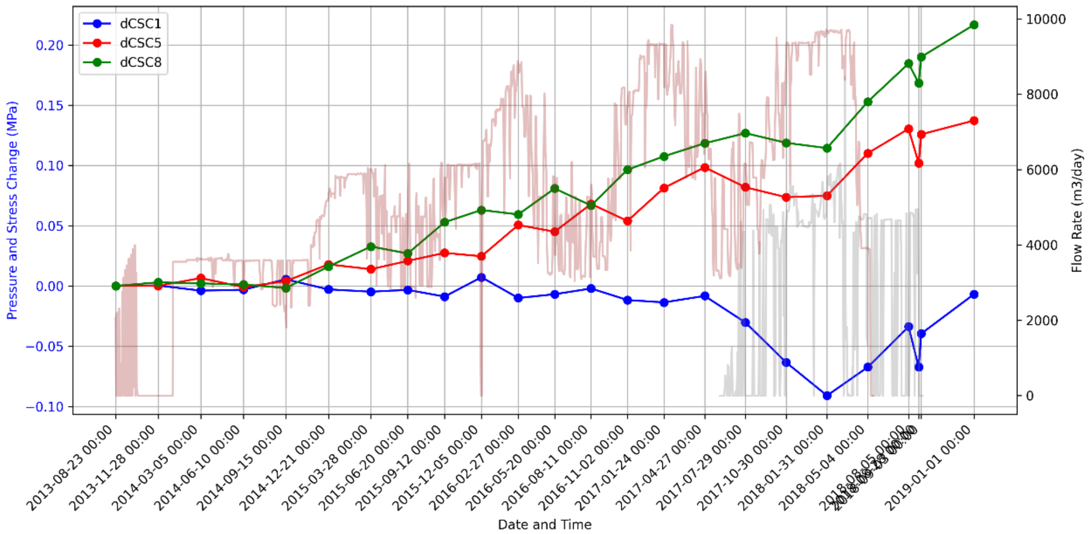

Figure G.18. Coulomb stress evolution for the three history-match scenario's HM1,HM5 and HM8, at the location of maximum temperature decrease of the Tegelen Fault.

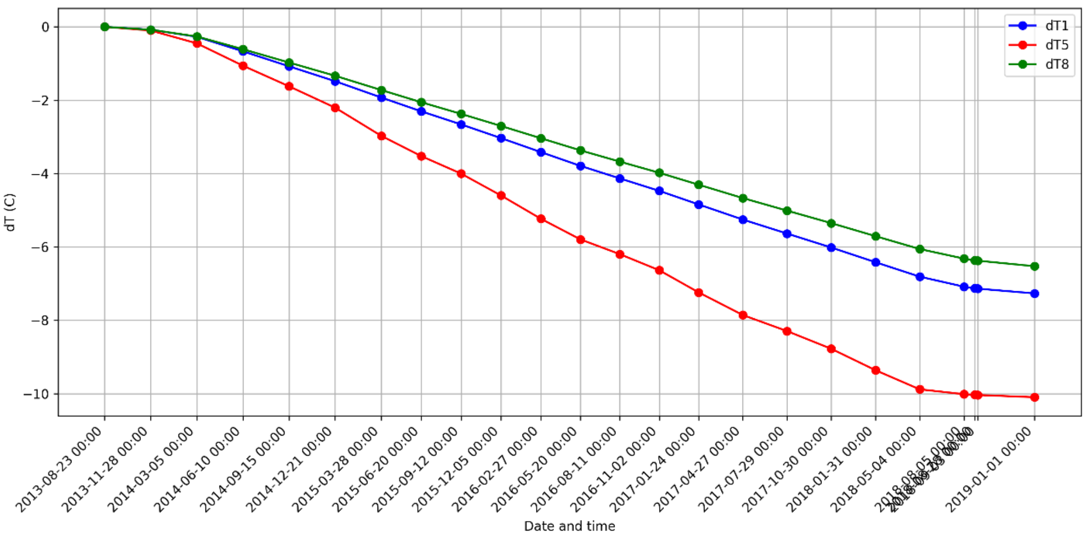

Figure G.19. Temperature evolution for the three history-match scenario's HM1,HM5 and HM8, at the location of maximum temperature decrease of the the Carboniferous Normal Fault.

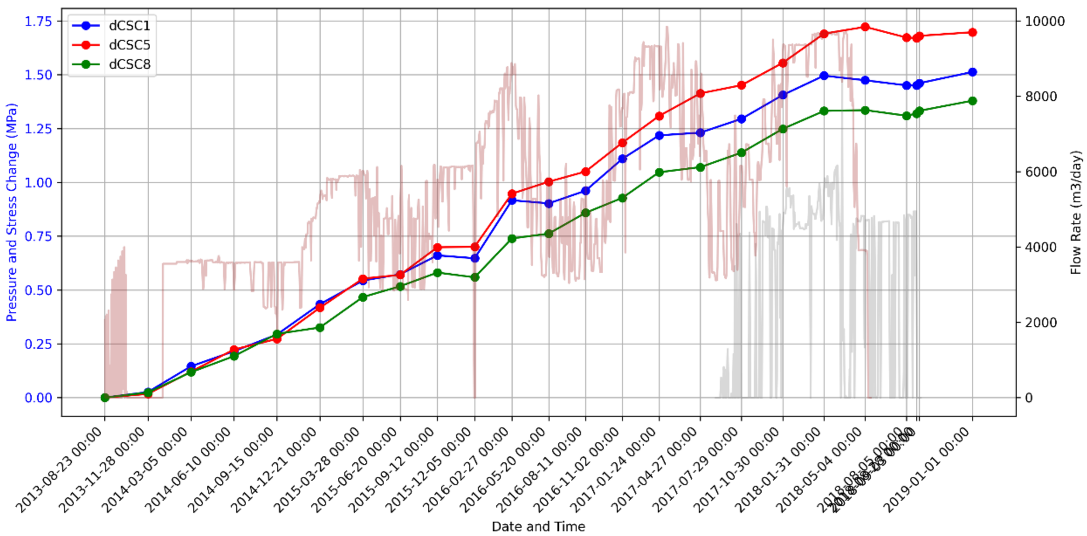

Figure G.20. Coulomb stress change for the three history-match scenario's HM1,HM5 and HM8, at the location of maximum temperature decrease of the the Carboniferous Normal Fault.

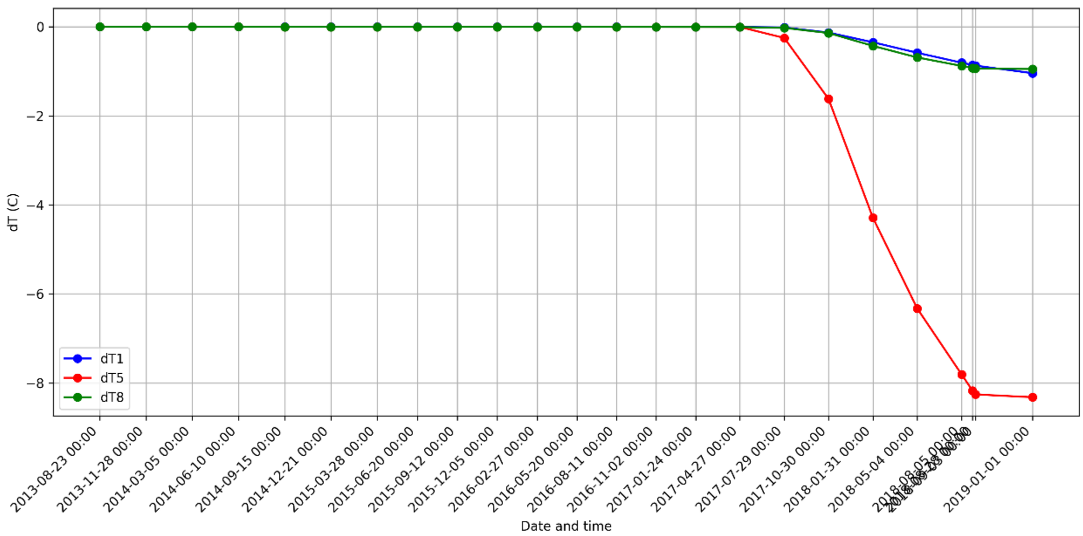

Figure G.21. Temperature evolution for the three history-match scenario's HM1,HM5 and HM8, at the location of maximum temperature decrease of the Western Pop-Up Fault.

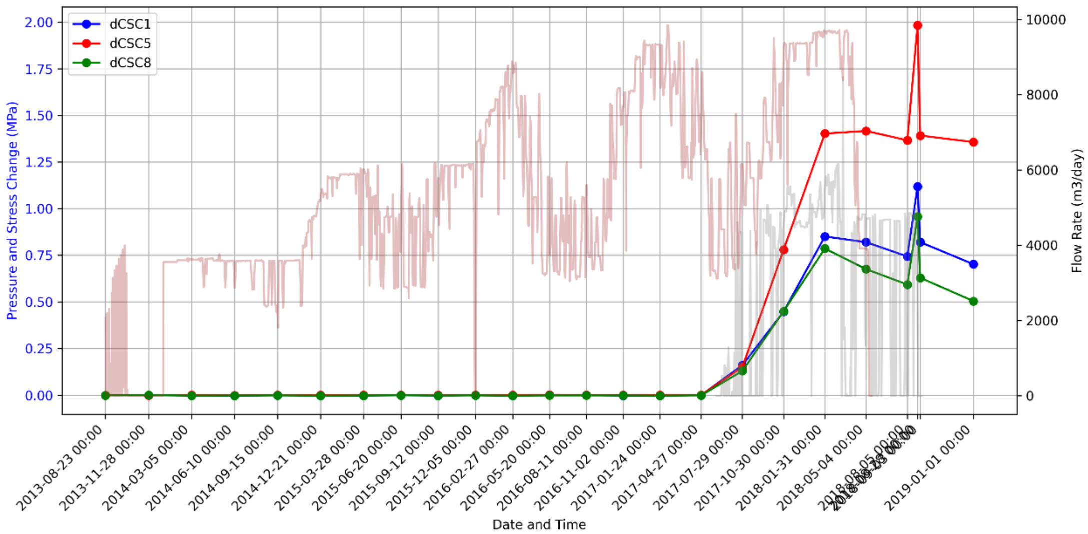

Figure G.22. Coulomb stress evolution for the three history-match scenario's HM1,HM5 and HM8, at the location of maximum temperature decrease of the Western Pop-Up Fault.

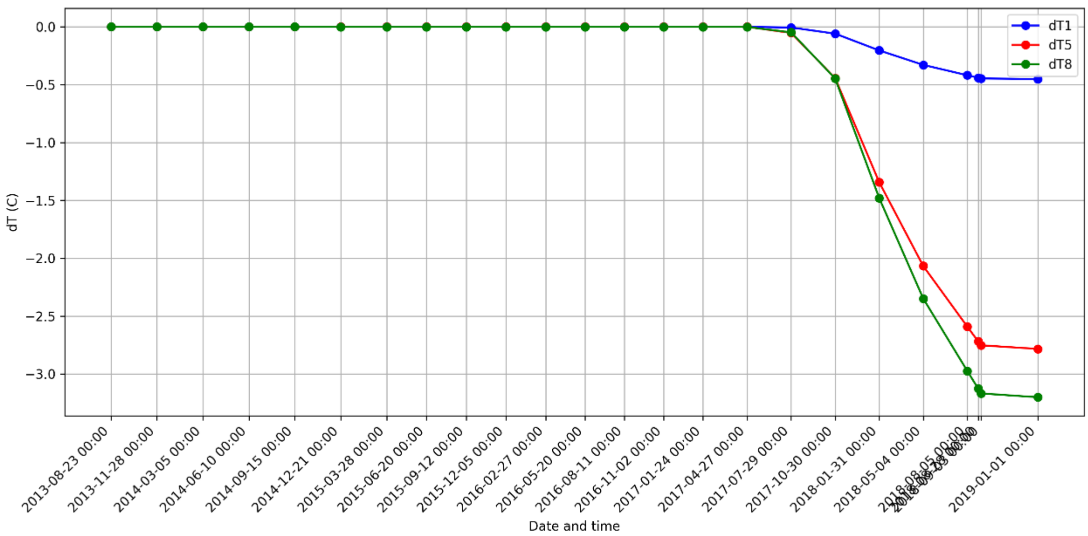

Figure G.23. Temperature evolution for the three history-match scenario's HM1,HM5 and HM8, at the location of maximum temperature decrease of the Eastern Pop-Up Fault.

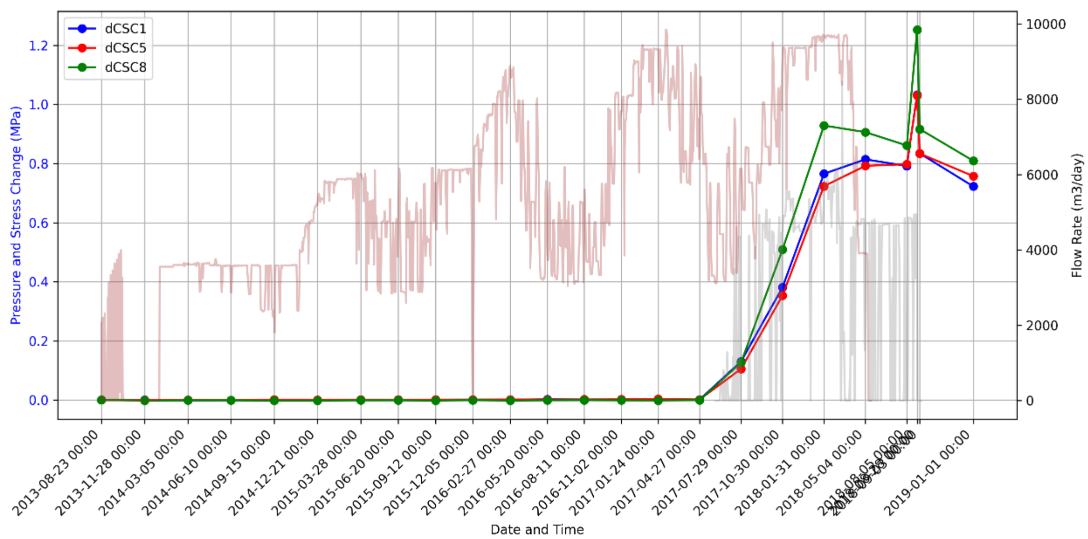

Figure G.24. Coulomb stress evolution for the three history-match scenario's HM1,HM5 and HM8, at the location of maximum temperature decrease of the Eastern Pop-Up Fault.

APPENDIX H - Document SGEO-002 – October 30, 2024 by Q-con. Design Seismic Monitoring Californië – Definition of Monitoring Concepts.

“Within the SafeGeo consortium Q-con was in the lead for the work on the monitoring network, reported in Section 8 of this report. Unforeseen external events, outside the influence of Q-con or SafeGeo, did not allow Q-con to finalize their work as planned. Thanks to the courtesy of Q-con a prepared draft document could be used and added to this report which enabled a proper finalization of this work by KNMI and TNO in SafeGeo project.”

Short REPORT

Design Seismic Monitoring Californië – Definition of Monitoring Concepts

Project: SafeGeo

Archive no.: SGEO002
Date: 30.10.2024

Q-con GmbH
Marktstr. 39
76887 Bad Bergzabern
Germany

Email: info@q-con.de
Tel.: +49 (0) 6343 939699

Document title:	Design Seismic Monitoring Californië – Definition of Monitoring Concepts
Project:	SafeGeo
Archive no.:	SGEO002
Version:	draft
Date:	30.10.2024
Author(s):	Dr. S. Baisch

Contents

1 BACKGROUND

1.1 Scope

- Propose a comprehensive set of different types of seismic monitoring options for the Californië geothermal field.
- The seismic monitoring focusses on detecting and locating earthquakes occurring in a predefined target area. The target area is approximately 4 km x 6 km, covering regions where previous seismicity occurred as well as an extended area around the GT05 injection well (Figure 1).
- Assess the expected performance of the monitoring networks.

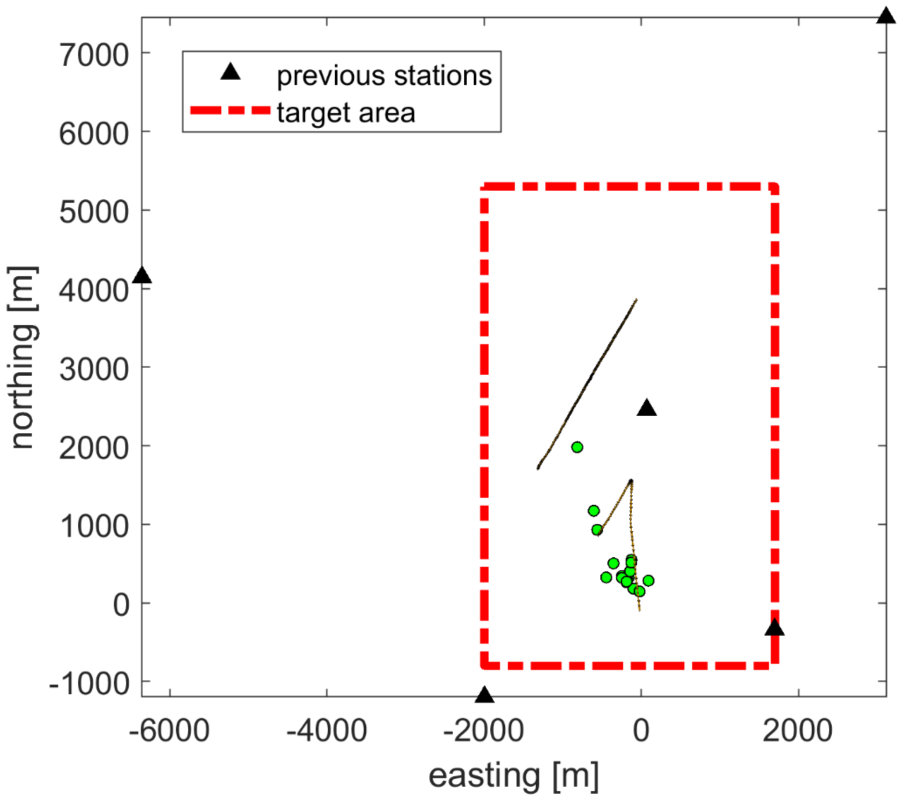

Figure 1: Definition of target area for monitoring future production (pilot phase) at Californië.

1.2 Relevant Factors

The performance of a seismic monitoring system is depending on the number of monitoring stations, their spatial distribution, and on the background noise level at the instruments sites.

The hypocentre location accuracy primarily depends on the station network geometry, i.e. the spatial distribution of stations which are recording an earthquake with sufficient signal-to-noise ratio. Hypocentre location accuracy tends to improve when using more stations.

The lower detection level of the network (magnitude of completeness) can be improved by reducing the seismic background noise level. This can be achieved by proper site selection or by using downhole instrumentation. Furthermore, the amplitude of the seismic signals is stronger the closer the recording instrument is to the source. Therefore, the lower detection level can be improved by instruments recording close to the seismic source.

2 MONITORING CONCEPTS

2.1 Surface Station Network

A surface station network consists of a minimum number of 4 to 5 seismic stations, which are azimuthally equally distributed around the target area.

With this type of network configuration, hypocentres of earthquakes are determined based on observed P- and S-wave travel times.

The depth of reservoir seismicity can be determined with higher accuracy if a station is operated in the epicentral region directly above the reservoir.

A surface station network has the following advantages:

- Maximum control on instrument deployment, e.g. regarding instrument levelling, instrument coupling etc.
- Ground vibrations are directly measured at the Earth surface, thus allowing a direct comparison to damage criteria.
- The frequency range for damage assessment is well covered (typical instrument configurations record signals in the frequency band 1-40 Hz or 1-80 Hz).
- Lowest costs compared to alternative options.

Compared to alternative monitoring concepts, the following disadvantages are identified:

- Reduced sensitivity due to comparatively large source-receiver distances and an increased noise level at the Earth's surface.

2.1.1 Previous Station Network

The previous station network serves as a baseline to compare with.

Code	X [m]	Y [m]	Z [m]	Lat [°]	Lon [°]	I95 [m/s]
K001	69	2459	0	6.093052518	51.42954838	3298
K002	-1996	-1196	0	6.063319664	51.39671074	2714
K003	1695	-336	0	6.116467288	51.40443739	3690
K004	3114	7447	0	6.136975808	51.4743532	919
K005	-6354	4147	0	6.000472829	51.44467267	1558

Table 1: Station coordinates in local system centred at 51.4074583333°/ 6.092058333333° and average I95 level of ground vibrations in vertical direction (measured values).

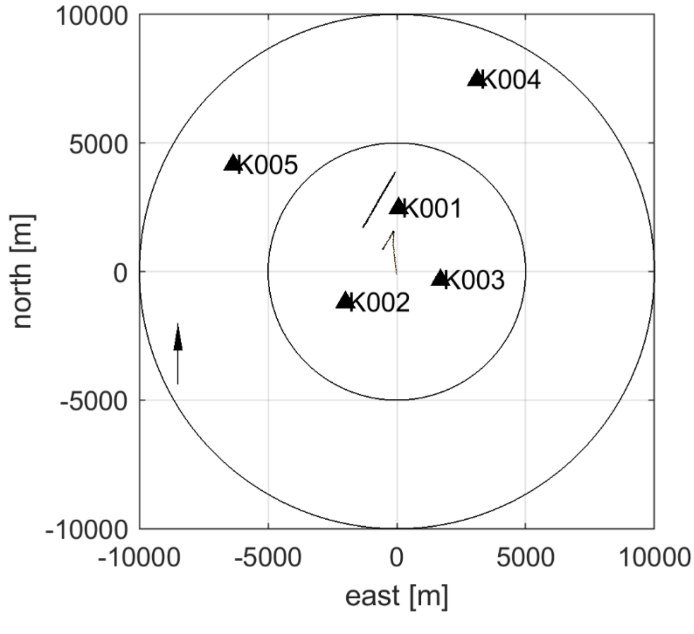

Figure 2: Station locations of the previously operated monitoring network. Local coordinates centred at 51.4074583333333°/ 6.09205833333333°.

Todo: simulate and compile MoC map & location error map for Mw=0.5

2.1.2 Extended Station Network

The extended network comprises the previous station locations extended by 3 stations. Additional stations were placed to improve the location accuracy and detection capabilities of the network near the previous region of seismic activity as well as near the future injection well GT05. The new locations are proposed based on geometrical criteria. The suitability of these locations (access, infrastructure, background noise level) has not been further investigated.

Keeping previous station locations avoids artificial bias from changing the network geometry. Furthermore, direct comparisons to previous earthquakes can be made, including e.g. relative hypocenter locations.

Code	X [m]	Y [m]	Z [m]	Lat [°]	Lon [°]	I95 [m/s]
K001	69	2459	0	6.093052518	51.42954838	3298
K002	-1996	-1196	0	6.063319664	51.39671074	2714
K003	1695	-336	0	6.116467288	51.40443739	3690
K004	3114	7447	0	6.136975808	51.4743532	919
K005	-6354	4147	0	6.000472829	51.44467267	1558
EXT1	-605	4536	0	6.083337644	51.44820647	2700
EXT2	-76	-113	0	6.090963843	51.40644321	2700
EXT3	1496	4100	0	6.113620369	51.44428808	2700

Table 2: Station coordinates in local system centred at 51.4074583333333°/ 6.09205833333333° and average I95 level of ground vibrations in vertical direction (black: measured values, grey: assumed values).

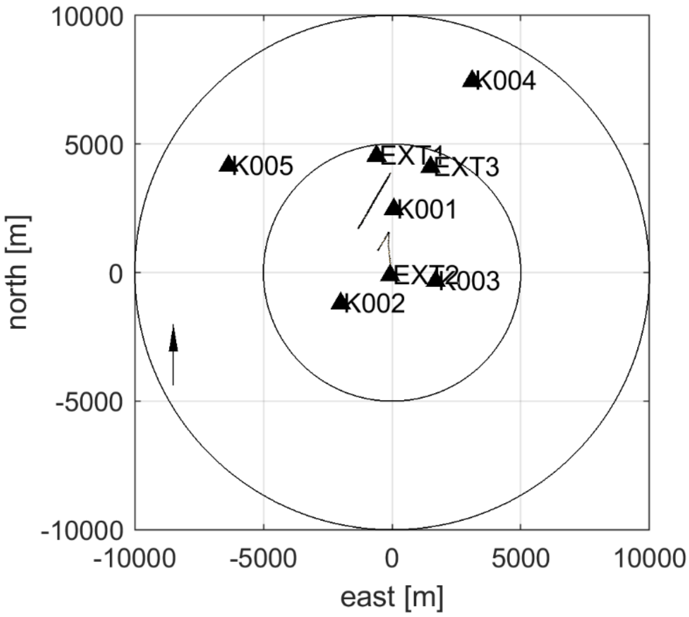

Figure 3: Station locations of the extended monitoring network. Local coordinates centred at 51.4074583333333°/ 6.09205833333333°.

Todo: simulate and compile MoC map & location error map for Mw=0.5

2.2 Shallow Monitoring Wells

To improve detection capabilities, monitoring instruments can be deployed in shallow observation wells. The typical configuration used by the KNMI comprises 200 m deep observation wells with geophones deployed at four different depth levels.

Theoretically, the deepest geophone should yield the best signal-to-noise ratio for earthquake signals coming from below. Therefore, the following performance assessment considers only the deepest geophone. It should be noted, however, that multi-level configurations add redundancy e.g. in case of instrument failure or coupling issues.

The geometrical design and the hypocentre location approach of a network with shallow monitoring instruments are identical to the ones described in section 2.1, resulting in similar hypocentre location errors.

To what extend the detection capabilities can be improved by shallow monitoring wells is depending on site specific details of the near-surface geology in combination with local noise characteristics. As a rule of thumb, the (surface) noise level decreases by a factor of approx. 10 in a 100 m deep monitoring well. This is partly due to near-surface amplification effects enhancing seismic vibrations at the Earth's surface. The near-surface amplification, however, also enhances seismic signals originating from the reservoir. This implies that the reduction of the noise level at depth correlates with a reduction of signal amplitudes. Therefore, the detection capabilities (determined by the signal-to-noise ratio, SNR) of the network is improved by a factor smaller than 10. Based on experience in NL, we expect that the signal-to-noise ratio can be improved by a factor of 6.5 when deploying instruments at 200 m depth (Ruigrok et al., 2023). This corresponds to a sensitivity increase of 0.8 magnitude units (M_L).

The disadvantages of this type of installation are:

- Limited control on instrument deployment at depth. This can result in a sensitivity loss due to borehole/instrument tilt or coupling issues.
- Ground vibrations are not measured at the Earth's surface and cannot be directly used for damage assessment.
- Larger costs compared to a surface network.

2.2.1 Basic Network

The basic network comprises the station configuration described in Table 1, while the SNR is assumed to have improved by a factor of 6.5.

Todo: simulate and compile MoC map & location error map for Mw=0.5

2.2.2 Extended Network

The extended network comprises the station configuration described in Table 2 while the SNR is assumed to have improved by a factor of 6.5.

Todo: simulate and compile MoC map & location error map for Mw=0.5

2.2.3 Combined with Surface Stations

ToDo: Based on previous simulations discuss characteristics of surface stations combined with shallow wells (e.g. sensitivity increase for those regions where 3 or more downhole stations record an event with sufficient SNR)

2.1 Geophone in Deep Observation well

Operating a single instrument in a deep observation well can significantly improve the lower detection limit. Seismic events of small magnitude, however, tend to be recorded only by the deep instrument, implying that neither their hypocentre nor their magnitude can be reliably determined.

Code	X [m]	Y [m]	Z [m]	Lat [°]	Lon [°]	I95 [m/s]
K001	69	2459	0	6.093052518	51.42954838	3298
K002	-1996	-1196	0	6.063319664	51.39671074	2714
K003	1695	-336	0	6.116467288	51.40443739	3690
K004	3114	7447	0	6.136975808	51.4743532	919
K005	-6354	4147	0	6.000472829	51.44467267	1558
EXT1	-76	-113	-2000	6.083337644	51.44820647	100

Table 3: Station coordinates in local system centred at 51.4074583333333°/ 6.09205833333333° and average I95 level of ground vibrations in vertical direction (black: measured values, grey: assumed values).

Simulate basic network + deep instrument @ GT03 for Mw=0.5

a) Single station detector
b) Three station detector

2.2 Geophone String in Deep Observation Well

In this configuration, a multi-level geophone string is deployed near the seismicity. This implies drilling a 2-3 km deep monitoring well, making this the most expensive monitoring solution discussed in the current study.

Due to the smaller source-receiver distances, the magnitude detection threshold for reservoir seismicity is significantly lower compared to (near-) surface monitoring concepts. This is illustrated in Figure 4 showing data from various hydraulic fracturing operations in the United States. At very short source-receiver distances, seismic events as small as Mw=-4 were detected. With increasing source-receiver distance, however, the detection capabilities quickly reduce (“viewing limit”). For example, at a source-receiver distance of 2 km, the lower detection threshold is in the order of M_w=-1.

This implies that e.g. a lower detection threshold of Mw=-1 throughout the entire target area cannot be achieved with a single geophone string.

With a single geophone string, the hypocentre location procedure cannot be based on simple triangulation concepts due to the linear network geometry. Additional information obtained from signal polarization properties are required to determine hypocentres. Data processing differs depending on the service provider. The typical processing steps, however, include:

1. hypocentral depth determination based on P-phase move-out (vertical geophone strings only),
2. distance to receiver determination based on differential travel times between the S- and P-phase,
3. azimuth (and eventually incidence) determination based on P-phase signal polarization. With this information, the hypocenter solution becomes unique.

The last step requires the exact knowledge of the individual geophone orientations. These are usually determined by calibration (perforation) shots in the treatment well at reservoir level. Uncertainties of the geophone orientations as well as of the P- phase steering vector lead to hypocentre location errors which are increasing with distance.

It should be noted that earthquake magnitudes determined with this type of monitoring configuration are subject to considerable uncertainty due to technical limitations (e.g. the geophone eigenfrequency typically is ≥ 15 Hz and a limited dynamic bandwidth of the recording system may cause magnitude saturation).

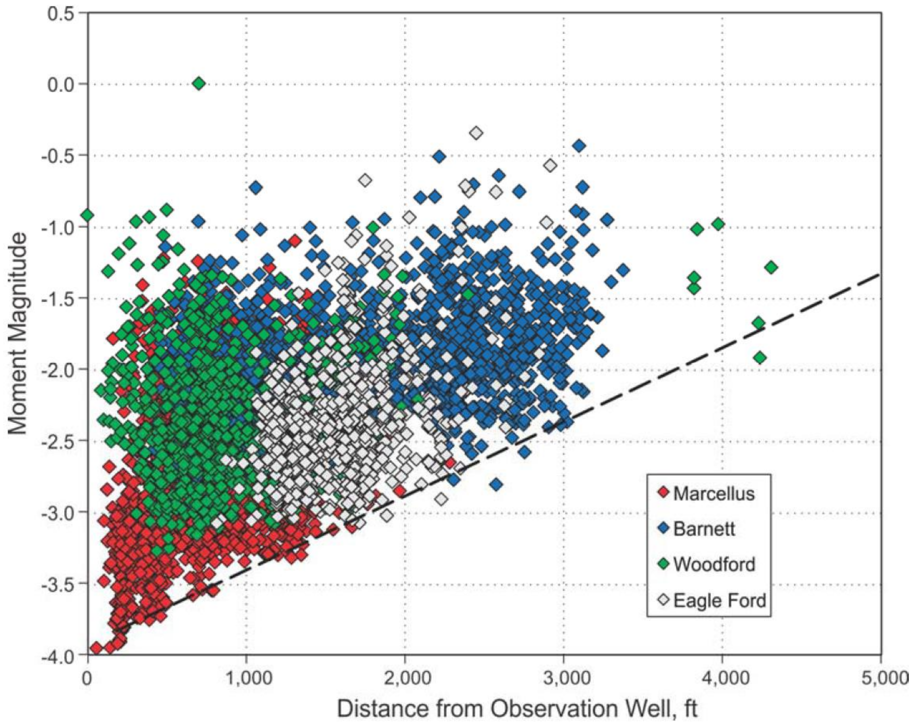

Figure 4: Moment magnitude of induced earthquakes plotted against the distance to the observation well. Observation data from different shale gas reservoirs according to the legend. Dashed line indicates the "viewing limit" of the recording instruments. The figure is taken from Warpinski et al., 2012.

3 REFERENCES

Ruigrok, E., Kruiver, P. P., & Dost, B. (2023). *Construction of earthquake location uncertainty maps for the Netherlands* (Technical Report No. TR-405) (p. 160). De Bilt: KNMI.

APPENDIX I - Table I. Summary of options for tests and measurements for the pilot phase

Options for data acquisition during the pilot phase Californië *		
	Data aquisition technique	How will it reduce uncertainties?
Structural geological & velocity model	3D seismic data from seismic survey 3D seismic data – covering Californië sites	- Distinguish between stratigraphic thinning/syn-depositional fault activity and the presence of faults to explain thickness differences within the Dinantian carbonates at the different wells. - Likely better understanding of exact location and extent of faults, as well as better understanding of orientations of faults and geological layers. - Better velocity model, which will lead to less uncertainty when calculating/estimating the hypocenter locations. - Focus should be on the imaging of the Paleozoic interval. For the current 2D seismic data available, this interval is often not well imaged. Possible: yes Remark: Expensive option
	Additional seismic lines - 2.5D seismic survey More 2D data to fill in data gaps between the wells	- Slightly better insights in the exact location of faults and their orientation within current data gaps. - Possibly also better grip on geological setting (see also point 1). - Prerequisite to be of added value is that the Paleozoic interval is well imaged. This is often not the case for the existing 2D seismic data Possible: yes Remark: Less expensive than 3D seismic, but also lower benefits in terms of reducing uncertainties.

	Velocity measurement: Sonic-density log over (entire or part) of borehole With sonic log: More information on interval velocities of the overburden. As a consequence better grip on seismic interpretation/seismic response and better insight in structural geological setting. With density log: Slightly better understanding of the seismic response	- Constrains acoustic velocities of especially the Namurian. Based on the current sonic log of CAL-GT-01, relatively low velocities for the Namurian are derived, but this is inferred only based on sonic data that is available at the very low part of the Namurian. - Being able to better quantify Namurian velocities will lead to more certainty in the seismic interpretation (both in terms of fault presence/orientation/dip of faults, as well as orientations/dip of geological layers) and in the hypocenter location estimates. Possible: yes Remarks: Added value for density log is less than sonic because there is usually a strong correlation between density and sonic. At the moment Gardner's relation is used to get insight in the seismic response. Discuss with acquisition expert to better distinguish between sonic log acquisition and VSP/checkshot data acquisition.
	Velocity measurement: Vertical seismic profiling (VSP) or checkshot Better constraints on interval velocity of the reservoir layers and the overburden. As a consequence better grip on seismic interpretation/seismic response and better insight in structural geological setting	- Constrains acoustic velocities of especially the Namurian. Based on the current sonic log of CAL-GT-01, relatively low velocities for the Namurian are derived, but this is inferred only based on sonic data that is available at the very low part of the Namurian. - Being able to better quantify Namurian velocities will lead to more certainty in the seismic interpretation (both in terms of fault presence/orientation/dip of faults, as well as orientations/dip of geological layers) and in the hypocenter location estimates. Possible: Likely yes (but should be discussed with data acquisition experts from service companies) Remarks: The benefit of a VSP or checkshot acquisition vs. sonic log acquisition is that VSP/Checkshot data are independent of the integrity of the borehole. If the borehole is (partly) collapsed, the sonic log will give unreliable results. Additionally, a VSP/checkshot data acquisition will also generate velocity information for the Mesozoic and Cenozoic intervals, without having to run a log over the entire interval (which is almost 2 km at the location of well CAL-GT-04)
	DAS-VSP in borehole DAS-VSP in shallow borehole, colocated with CPT	- Improve velocity model, o.a. to constrain hypocenter locations. In shallow boreholes and with CPT: For quantification of site-response and amplification, as input to the seismic hazard assessment

	Passive seismic S-wave survey	- Improve velocity model, o.a. to constrain hypocenter locations. Possible?: Feasibility to be assessed – w.r.t data quality, resolution and costs
	Cross-well tomography	- Detection of local velocity & structure between wells. Detection of velocity changes due to cooling, potential detection of karst? Possible: 2 wells needed for source-receiver configuration
	Cuttings: Description, sampling and petrographic analysis of Pont d'Arcole with focus on well CAL-GT-03 Better constraints on type of lithology below the Dinantian (i.e. is there a typical Pont d'Arcole present in well CAL-GT-03 or not?)	- The Pont d'Arcole is characterised by a deviating Gamma-Ray log signature in well CAL-GT-03. An explanation could be that the Pont d'Arcole is (partly) faulted out in this well and that the relatively high GR-values, which are now observed below the Dinantian, are in fact part of the damage zone of the Carboniferous normal fault. This would add certainty to the exact position of the Carboniferous normal fault. Possible: yes Remarks: Relatively cheap, but likely will not give absolute clarity on the presence of a fault damage zone. Hard to recognize damage zone in cuttings as slivers of Pont D'Arcole might have ended up in damage zone, or got mixed in the fluids while drilling.
Reservoir model	Standard log suite: Gamma-ray, Sonic, Density, Neutron, Resistivity, temperature log, Image log (FMI) temperature log in undisturbed situation FMI: more information on fracture network	- Constrain initial temperature - most measurements of temperature were done shortly after drilling. - In addition, a different temperature may be present near the Tegelen fault. - In the injectors, the temperature log could provide useful information on the temperature dissipation. - FMI: fracture network better known. - Combined logs: determine the position of faults in CAL-GT-03 Possible: FMI is possible in open hole wells, but CAL-GT-01 and 05 already have information available. Temperature log possible in all wells, except CAL-GT-02.
	Core samples, descriptions & laboratory analysis on cores	- measure thermal and reservoir properties in particular for formations below Zeeland Fm

		Possible: only on analogue samples from other sites or if sidetrack or sidewall samples are taken
	Well tests with downhole shut-in and limited WBS dual-porosity characteristics, improved estimate of permeability	- Different dual-porosity characteristics for different wells? Possible: possible in current wells (for Cal-GT-02, according to VITO only top reservoir is accessible)
	Interference tests connectivity between the wells	- Permeability between the wells Possible: possible in current wells (according to information from VITO only top reservoir in Cal-GT-02 is accessible)
	tracer test (Push-and-pull test) improved estimate of permeability around the well	- Better insight into permeability around the wells Possible: in CAL-GT-01/03/05
	PLT PLT for the injection wells are available, but not for the production wells	- Better insight in the inflow zones for the producers, which will enable better estimation of the connectivity and reduce uncertainty on initial temperature. Possible: Only possible in Cal-GT-01 (useful to combine with FMI), Cal-GT-04 is cased
	DTS with thermal back production test estimates of thermal properties and fracture density	- Fracture density is very important for understanding the progress of the thermal front Possible: in the producers, more difficult in the injectors due to historical cooling.
Geomechanical model	Well logs: Density, FMI, Caliper, Dipole Sonic In-situ stress field currently not constrained. Density log would help constrain the vertical stress at the site; information of FMI used to check consistency of stress directions. Dipole sonic to assess the dynamic elastic parameters of the reservoir and overburden	- Better estimate of density will improve the estimate of vertical stresses, which is one of the components of the stress field, determining initial criticality of the faults. - Additional FMI could be used to check consistency of direction of Shmax and Shmin directions (current estimate derived from existing FMI's). Possible: Density log possible. FMI possible in open hole wells; FMI available for GT-01, but not for deeper section (Devonian sst) --> would give more insight in fractures in lower sandstones. Quality of dipole sonic log depends on integrity of the borehole.

		Remarks: Sonic will give dynamic elastic parameters -> empirical relations needed or comparison to experimental tests on samples needed to translate to static elastic parameters.
	In-situ stress: Extended Leak Off Test (XLOT) or minifrac test Preferably minifrac test would help constrain in-situ stress field	- Estimate of magnitude of Shmin, which will help constrain the in-situ stress field and give insight initial criticality and reactivation potential of the fault. Possible: Likely yes (but should be discussed with data acquisition experts from service companies). Dedicated minifrac test with packers, not too close to fracture. (ideally in combination with image log, density log, sonic, caliper) Remark: generally it is difficult to constrain SHmax
	Core samples and or analogue samples: geomechanical tests / acoustic measurements	- Quantification of elastic parameters, thermo-elastic properties, cohesion, friction coefficient. (and if cores available – could also be used for hydrological parameters) Possible: No core samples are available for the Californië sites – only possible on analogue samples from other sites or quarries, or if sidewall samples are taken, or for sidetrack.
Monitoring before & during operations (in wells and at surface level)	Temporary mobile network of accelerometers	Insight in local noise levels for the benefit of optimal locations of permanent stations. Possible: Yes
	Null-measurement of seismicity	- Enables detecting any changes in magnitude-frequency relations of seismicity due to the restart of injection operations. Particularly useful if new monitoring stations are installed. Possible: Yes
	Accelerometers at surface level	- Monitor seismicity, as input to the seismic hazard assessment, assess the amplitudes surface ground motions due to the earthquakes in the context of damage assessment – see also chapter 8

		Possible: Yes
	Seismometers at or below surface level	- Monitor seismicity, as input to the seismic hazard assessment. See chapter 8. Possible: Yes
	Seismometers at intermediate depth in boreholes	- Monitor seismicity, as input to the seismic hazard assessment. Reduce noise levels. See chapter 8. Possible: Yes
	Seismometer in deep monitoring borehole	- Monitor seismicity, as input to the seismic hazard assessment. Reduce noise levels. See chapter 8. Possible: Yes
	Fiber optics: Distributed Acoustic Sensing (DAS) Distributed Acoustic Sensing (DAS) at surface level Distributed Temperature Sensing (DTS) Distributed strain sampling (DSS)	- DAS: Record microseismicity, at surface level: improved network aperture?, - DTS: measure distributed temperature profile (during injection/production tests), - DSS: detect strains in the rocks resulting e.g. from thermal contraction, poroelasic effects of fault slip.
	Borehole tiltmeters & extensometers	- Measures deformation in boreholes. To validate (cooling-induced) deformation and occurrence of aseismic deformation. Possible: Needs to be discussed with operator and technical experts. Preferably in borehole close to thermal & deformation front.
	Monitoring of flow rate, pressure, temperature and water composition	- For reservoir model validation and improvement
	Pulse test	- Permeability field, near-well cooling front, extent of cooling. Would be experimental (and likely highly challenging) in reservoir with fault and fracture dominated flow.

* The table gives a general overview of tests and measurements that could be performed to further constrain parameters, geology and reservoir behaviour. In section 9.2 more specifically options for data acquisition and tests are highlighted that can offer valuable information in a pilot phase at the Californië site

Energy & Materials Transition

Princetonlaan 6
3584 CB Utrecht
www.tno.nl